Universidade do Estado do Rio de Janeiro
Centro de Tecnologia e Ciências
Faculdade de Engenharia

Lívia Mantuano Corrêa

THERMAL ANALYSIS OF HEAT SINKS: AN ANALYTICAL APPROACH USING INTEGRAL TRANSFORMS

Rio de Janeiro, Brazil
2020

Lívia Mantuano Corrêa

THERMAL ANALYSIS OF HEAT SINKS: AN ANALYTICAL APPROACH USING INTEGRAL TRANSFORMS

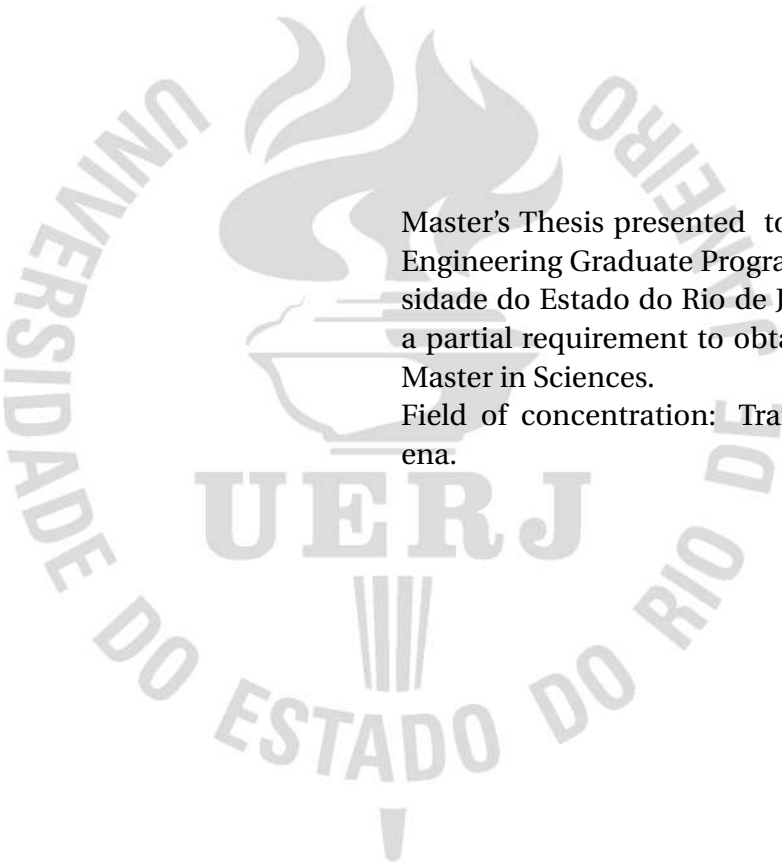

Master's Thesis presented to the Mechanical Engineering Graduate Program of the Universidade do Estado do Rio de Janeiro (UERJ) as a partial requirement to obtain the degree of Master in Sciences.
Field of concentration: Transport Phenomena.

Advisor: Prof. Daniel José Nahid Mansur Chalhub, DSc

Rio de Janeiro, Brazil

2020

CATALOGAÇÃO NA FONTE

UERJ / REDE SIRIUS / BIBLIOTECA CTC/B

C824 Corrêa, Lívia Mantuano.
Thermal analysis of heat sinks: an analytical approach using integral transforms / Lívia Mantuano Corrêa. – 2020.
146f.

Orientador: Daniel José Nahid Mansur Chalhub.
Dissertação (Mestrado) – Universidade do Estado do Rio de Janeiro, Faculdade de Engenharia.

1. Engenharia mecânica - Teses. 2. Calor - Transmissão - Teses. 3. Análise térmica - Teses. 4. Transformadas integrais - Teses. 5. Fluidodinâmica computacional - Teses. I. Chalhub, Daniel José Nahid Mansur. II. Universidade do Estado do Rio de Janeiro, Faculdade de Engenharia. III. Título.

CDU 536.6:517.44

Bibliotecária: Júlia Vieira – CRB7/6022

Assinatura

Data

Lívia Mantuano Corrêa

THERMAL ANALYSIS OF HEAT SINKS: AN ANALYTICAL APPROACH USING INTEGRAL TRANSFORMS

Master's Thesis presented to the Mechanical Engineering Graduate Program of the Universidade do Estado do Rio de Janeiro (UERJ) as a partial requirement to obtain the degree of Master in Sciences.
Field of concentration: Transport Phenomena.

Approved on August 19th, 2020.
Examining Committee:

Prof. Daniel José Nahid Mansur Chalhub, DSc (Advisor)
PPG-EM UERJ

Prof. Diego Campos Knupp, DSc
PPG-EM IPRJ-UERJ

Prof. Norberto Mangiavacchi, PhD
PPG-EM UERJ

Prof. Renan de Sousa Teixeira, DSc
PPGMMC UFRRJ

Prof. Rogério Martins Saldanha da Gama, DSc
PPG-EM UERJ

Rio de Janeiro, Brazil

2020

ACKNOWLEDGMENTS

Confesso que jamais imaginei que, às vésperas da entrega deste trabalho, o mundo estaria enfrentando tantas crises. Diante de tantas incertezas, gostaria de agradecer a todas as pessoas que me ajudaram de alguma forma a tornar a entrega deste trabalho possível, mesmo que não mencionadas.

Gostaria de agradecer ao meu orientador prof. Daniel Chalhub, com quem eu aprendi muito desde as aulas de termodinâmica, passando pela IC, TCC e mestrado. Trabalhando com ele, cultivei meu encanto pela pesquisa acadêmica e por transferência de calor. Foram muitos aprendizados ao longo desses anos e agradeço a este mestre por todos os ensinamentos, pela disponibilidade e paciência comigo.

Agradeço também aos professores do MECAN e do PPG-EM com quem tive aula, prof. Pontes, prof. Gustavo, prof. Marília, prof. Américo, prof. Luis Mariano, prof. Suzana e prof. Brant. Em especial, gostaria de agradecer ao prof. Norberto Mangiavacchi pela oportunidade de poder participar de diferentes projetos do laboratório GESAR e por todos os ensinamentos, lições de vida e comentários engraçados para descontrair um pouco a seriedade das reuniões.

Agradeço à banca de avaliação pela disponibilidade de examinar e contribuir ainda mais com este trabalho. Agradeço também à FAPERJ pela minha bolsa de mestrado e auxílio financeiro para apresentação de trabalho no ENCIT 2018, e à FAPESP pela oportunidade de participar da escola de energias renováveis (SPSASRE).

Gostaria de agradecer, em especial, ao grupo GESAR por todo o suporte, colaboração e amizade durante esses anos. Em especial, menciono Sônia, Jorge, Mário, Thaís, Leon, e o pessoal do LEN: Rachel, Ygor, Mariana, Daniel, Luis, Leandro, Haroldo, Carlos e Gabriel. Lembrarei com muito carinho desse grupo tão unido e colaborativo.

Além disso, gostaria de agradecer a meus pais e família pelos conselhos sábios e apoio em todos os momentos. Por fim, agradeço o apoio e companheirismo de meus amigos, presencialmente e à distância, que foram grandes incentivos para que eu conseguisse essa tão sonhada conquista.

ABSTRACT

CORRÊA, Lívia Mantuano. *Thermal Analysis of Heat Sinks: An Analytical Approach using Integral Transforms*. 2020. 146 p. Master's Thesis (Master in Mechanical Engineering) – Faculdade de Engenharia, Universidade do Estado do Rio de Janeiro, Rio de Janeiro, Brazil, 2020.

The present work develops an analytical approach using the Classical Integral Transform Technique (CITT) for solving heat transfer problems in heat sinks. The mathematical formulation is composed of a three-dimensional base and two-dimensional fins. The oncoming heat flux from a heated chip attached at the bottom of the base needs to be cooled to ensure its good performance and long service life. Fins coupled at the heat sink base's top are responsible for increase the heat transfer, and the air flows between fins contributing to the temperature's reduction of the system. The analytical methodology used is the Classical Integral Transform Technique, it is applied to solve the base and fins formulations. The fin-base coupling condition is then used to obtain the temperature field. OpenFOAM simulations are also performed for comparison purposes and to evaluate different shaped fins effectiveness. The developed analytical methodology innovates the study of heat transfer in heat sinks presenting the importance of 2D fin modeling for symmetrical and non-symmetrical cases.

Keywords: Heat Sinks; Heat Transfer; Classical Integral Transform Technique; Computational Fluid Dynamics.

RESUMO

CORRÊA, Lívia Mantuano. *Análise Térmica de Dissipadores de Calor: Uma Abordagem Analítica usando a Técnica da Transformada Integral.* 2020. 146 f. Master's Thesis (Master in Mechanical Engineering) – Faculdade de Engenharia, Universidade do Estado do Rio de Janeiro, Rio de Janeiro, Brazil, 2020.

O presente trabalho desenvolve uma abordagem analítica usando a Técnica de Transformação Integral Clássica (CITT) para resolver problemas de transferência de calor em dissipadores de calor. A formulação matemática é composta por uma base tridimensional e aletas bidimensionais. O fluxo de calor que se aproxima de um chip aquecido preso na parte inferior da base precisa ser resfriado para garantir seu bom desempenho e longa vida útil. As aletas acopladas na parte superior da base do dissipador de calor são responsáveis por aumentar a taxa de transferência de calor e, consequentemente, resfriar o sistema de forma mais eficiente. A metodologia utilizada é a Técnica da Transformada Integral Clássica, aplicada para resolver a formulação das aletas e da base, assim como um acoplamento de base-aleta é realizado em nos limites de seus domínios para obter o seu campo de temperatura. Simulações computacionais utilizando o software OpenFOAM também são realizadas para a verificação da metodologia analítica e análise da eficácia das diferentes geometrias de aleta. A metodologia desenvolvida inova no estudo da transferência de calor em dissipadores de calor, apresentando a importância da modelagem 2D de aletas para casos simétricos e não simétricos.

Palavras-chave: Dissipadores de Calor; Transferência de Calor; Técnica da Transformada Integral Clássica; Fluido-Dinâmica Computacional.

LIST OF FIGURES

LIST OF TABLES

LIST OF ABBREVIATIONS AND ACRONYMS

HS	Heat sink
CITT	Classical Integral Transform Technique
GITT	Generalized Integral Transform Technique
FVM	Finite Volume Methods
CFD	Computational Fluid Dynamics
OpenFOAM	Open-source Field Operation And Manipulation
PV	Photovoltaics
SSE	Solid-State Electronics

LIST OF SYMBOLS

T	Temperature, K
k	Thermal conductivity, W/(m·K)
L	Base dimension in x-direction, m
W	Base and fin dimension in y-direction, m
H	Base dimension in z-direction, m
H_a	Fin dimension in z-direction, m
T_f	Temperature of the surrounding air, K
T_{sur}	Temperature in the surroundings surfaces, K
T_{char}	Characteristic temperature, K
h	Heat transfer coefficient, W/(m^{2}K)
h_{conv}	Convective heat transfer coefficient, W/(m^{2}K)
h_{rad}	Radiative heat transfer coefficient, W/(m^{2}K)
k_f	Thermal conductivity of air, W/(m·K)
g	Gravity, m/s^2
$\dot{q}''_o$	Heat flux from the heated chip, W/m^2
$\dot{q}''_{base}$	Heat flux entering the fin from the base
$\dot{q}''_{fin}$	Heat flux leaving the base to the fin
n_{fin}	Number of fins
N	Normalization integrals

GREEK SYMBOLS

Θ	Dimensionless temperature
δ	Thickness of fin
ξ	Dimensionless Cartesian x-coordinate
η	Dimensionless Cartesian y-coordinate
ζ	Dimensionless Cartesian z-coordinate for the base
ζ_a	Dimensionless Cartesian z-coordinate for the fin
β, γ	Aspect ratios for the base
β_a, γ_a	Aspect ratios for the fin
Ξ, μ	Eigenfunction and eigenvalue in ξ-direction, respectively
Ψ, λ	Eigenfunction and eigenvalue in η-direction, respectively
α	Embracing parameter indicating the position of fins
α_{avg}	Average value of α for the fins layout
ΔT	Temperature range
ΔT_b	Average temperature difference between the heat sink and the environment
δ_a	Fin thickness

σ	Stefan-Boltzmann constant
ϵ	Surface emissivity
ϱ	Volumetric expansion coefficient
ν	Kinematic viscosity

Dimensionless numbers

Bi_H	Biot number for the base
Bi_{Ha}	Biot number for the fin
m_a	Dimensionless combination for 1D fin
A_1, A_2, A_3	Dimensionless combination for the boundary conditions
Pr	Prandtl number

Overscripts

$\bar{}$	Integral transform single transformation
$\bar{\bar{}}$	Integral transform double transformation

Subscripts

m	CITT index for ξ-direction
n	CITT index for η-direction
$\mathrm{n}_{\max}$	CITT's one transformed direction truncation order
$\mathrm{k}_{\max}$	CITT's two transformed directions truncation order
ic	Index for contact interface

SUMMARY

INTRODUCTION

The Solid-State Electronics (SSE) thermal management is a rolling and critical issue for modern electronic devices design found in diverse industrial applications such as high-performance computers, solar power generation, nuclear plant industries, aircraft, and so on.

The Moore's Law (MOORE, 1965) predicted the worldwide trend of miniaturization in the semiconductors industry and, as consequence, several innovative applications such as limited weight and space operations, high-performance computers, and consumer-aimed products, i.e. watches, smartphones, and intelligent cars became a reality (STREETMAN; BANERJEE et al., 1995).

These electronics have had their size decreased and, with more internal components concentrated, more power dissipation is required to ensure safe and efficient performance of the system, especially in multilayer chip stacks (RENFER et al., 2013). Electronic chip stacks technology can reach as high as 250 W/cm^2 in multilayer chip stacks of less than 0.3 cm^3 (ALFIERI et al., 2010). Peterson and Ortega (1994) assert that the average component temperature must be maintained equal or below the manufacturer's maximum specified service temperature in order to guarantee an effective performance and a long service life; in contrast, a violation of which can significantly compromise the reliability of the device. According to Lee, Early and Pellilo (1997), the failure rates of electronic components almost double when junction temperature increases by 10^{o}C beyond operating temperatures; thus, the electronic components' cooling has been substantially studied for over 30 years.

Cost-effective modifications such as heat sinks coupling are considered a key point to minimize SSE's temperature and ensure reliability. Heat Sinks are passive heat exchangers transferring the thermal energy from a heated electronic component to a cooling fluid medium, often air or a liquid coolant. They are designed to significantly increase the contact surface area between solid and fluid, thereby increasing the heat transfer and, consequently, regulating the device's temperature at optimal levels. Heat sinks are generally composed by a set of fins and can be designed as (PINHEIRO; SPHAIER; ALVES, 2018):

Closed-sandwich configuration: fins are perpendicularly connected to two parallel base surfaces as schematically depicted in Figure 1a. Mostly used on microchannel heat sinks design (QU; MUDAWAR, 2002).

Open-sandwich configuration: fins are perpendicularly connected to one single base surface as shown in Figure 1b. Air-cooled microelectronics, power electronics components, and solar energy are some of this heat sink design applications (ANAND; KIM; FLETCHER, 1992; ARULARASAN; VELRAJ, 2010).

The performance of heat sinks is dependent on several parameters such as the ge-

Figure 1 - Parallel plate heat sink configuration examples. This type of heat exchanger is composed by a set of fins and may be connected by one or two parallel plates on the fins edges.

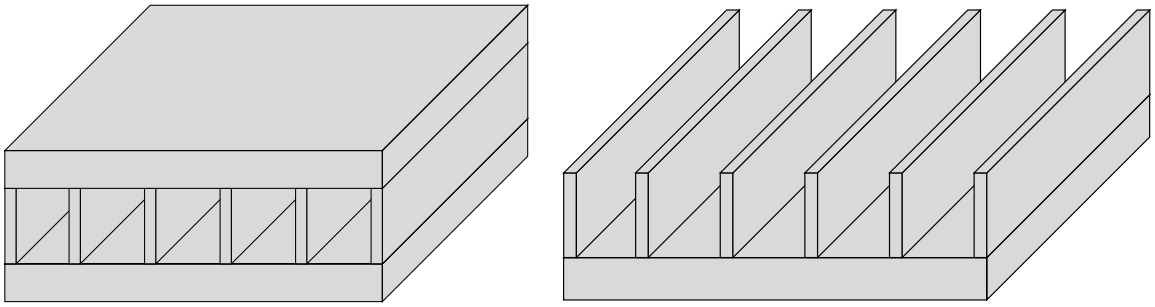

(a) Closed Sandwich configuration

(b) Open Sandwich configuration

ometry of the fin, quantity of fins, fluid's properties, and the heat sink's thermal properties (LEHTINEN, 2005). These parameters define the thermal resistance of the heat sink.

Thermal resistance of the Heat Sink

Thermal resistance is considered an essential index to demonstrate the thermal dissipation capability and is usually determined experimentally using an infrared technique (LU et al., 2012). It indicates if the heat is being well conducted in a device and is widely considered when choosing and designing heat sinks (SIMONS, 2015). The series thermal resistance of a heat sink system is usually composed by:

- The resistance from the device requiring more power dissipation (diodes, integrated circuits). It is usually given by the device manufacturer.
- The resistance between the device and the heat sink. It depends on factors such as the assembly method, the surface roughness, and the thermal grease type. This resistance can be neglected in most models (COROMINAS, 2010).
- The resistance between the base of the heat sink and the environment air. Hence, the set of fins and fluid channels compose a parallel thermal resistance.

Figure 2 describes an example of a heat sink thermal resistance scheme, where the resistance between the device and the heat sink is neglected. As the engineering keeps developing more efficient materials, compositions, and geometries for the fins and channels, solve the heat sink differential equation formulations and obtain their temperature fields becomes essential in order to closely analyze the heat sink performance modifications.

Figure 2 - Example of a heat sink (HS) thermal resistance. The left image shows its layout, the components of the thermal system, and the temperature range of the system where T_{chip} and T_{air} are the maximum and minimum temperatures, respectively. The right scheme describes the thermal circuit for the HS exemplified.

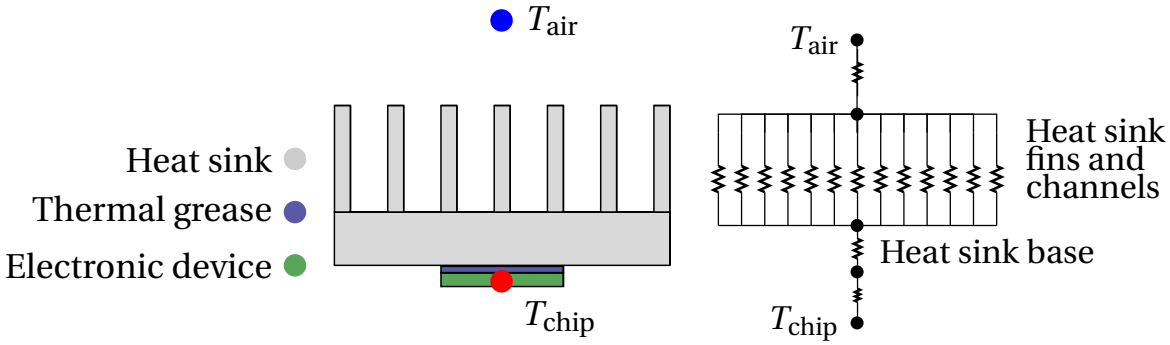

Literature Review

The reduction of the temperature of Solid-State Electronics provides a wide range of industrial applications; hence, it has been motivating a significant variety of studies in this field. Incropera (1988) published a comprehensive review of convection cooling options in which different types of heat sinks are mentioned.

The review performed by Adham, Mohd-Ghazali and Ahmad (2013) was devoted to the overall thermal and hydrodynamic performance enhancement of microchannel heat sinks. An extensive comparative study of the available literature on forced convection in microchannel heat sinks is provided considering different coolant types, channel geometries, flow conditions, heat sink materials, and the nature of work (analytical, numerical, or experimental). Several conclusions can be drawn from this review, for instance, the growing interest in microchannel heat sinks asserting the development of research in this area. Recent studies also indicate that nanofluids possess a promising prospective for new electronics cooling devices, reducing working temperatures and decreasing the size of cooling devices are the main benefits of employing nanofluids as a coolant in electronics in comparison with ordinary liquids. The review from Kumar et al. (2018) explores the nanofluids interest and applications in microchannel heat sinks for performance improvement.

The parallel plate heat sink can suffer some improvements for an enhanced heat transfer, thus a continuing research theme on heat sinks is the thermal dissipation promoted by the fins. Several works about analysis and optimization of their fins were published. Ong et al. (2005), for instance, analyzed different geometries fins optimizations for maximum heat dissipation on electronic components. Rectangular, parabolic, cylindrical, and concave spines profiles were evaluated. Azarkish, Sarvari and Behzadmehr (2010), Azarkish, Farahat

and Sarvari (2012) investigated the geometry of the longitudinal fins with a variable cross-sectional area achieving its optimum fin profile by genetic algorithm and Particle Swarm Optimization to optimize the maximum heat loss for a specific fin volume. Another interesting work evaluating fin profile was published by Cuce and Cuce (2014), where the heat transfer from a longitudinal fin with step change was analyzed. Different rectangular fins configurations were tested to produce the maximum heat loss in a specific volume and length numerically exposed to convection and radiation heat transfer. Mosayebidorcheh et al. (2015) developed a formulation for rectangular, triangular, and parabolic fin profiles and optimize them for different materials. A recent paper from Shaeri and Bonner III (2019) proposed an analytical model of laterally perforated-finned heat sinks to predict the average Nusselt numbers in forced convection laminar flows. The developed model used experimental data acquired from testing air-cooled heat sinks including square cross-sectional perforations distributed equidistantly along the length of the fins. In summary, the fins' geometry is a relevant topic to be evaluated for heat transfer enhancement in heat sinks.

Several works (AZARKISH; SARVARI; BEHZADMEHR, 2010; AZARKISH; FARAHAT; SARVARI, 2012; CUCE; CUCE, 2014; MOSAYEBIDORCHEH et al., 2015; BABAELAHI; ESHRAGHI, 2017; PINHEIRO; SPHAIER; ALVES, 2018; SINGH; KUMAR; RAI, 2018) analyze fins considering one-dimensional heat conduction. The applicability of assuming a one-dimensional fin with a two-dimensional coating instead of considering both two-dimensional was evaluated by Xia and Jacobi (2004). The heat conduction of a composite medium composed of fin and coating material was analyzed and, despite some one-dimensional fin formulation advantages such as a simpler calculation and a fast convergence, the two-dimensional fins assumption provides a more accurate model. The necessity of the traditional one-dimensional fin model replacement to a two-dimensional heat conduction model is explained by Aziz and Makinde (2010) to ensure accurate thermal performance predictions on orthotropic characteristics of advanced heat sink materials. The two-dimensional orthotropic pin fin heat conduction is solved by Zubair, Arif and Sharqawy (2010), moreover, an isotropic fin is considered instead of an orthotropic one. Ma, Behbahani and Tsuei (1991), Lehtinen (2005), Malekzadeh and Rahideh (2009), Bouaziz (2009), Moitsheki and Rowjee (2011) have also developed two-dimensional fins studies.

As mentioned previously, the thermal resistance of heat sinks depends on several designs and material parameters that directly impacts its performance. For this reason, optimization studies are relevant to the purpose of the thermal performance of heat sinks enhancement. Kim (2004) presents different optimization methods for the minimization of the thermal resistance of the microchannel heat sink. The fin model considers unidirectional conduction, constant heat transfer coefficient, and uniform fluid temperature assumptions, while the porous medium model is based on the volume-averaging of velocity and temperatures in the direction perpendicular to the flow direction. Both analytical models were verified with a three-dimensional numerical optimization method. The minimization of overall

thermal resistance with genetic algorithms is used by Wei and Joshi (2003). In this work, the thermal resistance for a two-layered stacked microchannel heat sink can be minimized by optimizing the aspect ratio, fin width, and the channel to fin width ratio. From this study's conclusions, the thermal resistance of an optimized stacked microchannel has a strong dependence on the channel length. The shorter the channel, the smaller the thermal resistance for the optimized microchannel. The minimization of the thermal resistance was also considered by Copeland (2000) to calculate the optimum dimensions of fin thickness and pitch under realistic operating conditions for forced convection heat sinks. Also, there is the research developed by Türkakar and Okutucu-Özyurt (2012) regarding a dimensional optimization of silicon heat sinks for located multiple heat sources by minimizing the thermal resistance at constant pumping power. Khan, Yovanovich and Culham (2006) used the entropy generation minimization (EGM) procedure to minimize the overall performance of microchannel heat sinks. From the optimization performed, the combined effects of thermal resistance and pressure drop assessed simultaneously as the heat sink interacts with the surrounding flow field. As can be seen, there are several optimization studies in heat sinks available in the literature. The heat sinks thermal design optimization review presented by Ahmed et al. (2018) summarizes investigations for developing the thermal performance of the heat sinks, limitations, and unsolved proposed solutions regarding the passive and active techniques utilized for enhancing the heat removal from heat sinks.

Integral Transform Technique

The Integral Transform Technique (MIKHAILOV; OZISIK, 1984; COTTA, 1993) is a powerful method for solving differential equations based on expansions of the sought solution in terms of an infinite orthogonal basis of eigenfunctions (CHALHUB, 2015), and is classified as Classical or Generalized. The method has advanced through both mathematical and computational aspects, as described by Cotta et al. (2020), to challenge applications that may pose difficulties to the well-established numerical methods.

The Classical Integral Transform Technique (CITT) is an all analytical method, especially applied in linear problems. The method transforms Partial Differential Equations (PDE) into a system of Ordinary Differential Equations (ODE) that can be solved using available computational implementation, subroutines, and libraries.

Due to the technique's evolutionary development, an integral transforms generalization can be applied to non-transformable systems, including nonlinear problems, making the method applicable to a virtually infinite number of problems (CHALHUB, 2015). The Generalized Integral Transform Technique (GITT) is usually applied in cases where a term cannot be transformed; thus, the Generalized method is classified as a hybrid computational-analytical technique (COTTA et al., 2020).

The results achieved using integral transforms match with other well-established experimental and fully-numerical methodologies (Naveira-Cotta; COTTA; ORLANDE, 2011). According to Cotta (1993) and Chalhub (2011), the systematic solution methodology; the reduction of processing time; prescribed error control; fast convergence; and the solution in a continuous domain because of the non-existence of discretization meshes are significant advantages presented by the CITT analytical approach against numerical methodologies.

The Integral Transform Technique was previously applied to electronic problems. Dantas (1996), Dantas and Orlande (1996) applied the integral transform technique on an encapsulated microchip and obtained the solution considering different thermal conductivity layers over the chip thickness. More recently, the thermal behavior of electronic components, with one or multiple hot spots, was studied by Corrêa (2018) using single and double transformations of the Classical Integral Transform Technique (CITT). Even though both methodologies achieved the same final values, the single transformation was evaluated as more efficient for this problem because it required fewer terms to be summed to the full convergence. The verification between analytical and numerical results confirmed that CITT and Finite Difference Method (FDM) converge to the same final value.

Motivated with heat sinks for electronic components applications, Knupp (2010) provided experimental and theoretical results using the Generalized Integral Transform Technique to thermally analyze a nanocomposite made from the dispersion of aluminum oxide in a polyester matrix. Also, two recent works using the Integral Transform Technique on heat sinks were published. The application of the Integral Transforms for solving the conjugated radiation-conduction in a finned-tube configuration problem for transient closed and open sandwich configurations was proposed by Pinheiro, Sphaier and Alves (2018). In the same year, Corrêa and Chalhub (2018) presented an integral transforms approach for heat sinks considering different values for the heat transfer coefficient depending on the position of the fins. This work is attached in Appendix D.

Finite Volume Method

Finally, an efficient way to verify the consistency of an analytical method is by comparing it using Computational Fluid Dynamics. Computational Fluid Dynamics (CFD) has revolutionized engineering design practices since its start in the late 1950s and has impacted practically all areas of human economy and social activities: energy, electronics, transportation, health physics, food processing, propulsion, pharmaceutical sciences, and many others fields (RUNCHAL, 2020). Patankar and Spalding (1971) presented a general, numerical, marching procedure for the calculation of transport processes in three-dimensional flows. Further advances in the prediction of parabolic flows came from the development of the models for turbulence, radiation, and chemical reaction (PATANKAR; SPALDING, 1973;

PATANKAR, 1980; LAUNDER; SPALDING, 1983). Some developments in the various aspects of computational techniques are reviewed by Patankar (1988) and Spalding (2013).

CFD methods divide the domain into discrete components, and evaluate the mathematical formulations, mostly partial differential equations (PDE), in the discrete domain. The methods differ by the type of the discrete component (node, volume, or element) and how the formulations are expressed. The Finite Difference Method (FDM) is based on expressing the "derivatives" in terms of Taylor series and the Finite Element Method (FEM) is based on linear or non-linear mathematical function, both primarily "mathematical" methods. The Finite Volume Method (FVM) developed by Spalding and his students, however, has its concepts in terms of the transferred rates between adjacent volumes, an approach based on the physics of the problem (RUNCHAL, 2020).

The Finite Volume Method (FVM) uses the integral form of the conservation equations directly in the physical space. The computational domain is divided into a finite number of control volumes and an algebraic equation for each control volume is obtained. One advantage of FVM is the representation of the grid by either structured or unstructured mesh. Another attractive feature is that the method does not require equations transformation in terms of the body-fitted coordinate system as required in the Finite Difference Method (TU; YEOH; LIU, 2018).

A substantial variety of works about heat sinks using numerical methods were published recently. A detailed approach of metal foams applied on heat sinks was implemented by Al-Athel et al. (2017) in a finite element analysis and validated with experiments. Limbasiya, Roy and Harichandan (2017) presented a numerical study using the SIMPLE algorithm for cooling of fins with forced air convection in a single microchannel heat sink where it was concluded the better performance of staggering heat sinks over standard ones. Zaretabar, Asadian and Ganji (2018) present a numerical heat transfer simulation of a heat sink installed on a square chip of a computer using the fourth-order Runge-Kutta method to solve the non-linear heat transfer equation. Also, the research developed by Malek and Shabani (2018) simulates macro and microscope heat transfer utilizing different formulations for different scales. The used methodology is based on spectral methods, solving it numerically by spectral discretization and finite differences method. The microscope analysis uses the dual-phase lag formulation and for the macroscope problems, based on the Fourier Law, commercial software was used for the simulations.

The finite volume method (FVM) has been utilized for analyzing heat transfer in heat sinks. A hybrid heat sink was solved by Krishnan, Garimella and Kang (2005) using a finite-volume method on an orthogonal, rectangular grid. Bushehri, Ramin and Salimpour (2015) proposed a new method for coupling equations between fluid and solid domains with temperature jump boundary conditions and implemented in the open-source computational fluid dynamics package, the finite volume method based OpenFOAM. The recent publication from Lampio and Karvinen (2018) compares some simple analytical and computational

fluid dynamics (CFD) solutions using OpenFOAM. The presented method solves convection heat transfer from analytical equations while conduction is used is solved numerically. In summary, due to its large number of works available, especially in heat sinks, the finite volume method leads to be an excellent numerical method to verify the integral transforms of the analytical results.

In summary, the available literature shows different numerical approaches for conducting heat in heat sinks. However, analytical methodologies are still little explored for this type of problem, especially considering the fin's heat conduction in more than one direction.

Objectives

The main goal of the present work is to propose an analytical approach to solve heat transfer problems in heat sinks (HS). The analytical methodology solves the three-dimensional base and two-dimensional fins' formulations, and couple the analytical solutions to obtain the HS' temperature field. This approach suits open-sandwich [1] parallel plate heat sink. In addition, the dimensionless problem facilitates the overall value group visualization within a range of intervals in the parameters. The methodology used in this work is the Classical Integral Transform Technique (CITT). The CITT results are verified using OpenFOAM, a FVM open-source software.

Dissertation Organization

The present dissertation is organized in chapters. Chapter 1 demonstrates the formulations used in this work, divided into the sections of fin and base formulations, the fin-base coupling condition, and the heat transfer coefficient.

The analytical methodology is described in Chapter 2, where the Classical Integral Transform Technique is applied in the different parts of the heat sink. The 3D base and 2D fin formulations are solved separately and coupled. Then, a simplified model of the heat sink considering 2D base and 1D fin is solved and used as a benchmark.

In Chapter 3, the verification methodology using the OpenFOAM software is described.

The results are presented and discussed in Chapter 4. First, the methodology convergence is shown as well as the comparison between the CITT formulations, considering three different heat sink cases for different applications. The comparison between OpenFOAM numerical results and CITT are presented as well as different fin-shaped heat sinks

[1] Figure 1b

thermal analysis using OpenFOAM. Symmetric and non-symmetric heat sink problems are, then, solved using the proposed methodology. Finally, different possibilities to enhance the heat transfer promoted by heat sinks are shown.

Finally, Chapter 5 concludes the presented work and enumerates possible future works.

1 MATHEMATICAL FORMULATION

The purpose of this chapter is to present the mathematical model for the heat conduction in heat sinks utilized for cooling electronic components. The model is composed of two-dimensional fins coupled to a three-dimensional base.

The fins coupled at the top of the heat sink's base are responsible for increasing the heat transfer and, consequently, cool the system. They are thermally connected to the base by the interface contact surface (HAHN; OZISIK, 2012), in this work a perfect contact is considered. The base and fins are considered to be manufactured using the same material, therefore, base and fins have the same physical properties.

Figure 3 shows a scheme of the parts of the heat sink: the fin in 3a, the base and the fin-base contact interface in 3b, and the complete scheme of a one-fin heat sink in 3c.

This chapter is divided in the following parts:

- Fins formulations
- Base formulations
- Fin-base coupling condition
- The Convection-Radiation Heat Transfer Coefficient

1.1 **Fins formulations**

An extended surface is an extrusion of a relatively small cross-sectional area from a large body into a fluid at a different temperature. Extended surfaces have wide industrial applications such as fins attached to the walls of heat transfer equipment to increase the rate of cooling (KREITH; MANGLIK; BOHN, 2012).

An energy balance for a small element of the fin is performed to derive an equation for temperature distribution in steady-state for the fins. Figure 4 illustrates the scheme of the fin. Since the fin thickness is much smaller when compared to its height and width, the thickness is partially lumped (HAHN; OZISIK, 2012; CORRÊA, 2018). The enlargement of the dimensions must be noticed for better visualization and the direction of fluxes in the control volume (CV). The dimensions of the fin are H_a, W and δ. This present formulation considers a rectangular geometry for the fin.

Figure 3 - One-fin heat sink scheme. The problem formulation is divided in three parts: the fins, the base and the solutions coupling.

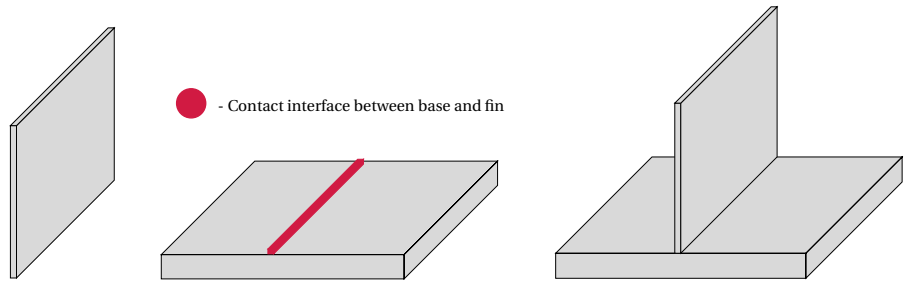

(a) Fin (b) Base and fin-base contact interface (c) Heat sink

rate of heat flow by conduction into element at z	+	rate of heat flow by conduction into element at y	=	rate of heat flow by conduction out of element at z + dz	+	rate of heat flow by conduction out of element at y + dy	+	rate of heat flow leaving from surface

$$\dot{q}''_z \delta \Delta y + \dot{q}''_y \delta \Delta z = \dot{q}''_{z+\Delta z} \delta \Delta y + \dot{q}''_{y+\Delta y} \delta \Delta z + 2\dot{q}''_{conv} \Delta y \Delta z \tag{1}$$

where:

$\dot{q}''_z \rightarrow$ heat flux entering z-direction

$\dot{q}''_y \rightarrow$ heat flux entering y-direction

$\dot{q}''_{z+\Delta z} \rightarrow$ heat flux leaving z-direction

$\dot{q}''_{y+\Delta y} \rightarrow$ heat flux leaving y-direction

$\dot{q}''_{out} \rightarrow$ Heat flux leaving the fin by its walls

$\Delta z \rightarrow z$-direction CV dimension

$\Delta y \rightarrow y$-direction CV dimension

$\delta \rightarrow$ thickness on x-direction CV dimension

Expanding the outlet heat flux term and dividing by $(\Delta y \Delta z)$, the following equation is found:

$$-\frac{\dot{q}''_{z+\Delta z} - \dot{q}''_z}{\Delta z}\delta - \frac{\dot{q}''_{y+\Delta y} - \dot{q}''_y}{\Delta y}\delta = 2h(T - T_f) \tag{2}$$

Figure 4 - Infinitesimal volume control for the fin. The heat fluxes indicate the heat conduction for the two directions, y and z. Since the temperature does not vary in its thickness δ, the x-direction is lumped. Heat is dissipated in both sides of the fin as indicated by $\dot{q}''_{out}$.

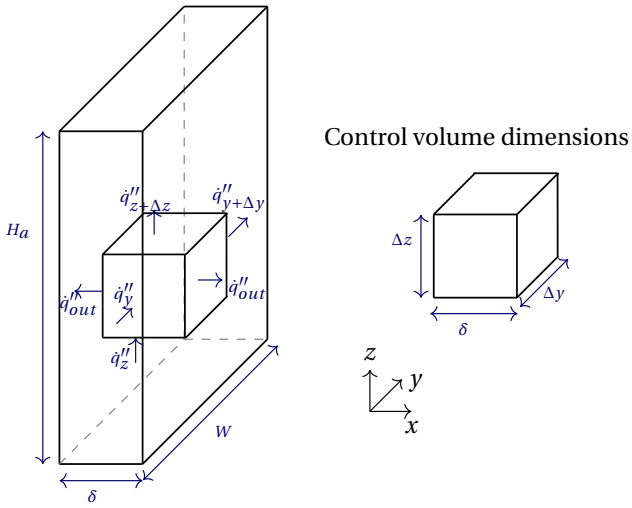

where h is the heat transfer coefficient, T is the temperature, and T_f is the surrounding air temperature. The heat transfer coefficient h estimation is described in Section 1.4.

The partial derivatives are obtained using the definition of limits for the heat fluxes on (3). Then, on equation (4), the heat flux is rewritten applying the Fourier law of heat conduction:

$$-\frac{\partial\left(\dot{q}''_z\right)}{\partial z}\delta-\frac{\partial\left(\dot{q}''_y\right)}{\partial y}\delta=2h(T-T_f) \tag{3}$$

$$\frac{\partial}{\partial z}\left(k_z\frac{\partial T}{\partial z}\right)+\frac{\partial}{\partial y}\left(k_y\frac{\partial T}{\partial y}\right)=\frac{2h(T-T_f)}{\delta} \tag{4}$$

where k_z and k_y are the thermal conductivity in z-direction and y-direction, respectively.

Considering that k_z and k_y do not depend on their partial derivatives:

$$k_z\left(\frac{\partial^2 T}{\partial z^2}\right)+k_y\left(\frac{\partial^2 T}{\partial y^2}\right)=\frac{2h(T-T_f)}{\delta} \tag{5}$$

Equation (5) is the formulation for two-dimensional fins considering orthotropic materials, whose thermal conductivity differ along orthogonal axes (HAHN; OZISIK, 2012). In this work, the material is considered isotropic. The thermal conductivity is independent of direction on isotropic media (HAHN; OZISIK, 2012). In other words, $k_z = k_y = k$.

$$k\left(\frac{\partial^2 T}{\partial z^2}\right)+k\left(\frac{\partial^2 T}{\partial y^2}\right)=\frac{2h(T-T_f)}{\delta} \tag{6}$$

1.1.1 2D fin formulation

The formulation for rectangular isotropic 2D fins is written as:

$$\frac{\partial^2 T}{\partial z^2} + \frac{\partial^2 T}{\partial y^2} = \frac{2h(T - T_f)}{k\delta} \quad \text{for} \quad 0 \le y \le W \quad \text{and} \quad 0 \le z \le H_a \tag{7a}$$

$$-k\left.\frac{\partial T}{\partial z}\right|_{z=0} = \dot{q}''_{\text{base}}; \quad \left.\frac{\partial T}{\partial z}\right|_{z=H_a} = 0; \quad \left.\frac{\partial T}{\partial y}\right|_{y=0} = 0; \quad \left.\frac{\partial T}{\partial y}\right|_{y=W} = 0 \tag{7b}$$

where $\dot{q}''_{\text{base}}$ is the fin-base contact interface flux, W and H_a are the dimensions of the fin in y and z directions respectively and δ is half of the thickness of the fin. The surfaces $z = H_a$, $y = 0$, and $y = W$ present much smaller surface areas. For this reason, insulation is considered for the fins' top ($z = H_a$) and width ($y = 0$ and $y = W$) boundaries.

The non-dimensionalization of the two-dimensional fins leads to the following mathematical formulation:

$$\frac{\partial^2 \Theta}{\partial \zeta_a^2} + \gamma_a^2 \frac{\partial^2 \Theta}{\partial \eta^2} - (2\text{Bi}_{H_a}\beta_a)\Theta = 0 \quad \text{for} \quad 0 \le \eta \le 1 \quad \text{and} \quad 0 \le \zeta_a \le 1 \tag{8a}$$

$$\left.\frac{\partial \Theta}{\partial \zeta_a}\right|_{\zeta_a=0} = -A_1 \dot{q}''_{base}; \quad \left.\frac{\partial \Theta}{\partial \zeta_a}\right|_{\zeta_a=1} = 0; \quad \left.\frac{\partial \Theta}{\partial \eta}\right|_{\eta=0} = 0; \quad \left.\frac{\partial \Theta}{\partial \eta}\right|_{\eta=1} = 0, \tag{8b}$$

The non-dimensional groups are defined as:

$$\zeta_a = \frac{z}{H_a}; \quad \eta = \frac{y}{W}; \quad \Theta = \frac{T - T_f}{\Delta T}; \tag{9a}$$

$$\beta_a = \frac{H_a}{\delta}; \quad \gamma_a = \frac{H_a}{W}; \quad \text{Bi}_{H_a} = \frac{hH_a}{k}; \quad A_1 = \frac{H_a}{k\Delta T}, \tag{9b}$$

where ζ_a and η are the dimensionless versions of z and y, Θ is the dimensionless temperature, β_a and γ_a are aspect ratios, Bi_{H_a} is the Biot number and A_1 is a value which combines the height of the fin, its thermal conductivity and the range of temperature expected for the problem (ΔT).

The Biot number is the ratio of conductive thermal resistance to convective resistance and is used in problems concerning simultaneous conduction and convection heat transfer mechanisms (REMSBURG, 2011). For this work, the heat transfer coefficient h is a combination of convection and radiation, described in section 1.4.

1.1.2 1D fin formulation

The formulation for the one-dimensional fin is also obtained using the energy equation in steady-state. Çengel (2012) and several authors had demonstrated how to obtain this formulation. The fin dimensionless formulation considering the variables used in this work

is:

$$\frac{\mathrm{d}^2\Theta}{\mathrm{d}\zeta_a^2} - m_a^2\Theta = 0 \tag{10a}$$

$$\left.\frac{\mathrm{d}\Theta}{\mathrm{d}\zeta_a}\right|_{\zeta_a=0} = -A_1\dot{q}''_{base}; \quad \left.\frac{\mathrm{d}\Theta}{\mathrm{d}\zeta_a}\right|_{\zeta_a=1} = 0. \tag{10b}$$

The dimensionless groups are:

$$\mathrm{Bi}_{H_a} = \frac{hH_a}{k}; \qquad m_a^2 = \frac{\mathrm{Bi}_a P H_a}{A_c}; \qquad A_1 = \frac{H_a}{k\Delta T} \tag{11}$$

where Bi_a is the Biot number for the fin, P is the perimeter of the fin, h is the heat transfer coefficient, k is the thermal conductivity, A_c is the transversal area in ζ_a direction. The dimensionless group A_1 was mentioned on section 1.1.1.

1.2 **Base formulations**

1.2.1 3D base formulation

The 3D-base heat conduction formulation is obtained from the first law of thermodynamics:

$$\frac{D\dot{E}}{Dt} = \sum \dot{E}_{in} - \sum \dot{E}_{out} + \dot{E}_{gen} \tag{12}$$

$$E = e\Delta x\Delta y\Delta z; \quad e = e_c + e_p + u; \quad \mathrm{d}u = c_v\mathrm{d}T \tag{13}$$

where e is the total energy, $\dot{E}_{in}$ and $\dot{E}_{out}$ are the total energy entering and leaving the control volume (CV), respectively, $\dot{E}_{gen}$ is the generated energy in the CV, e_c is the kinetic energy, e_p is the potential energy, u is the internal energy, c_v is the specific heat at constant volume and ρ is the specific mass.

The following simplifying assumptions are presented:

1. Kinetic and potential energies variations are negligible.
2. Heat conduction is the heat transfer mechanism for steady solids and liquids, therefore the velocity stream is negligible.
3. The base is composed of solid material, therefore the volume variation is negligible and the specific heat at constant volume is considered the same as the specific heat at constant pressure ($c_v = c_p$).
4. Pressure drop is negligible.

Figure 5 - Infinitesimal volume control for the heat sink's base. The heat fluxes indicate the heat conduction for the three dimensions.

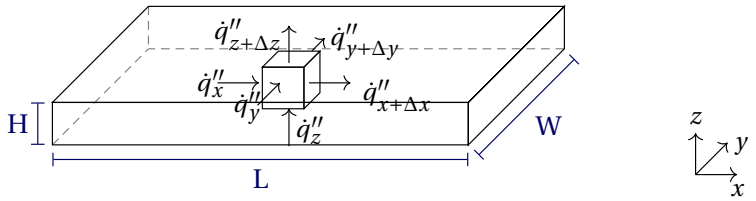

5. The base of the heat sink is isotropic and presents the same material properties of the fins.

6. Steady-state.

7. Heat generation by Joule effect, physical or chemical reactions (PONTES; MANGIAVACCHI, 2016) non-existent.

Figure 5 illustrates the volume control scheme, the heat fluxes the dimensions of the 3D base. Considering the assumption 1 and 7, the equation is rewritten as:

$$\frac{Du}{Dt}\Delta x\Delta y\Delta z = \dot{q}''_x\Delta y\Delta z + \dot{q}''_y\Delta x\Delta z + \dot{q}''_z\Delta x\Delta y - \left(\dot{q}''_{x+\Delta x}\Delta y\Delta z + \dot{q}''_{y+\Delta y}\Delta x\Delta z + \dot{q}''_{z+\Delta z}\Delta x\Delta y\right) \quad (14)$$

Using the assumption 2:

$$\rho\frac{\partial u}{\partial t} = -\frac{\dot{q}''_{x+\Delta x} - \dot{q}''_x}{\Delta x} - \frac{\dot{q}''_{y+\Delta y} - \dot{q}''_y}{\Delta y} - \frac{\dot{q}''_{z+\Delta z} - \dot{q}''_z}{\Delta z} \quad (15)$$

Applying the limits in the heat fluxes, expanding the heat fluxes by the Fourier law and, using assumptions 3 and 4, the Biot-Fourier equation is obtained:

$$\rho c_p\frac{\partial T}{\partial t} = \frac{\partial}{\partial x}\left(k_x\frac{\partial T}{\partial x}\right) + \frac{\partial}{\partial y}\left(k_y\frac{\partial T}{\partial y}\right) + \frac{\partial}{\partial z}\left(k_z\frac{\partial T}{\partial z}\right) \quad (16)$$

The assumption 5 and 6 are considered and the following formulation on equation (17) is proposed for the heat sink base.

$$k\left(\frac{\partial^2 T}{\partial x^2} + \frac{\partial^2 T}{\partial y^2} + \frac{\partial^2 T}{\partial z^2}\right) = 0 \quad (17)$$

Figure 6 shows the front view of an one-fin heat sink example and indicates the problem schematic, their dimensions, and heat fluxes positions. The fin receives the contact interface flux in all its width extension and the increased surface contact area is responsible

Figure 6 - Heat sink front view. The arrows indicate the heat flux vectors. $\dot{q}''_o$ indicates the heat flux from the electronic device to the base of the heat sink and the color red was designated to indicated a higher gradient. The orange arrows indicate the heat flux moving from the base's top to the fin's bottom edge. Finally, the light blue arrows indicate convection at the top of the heat sink base, except where the fin is located. The dimensions of the heat sink are indicated in darker blue.

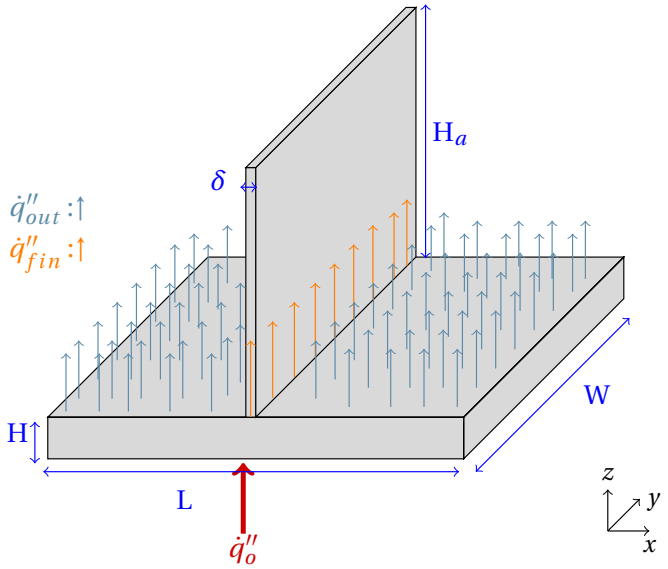

for more efficient heat dissipation. The vacancy of fins, which allows the airflow to cool the remaining parts of the top surface of the HS, is indicated by the convection heat flux in light blue. The oncoming heat flux $\dot{q}''_o$, from a heated chip, is indicated by the red arrow at the bottom of the base. Because heat sinks are widely applied in industry, there is a vast range of different chips and heat sinks dimensions. Two different heated electronic devices' contact areas are exemplified in Figure 7, where the HS's bottom $z = 0$ is observed.

The present work considers a perfect contact between base and fin, assuming they are manufactured together. The oncoming chip heat flux is described as the boundary condition on the bottom of the base of the heat sink and, in this work, insulation is considered for the other boundaries. The fin-base contact interface heat flux is combined with the convective

Figure 7 - Examples of heated chips at the HS's base

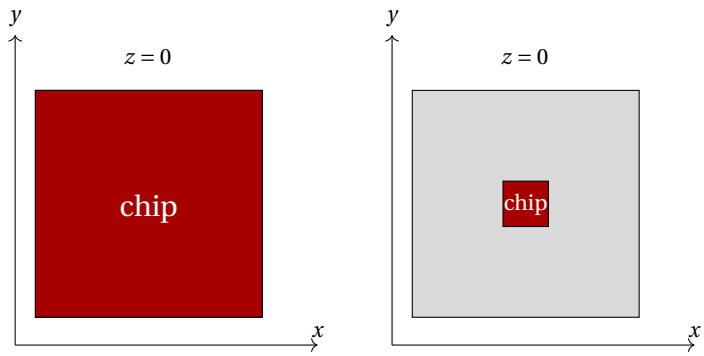

heat flux to produce a switch function.

$$\frac{\partial^2 T}{\partial x^2}+\frac{\partial^2 T}{\partial y^2}+\frac{\partial^2 T}{\partial z^2}=0 \quad \text{for} \quad 0\le x\le L, \quad 0\le y\le W \quad \text{and} \quad 0\le z\le H \tag{18a}$$

$$-k\frac{\partial T}{\partial z}\bigg|_{z=0}=\dot{q}''_o(x,y); \quad -k\frac{\partial T}{\partial z}\bigg|_{z=H}=\alpha(x)\dot{q}''_{\text{out}}+(1-\alpha(x))\dot{q}''_{\text{fin}}; \tag{18b}$$

$$\frac{\partial T}{\partial x}\bigg|_{x=0}=0; \quad \frac{\partial T}{\partial x}\bigg|_{x=L}=0; \quad \frac{\partial T}{\partial y}\bigg|_{y=0}=0; \quad \frac{\partial T}{\partial y}\bigg|_{y=W}=0;, \tag{18c}$$

where T is the temperature, k is the thermal conductivity, $\dot{q}_o$ is the oncoming heat flux from the chip, $\dot{q}''_{\text{out}}$ is the outlet heat flux at the top of the base, $\dot{q}''_{\text{fin}}$ is the fin-base contact interface heat flux and L, W and H are the dimensions of the fin in x, y and z directions respectively. The surfaces $x=0$, $x=L$, $y=0$, and $y=W$ present much smaller surface areas. For this reason, insulation is considered for those boundaries. The parameter α is the switch function, it simplifies the integral transform technique solution and, defined as 0 or 1, indicates the position of the fins and, the output flow present at a given position of x-direction:

$$\alpha=\begin{cases}0 & \text{if the top is in contact with the fin, } (\dot{q}''_{\text{fin}})\\ 1 & \text{if there is only outlet heat flux in this position, } (\dot{q}''_{\text{out}}=h(T-T_f))\end{cases} \tag{19}$$

The nondimensionalization of the 3D base is expressed on equation (20):

$$\frac{\partial^2\Theta}{\partial\zeta^2}+\beta^2\frac{\partial^2\Theta}{\partial\xi^2}+\gamma^2\frac{\partial^2\Theta}{\partial\eta^2}=0 \quad \text{for} \quad 0\le\xi\le 1, \quad 0\le\eta\le 1 \quad \text{and} \quad 0\le\zeta\le 1 \tag{20a}$$

$$\frac{\partial\Theta}{\partial\zeta}\bigg|_{\zeta=0}=-A_2\dot{q}''_o(\xi,\eta); \quad \frac{\partial\Theta}{\partial\zeta}\bigg|_{\zeta=1}=(-\alpha(\xi))\text{Bi}_H\Theta+(\alpha(\xi)-1)A_2\dot{q}''_{\text{fin}}; \tag{20b}$$

$$\frac{\partial\Theta}{\partial\xi}\bigg|_{\xi=0}=0; \quad \frac{\partial\Theta}{\partial\xi}\bigg|_{\xi=1}=0; \quad \frac{\partial\Theta}{\partial\eta}\bigg|_{\eta=0}=0; \quad \frac{\partial\Theta}{\partial\eta}\bigg|_{\eta=1}=0, \tag{20c}$$

The non-dimensional groups are defined as:

$$\zeta = \frac{z}{H}; \quad \xi = \frac{x}{L}; \quad \eta = \frac{y}{W}; \quad \Theta = \frac{T - T_f}{\Delta T}; \tag{21}$$

$$\beta = \frac{H}{L}; \quad \gamma = \frac{H}{W}; \quad \mathrm{Bi}_H = \frac{hH}{k}; \quad A_2 = \frac{H}{k\Delta T}, \tag{22}$$

where ζ, ξ and η are the dimensionless versions of z, x and y, Θ is the dimensionless temperature, β and γ are aspect ratios, Bi_H is the Biot number and A_2 is a value which combines the height of the fin, its thermal conductivity and the range of temperature expected for the problem(ΔT). The parameter α is shown depending on the position of the fin, now indicated as $\alpha(\xi)$.

1.2.2 2D base formulation

The 2D base (x,z) formulation considers heat conduction only in ζ and ξ directions, dimensionless versions of z and x, respectively, and shown in the following equation (23). This formulation will be used as a benchmark problem. Figure 8a shows a scheme for this base formulation coupled to one fin.

$$\frac{\partial^2\Theta}{\partial\zeta^2} + \beta^2\frac{\partial^2\Theta}{\partial\xi^2} = 0 \quad \text{for} \quad 0 \le \xi \le 1 \quad \text{and} \quad 0 \le \zeta \le 1 \tag{23a}$$

$$\left.\frac{\partial\Theta}{\partial\xi}\right|_{\xi=0} = 0; \qquad \left.\frac{\partial\Theta}{\partial\xi}\right|_{\xi=1} = 0; \tag{23b}$$

$$\left.\frac{\partial\Theta}{\partial\zeta}\right|_{\zeta=0} = -A_2\dot{q}''_o(\xi); \qquad \left.\frac{\partial\Theta}{\partial\zeta}\right|_{\zeta=1} = [-\alpha(\xi)]\mathrm{Bi}_H\Theta + [\alpha(\xi) - 1]A_2\dot{q}''_{\mathrm{fin}}, \tag{23c}$$

A 2D base formulation considering heat conduction in directions ξ and η, dimensionless versions of x and y, was developed and solved on (CORRÊA; CHALHUB, 2018). This conference proceeding article is available on Appendix D.

An 1D base formulation for benchmark purposes, considering heat conduction only in the ζ-direction, dimensionless z, was developed in Appendix B.

1.3 **Fin-base coupling**

Hahn and Ozisik (2012) define, for one-dimensional problems, the interface boundary conditions in an imperfect thermal contact as the equality between the heat conduction in the first solid, the heat transfer across the gap, and the heat conduction in the second

Figure 8 - Schemes for the 2D base-1D fin and fin-base contact interface. The arrows indicate the heat fluxes. The left scheme indicates the heat fluxes entering and leaving the 2D base while the right scheme focus on the fin-base contact interface heat fluxes considering a perfect interface contact.

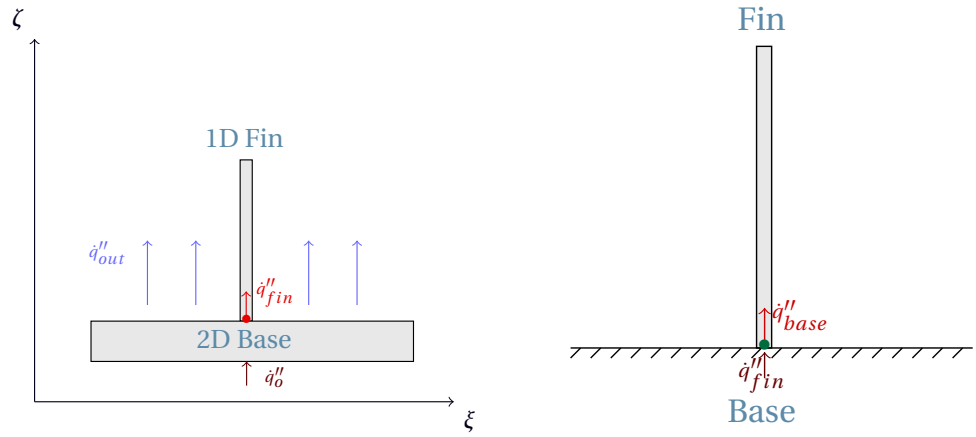

(a) Scheme of the 2D base-1D fin formulation (b) Fin-base coupling scheme

solid, obtained from the energy equation and shown below:

$$-k_1 \left.\frac{\mathrm{d}T_1}{\mathrm{d}x}\right|_{z=ic} = h_c(T_1 - T_2)_{ic} = -k_2 \left.\frac{\mathrm{d}T_2}{\mathrm{d}z}\right|_{z=ic} \tag{24}$$

where h_c is the contact conductance for the interface, ic is the contact interface and k_1 and k_2 are the thermal conductivity for each solid. If $h_c \to \infty$, a perfect contact is considered and, consequently, the temperature continuity in z-direction ($T_1 = T_2$) (LEHTINEN, 2005).

Two assumptions are performed in order to couple the fin and base equations, which are considered having perfect contact:

1. Temperature continuity.

$$\Theta_{\text{base}}(\text{position of the fin, top of the base}) = \Theta_{\text{fin}}(\text{bottom of the fin}) \tag{25}$$

2. Flux continuity.

$$\dot{q}''_{\text{base}} = \dot{q}''_{\text{fin}} \tag{26}$$

Figure 8b shows the fin-base coupling scheme and the required conditions for the perfect interface contact.

These mathematical equalities are performed with the base and fins' analytical solutions and the value of $\dot{q}''_{\text{base}}$ and $\dot{q}''_{\text{fin}}$ are obtained. The base and fins' equations are solved

again replacing the unknown values for the new calculated values and finally, obtaining the temperature field for the coupled fin-base heat sink.

1.4 **The Convection-Radiation Heat Transfer Coefficient**

The heat transfer coefficient used in this work combines both convection and radiation effects, as defined by Çengel and Ghajar (2011) in Equation (27).

$$h = h_{\text{conv}} + h_{\text{rad}} \tag{27}$$

where h_{conv} is estimated from a natural convection correlation, and h_{rad} is estimated from the linearized radiative heat transfer coefficient.

1.4.1 Convective heat transfer coefficient

For the convection heat transfer coefficient, the correlation for its average value along isothermal vertical channels spaced s unit apart is defined on Equation (28) (BEJAN; KRAUS, 2003; FURUKAWA; YANG; TORII, 2008).

$$h_{\text{conv}} = \frac{k_f}{s}\left(\frac{576}{\text{El}^2} + \frac{2.873}{\text{El}^{1/2}}\right)^{-1/2} \tag{28}$$

The Elenbaas number (El) is a gap-based Rayleigh number used to find the Nusselt number of natural convection flow between vertical plates (REMSBURG, 2011). This dimensionless number is applied in the design of heat sinks and on the flow between cards in electronic boards. The Elenbaas number is a tribute to W. Elenbaas by Bejan and Kraus (2003) and is defined on equation (29) (BAR-COHEN; IYENGAR; KRAUS, 2003; LAMPIO; KARVINEN, 2018).

$$\text{El} = \frac{\varrho g \,\text{Pr}\, s^4 \Delta T_b}{\nu^2 W}, \quad \text{Pr} = \frac{\nu}{\alpha_f} \tag{29}$$

where k_f is the thermal conductivity, s is the channel's thickness (or the space between two fins), ϱ is the volumetric expansion coefficient, g is the gravity, Pr is the Prandtl number, ν is the kinematic viscosity, W is the vertical channel's length, α_f is the thermal diffusivity and ΔT_b is the average temperature difference between the heat sink and the environment air (FURUKAWA; YANG; TORII, 2008). Hence, ϱ, ν, k_f, α_f and Pr are evaluated at the fluid bulk temperature(T_f). Figure 9 illustrates the design parameters scheme of the plate-fin heat sink, indicating also the fin thickness and the channel spacing.

Figure 9 - Design parameters of plate-fin heat sink. W is the vertical channel's length, s is the channel spacing, δ is the fin thickness, L is the HS base length, H is the base height and H_a is the fin height.

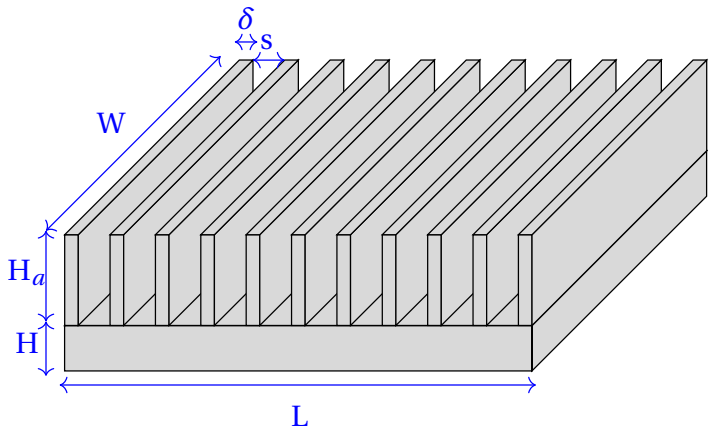

This work estimates the convective heat transfer coefficient for natural convection. However, the formulation can be implemented for forced convection situations if the appropriate correlation is considered.

1.4.2 Radiative heat transfer coefficient

The radiative heat transfer between two surfaces or between a surface and its surroundings is not linearly dependent on the temperature difference (BEJAN; KRAUS, 2003). The heat transfer rate by radiation is defined by Çengel and Ghajar (2011) as:

$$\dot{q}''_{\text{rad}} = \epsilon\sigma\left(T^4 - T_{\text{sur}}^4\right) \tag{30}$$

where T_{sur} is the temperature in its surroundings surfaces (BEJAN; KRAUS, 2003). ϵ is the surface emissivity, which varies in the $0 \leq \epsilon \leq 1$ range and $\sigma = 5.67 \times 10^{-8}\text{W/m}^2\text{K}^4$ is the Stefan-Boltzmann constant (SHABANY, 2008). The mutual irradiation between fins (SPARROW; ECKERT, 1962; SOBRAL, 2017) is not considered in this work.

Kalogirou (2013) states the linearized of the equation in terms of the differences of temperatures to the first power, similar to the heat transfer rate by convection.

$$\dot{q}''_{\text{rad}} = \epsilon\sigma\left(T^2 + T_{\text{sur}}^2\right)\left(T^2 - T_{\text{sur}}^2\right) \tag{31}$$

$$\dot{q}''_{\text{rad}} = \epsilon\sigma\left(T^2 + T_{\text{sur}}^2\right)(T + T_{\text{sur}}) \times (T - T_{\text{sur}}) \tag{32}$$

Considering the heat transfer rate by radiation as:

$$\dot{q}''_{\text{rad}} = h_{\text{rad}} \times (T - T_{\text{sur}}) \tag{33}$$

The heat transfer coefficient by radiation is, then, defined as:

$$h_{\text{rad}} = \epsilon\sigma \left(T^2 + T_{\text{sur}}^2\right)(T + T_{\text{sur}}) \tag{34}$$

The following manipulations are performed considering the characteristic temperature as T_{char} (FOKAIDES; KALOGIROU, 2011):

- For $(T + T_{\text{sur}})$:

$$T_{\text{char}} = \frac{T + T_{\text{sur}}}{2} \tag{35}$$

$$T + T_{\text{sur}} = 2T_{\text{char}} \tag{36}$$

- For $(T^2 + T_{\text{sur}}^2)$:

$$(T + T_{\text{sur}})^2 = (2T_{\text{char}})^2 \tag{37}$$

$$T^2 + 2T \times T_{\text{sur}} + T_{\text{sur}}^2 = 4T_{\text{char}}^2 \tag{38}$$

$$T^2 + T_{\text{sur}}^2 = 4T_{\text{char}}^2 - 2T \times T_{\text{sur}}, \quad T_{\text{char}}^2 \approx T \times T_{\text{sur}} \tag{39}$$

$$T^2 + T_{\text{sur}}^2 \approx 2T_{\text{char}}^2 \tag{40}$$

$$\left(T^2 + T_{\text{sur}}^2\right)(T + T_{\text{sur}}) \approx 2T_{\text{char}}^2 \times 2T_{\text{char}} \approx 4T_{\text{char}}^3 \tag{41}$$

It must be noticed that Equation (39) is valid when T and T_{sur} have close values. This approximation was also mentioned by Marin (2009).

Substituting the terms, the linearized radiative heat transfer coefficient (KALOGIROU, 2013) can be estimated as:

$$h_{\text{rad}} \approx 4\epsilon\sigma T_{\text{char}}^3 \tag{42}$$

This approach considers the minimum temperature to obtain the lowest heat transfer coefficient by radiation. Therefore, the characteristic temperature (T_{char}) assumes the same magnitude as the surrounding fluid temperature ($T_{\text{char}} \approx T_f$). This approximation estimates the radiative heat transfer coefficient by its minimum value, consequently, the heat sink would not operate at a higher temperature than the calculated.

2 CLASSICAL INTEGRAL TRANSFORM TECHNIQUE

The Integral Transform Technique provides a systematic, efficient, and straightforward approach for homogeneous, nonhomogeneous, steady-state, transient boundary value problems. The steps for the application of the method are enumerated:

1. Define the transformed directions. For this work, the integral transformation is applied in one or two spatial directions, leaving the remaining direction not transformed.
2. Solve the appropriate Sturm-Liouville eigenvalue problem (HAHN; OZISIK, 2012). The Helmholtz's equation is suited by cartesian coordinates.
3. Define the transformation pair.
4. Apply the integral transformation in the differential equation.
5. Solve the transformed equations, utilizing the transformed boundary conditions.
6. Apply the inversion formula and sum to a finite value until the full convergence for the desired solution.

Each heat sink solution is going to be described in the following sections.

2.1 **3D base and 2D fin**

2.1.1 Solution by CITT for the 2D rectangular fin

The Classical Integral Transform Technique (CITT) is applied to solve the 2D fin formulation. The rectangular isotropic fin formulation (equation, boundary conditions, and non-dimensional groups) demonstrated in section 1.1.1 are shown again:

$$\frac{\partial^2\Theta}{\partial\zeta_a^2}+\gamma_a^2\frac{\partial^2\Theta}{\partial\eta^2}-(2\mathrm{Bi}_{H_a}\beta_a)\Theta=0 \quad \text{for} \quad 0\le\eta\le 1 \quad \text{and} \quad 0\le\zeta_a\le 1 \tag{43a}$$

$$\left.\frac{\partial\Theta}{\partial\zeta_a}\right|_{\zeta_a=0}=-A_1\dot{q}''_{\text{base}}(\eta); \quad \left.\frac{\partial\Theta}{\partial\zeta_a}\right|_{\zeta_a=1}=0; \quad \left.\frac{\partial\Theta}{\partial\eta}\right|_{\eta=0}=0; \quad \left.\frac{\partial\Theta}{\partial\eta}\right|_{\eta=1}=0 \tag{43b}$$

$$\zeta_a=\frac{z}{H_a}; \quad \eta=\frac{y}{W}; \quad \Theta=\frac{T-T_f}{\Delta T}; \tag{43c}$$

$$\beta_a=\frac{H_a}{\delta}; \quad \gamma_a=\frac{H_a}{W}; \quad \mathrm{Bi}_{H_a}=\frac{hH_a}{k}; \quad A_1=\frac{H_a}{k\Delta T}, \tag{43d}$$

In order to establish the transformation pair, the temperature field is written firstly as functions of orthogonal eigenfunctions obtained from the following auxiliary eigenvalue

problem known as the Helmholtz classic problem in cartesian coordinates. The η-direction is transformed for the 2D-fin. The eigenvalue problem proposed to be solved on the fin is in the η direction, where the corresponding solutions $\Psi_n(\eta)$ are called eigenfunctions and λ_n are the eigenvalues. For this particular problem, the case where λ= 0 also exists.

$$\Psi''_n(\eta) + \lambda_n^2 \Psi_n(\eta) = 0 \tag{44a}$$

$$\Psi'_n(0) = 0; \quad \Psi'_n(1) = 0. \tag{44b}$$

The eigenfunctions are, in fact, orthogonal functions (HAHN; OZISIK, 2012):

$$\int_0^1 \Psi_n(\eta)\Psi_l(\eta)\mathrm{d}\eta = \begin{cases} 0 & \text{if } n \neq l \\ N_{y_n} & \text{if } n = l \end{cases} \tag{45}$$

where the norm, or normalization integral, is defined as:

$$N_{y_n} = \int_0^1 \Psi_n^2(\eta)\mathrm{d}\eta \tag{46}$$

Solving the differential equation, the general eigenfunction solution is formed by sines and cosines. The boundary conditions exclude the sine term from the solution and eigenvalues λ_n are obtained. The solutions for the eigenvalue problem are:

For $\lambda > 0$:

$$\lambda_n = n\pi; \tag{47}$$

$$\Psi_n(\eta) = \cos(\lambda_n \eta); \tag{48}$$

For $\lambda = 0$:

$$\lambda_0 = 0; \tag{49}$$

$$\Psi_0(\eta) = 1. \tag{50}$$

After solving the auxiliary eigenvalue problem, the transformation pair must be defined before transform the dimensionless differential equation and the boundary conditions. The transformation pair is defined as:

$$\text{Transformation} \quad \Rightarrow \quad \bar{\Theta}_n(\zeta_a) = \int_0^1 \Theta\Psi_n(\eta)\mathrm{d}\eta \tag{51}$$

$$\text{Inversion} \quad \Rightarrow \quad \Theta(\eta,\zeta_a) = \sum_{n=0}^{\infty} \frac{\bar{\Theta}_n(\zeta_a)\Psi_n(\eta)}{N_{y_n}} \tag{52}$$

The integral transformation in η-direction is then applied in the dimensionless equa-

tion (43a):

$$\int_0^1 \frac{\partial^2 \Theta}{\partial \zeta_a^2} \Psi_n \mathrm{d}\eta + \gamma_a^2 \int_0^1 \frac{\partial^2 \Theta}{\partial \eta^2} \Psi_n \mathrm{d}\eta - 2\mathrm{Bi}_{H_a} \beta_a \int_0^1 \Theta \Psi_n \mathrm{d}\eta = 0 \tag{53}$$

The transformed equations (54) and (56) are obtained from the equation (53) using the transformating procedure (51), which consists in substitute the transformation integrals for the transformation term $\bar{\Theta}_n(\zeta_a)$ and obtain the transformed equations.

- For $\lambda > 0$:

$$\bar{\Theta}_n'' - (\gamma_a^2 \lambda_n^2 + 2\mathrm{Bi}_{H_a} \beta_a) \bar{\Theta}_n = 0 \tag{54}$$

The transformed boundary conditions are:

$$\bar{\Theta}_n'(0) = -A_1 \int_0^1 \dot{q}''_{\mathrm{base}}(\eta) \Psi_n \mathrm{d}\eta; \quad \bar{\Theta}_n'(1) = 0 \tag{55}$$

- For $\lambda = 0$:

$$\bar{\Theta}_0'' - (2\mathrm{Bi}_{H_a} \beta_a) \bar{\Theta}_0 = 0 \tag{56}$$

The transformed boundary conditions are:

$$\bar{\Theta}_0'(0) = -A_1 \int_0^1 \dot{q}''_{\mathrm{base}}(\eta) \mathrm{d}\eta; \quad \bar{\Theta}_0'(1) = 0 \tag{57}$$

The analytical solutions for the differential transformed equations are:

$$\bar{\Theta}_n(\zeta_a) = \frac{A_1 e^{\left(-\zeta_a \sqrt{2\mathrm{Bi}_{H_a} \beta_a + \pi^2 \gamma_a^2 n^2}\right)} \left(e^{2\zeta_a \sqrt{2\mathrm{Bi}_{H_a} \beta_a + \pi^2 \gamma_a^2 n^2}} + e^{2\sqrt{2\mathrm{Bi}_{H_a} \beta_a + \pi^2 \gamma_a^2 n^2}}\right)}{\left(e^{2\sqrt{2\mathrm{Bi}_{H_a} \beta_a + \pi^2 \gamma_a^2 n^2}} - 1\right) \sqrt{2\mathrm{Bi}_{H_a} \beta_a + \pi^2 \gamma_a^2 n^2}} \times \int_0^1 \dot{q}''_{\mathrm{base}}(\eta) \cos(n\pi\eta) \mathrm{d}\eta \tag{58}$$

$$\bar{\Theta}_0(\zeta_a) = \frac{A_1 e^{-\zeta_a \sqrt{2\mathrm{Bi}_{H_a} \beta_a}} \left(e^{2\zeta_a \sqrt{2\mathrm{Bi}_{H_a} \beta_a}} + e^{2\sqrt{2\mathrm{Bi}_{H_a} \beta_a}}\right)}{\left(e^{2\sqrt{2\mathrm{Bi}_{H_a} \beta_a}} - 1\right) \sqrt{2\mathrm{Bi}_{H_a} \beta_a}} \int_0^1 \dot{q}''_{\mathrm{base}}(\eta) \mathrm{d}\eta \tag{59}$$

The final temperature field, finally, is obtained using the inversion formula (60). The inversion formula combines the transformed equations solutions $\bar{\Theta}(\zeta_a)$, the eigenfunction

$\Psi(\eta)$, and the norm N_{y_n}. The summation is truncated to a finite value (n_{max}).

$$\Theta(\eta,\zeta_a) = \sum_{n=0}^{\infty} \frac{\bar{\Theta}_n(\zeta_a)\Psi_n(\eta)}{N_{y_n}} \tag{60}$$

This summation ends up as literal because $\dot{q}''_{base}$ is not defined at this point.

2.1.2 Solution by CITT for the 3D base

The three-dimensional model requires two transformed directions. The consequence of using a double transformation is having a double summation for the inversion term, therefore, the solution's convergence requires more terms summed (CHALHUB, 2015). Nevertheless, the method is still full analytical, the reason which turns the CITT such an efficient method.

The transformed directions for the base are ξ and η, the dimensionless versions of x and y. The appropriate eigenvalue problems are shown below and, because both directions present the same boundary conditions, they are similar.

The eigenvalue problem in the direction ξ is:

$$\Xi''_m(\xi) + \mu_m^2 \Xi_m(\xi) = 0 \tag{61a}$$

$$\Xi'_m(0) = 0; \quad \Xi'_m(1) = 0. \tag{61b}$$

For $m > 0$:

$$\mu_m = m\pi; \tag{61c}$$

$$\Xi_m(\xi) = \cos(\mu_m \xi); \tag{61d}$$

For $m = 0$:

$$\mu_0 = 0; \tag{61e}$$

$$\Xi_0(\xi) = 1; \tag{61f}$$

The eigenvalue problem in the direction η is:

$$\Psi''_n(\eta) + \lambda_n^2 \Psi_n(\eta) = 0 \tag{62a}$$

$$\Psi'_n(0) = 0; \quad \Psi'_n(1) = 0. \tag{62b}$$

For $n > 0$:

$$\lambda_n = n\pi; \tag{62c}$$

$$\Psi_n(\eta) = \cos(\lambda_n \eta); \tag{62d}$$

For $n = 0$:

$$\lambda_0 = 0; \tag{62e}$$

$$\Psi_0(\eta) = 1. \tag{62f}$$

Following to the step 3, the transformation pair for the 3D base is:

$$\text{Transformation} \quad \Rightarrow \quad \bar{\bar{\Theta}}_{nm}(\zeta) = \int_0^1 \int_0^1 \Theta \Psi_n(\eta) \Xi_m(\xi) \mathrm{d}\eta \mathrm{d}\xi \tag{63}$$

$$\text{Inversion} \quad \Rightarrow \quad \Theta = \sum_{n=0}^{\infty} \sum_{m=0}^{\infty} \frac{\bar{\bar{\Theta}}_{nm}(\zeta) \Psi_n(\eta) \Xi_m(\xi)}{N_{y_n} N_{xm}} \tag{64}$$

The norms (CHALHUB, 2015) are defined as:

$$N_{y_n} = \int_0^1 \Psi_n^2(\eta) \mathrm{d}\eta; \qquad N_{xm} = \int_0^1 \Xi_m^2(\xi) \mathrm{d}\xi \tag{65}$$

The base formulation (20) is written again:

$$\frac{\partial^2 \Theta}{\partial \zeta^2} + \beta^2 \frac{\partial^2 \Theta}{\partial \xi^2} + \gamma^2 \frac{\partial^2 \Theta}{\partial \eta^2} = 0 \quad \text{for} \quad 0 \le \xi \le 1, \quad 0 \le \eta \le 1 \quad \text{and} \quad 0 \le \zeta \le 1 \tag{66a}$$

$$\left.\frac{\partial \Theta}{\partial \zeta}\right|_{\zeta=0} = -A_2 \dot{q}_o''(\xi, \eta); \qquad \left.\frac{\partial \Theta}{\partial \zeta}\right|_{\zeta=1} = (-\alpha(\xi))\mathrm{Bi}_H \Theta + (\alpha(\xi) - 1) A_2 \dot{q}_{\mathrm{fin}}''; \tag{66b}$$

$$\left.\frac{\partial \Theta}{\partial \xi}\right|_{\xi=0} = 0; \qquad \left.\frac{\partial \Theta}{\partial \xi}\right|_{\xi=1} = 0; \qquad \left.\frac{\partial \Theta}{\partial \eta}\right|_{\eta=0} = 0; \qquad \left.\frac{\partial \Theta}{\partial \eta}\right|_{\eta=1} = 0, \tag{66c}$$

The integral transformation (63) is applied on equation (20), including the boundary conditions. The objective of this step substitute the transformation integrals for the transformation term $\bar{\bar{\Theta}}_{nm}(\zeta)$ and obtain the transformed equations.

$$\int_0^1 \int_0^1 \frac{\partial^2 \Theta}{\partial \zeta^2} \Psi_n(\eta) \Xi_m(\xi) \mathrm{d}\eta \mathrm{d}\xi + \beta^2 \int_0^1 \int_0^1 \frac{\partial^2 \Theta}{\partial \xi^2} \Psi_n(\eta) \Xi_m(\xi) \mathrm{d}\eta \mathrm{d}\xi + \gamma^2 \int_0^1 \int_0^1 \frac{\partial^2 \Theta}{\partial \eta^2} \Psi_n(\eta) \Xi_m(\xi) \mathrm{d}\eta \mathrm{d}\xi = 0 \tag{67}$$

$$\bar{\bar{\Theta}}'(0) = -A_2 \int_0^1 \int_0^1 \dot{q}_o''(\xi, \eta) \Psi_n(\eta) \Xi_m(\xi) \mathrm{d}\eta \mathrm{d}\xi = -A_2 \bar{\bar{Q}} \tag{68}$$

Figure 10 - Boundary condition at the top of the base. This condition is ξ-dependent. On ξ-positions where the fins are located, the heat is transferred at the fin-base interface. Between fins, the convection is the cooling mechanism.

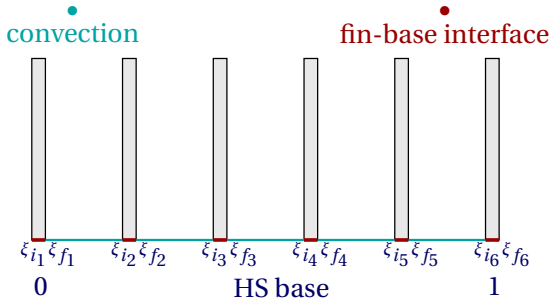

$$\bar{\bar{\Theta}}'(1) = \int_0^1 \int_0^1 -\alpha(\xi)\mathrm{Bi}_H\Theta(\xi,\eta,1)\Xi_m(\xi)\Psi_n(\eta)\mathrm{d}\eta\mathrm{d}\xi + A_2\int_0^1\int_0^1(\alpha(\xi)-1)\dot{q}''_{\mathrm{fin}}(\eta)\Xi_m(\xi)\Psi_n(\eta)\mathrm{d}\eta\mathrm{d}\xi \quad (69)$$

For the first term of Equation (67), the partial derivatives in ζ are removed from the integration. The final form of this term is: $\bar{\bar{\Theta}}''$. For the second and third terms, integration by parts is necessary to obtain the transformed terms. The transformed equation is shown on Equation (70).

$$\bar{\bar{\Theta}}''_{nm} - (\beta^2\mu_m^2 + \gamma^2\lambda_n^2)\bar{\bar{\Theta}}_{nm} = 0 \quad (70)$$

2.1.2.1 Boundary condition transformation

Due to the transformed boundary condition $\bar{\bar{\Theta}}'(1)$ complexity, which is shown in equation (69), some simplifications are performed to obtain a full analytical solution. Figure 10 shows an example scheme of fin limits at the base domain.

Convective term: The parameter $\alpha(\xi)$, which was defined previously as a switch function (19), and its ξ-dependence turns the transformation impracticable to be obtained for the convective term. Consequently, $\alpha(\xi)$ is approximated to an average value α_{avg}, described in Equation (71). This approximation simplifies the achievement of the analytical solution because the convective term is able to be transformed using Equation (71).

$$\alpha_{\mathrm{avg}} = \int_0^1 \alpha(\xi)\mathrm{d}\xi \quad (71)$$

The convection term (72) is then written considering an average value for α, α_{avg}, a constant value for the ξ-domain:

$$-\int_0^1\int_0^1 \alpha(\xi)\text{Bi}_H\Theta(\xi,\eta,1)\Xi_m(\xi)\Psi_n(\eta)\text{d}\eta\text{d}\xi = \\ -\alpha_{\text{avg}}\text{Bi}_H\int_0^1\int_0^1 \Theta(\xi,\eta,1)\Xi_m(\xi)\Psi_n(\eta)\text{d}\eta\text{d}\xi = -\alpha_{\text{avg}}\text{Bi}_H\bar{\bar{\Theta}}_{nm} \quad (72)$$

Fin-base interface term: The term which connects fin-base is rewritten substituting the $\alpha(\xi)$ for 0 at the regions where the fins are located.

$$A_2\int_0^1\int_0^1 (\alpha(\xi)-1)\,\dot{q}''_{\text{fin}}(\eta)\Xi_m(\xi)\Psi_n(\eta)\text{d}\eta\text{d}\xi = \\ -A_2\sum_{j=1}^{\text{n}_{\text{fin}}}\int_{\xi_{i_j}}^{\xi_{f_j}}\int_0^1 \dot{q}''_{\text{fin}}(\eta)\Xi_m(\xi)\Psi_n(\eta)\text{d}\eta\text{d}\xi \quad (73)$$

where n_{fin} is the number of fins, ξ_i refers to the position where the fin begins and ξ_f where it ends, as shown in figure 10.

Base's top transformed boundary condition: After using the simplifications, convection and interface contact terms are reunited and the transformed top boundary condition is defined.

$$\bar{\bar{\Theta}}'(1) = -\alpha_{\text{avg}}\text{Bi}_H\bar{\bar{\Theta}}(1) - A_2\sum_{j=1}^{\text{n}_{\text{fin}}}\int_0^1\int_{\xi_{i_j}}^{\xi_{f_j}} \dot{q}''_{\text{fin}}(\eta)\Psi_n(\eta)\Xi_m(\xi)\text{d}\xi\text{d}\eta \quad (74)$$

2.1.2.2 Transformed equations

The transformed equations for the 3D base are shown below with the boundary conditions. Each combination of the eigenvalues λ and μ has a different transformed equation, and consequently, a different analytical solution.

- For λ and $\mu > 0$:

$$\bar{\bar{\Theta}}''_{nm} - (\beta^2\mu_m^2 + \gamma^2\lambda_n^2)\bar{\bar{\Theta}}_{nm} = 0 \quad (75)$$

The transformed boundary conditions are:

$$\bar{\bar{\Theta}}'_{nm}(0) = -A_2\int_0^1\int_0^1 \dot{q}''_o(\xi,\eta)\Xi_m(\xi)\Psi_n(\eta)\text{d}\eta\text{d}\xi = -A_2\bar{\bar{Q}}_{nm} \quad (76)$$

$$\bar{\bar{\Theta}}'_{nm}(1) = -\alpha_{\text{avg}}\text{Bi}_H\bar{\bar{\Theta}}_{nm}(1) - A_2\sum_{j=1}^{\text{n}_{\text{fin}}}\int_0^1\int_{\xi_{i_j}}^{\xi_{f_j}} \dot{q}''_{\text{fin}}(\eta)\Psi_n(\eta)\Xi_m(\xi)\text{d}\xi\text{d}\eta \quad (77)$$

The analytical solution for the general transformed equation is:

$$\bar{\bar{\Theta}}_{nm}(\zeta) = \frac{C_{nm}(\zeta) - D_{nm}(\zeta) - E_{nm}(\zeta) \times F_{nm}}{G_{nm} + H_{nm}} \tag{78}$$

where:

$$C_{nm}(\zeta) = A_2 \bar{\bar{Q}}_{nm} \pi \sqrt{\beta^2 m^2 + \gamma^2 n^2} \cosh\left[\pi(\zeta - 1)\sqrt{\beta^2 m^2 + \gamma^2 n^2}\right] \tag{79}$$

$$D_{nm}(\zeta) = A_2 \bar{\bar{Q}}_{nm} \alpha_{\text{avg}} \text{Bi}_H \sinh\left[\pi(\zeta - 1)\sqrt{\beta^2 m^2 + \gamma^2 n^2}\right] \tag{80}$$

$$E_{nm}(\zeta) = \pi A_2 \sqrt{\beta^2 m^2 + \gamma^2 n^2} \cosh\left(\pi\zeta\sqrt{\beta^2 m^2 + \gamma^2 n^2}\right) \tag{81}$$

$$F_{nm} = \sum_{j=1}^{\text{n}_{\text{fin}}} \int_0^1 \int_{\xi_{i_j}}^{\xi_{f_j}} \dot{q}''_{\text{fin}}(\eta) \cos(\lambda_n \eta) \cos(\mu_m \xi) \text{d}\xi \text{d}\eta \tag{82}$$

$$G_{nm} = \pi \alpha_{\text{avg}} \text{Bi}_H \sqrt{\beta^2 m^2 + \gamma^2 n^2} \cosh\left(\pi\sqrt{\beta^2 m^2 + \gamma^2 n^2}\right) \tag{83}$$

$$H_{nm} = \pi^2 \left(\beta^2 m^2 + \gamma^2 n^2\right) \sinh\left(\pi\sqrt{\beta^2 m^2 + \gamma^2 n^2}\right) \tag{84}$$

- For $\lambda > 0$ and $\mu = 0$:

$$\bar{\bar{\Theta}}''_{n0} - (\gamma^2 \lambda_n^2)\bar{\bar{\Theta}}_{n0} = 0 \tag{85}$$

The transformed boundary conditions are:

$$\bar{\bar{\Theta}}'_{n0}(0) = -A_2 \int_0^1 \int_0^1 \dot{q}''_o(\xi, \eta) \Psi_n(\eta) \text{d}\eta \text{d}\xi = -A_2 \bar{\bar{Q}}_{n0} \tag{86}$$

$$\bar{\bar{\Theta}}'_{n0}(1) = -\alpha_{\text{avg}} \text{Bi}_H \bar{\bar{\Theta}}_{n0}(1) - A_2 \sum_{j=1}^{\text{n}_{\text{fin}}} \int_0^1 \int_{\xi_{i_j}}^{\xi_{f_j}} \dot{q}''_{\text{fin}}(\eta) \Psi_n(\eta) \text{d}\xi \text{d}\eta \tag{87}$$

The analytical solution for the transformed equation where $\lambda > 0$ and $\mu = 0$ is:

$$\bar{\bar{\Theta}}_{n0}(\zeta) = \frac{C_{n0}(\zeta) - D_{n0}(\zeta) - E_{n0}(\zeta) \times F_{n0}}{G_{n0} + H_{n0}} \tag{88}$$

where:

$$C_{n0}(\zeta) = A_2 \bar{\bar{Q}}_{n0} \pi \gamma n \cosh\left[\pi(\zeta-1)\gamma n\right] \tag{89}$$

$$D_{n0}(\zeta) = A_2 \bar{\bar{Q}}_{n0} \alpha_{\text{avg}} \text{Bi}_H \sinh\left[\pi(\zeta-1)\gamma n\right] \tag{90}$$

$$E_{n0}(\zeta) = \pi A_2 \gamma n \cosh\left(\pi \zeta \gamma n\right) \tag{91}$$

$$F_{n0} = \sum_{j=1}^{\text{n}_{\text{fin}}} (\xi_{f_j} - \xi_{i_j}) \int_0^1 \dot{q}''_{\text{fin}}(\eta) \cos(\lambda_n \eta) \text{d}\eta \tag{92}$$

$$G_{n0} = \pi \alpha_{\text{avg}} \text{Bi}_H \gamma n \cosh\left(\pi \gamma n\right) \tag{93}$$

$$H_{n0} = \pi^2 \gamma^2 n^2 \sinh\left(\pi \gamma n\right) \tag{94}$$

- For $\lambda = 0$ and $\mu > 0$:

$$\bar{\bar{\Theta}}''_{0m} - (\beta^2 \mu_m^2) \bar{\bar{\Theta}}_{0m} = 0 \tag{95}$$

The transformed boundary conditions are:

$$\bar{\bar{\Theta}}'_{0m}(0) = -A_2 \int_0^1 \int_0^1 \dot{q}''_o(\xi, \eta) \Xi_m(\xi) \text{d}\eta \text{d}\xi = -A_2 \bar{\bar{Q}}_{0m} \tag{96}$$

$$\bar{\bar{\Theta}}'_{0m}(1) = -\alpha_{\text{avg}} \text{Bi}_H \bar{\bar{\Theta}}_{0m}(1) - A_2 \sum_{j=1}^{\text{n}_{\text{fin}}} \int_0^1 \int_{\xi_{i_j}}^{\xi_{f_j}} \dot{q}''_{\text{fin}}(\eta) \Xi_m(\xi) \text{d}\xi \text{d}\eta \tag{97}$$

The analytical solution for the transformed equation where $\lambda = 0$ and $\mu > 0$ is:

$$\bar{\bar{\Theta}}_{0m}(\zeta) = \frac{C_{0m}(\zeta) - D_{0m}(\zeta) - E_{0m}(\zeta) \times F_{0m}}{G_{0m} + H_{0m}} \tag{98}$$

where:

$$C_{0m}(\zeta) = A_2 \bar{\bar{Q}}_{0m} \pi \beta m \cosh\left[\pi(\zeta-1)\beta m\right] \tag{99}$$

$$D_{0m}(\zeta) = A_2 \bar{\bar{Q}}_{0m} \alpha_{\text{avg}} \text{Bi}_H \sinh\left[\pi(\zeta-1)\beta m\right] \tag{100}$$

$$E_{0m}(\zeta) = \pi A_2 \beta m \cosh\left(\pi \zeta \beta m\right) \tag{101}$$

$$F_{0m} = \sum_{j=1}^{\text{n}_{\text{fin}}} \int_0^1 \int_{\xi_{i_j}}^{\xi_{f_j}} \dot{q}''_{\text{fin}}(\eta) \cos(\mu_m \xi) \text{d}\xi \text{d}\eta \tag{102}$$

$$G_{0m} = \pi \alpha_{\text{avg}} \text{Bi}_H \beta m \cosh\left(\pi \beta m\right) \tag{103}$$

$$H_{0m} = \pi^2 \left(\beta^2 m^2\right) \sinh\left(\pi \beta m\right) \tag{104}$$

- For $\lambda = 0$ and $\mu = 0$:

$$\bar{\bar{\Theta}}''_{00} = 0 \tag{105}$$

The transformed boundary conditions are:

$$\bar{\bar{\Theta}}'_{00}(0) = -A_2 \int_0^1 \int_0^1 \dot{q}''_o(\xi,\eta)\mathrm{d}\eta\mathrm{d}\xi = -A_2 \bar{\bar{Q}}_{00} \tag{106}$$

$$\bar{\bar{\Theta}}'_{00}(1) = -\alpha_{\mathrm{avg}}\mathrm{Bi}_H \bar{\bar{\Theta}}_{00}(1) - A_2 \sum_{j=1}^{\mathrm{n_{fin}}} \int_0^1 \int_{\xi_{i_j}}^{\xi_{f_j}} \dot{q}''_{\mathrm{fin}}(\eta)\mathrm{d}\xi\mathrm{d}\eta \tag{107}$$

The analytical solution for the transformed equation where $\lambda = 0$ and $\mu = 0$ is:

$$\bar{\bar{\Theta}}_{00}(\zeta) = \frac{A_2 \bar{\bar{Q}}_{00}[1 + \mathrm{Bi}_H(\alpha_{\mathrm{avg}} - \alpha_{\mathrm{avg}}\zeta)] - A_2 \sum_{j=1}^{\mathrm{n_{fin}}}(\xi_{f_j} - \xi_{i_j}) \int_0^1 \dot{q}''_{\mathrm{fin}}(\eta)\mathrm{d}\eta}{\mathrm{Bi}_H \alpha_{\mathrm{avg}}} \tag{108}$$

2.1.2.3 Reordering Procedure

The inversion formula indicated in equation (64) is applied to obtain the dimensionless temperature field (Θ) for the HS base.

$$\Theta(\xi,\eta,\zeta) = \sum_{n=0}^{\infty}\sum_{m=0}^{\infty} \frac{\bar{\bar{\Theta}}_{nm}(\zeta)\Psi_n(\eta)\Xi_m(\xi)}{N_{y_n}N_{xm}} \tag{109}$$

The consequence of having a double summation is the necessity of more terms to be summed for full convergence. The double summation may be reduced to one if the reordering procedure is performed. The reordering procedure (COTTA; MIKHAILOV, 1997) selects the combinations of n and m with more significant values to be summed first, enabling faster convergence to the final solution of the temperature field of the base of the HS. For this reordering procedure, the CITT index pair (n,m) is sorted in descending order, whose summation order is indicated by the single index k.

$$\sum_{n=0}^{\infty}\sum_{m=0}^{\infty} \rightarrow \sum_{k=0}^{\infty} \tag{110}$$

2.1.3 Analytical solutions coupling

In this step of the methodology, the fin-base interface heat flux is calculated. The unknown heat fluxes $\dot{q}''_{\mathrm{base}}$ and $\dot{q}''_{\mathrm{fin}}$ are obtained using assumptions to couple fin and base equations. As it was mentioned previously on section 1.3, a perfect contact on the fin-base interface is considered and, for this reason:

$$\dot{q}''_{\mathrm{base}}(\eta) = \dot{q}''_{\mathrm{fin}}(\eta) = \dot{q}''_{ic}(\eta) \tag{111}$$

Figure 11 - 2D view of the fin-base coupling. The direction of the heat fluxes are indicated on the scheme. Also, the base-fin perfect contact interface is defined as both heat fluxes with the same magnitude and the temperature at the top of the base at the same ξ of the fin, having the same magnitude as bottom of the fin.

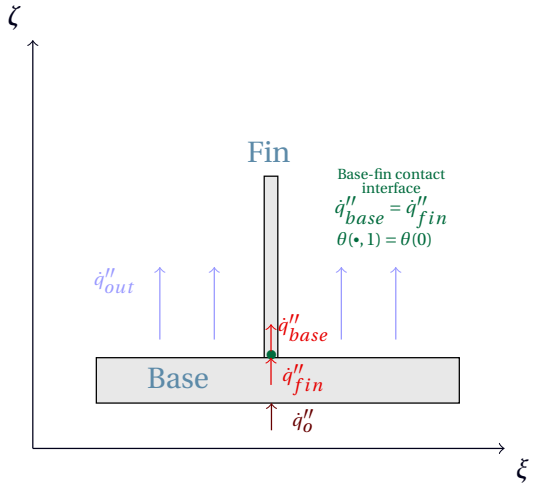

which is now denominated as $\dot{q}''_{ic}$, contact interface heat flux.

For dealing with two equations and two variables, one more condition is required to solve the system. The temperature of the contact between fin and base must be equal. The coupling equations are solved, in this case, considering η coordinate.

$$\Theta_{\text{base}}(\xi_{\text{avg}}, \eta_x, 1) = \Theta_{\text{fin}}(\eta_x, 0), \quad \xi_{\text{avg}} = \frac{\xi_i + \xi_f}{2} \tag{112}$$

$$\dot{q}''_{\text{base}}(\eta_x) = \dot{q}''_{\text{fin}}(\eta_x) = \dot{q}''_{ic}(\eta_x) \tag{113}$$

where Θ_{base} is the temperature of the base, Θ_{fin} is the temperature of the fin, ξ_i is the position where the fin begins, ξ_f is the position where the fin ends, ξ_{avg} is the fin's middle position and η_x is a selected position in η-direction. The figure 11 illustrates the fin-base coupling for one-fin heat sink. The heat flux for each fin is calculated from the equations (112) and (113), using the base and fins CITT solutions.

The fin-base interface heat flux is approached using the eigenfunction expansion. In other words, the heat flux is defined as an inversion term and its transformation is used to find the fin-base coupling. The great advantage of the eigenfunction expansion heat flux is to solve the system in several different positions and increase its accuracy as more positions are

Figure 12 - η-positions scheme for fin-base coupling. The more positions are selected, the more accurate is the fin-base coupling.

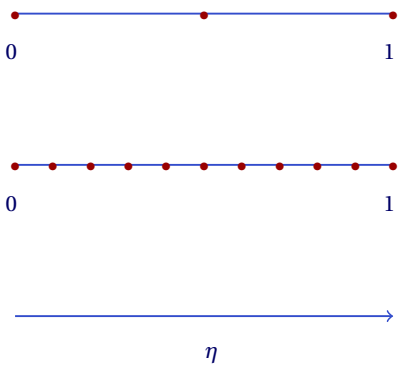

considered. It is a more accurate approach than the polynomial function approach[2], which considers limited positions depending on the polynomial degree. As can be concluded in Figure 12, the more η_x-positions are considered, the more accurate is the fin-base coupling.

The fin-base interface heat flux transformation pair and its norm are defined as:

$$\text{Inversion} \quad \Rightarrow \quad \dot{q}''_{ic}(\eta) = \sum_{p=0}^{\infty} \frac{\bar{q}''_{ic_p} \Psi_p(\eta)}{N_{\Psi p}} = \dot{q}''_{\text{fin}}(\eta) = \dot{q}''_{\text{base}}(\eta) \tag{114}$$

$$\text{Transformation} \quad \Rightarrow \quad \bar{q}''_{ic_p} = \int_0^1 \dot{q}''_{ic}(\eta) \Psi_p(\eta) \mathrm{d}\eta \tag{115}$$

$$\text{Norm} \quad \Rightarrow \quad N_{\Psi p} = \int_0^1 \Psi_p^2 \mathrm{d}\eta \tag{116}$$

where Ψ_p is a generic eigenfunction and p is summed until $\mathrm{n_{max}}$ η-positions.

For the 2D fin formulation, the transformed boundary condition at the bottom edge is described on equation (55) as:

$$\bar{\Theta}'_n(0) = -A_1 \int_0^1 \dot{q}''_{\text{ic}}(\eta) \Psi_n \mathrm{d}\eta = -A_1 \bar{q}''_{ic_p} \tag{117}$$

For the 3D base formulation, the top boundary condition is described on equation

[2] The use of polynomial functions is a different approach to model the heat fluxes that may vary for different η-positions. It is described in Appendix C and was previously implemented by Corrêa and Chalhub (2019).

(74), the fin-base interface part is rewritten on Equation (118).

$$\sum_{j=1}^{\mathrm{n_{fin}}} \int_{\xi_{i_j}}^{\xi_{f_j}} \left(\int_0^1 \dot{q}''_{\mathrm{ic}}(\eta) \Psi_n(\eta) \Xi_m(\xi) \mathrm{d}\eta \right) \mathrm{d}\xi = \sum_{j=1}^{\mathrm{n_{fin}}} \bar{q}''_{ic_{nj}} \int_{\xi_{i_j}}^{\xi_{f_j}} \Xi_m(\xi) \mathrm{d}\xi \tag{118}$$

The transformed boundary condition for the top of the 3D base, used before the fin-base coupling, becomes:

$$\bar{\bar{\Theta}}'_{nm}(1) = -\alpha_{\mathrm{avg}} \mathrm{Bi}_H \bar{\bar{\Theta}}_{nm}(1) - A_2 \sum_{j=1}^{\mathrm{n_{fin}}} \bar{q}''_{ic_{nj}} \int_{\xi_{i_j}}^{\xi_{f_j}} \Xi_m(\xi) \mathrm{d}\xi \tag{119}$$

where the transformed $\bar{q}''_{ic_{nj}}$ are now the values to be obtained and $\mathrm{n_{max}}$ different positions are summed.

After performing the fin-base coupling, each $\bar{q}''_{ic_n}$ for each j fin is obtained. Then, $\bar{q}''_{ic_n}$ is used on equations (117) and (119) to solve the fins and base solutions and the temperature field is obtained.

2.2 **2D base and 1D fin: Benchmark problem**

The simplified formulation for the heat sink, considering one-dimensional fins and two-dimensional base, is a benchmark problem. The scheme for this model is illustrated on Figure 13.

The general analytical solution for the 1D fin is indicated in (10a):

$$\Theta(\zeta_a) = C_1 e^{m_a \zeta_a} + C_2 e^{-m_a \zeta_a} \tag{120}$$

where C_1 and C_2 are constants.

Applying the boundary conditions, the solution for 1D fin is:

$$\Theta_j(\zeta_a) = \frac{A_1 e^{-\zeta_a m_a} \left(e^{2\zeta_a m_a} + e^{2m_a} \right)}{\left(e^{2m_a} - 1 \right) m_a} \dot{q}''_{\mathrm{base}_j} \tag{121}$$

where $\dot{q}''_{\mathrm{base}}$ is an unknown value and the index j indicates this solution is applicable to each unique fin j fin.

Figure 13 - 1D fins and 2D base scheme illustration. This benchmark problem considers heat conduction only the ξ and ζ directions, as indicated by the axes, which are the dimensionless versions x and z, respectively. The heated chip is indicated in red attached on the bottom surface of the HS's base.

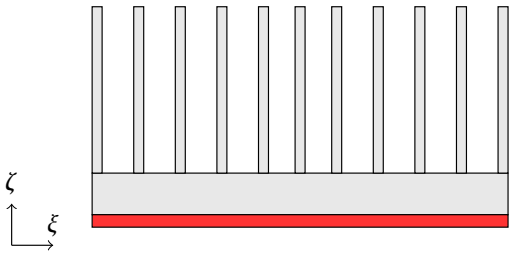

2.2.1 Solution by CITT of the 2D base

The Helmholtz problem is used again as the auxiliary eigenvalue problem:

$$\Xi''_m(\xi) + \mu_m^2 \Xi_m(\xi) = 0 \tag{122a}$$

$$\Xi'_m(0) = 0; \quad \Xi'_m(1) = 0. \tag{122b}$$

For $\mu = 0$, the solution of the eigenvalue problem is given by:

$$\Xi_0(\xi) = 1; \qquad \mu_0 = 0; \tag{123}$$

and for $\mu > 0$:

$$\Xi_m(\xi) = \cos(\mu_m \xi); \qquad \mu_m = m\pi, \quad \text{for} \quad m = 1,2,3,\ldots \tag{124}$$

To apply the CITT, the transformation pair is defined.

$$\text{Transformation} \quad \Rightarrow \quad \bar{\Theta}_m(\zeta) = \int_0^1 \Theta \Xi_m(\xi) \mathrm{d}\xi \tag{125}$$

$$\text{Inversion} \quad \Rightarrow \quad \Theta = \sum_{m=0}^{\infty} \frac{\bar{\Theta}(\zeta)\Xi_m(\xi)}{N_m}, \qquad N_m = \int_0^1 \Xi_m^2 \mathrm{d}\xi \tag{126}$$

where $\bar{\Theta}_m(\zeta)$ and $\Xi_m(\xi)$ are the functions to be solved separally in order to find the temperature field and are eigenfunctions. $\bar{\Theta}_m(\zeta)$ is also the transformed version of Θ. N_m is the norm.

The Equation (23a) is written again, multiplied by Ξ_m and integrated in the domain

for ξ.

$$\int_0^1 \frac{\partial^2 \Theta}{\partial \zeta^2} \Xi_m \mathrm{d}\xi + \beta^2 \int_0^1 \frac{\partial^2 \Theta}{\partial \xi^2} \Xi_m \mathrm{d}\xi = 0 \tag{127a}$$

- For $\mu > 0$:

$$\bar{\Theta}_m'' - (\beta^2 \mu_m^2)\bar{\Theta}_m = 0 \tag{128}$$

The transformed boundary conditions are:

$$\bar{\Theta}_m'(0) = -A_2 \int_0^1 \dot{q}_o''(\xi)\Xi_m \mathrm{d}\xi \tag{129a}$$

$$\bar{\Theta}_m'(1) = \bar{\Theta}_m'(1) = -\alpha_{\text{avg}} \mathrm{Bi}_H \bar{\Theta}_m(1) - A_2 \sum_{j=1}^{\mathrm{n_{fin}}} \int_{\xi_{i_j}}^{\xi_{f_j}} \dot{q}''_{\mathrm{fin}_j} \Xi_m(\xi) \mathrm{d}\xi \tag{129b}$$

where $\mathrm{n_{fin}}$ is the number of fins, ξ_i refers to the position where the fin begins and ξ_f where it ends, as shown in figure 10. α_{avg} is the average value for α.

The transformed equation admits an analytical solution for $\mu > 0$.

$$\begin{aligned}\bar{\Theta}_m(\zeta) = \\ \frac{A_2 e^{-m\pi\beta\zeta}}{m\pi\beta[\mathrm{Bi}_H \alpha_{\text{avg}}(1+e^{2m\pi\beta}) + m\pi\beta(-1+e^{2m\pi\beta})]} \Big[\mathrm{Bi}_H \alpha_{\text{avg}} \left(e^{2m\pi\beta} - e^{2m\pi\beta\zeta} \right) + \\ m\pi\beta \left(e^{2m\pi\beta} + e^{2m\pi\beta\zeta} \right) \int_0^1 \dot{q}_o''(\xi) \cos(m\pi\xi) \mathrm{d}\xi + \\ -m\pi\beta e^{m\pi\beta\zeta}(1+e^{2m\pi\beta\zeta}) \sum_{j=1}^{\mathrm{n_{fin}}} \dot{q}''_{\mathrm{fin}_j} \frac{(\sin(m\pi\xi_{f_j}) - \sin(m\pi\xi_{f_i}))}{m\pi} \Big]\end{aligned} \tag{130}$$

- For $\mu = 0$, the transformed equation is similar to the 1D LaPlace equation:

$$\bar{\Theta}_0'' = 0 \tag{131}$$

The transformed boundary conditions are:

$$\bar{\Theta}_0'(0) = -A_2 \int_0^1 \dot{q}_o''(\xi) \mathrm{d}\xi; \tag{132a}$$

$$\bar{\Theta}_0'(1) = -\alpha_{\text{avg}} \mathrm{Bi}_H \bar{\Theta}_0(1) - A_2 \sum_{j=1}^{\mathrm{n_{fin}}} \int_{\xi_{i_j}}^{\xi_{f_j}} \dot{q}''_{\mathrm{fin}_j} \mathrm{d}\xi \tag{132b}$$

The transformed equation for admits the following analytical solution $\mu = 0$.

$$\bar{\Theta}_0(\zeta) = A_2 \int_0^1 \dot{q}_o''(\xi) \mathrm{d}\xi \left(\frac{1}{\mathrm{Bi}_H \alpha_{\text{avg}}} + 1 - \zeta \right) - \frac{A_2}{\mathrm{Bi}_H \alpha_{\text{avg}}} \sum_{j=1}^{\mathrm{n_{fin}}} \dot{q}''_{\mathrm{fin}_j} (\xi_{f_j} - \xi_{i_j}) \tag{133}$$

where $\dot{q}''_{\text{fin}}$ is also an unknown value. The inversion formula (126) is used and the summation is truncated to a finite value (n_{max}) and literal, with the $\dot{q}''_{\text{fin}}$ summation terms.

The fin-base coupling is also performed for the 2D base and 1D fin. In this case, the η-direction is not considered and, consequently, the heat flux for each fin is a constant value. The fin-base coupling equations are shown below.

$$\dot{q}''_{\text{base}} = \dot{q}''_{\text{fin}} = \dot{q}''_{ic} \tag{134}$$

$$\Theta_{\text{base}}(\xi_{\text{avg}}, 1) = \Theta_{\text{fin}}(0), \quad \xi_{\text{avg}} = \frac{\xi_i + \xi_f}{2} \tag{135}$$

where Θ_{base} is the temperature of the base, Θ_{fin} is the temperature of the fin, ξ_i is the position where the fin begins, ξ_f is the position where the fin ends, and ξ_{avg} is exactly in the middle of the fin.

The equations (134) and (135) create a system of equations which is solved and $\dot{q}''_{ic}$ is obtained. The value obtained for $\dot{q}''_{ic}$ is inserted on the solutions (121) for the 1D fin and (130) and (133) for the 2D base.

3 COMPUTATIONAL FLUID DYNAMICS

Simulations using numerical analysis provide faster and cheaper results when compared to experimental validation. To obtain an approximate solution numerically, discretization methods approximate the differential equations by a system of algebraic equations, which can then be solved on a computer. The approximations are applied to spatial and time small domains so the numerical solution provides results at discrete locations in space and time (FERZIGER; PERIĆ, 2002). Based on partial differential equation discretization methods, Computational Fluid Dynamics (CFD) has been used for several applications such as mechanical, aerospace, biological, meteorological, and environmental fields. The literature review section indicated the Finite Volume Method as an efficient verification method and, for this reason, it was chosen as the discretization method for the heat sinks CFD simulation to be used on this present work.

The Finite Volume Method (FVM) is a numerical technique that, using conservation laws, transforms the partial differential equations representing over differential volumes into discrete algebraic equations over finite volumes (MOUKALLED et al., 2016). In FVM, some terms in the conservation equation are turned into face fluxes and evaluated at the finite volume faces. Because the flux entering a given volume is identical to that leaving the adjacent volume, the FVM is strictly conservative. This inherent conservation property of the FVM makes it the preferred method in CFD. Another important attribute of the FVM is the formulation in the physical space using unstructured polygonal meshes. Hence, it allows the implementation of a variety of boundary conditions in a non-invasive manner, since the unknown variables are evaluated at the centroids of the volume elements, not at their boundary faces (MOUKALLED et al., 2016).

3.1 **OpenFOAM**

OpenFOAM (Open Field Operation and Manipulation) is an opensource software package and C++ modules library based on the cell-centered Finite Volume Method with extensive CFD and multiphysics capabilities. It solves computational continuum mechanics problems utilizing features of Objected Oriented Programming (OOP).

Some advantages of OpenFOAM are cost-effectiveness, parallel computing, source code, redistribution of code, and collaborative development. It lacks enhancement on the documentation and GUI user-friendliness, though.

3.2 **The CFD simulation for the heat sink**

The Computational Fluid Dynamics simulations, in general, are composed of the steps enumerated below. Hence, the implementation performed in this present works is also described.

1. Define the geometry to be analyzed.

   The geometry and the mesh of the heat sink simulation were generated using the open-source mesh generator *Gmsh*. After setting the characteristic length of the base of the HS, the other dimensions were defined following this parameter by the aspect ratio. The developed script allows us to define the number and shape of the fins, rectangular, triangular, or parabolic, and generate multiple different geometries using the same code.

2. Generate the mesh from the geometric model

   The 3D mesh was generated using the Graphical User Interface (GUI) of *Gmsh*. The software generates triangular and tetrahedral elements by default because it generates unstructured meshes. Unstructured meshes are well suited for handling arbitrary shape geometries, especially for domains having high curvature boundaries (TU; YEOH; LIU, 2018). When the geometry does not present curve complexities, however, structured meshes are preferred because this type of mesh allows easy data management and connectivity to occur regularly, which makes programming easy. The connectivity is straightforward as the adjacent cells to a given elemental face are identified by the indices, and the cell edges form continuous mesh lines that begin and end on opposite elemental faces. Because the heat sink geometric model is composed of squared and rectangular sides, the elements were recombined to generate quadrilateral shapes.

3. Define the problem solution:

   (a) Mathematical model

   One advantage of the OpenFOAM package is the implementation of several multiphysics solvers and tutorials. The chosen solver used in the simulation was the *laplacianFoam*. This application solves the Laplace equation for unsteady, isotropic diffusion.

   (b) Boundary conditions

   The same boundary conditions applied in the analytical problem were implemented in the OpenFOAM simulation. This convective boundary condition, considering the combined heat transfer coefficient and T_f, was applied at the base's

top and in the fins wet area. The source heat flux from the heated chip was introduced at the base's bottom boundary as a fixed constant gradient. The other boundaries were considered as *zeroGradient*.

(c) Spatial and Temporal discretization schemes

The Euler discretization is used on the temporal scheme and the Gauss linear is used on the spatial scheme.

4. Process the problem:

Run the solver on the meshed geometry using the defined boundary and initial conditions. Version 7 of OpenFOAM was used for the simulation.

5. Visualization and interpretation of results:

The post-processing analysis of the simulations is performed using the opensource software *paraview*. This step is described in the Results section.

4 RESULTS

This chapter provides results and analysis from the formulations and methodologies presented in the previous chapters. Heat sinks have wide heat transfer enhancement applications, different scales of passive heat exchanger devices can then be found in the industry. The present work handles with dimensionless parameters and part of the selected values were based on the examples from the work of Lehtinen (2005) and Mosayebidorcheh et al. (2015). Dimensionless formulations reduce the number of parameters in the problem with a clearer perspective about the effect of these key-parameters on the overall problem (CORRÊA, 2018). Table 1 indicates the heat sink dimensions considering two different industry applications: for overheated chips in electronics cooling, and to promote a better heat transfer for photovoltaic cell in photovoltaics efficiency enhancement (POPOVICI et al., 2016). Heat sinks in mm-scale and cm-scale are usually used in those cases, respectively. Figure 9 is shown again aiming a clearer view of the chosen dimensions.

4.1 **Formulations comparison and CITT convergence**

The objective of this section is to present the 2Dbase-1Dfin and 3Dbase-2Dfin formulations results. The same values for the parameters, source heat flux, and six-equally spaced fins are considered in both formulations. The fins are enumerated from left to right, the fin whose initial edge is in $\xi = 0$ is enumerated as 1 and the fin whose final edge is in $\xi = 1$ is enumerated as 6. This layout is presented in Table 2, also with an illustrating scheme. Because all the fins have the same properties, dimensions, and convection rates, they are considered equal to each other. The thermal properties of aluminum were considered for the heat sink and the air is the cooling fluid at 25^oC. For this layout, the $\alpha_{\text{avg}} = 0.76$.

The heated chip, in this case, occupies the entire HS bottom base surface domain with the constant heat flux of $\dot{q}''_o = 2000$ W/m^2. Table 3 shows the selected dimensionless values for the approach on both photovoltaic case and electronic case heat sinks. More details about the chosen values are explained in Appendix A.

4.1.1 cm-scaled heat sink

The first heat sink case is cm-scaled and simulates an application in the photovoltaics (PV) industry, reasoning the case's name, although this type of heat sink may be also used in several engineering fields.

Figure 14 presents the thermal profile of the base and fins for the cm-scaled heat sink

Table 1 - Heat sink design parameters for photovoltaics and electronics applications. The fin thickness δ is defined as $0.04 \times W$ and two different fin height are used in this chapter: $H_a = 0.8 \times W$ and $H_a = 1.0 \times W$, where W is the HS width. Figure 9 is shown again.

cm-scaled HS		mm-scaled HS	
L	20 cm	L	10 mm
W	20 cm	W	10 mm
H	2 cm	H	1 mm

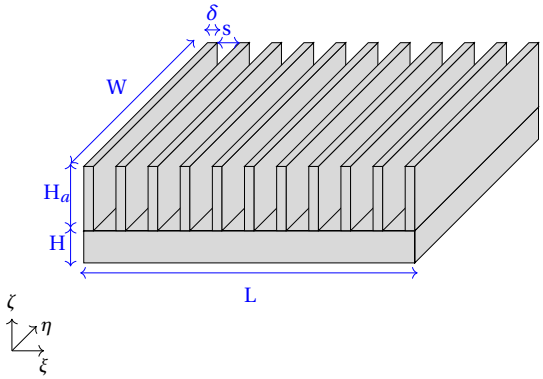

Table 2 - Six-fin heat sink layout. The dark blue strips indicate the location of the fins while the channels are indicated in yellow. δ is defined as $0.04 \times W$, ξ_i and ξ_f indicate the fin edges. W is the HS width.

Fin	1	2	3	4	5	6
ξ_i	0	0.192	0.384	0.576	0.768	0.96
ξ_f	0.04	0.232	0.424	0.616	0.808	1

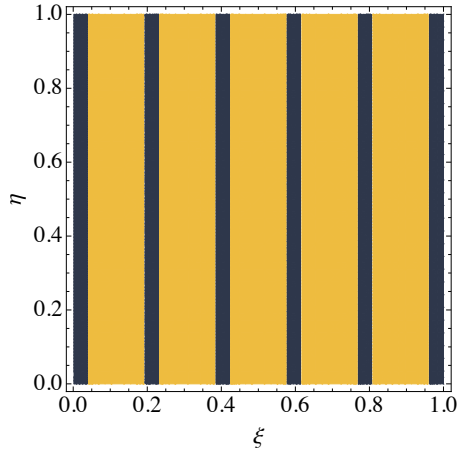

Table 3 - Dimensionless parameters for the formulations results using the thermal properties of aluminum as the HS material and air as cooling fluid at 25^oC. The aspect ratios β, γ, β_a, and γ_a are the same for both photovoltaics and electronics heat sink. The photovoltaics heat sink presents, conversely, higher values for the convective-parameters $\mathrm{Bi}_H, \mathrm{Bi}_{H_a}\beta_a$, and m_a than the electronics HS. The fin height is $H_a = 0.8 \times W$, where W is the HS width.

cm-scaled case HS				mm-scaled case HS			
3D Base-2D Fin		2D Base-1D Fin		3D Base-2D Fin		2D Base-1D Fin	
$\mathrm{Bi}_H =$	8.03×10^{-4}	$\mathrm{Bi}_H =$	8.03×10^{-4}	$\mathrm{Bi}_H =$	1.965×10^{-5}	$\mathrm{Bi}_H =$	1.965×10^{-5}
$\beta = \gamma =$	0.1	$\beta =$	0.1	$\beta = \gamma =$	0.1	$\beta =$	0.1
$A_1 =$	8.0×10^{-6}	$A_1 =$	8.0×10^{-6}	$A_1 =$	4.0×10^{-7}	$A_1 =$	4.0×10^{-7}
$A_2 =$	1.0×10^{-6}	$A_2 =$	1.0×10^{-6}	$A_2 =$	5.0×10^{-8}	$A_2 =$	5.0×10^{-8}
$\mathrm{Bi}_{H_a}\beta_a =$	0.12848	$m_a =$	0.52	$\mathrm{Bi}_{H_a}\beta_a =$	0.003144	$m_a =$	0.08
$\gamma_a =$	0.8			$\gamma_a =$	0.8		

considering the heated chip attached to the base. The inlet heat flux presents constant intensity and the same length and width dimensions of the HS base. The heat transfer coefficient is 3 and 5.03 for radiation and convection, respectively, which leads to the combined heat transfer coefficient as $8.03 \mathrm{W/m^2K}$.

The results in Figure 14 confirm a similar behavior of heat dissipation in the heat sink base using the different formulations. A kindred thermal profile can be observed for the fins in Figures 14a and 14b. The six-fin layout is symmetric, the fins located in the middle of the domain, 2-5 and 3-4, present higher temperatures, also observing the proximity of these fins curves at Figures 14a-14b. Analyzing the isotherms for the thermal profile of the base on Figures 14c and 14d, the source of heat flows from the bottom of the base, the heat dissipation is majorly promoted by the fins at the top of the base. It must be noticed the existence of aspect ratio in the Figures 14c and 14d, for a better examination of the achieved results, the results are shown in a square plot. The temperature range of the base is shown at the right of the contour plots.

Heatlines (DENG; TANG, 2002) are also shown with isotherms in Figure 14d. Isotherms of the primitive variables, such as temperature, velocity, or pressure, are important to visualize the levels of the variables through the domain (COSTA, 1999). Stream functions and streamlines are widely used tools to visualize the momentum transport of fluid flow. To observe the heat transfer by fluid flow, Kimura and Bejan (1983) introduced in 1983 the energy analog concept of heat function and heatlines. Heatlines complement the visualization of the energy flow in the domain and have been used in different types of problems like convective heat transfer, reactive and turbulent flows (MAHAPATRA et al., 2018).

For the heat sink problem, a simplified heat function considering only heat conduction at the HS's base is considered for better visualization of the heat fluxes from the heated chip to the coupled fins.

Figure 14 - Temperature field Θ for the cm-scaled case heat sink comparing the 2Dbase-1Dfin and the 3Dbase-2Dfin formulations. The solutions were calculated for n_{max} = 500 and k_{max} = 128000, respectively. The six-fin layout is symmetrical.

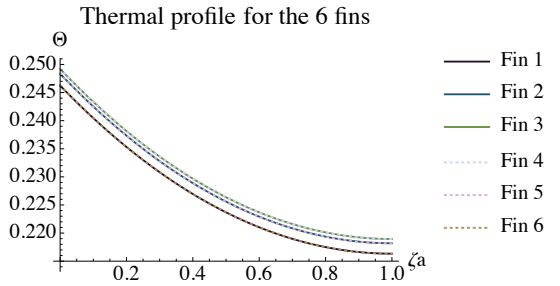

(a) Thermal profile of the fins considering the 1D formulation.

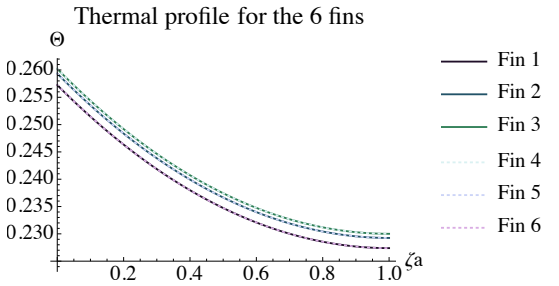

(b) Thermal profile of the fins considering the 2D formulation.

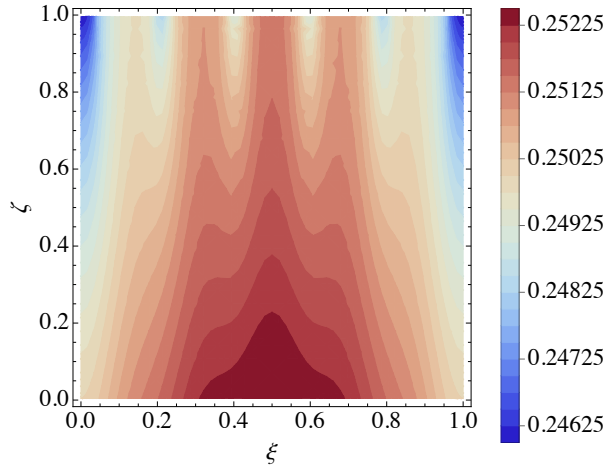

(c) Thermal profile of the base considering the 2D formulation.

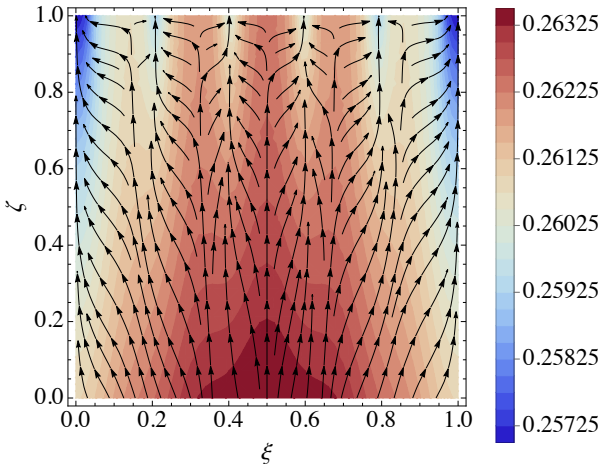

(d) Thermal profile of the base considering the 3D formulation for $\eta = 0.5$ and heatlines.

Table 4 - CITT Convergence Table of the temperature at the fin-base contact-interface for the cm-scaled heat sink case. The six-fin layout is symmetric. n_{max} are the terms summed for the 2D base, and k_{max} refers to the summed sorted terms for the 3D base.

	Fin 1	Fin 2	Fin 3	Fin 4	Fin 5	Fin 6
n_{max}	2Dbase-1DFin					
50	0.246253	0.248338	0.249199	0.249199	0.248338	0.246253
100	0.246241	0.248353	0.249215	0.249215	0.248353	0.246241
200	0.246243	0.248350	0.249212	0.249212	0.248350	0.246241
300	0.246241	0.248347	0.249209	0.249209	0.248347	0.246241
400	0.246244	0.248350	0.249211	0.249211	0.248350	0.246244
500	0.246244	0.248349	0.249211	0.249211	0.248349	0.246244
600	0.246244	0.248349	0.249211	0.249211	0.248349	0.246244
700	0.246244	0.248349	0.249211	0.249211	0.248349	0.246244
k_{max}	3Dbase-2DFin					
1800	0.257256	0.259322	0.260176	0.260176	0.259322	0.257256
3200	0.257235	0.259337	0.260195	0.260195	0.259337	0.257235
5000	0.257233	0.259340	0.260200	0.260200	0.259340	0.257233
6050	0.257231	0.259341	0.260200	0.260200	0.259341	0.257231
7200	0.257232	0.259339	0.260199	0.260199	0.259339	0.257232
9800	0.257239	0.259334	0.260194	0.260194	0.259334	0.257239
11250	0.257238	0.259334	0.260194	0.260194	0.259334	0.257238
12800	0.257239	0.259334	0.260194	0.260194	0.259334	0.257239

The heatlines for the base of the heat sinks are obtained by:

$$\dot{q}''_z = -k\frac{\partial T}{\partial z} \rightarrow \dot{q}''_\zeta = -\frac{k\Delta T}{H}\frac{\partial \Theta}{\partial \zeta} = -\frac{1}{A_2}\frac{\partial \Theta}{\partial \zeta} \tag{136}$$

$$\dot{q}''_x = -k\frac{\partial T}{\partial x} \rightarrow \dot{q}''_\xi = -\frac{k\Delta T}{L}\frac{\partial \Theta}{\partial \xi} = -\frac{1}{A_3}\frac{\partial \Theta}{\partial \xi} \tag{137}$$

The heatlines in Figure 14d indicate the heat leaving the heated chip source, and converging at the fins' proximities.

The CITT convergence at the fin-base interface is shown at the middle position of the six fins in Table 4. As can be seen, the 2Dbase-1Dfin CITT methodology obtains the six-digit convergence summing 500 terms. For the 3Dbase-2Dfin CITT methodology, however, more terms need to be added because of the double summation and, therefore, it was necessary to sum 12800 in order to achieve the six-digit convergence.

The solutions in Figure 14 have several similarities for both the base and the fins, despite the use of a more simplified formulation (2Dbase-1Dfin). The dimensionless temperature magnitudes in Table 4, however, exhibit small variations between the formulations. This effect can be explained by obtaining the fin-base contact interface heat fluxes $\dot{q}''_{ic}$.

4.1.2 Fin-base contact interface heat flux

The results for the CITT were based on the contact-interface heat fluxes $\dot{q}''_{ic}$ convergence. Before the fin-base coupling step, the base solutions were summed to a maximum value, and the truncated temperature field was compared with the fin solution, as well as the fin-base heat fluxes($\dot{q}''_{\text{base}} = \dot{q}''_{\text{fin}}$). For the 2D base, the maximum value was indicated by n_{max}. For the 3D base, the solution was summed until the maximum value of $k_{max} = n^2_{max} \div 2$, after the reordering procedure, where n_{max} is the number of summed values for the 2D fin solution. The Tables 5 and 6 show the $\dot{q}''_{ic_j}$ convergence for the $j = 6$ fins.

The results from Table 5 demonstrate that the six-digit convergence was easily achieved using the 2Dbase-1Dfin formulation. This precision was achieved after summing 500 terms for the cm-scaled case. For the 3Dbase-2Dfin formulation, the results achieved a six-digit convergence precision after summing 12800 terms. The necessity of having more terms is justified by the double transformation of the 3D base and the coupling using truncated results for the 2D fins and the 3D base.

Different behavior is observed in the results from Table 6, where the six-digit convergence for both formulations required fewer terms summed for the mm-scaled case. The 2Dbase-1Dfin formulation converged with 100 terms and 4050 terms for most positions using the 3Dbase-2Dfin formulation for the electronic heat sink case.

The relative deviation percentage is used to verify the accuracy between the analytical methodologies and is described as:

$$\%R\varepsilon = \frac{\dot{q}''_{ic_{\text{2D1D}}} - \dot{q}''_{ic_{\text{3D2D}}}}{\dot{q}''_{ic_{\text{2D1D}}}} \times 100 \tag{138}$$

where $\dot{q}''_{ic_{\text{2D1D}}}$ is the converged value of 2Dbase-1Dfin with $n_{max} = 500$ and $\dot{q}''_{ic_{\text{3D2D}}}$ is the value for each one of the described k_{max}.

As can be seen, the relative deviation is paltry, between 0.128016% and 0.386216%. However, as the heat fluxes hit high intensities as 7×10^3, a small variation in the temperature field between the 2Dbase-1Dfin and 3Dbase-2Dfin formulations is exposed on Tables 7 and 8.

The more complete physical modeling, the more accurate is implemented formulation. For this reason, the results from the 3Dbase-2Dfin formulation are the most accurate.

Table 5 - Convergence Table of the contact interface heat flux $\dot{q}''_{ic}$ for the cm-scaled heat sink case. For the 2D base, the solution is summed for n_{max} values before performing the fin-base coupling. The underlined terms indicate the six-digit convergence achieved. The $k_{max} = n^2_{max} \div 2$ highest sorted terms were summed in the 3D base inversion, where n_{max} is the number of terms summed in the 2D fin inversion. The six-fin layout is symmetric and, consequently, $\dot{q}''_{ic_1} = \dot{q}''_{ic_6}$, $\dot{q}''_{ic_2} = \dot{q}''_{ic_5}$, and $\dot{q}''_{ic_3} = \dot{q}''_{ic_4}$. The relative deviation is calculated between the converged value of 2Dbase-1Dfin with $n_{max} = 500$ and each one of the described k_{max} for the 3Dbase-2DFin. The more terms are summed for the 3Dbase-2Dfin, the lower is the relative deviation among the fins.

	$\dot{q}''_{ic_1}$	$\dot{q}''_{ic_2}$	$\dot{q}''_{ic_3}$	$\dot{q}''_{ic_4}$	$\dot{q}''_{ic_5}$	$\dot{q}''_{ic_6}$
n_{max}	2Dbase-1Dfin					
50	7646.28	7711.01	7737.75	7737.75	7711.01	7646.28
100	7645.90	7711.49	7738.25	7738.25	7711.49	7645.90
200	7645.98	7711.40	7738.16	7738.16	7711.40	7645.98
300	7645.99	7711.38	7738.14	7738.14	7711.38	7645.99
400	7646.00	7711.38	7738.14	7738.14	7711.38	7646.00
500	7646.00	7711.38	7738.13	7738.13	7711.38	7646.00
600	7646.00	7711.38	7738.13	7738.13	7711.38	7646.00
700	7646.00	7711.38	7738.13	7738.13	7711.38	7646.00
k_{max}	3Dbase-2Dfin					
50	7613.93	7686.63	7714.06	7714.06	7686.63	7613.93
200	7617.18	7684.32	7711.45	7711.45	7684.32	7617.18
450	7620.86	7683.04	7708.38	7708.38	7683.04	7620.86
800	7621.17	7682.52	7707.91	7707.91	7682.52	7621.17
1250	7620.86	7682.47	7707.94	7707.94	7682.47	7620.86
1800	7621.20	7682.40	7707.75	7707.75	7682.40	7621.20
2450	7621.07	7682.59	7707.88	7707.88	7682.59	7621.07
3200	7620.59	7682.86	7708.26	7708.26	7682.86	7620.59
4050	7620.47	7682.92	7708.42	7708.42	7682.92	7620.47
5000	7620.52	7682.94	7708.42	7708.42	7682.94	7620.52
6050	7620.44	7682.98	7708.42	7708.42	7682.98	7620.44
7200	7620.49	7682.91	7708.37	7708.37	7682.91	7620.49
9800	7620.68	7682.75	7708.25	7708.25	7682.75	7620.68
11250	7620.65	7682.76	7708.25	7708.25	7682.76	7620.65
12800	7620.67	7682.75	7708.25	7708.25	7682.75	7620.67
k_{max}	Relative deviation between formulations					
50	0.419523%	0.320931%	0.311090%	0.311090%	0.320931%	0.419523%
200	0.376990%	0.350799%	0.344786%	0.344786%	0.350799%	0.376990%
450	0.328858%	0.367393%	0.384544%	0.384544%	0.367393%	0.328858%
800	0.324770%	0.374135%	0.390556%	0.390556%	0.374135%	0.324770%
1250	0.328765%	0.374833%	0.390259%	0.390259%	0.374833%	0.328765%
1800	0.324381%	0.375716%	0.392669%	0.392669%	0.375716%	0.324381%
2450	0.326041%	0.373255%	0.390971%	0.390971%	0.373255%	0.326041%
3200	0.332406%	0.369831%	0.386121%	0.386121%	0.369831%	0.332406%
4050	0.333902%	0.368961%	0.383959%	0.383959%	0.368961%	0.333902%
5000	0.333332%	0.368762%	0.384034%	0.384034%	0.368762%	0.333332%
6050	0.334264%	0.368244%	0.384044%	0.384044%	0.368244%	0.334264%
7200	0.333597%	0.369132%	0.384617%	0.384617%	0.369132%	0.333597%
9800	0.331192%	0.371176%	0.386230%	0.386230%	0.371176%	0.331192%
11250	0.331504%	0.371068%	0.386230%	0.386230%	0.371068%	0.331504%
12800	0.331180%	0.371149%	0.386216%	0.386216%	0.371149%	0.331180%

Table 6 - Convergence Table of the contact interface heat flux $\dot{q}''_{ic}$ for the mm-scaled heat sink case. For the 2D base, the solution is summed for n_{max} values before performing the fin-base coupling. The underlined terms indicate the six-digit convergence achieved. The $k_{max} = n^2_{max} \div 2$ highest sorted terms were summed in the 3D base inversion, where n_{max} is the number of terms summed in the 2D fin inversion. The six-fin layout is symmetric and, consequently, $\dot{q}''_{ic_1} = \dot{q}''_{ic_6}$, $\dot{q}''_{ic_2} = \dot{q}''_{ic_5}$, and $\dot{q}''_{ic_3} = \dot{q}''_{ic_4}$. The relative deviation is calculated between the converged value of 1DFin-2Dbase with $n_{max} = 500$ and each one of the described k_{max} for the 3Dbase-2DFin. The more terms are summed for the 3Dbase-2DFin, the lower is the relative deviation among the fins.

	$\dot{q}''_{ic_1}$	$\dot{q}''_{ic_2}$	$\dot{q}''_{ic_3}$	$\dot{q}''_{ic_4}$	$\dot{q}''_{ic_5}$	$\dot{q}''_{ic_6}$
n_{max}	2Dbase-1DFin					
50	7729.26	7730.97	7731.69	7731.69	7730.97	7729.26
100	7729.25	7730.98	7731.70	7731.70	7730.98	7729.25
200	7729.25	7730.98	7731.70	7731.70	7730.98	7729.25
300	7729.25	7730.98	7731.70	7731.70	7730.98	7729.25
400	7729.25	7730.98	7731.70	7731.70	7730.98	7729.25
500	7729.25	7730.98	7731.70	7731.70	7730.98	7729.25
k_{max}	3Dbase-2DFin					
50	7719.17	7721.15	7721.91	7721.91	7721.15	7719.17
200	7719.26	7721.09	7721.84	7721.84	7721.09	7719.26
450	7719.36	7721.06	7721.76	7721.76	7721.06	7719.36
800	7719.37	7721.05	7721.75	7721.75	7721.05	7719.37
1250	7719.36	7721.04	7721.75	7721.75	7721.04	7719.36
1800	7719.37	7721.04	7721.74	7721.74	7721.04	7719.37
2450	7719.37	7721.05	7721.75	7721.75	7721.05	7719.37
3200	7719.35	7721.05	7721.76	7721.76	7721.05	7719.35
4050	7719.35	7721.06	7721.76	7721.76	7721.06	7719.35
5000	7719.35	7721.06	7721.76	7721.76	7721.06	7719.35
6050	7719.35	7721.06	7721.76	7721.76	7721.06	7719.35
7200	7719.35	7721.06	7721.76	7721.76	7721.06	7719.35
9800	7719.35	7721.05	7721.76	7721.76	7721.05	7719.35
11250	7719.35	7721.05	7721.76	7721.76	7721.05	7719.35
12800	7719.35	7721.05	7721.76	7721.76	7721.05	7719.35
k_{max}	Relative deviation between formulations					
50	0.130376%	0.127153%	0.126634%	0.126634%	0.127153%	0.130376%
200	0.129244%	0.127940%	0.127508%	0.127508%	0.127940%	0.129244%
450	0.127948%	0.128370%	0.128588%	0.128588%	0.128370%	0.127948%
800	0.127836%	0.128545%	0.128742%	0.128742%	0.128545%	0.127836%
1250	0.127942%	0.128560%	0.128728%	0.128728%	0.128560%	0.127942%
1800	0.127822%	0.128585%	0.128797%	0.128797%	0.128585%	0.127822%
2450	0.127868%	0.128521%	0.128753%	0.128753%	0.128521%	0.127868%
3200	0.128041%	0.128430%	0.128622%	0.128622%	0.128430%	0.128041%
4050	0.128082%	0.128408%	0.128565%	0.128565%	0.128408%	0.128082%
5000	0.128066%	0.128403%	0.128568%	0.128568%	0.128403%	0.128067%
6050	0.128099%	0.128380%	0.128559%	0.128559%	0.128380%	0.128099%
7200	0.128082%	0.128403%	0.128573%	0.128573%	0.128403%	0.128082%
9800	0.128016%	0.128457%	0.128616%	0.128616%	0.128457%	0.128016%
11250	0.128025%	0.128454%	0.128616%	0.128616%	0.128454%	0.128025%
12800	0.128016%	0.128457%	0.128616%	0.128616%	0.128457%	0.128016%

Table 7 - Temperature field Θ for the cm-scaled heat sink case with $n_{max} = 500$ and $k_{max} = 12800$. The fins' locations ξ_i and ξ_f are indicated on Table 2, and $\xi_{avg} = (\xi_i + \xi_f) \div 2$.

Position	Fin 1	Fin 2	Fin 3	Fin 4	Fin 5	Fin 6	Description
	2Dbase-1Dfin						
$\Theta_{fin}(1)$	0.216331	0.218181	0.218938	0.218938	0.218181	0.216331	Top of fin
$\Theta_{fin}(0)$	0.246244	0.248349	0.249211	0.249211	0.248349	0.246244	Bottom of fin
$\Theta_{base}(\xi_{avg}, 1)$	0.246244	0.248349	0.249211	0.249211	0.248349	0.246244	Top of Base
$\Theta_{base}(\xi_{avg}, 0)$	0.250057	0.251565	0.252433	0.252433	0.251565	0.250057	Bottom of Base
	3Dbase-2Dfin						
$\Theta_{fin}(0.5, 1)$	0.227392	0.229244	0.230005	0.230005	0.229244	0.227392	Top of fins
$\Theta_{fin}(0.5, 0)$	0.257239	0.259334	0.260194	0.260194	0.259334	0.257239	Bottom of fins
$\Theta_{base}(\xi_{avg}, 0.5, 1)$	0.257239	0.259334	0.260194	0.260194	0.259334	0.257239	Top of Base
$\Theta_{base}(\xi_{avg}, 0.5, 0)$	0.261050	0.262554	0.263421	0.263421	0.262554	0.261050	Bottom of Base

Table 8 - Temperature field Θ for the mm-scaled heat sink case with $n_{max} = 500$ and $k_{max} = 12800$. The fins' locations ξ_i and ξ_f are indicated on Table 2, and $\xi_{avg} = (\xi_i + \xi_f) \div 2$.

Position	Fin 1	Fin 2	Fin 3	Fin 4	Fin 5	Fin 6	Description
	2Dbase-1Dfin						
$\Theta_{fin}(1)$	0.482563	0.482671	0.482716	0.482716	0.482671	0.482563	Top of fins
$\Theta_{fin}(0)$	0.484108	0.484217	0.484262	0.484262	0.484217	0.484108	Bottom of fins
$\Theta_{base}(\xi_{avg}, 1)$	0.484108	0.484217	0.484262	0.484262	0.484217	0.484108	Top of Base
$\Theta_{base}(\xi_{avg}, 0)$	0.484300	0.484377	0.484422	0.484422	0.484377	0.484300	Bottom of Base
	3Dbase-2Dfin						
$\Theta_{fin}(0.5, 1)$	0.490539	0.490647	0.490692	0.490692	0.490647	0.490539	Top of fins
$\Theta_{fin}(0.5, 0)$	0.492082	0.492190	0.492235	0.492235	0.492190	0.492082	Bottom of fins
$\Theta_{base}(\xi_{avg}, 0.5, 1)$	0.492082	0.492190	0.492235	0.492235	0.492190	0.492082	Top of Base
$\Theta_{base}(\xi_{avg}, 0.5, 0)$	0.492274	0.492351	0.492396	0.492396	0.492351	0.492274	Bottom of Base

Tables 7 and 8 show the final temperature using both formulations at key positions: the ζ-edges of the base and fins. As expected by the perfect contact at the fin-base coupling, $\Theta_{fin}(0) = \Theta_{base}(\xi_{avg}, 1)$ and $\Theta_{fin}(0.5, 0) = \Theta_{base}(\xi_{avg}, 0.5, 1)$. The symmetric problem is once again exhibited by the fins temperature, $\Theta_{at\ 1^{st}fin} = \Theta_{at\ 6^{th}fin}$, $\Theta_{at\ 2^{nd}fin} = \Theta_{at\ 5^{th}fin}$ and $\Theta_{at\ 3^{rd}fin} = \Theta_{at\ 4^{th}fin}$.

Figure 15 - Fin-base contact-interface heat fluxes $\dot{q}''_{ic}$. For the case where the heated chip occupies the whole base surface domain, the problem does not vary in η-direction. The six-fin layout is symmetric and, consequently, $\dot{q}''_{ic_1} = \dot{q}''_{ic_6}$, $\dot{q}''_{ic_2} = \dot{q}''_{ic_5}$, and $\dot{q}''_{ic_3} = \dot{q}''_{ic_4}$.

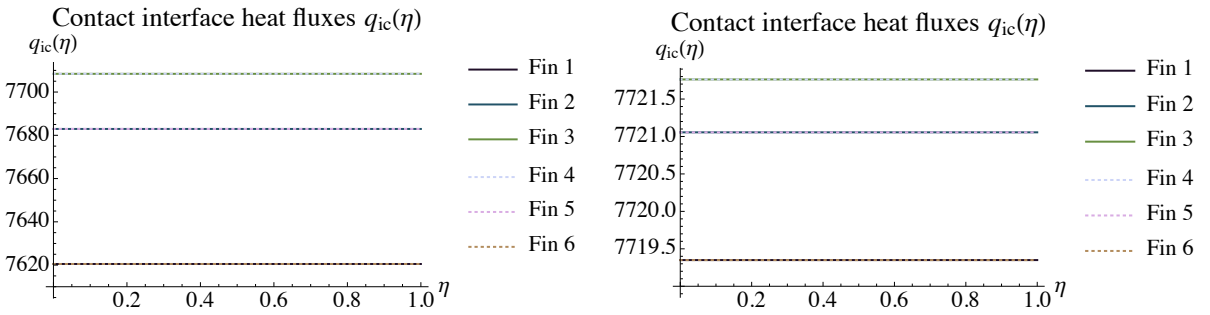

(a) Heat fluxes in the cm-scaled case.

(b) Heat fluxes in the mm-scaled case.

It is important to notice, for this first section 4.1, the heated chip heat flux does not vary in η-direction and, consequently, this problem preserves the same behavior on the width domain. Consequently, the heat fluxes do not vary in the η-direction, as can be seen in Figure 15, for both photovoltaic and electronic cases.

Another interesting remark in Figures 15a and 15b is the heat flux intensities passing through the fins. For both cases, lower intensities are noticed in the fins 1 and 6, compared with the other fins. For the cm-scaled heat sink case 15a, however, there is a significant intensity range between the middle-domain fins to the edge-domain fins. This behavior is not seen in the cm-scaled heat sink case 15b, where the heat fluxes fit a less expressive magnitude range.

4.1.3 mm-scaled heat sink

The mm-scaled heat sink is a necessity from the electronics industry and several engineering fields, which require heat dissipation from heated components to ensure the safe and efficient performance of these systems.

Figure 16 presents the thermal profile of the base and fins. Once again, the chip has the same length and width dimensions of the HS base. The heat transfer coefficients are 3 for radiation and 0.93 for convection, which leads, in this problem, to the utilization of the combined heat transfer coefficient as 3.93W/m^{2}K. One of the consequences of using a lower heat transfer coefficient is a less expressive temperature reduction on the heat sink profile, which is remarked on the thermal profile amplitudes of Figure 16. This behavior is also applicable to the heat flux intensities passing through the fins, Figure 15b.

Figure 16 - Temperature field Θ for the mm-scaled heat Sink comparing the 2Dbase-1Dfin and the 3Dbase-2Dfin formulations. The solutions were calculated for $n_{max} = 500$ and $k_{max} = 12800$, respectively. The six-fin layout is symmetrical. The temperature reduction is less expressive than the previous photovoltaics case.

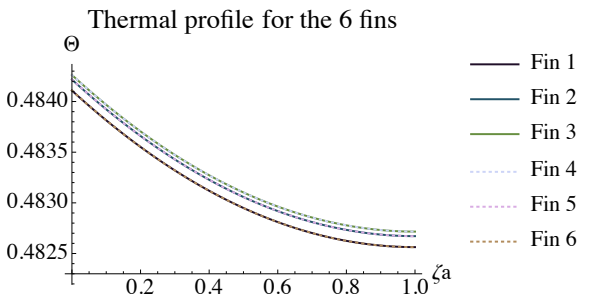

(a) Thermal profile of the fins considering the 1D formulation.

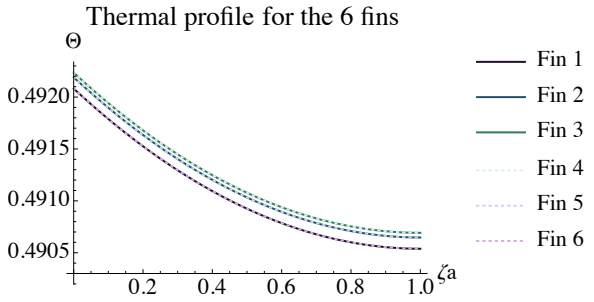

(b) Thermal profile of the fins considering the 2D formulation.

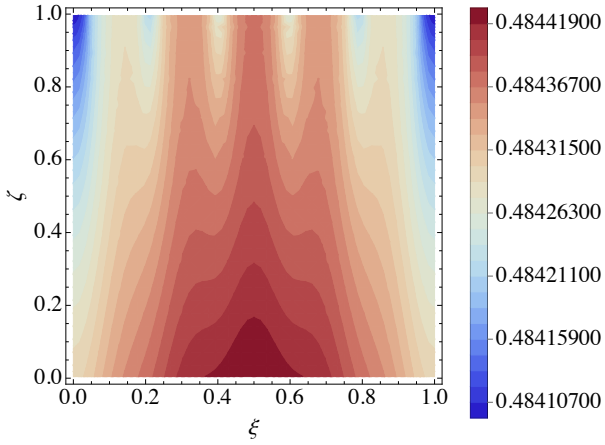

(c) Thermal profile of the base considering the 2D formulation.

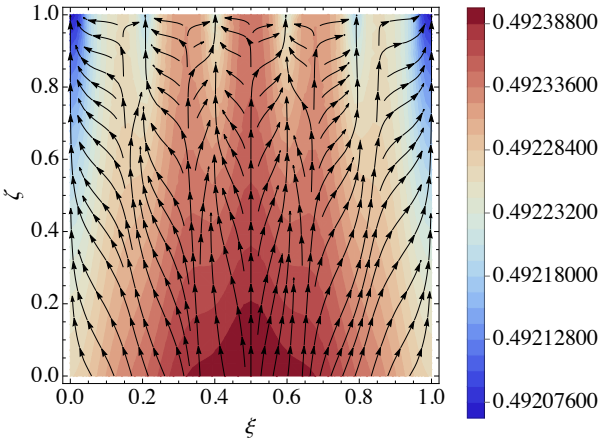

(d) Thermal profile of the base considering the 3D formulation for $\eta = 0.5$ and heatlines.

Table 9 - CITT Convergence Table of the temperature at the fin-base contact-interface for the mm-scaled heat sink case using the 3Dbase-2Dfin methodology. The six-fin layout is symmetric.

k_{max}	Fin 1	Fin 2	Fin 3	Fin 4	Fin 5	Fin 6
1800	0.492083	0.492189	0.492234	0.492234	0.492189	0.492083
3200	0.492082	0.492190	0.492235	0.492235	0.492190	0.492082
5000	0.492082	0.492190	0.492235	0.492235	0.492190	0.492082
6050	0.492082	0.492190	0.492235	0.492235	0.492190	0.492082
7200	0.492082	0.492190	0.492235	0.492235	0.492190	0.492082
9800	0.492082	0.492190	0.492235	0.492235	0.492190	0.492082
11250	0.492082	0.492190	0.492235	0.492235	0.492190	0.492082
12800	0.492082	0.492190	0.492235	0.492235	0.492190	0.492082

The CITT convergence for the mm-scaled heat sink case is shown in Table 9. The dimensionless temperature field presented a similar convergence behavior as previously seen in Table 6, a faster convergence rate to achieve the six-digit precision when compared with the cm-scaled HS case.

4.1.4 Small heated chip heat sink case

The cm-scaled heat sink is shown in this case coupled to a small heated chip. The constant intensity of $\dot{q}''_o = 25$ W/cm^2 is illustrated in Figure 17b, with a surface area of $0.01 \times W^2$, based on the HS width W, and located at the bottom center of the base. The 2Dbase-1Dfin formulation cannot be used in this problem because the source term varies in the η-direction.

The same parameters on Table 3 for the cm-scaled heat sink case were used, the same heat transfer coefficient 8.03 W/m^{2}K is considered. The symmetric HS layout is shown in Figure 17a and the contact-interface heat fluxes is shown of Figure 18. Figures 17 and 19 present the thermal profile for the 3D base and 2D fins, respectively.

A significant increase of the heat flux magnitude is noticed between $\eta = 0.4$ and $\eta = 0.6$, at the small chip location proximities, when Figure 18 is analyzed. The temperatures in this region, consequently, are higher than in other parts of the HS, as can be seen in Figures 17c, 17d, 17e and 17f. Figure 17c exhibits the base's thermal profile and heatlines directing to the six fins for $\eta = 0.5$, it must be noticed also the existence of aspect ratio on the for a better examination, the achieved results are shown in a square plot. Figure 17f also indicates the position of the fins by examining the temperature reduction strips in the base contour plot for $\zeta = 1$.

The CITT convergence for the small heated chip case is shown in Table 10 at the fin-base contact interface for the six fins. This case presents a difficulty to obtain the six-digit

Figure 17 - Results for the 3D base of the seven-fin case. ξ, η, and ζ are the dimensionless length, width, and height, respectively. The solutions were calculated for $k_{max} = 12800$. The temperatures in the heated chip's neighborhood are higher than in other parts of the HS. Temperature reduction is noticed at the fins' proximities. The heatlines 17c indicate the fins positions at the top of the base.

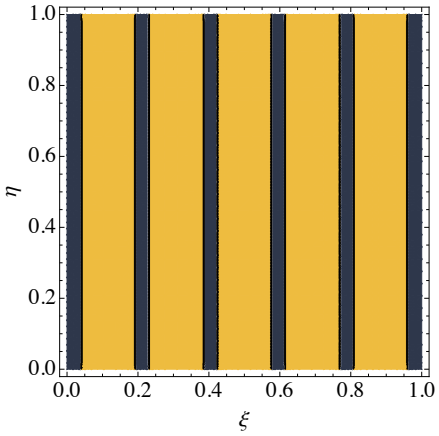

(a) Six-fin heat sink layout.

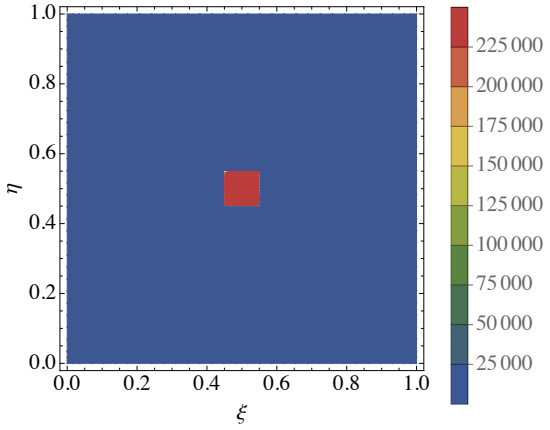

(b) Chip intensity at the bottom of the 3D base.

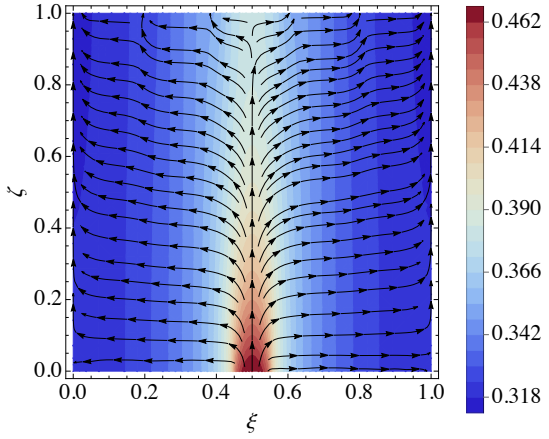

(c) Base's isotherms and heatlines at $\eta = 0.5$.

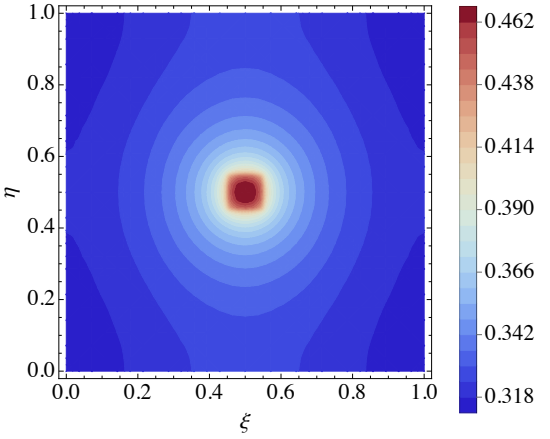

(d) Thermal profile of the base at $\zeta = 0$.

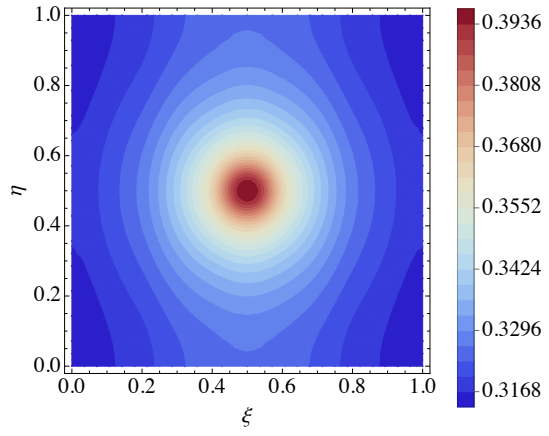

(e) Thermal profile of the base at $\zeta = 0.5$.

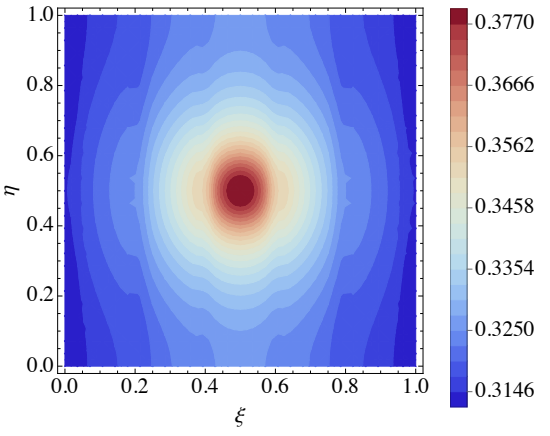

(f) Thermal profile of the base at $\zeta = 1$.

Table 10 - CITT Convergence Table of the temperature at the fin-base contact-interface for the small heated chip heat sink case using the cm-scaled heat sink. This case uses 3Dbase-2Dfin formulation. The six-fin layout is symmetric.

k_{max}	Fin 1	Fin 2	Fin 3	Fin 4	Fin 5	Fin 6
1800	0.314899	0.325671	0.356061	0.356061	0.325671	0.314899
3200	0.314879	0.325706	0.356171	0.356171	0.325706	0.314879
5000	0.314875	0.325721	0.356218	0.356218	0.325721	0.314875
6050	0.314871	0.325722	0.356212	0.356212	0.325722	0.314871
7200	0.314874	0.325717	0.356195	0.356195	0.325717	0.314874
9800	0.314882	0.325706	0.356162	0.356162	0.325706	0.314882
11250	0.314881	0.325706	0.356159	0.356159	0.325706	0.314881
12800	0.314882	0.325706	0.356163	0.356163	0.325706	0.314882

Figure 18 - Six-fin contact-interface heat fluxes $\dot{q}''_{ic}$ for the cm-scaled heat sink with the small chip attached at the center of the base's bottom. A significant increase of the heat flux magnitude can be noticed in the fins near the chip location. This problem is symmetric and, consequently, $\dot{q}''_{ic_1} = \dot{q}''_{ic_6}$, $\dot{q}''_{ic_2} = \dot{q}''_{ic_5}$, and $\dot{q}''_{ic_3} = \dot{q}''_{ic_4}$.

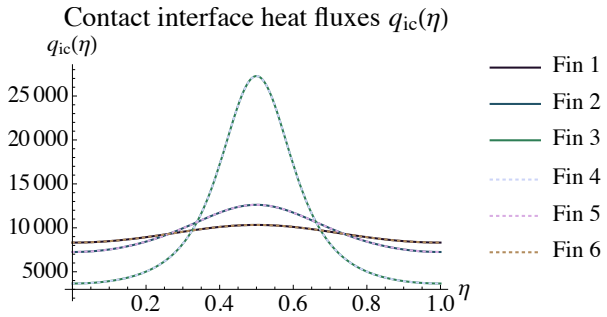

convergence especially for fins 3 and 4, near the heated chip's location.

A 2D fin scheme is illustrated in Figure 19a to indicate the selected η positions for the fins' thermal profiles. The contact-interface heat fluxes $\dot{q}''_{ic}$ for six fins are shown in Figure 18 with the small chip attached at the center of the base's bottom. A significant increase of the heat flux magnitude can be noticed in the fins near the chip location. This problem is symmetric and, consequently, $\dot{q}''_{ic_1} = \dot{q}''_{ic_6}$, $\dot{q}''_{ic_2} = \dot{q}''_{ic_5}$, and $\dot{q}''_{ic_3} = \dot{q}''_{ic_4}$.

This small squared heat source case succeeds in exemplifying the importance of 2D-Fin modeling. For sources where the heat flux is not uniform in the η-direction, the temperature profile varies in distinct width positions, as can be seen in Figure 19. Fins 1, 2, 5, and 6 located far from the heat source present a similar behavior for different η-positions during the fin's length ζ_a. Fins 3 and 4 at the HS center, however, present an expressive temperature variation near the fin-base contact interface. The fins' tip, however, converges to the same temperature despite the η-position. Hence, it can be concluded that the temperature variation in the fins' width is more expressive in fins near non-uniform heat sources.

Figure 19 - 2D fins thermal profile of the six-fin small heated chip case. The selected η-positions are indicated by the blue vertical lines in 19a. The fins temperature varies for different η positions, especially for fins located closer to the heated chip (fins 3 and 4) near the fin-base contact interface.

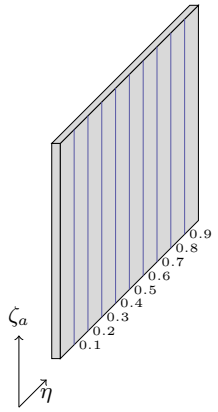

(a) 2D-fin scheme.

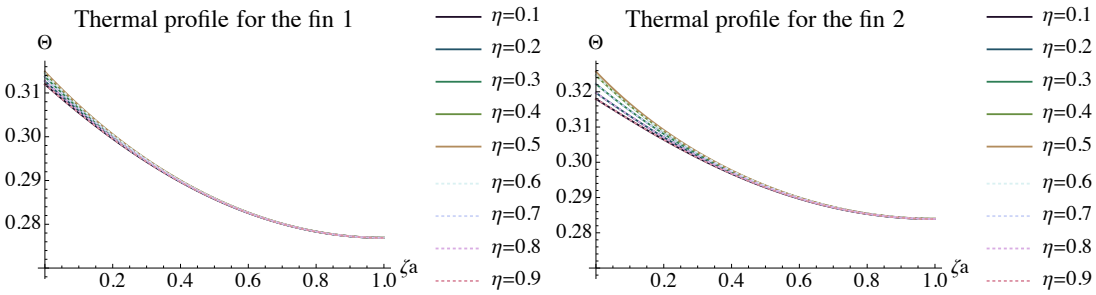

(b) Thermal profile for fin 1.

(c) Thermal profile for fin 2.

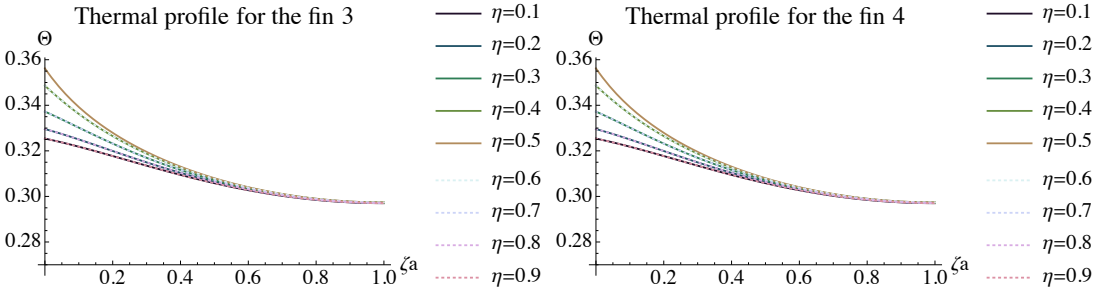

(d) Thermal profile for fin 3.

(e) Thermal profile for fin 4.

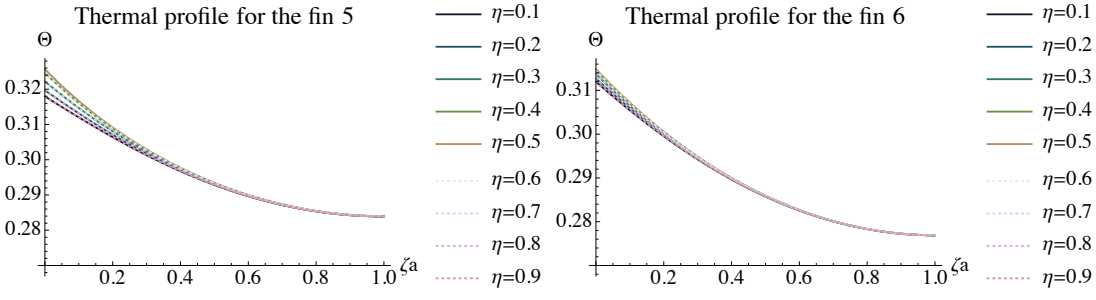

(f) Thermal profile for fin 5.

(g) Thermal profile for fin 6.

Table 11 - Number of elements for the different tested meshes used on the OpenFOAM simulations.

	cm-scaled HS case		mm-scaled HS case		small heated chip HS case	
Type	Number of nodes	Number of elements	Number of nodes	Number of elements	Number of nodes	Number of elements
40	35875	45904	35834	45862	26022	132066
60	104737	127454	104554	127454	77587	419003
80	233199	273358	233847	274014	166580	933767
100	429351	491516	429856	492026	290908	1639868

4.2 **OpenFOAM mesh convergence and methodologies comparison**

4.2.1 Mesh convergence

The heat sink cases in the previous section 4.1 are compared with simulations using the CFD software OpenFOAM in this section.

Four different meshes were tested to evaluate the mesh convergence of the heat sink for the cm-scaled heat sink, for the mm-scaled heat sink, and the small heated chip cm-scaled heat sink cases. The grid size (W/R) is composed of W dimension, which is the heat sink's width, divided by the arbitrary number R, which represents the quantity of elements lengths in one HS line, defined during the geometry creation. The mesh refinement was performed increasing the R number, initially 40, then, 60, 80, and 100. The number of nodes and elements for each tested mesh is shown in Table 11.

The mesh convergence is evaluated considering the relative error percentage between two meshes. The relative error percentage ($R\varepsilon_R$) was calculated as:

$$R\varepsilon_R = \left| \frac{T_{\text{OpenFOAM}_{R+20}} - T_{\text{OpenFOAM}_R}}{T_{\text{OpenFOAM}_{R+20}}} \right| \times 100\% \tag{139}$$

where R indicates the mesh types 40,60 and 80. $T_{\text{OpenFOAM}_{R+20}}$ indicates the more refined mesh type and T_{OpenFOAM_R} the less refined mesh type results.

Figure 20 - OpenFOAM mesh convergence. Four different meshes were tested, where the initial grid size (W/R) is composed of the heat sink's width W divided by the arbitrary number R. The refinement was performed reducing the grid size, changing the initial arbitrary number 40 to 60, 80, and 100. The meshes for the cm-scaled heat sink case are presented.

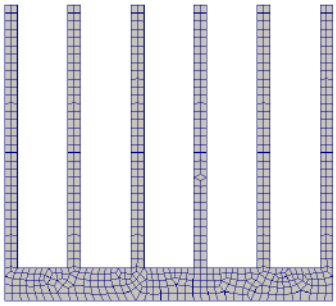

(a) Heat sink mesh for $W \div 40$ elements length.

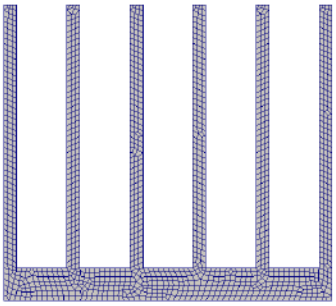

(b) Heat sink mesh for $W \div 60$ elements length.

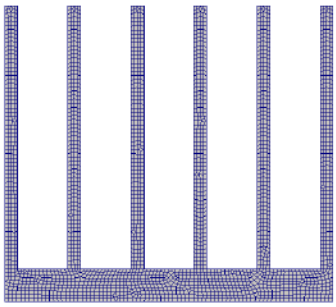

(c) Heat sink mesh for $W \div 80$ elements length.

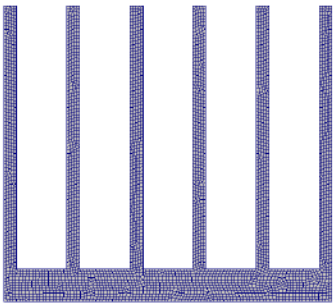

(d) Heat sink mesh for $W \div 100$ elements length.

4.2.1.1 cm-scaled heat sink

Firstly, the results for the cm-scaled heat sink are presented. The meshes utilized in this case are exhibited in Figure 20. Initially, a fewer elemented mesh 20a is used, then followed by more refined meshes, 20b, 20c and 20d. Table 12 shows the achieved results, in Kelvin, for the selected positions indicated in Figure 21 using OpenFOAM, for x and z. Figure 22 presents the relative error percentage between the meshes, calculated using Equation (139), and indicates the relative error reduction as the mesh is refined.

Figure 21 - Enumerated selected positions for mesh convergence for the cm-scaled heat sink case. The 2D view indicates the x and z locations of each selected position. For the evaluated cases in this section, the results do not vary in y-direction. Two positions are at the HS's base, one at the fin-base contact interface and two at the fins.

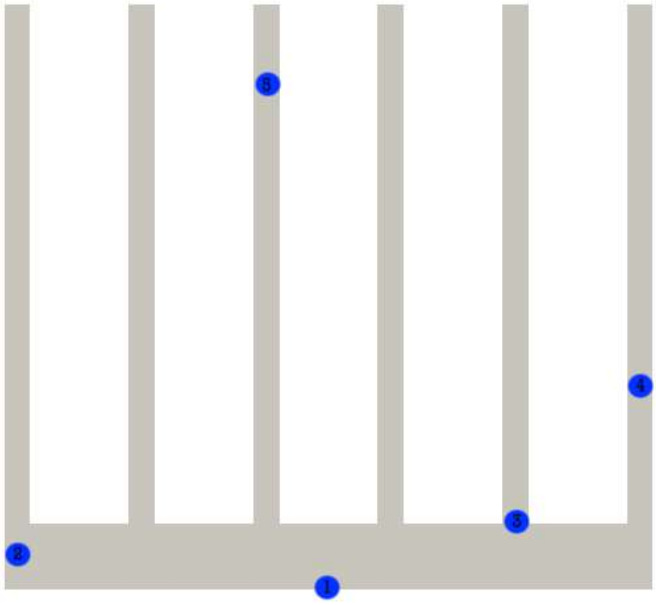

Table 12 - Temperature field T_{OpenFOAM} at different positions (x, y, z) using OpenFOAM for the cm-scaled heat sink case. The two first positions are located at the HS's base, the third is located at the fin-base contact interface, and the final positions at the HS's fins. The selected positions are indicated in Figure 21.

Type R	$T(0.1000, 0.10, 0)$	$T(0.004, 0.15, 0.01)$	$T(0.1576, 0.08, 0.02)$	$T(0.196, 0.18, 0.05)$	$T(0.0808, 0.07, 0.16)$
Type 40	324.330	323.974	323.925	322.709	321.030
Type 60	324.229	323.857	323.828	322.660	321.094
Type 80	324.307	323.941	323.899	322.681	321.030
Type 100	324.296	323.925	323.890	322.690	321.052

As can be seen in Figure 22, the relative error percentage is reduced as the mesh is refined, hence the mesh convergence is confirmed. The base and interface positions present, also, a similar convergence behavior as the mesh is refined.

Figure 23 shows the heat sink and fins thermal profile for the most refined mesh, type 100, in the cm-scaled heat sink case. Analyzing Figure 23b, it can be noticed the temperature profile poorly variation in y-direction. The thermal amplitude between the base's bottom and fin's top is 3.546K.

Figure 22 - Relative error percentage for the cm-scaled heat sink mesh refinement. The selected positions converge as the mesh is refined. In special, the base, blue tones, and interface, indicated in green, positions present a similar convergence behavior as the mesh is refined.

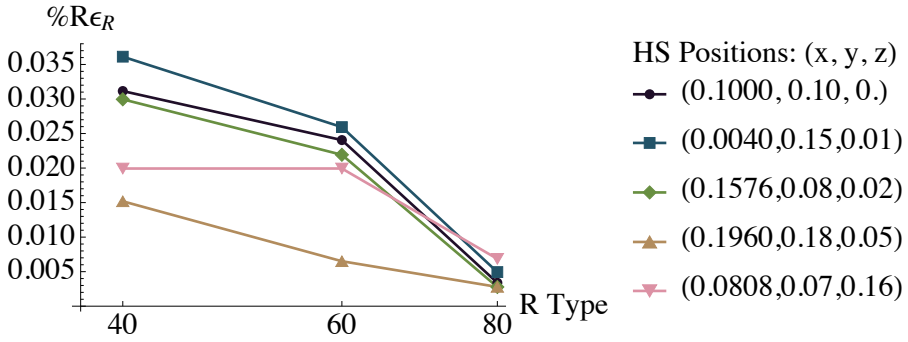

Figure 23 - Results for the six-fin for the cm-scaled heat sink case using OpenFOAM type 100.

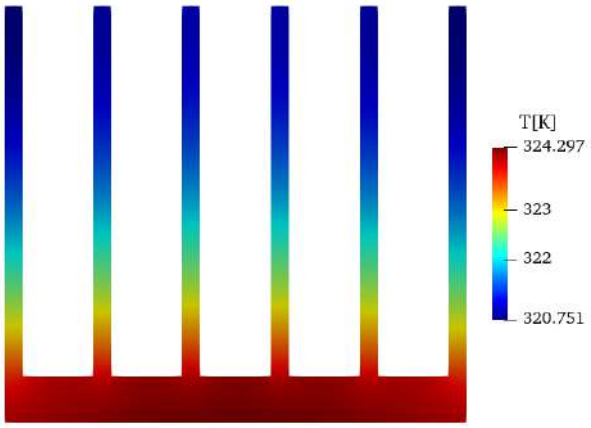

(a) 2D view of the six-fin heat sink thermal profile.

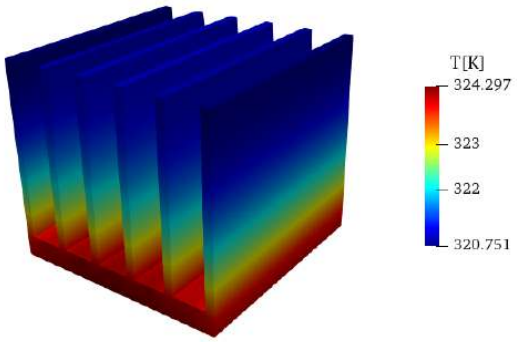

(b) 3D view of the six-fin heat sink thermal profile.

Table 13 - Temperature field T_{OpenFOAM} at different positions (x, y, z) using OpenFOAM for the mm-scaled heat sink case.

Type R	$T(0.004, 0.001, 0)$	$T(0.007, 0.0008, 0.0005)$	$T(0.0002, 0.0004, 0.0015)$	$T(0.00596, 0.00025, 0.0090)$
Type 40	347.237	347.233	347.190	347.069
Type 60	347.232	347.227	347.185	347.071
Type 80	347.236	347.231	347.189	347.069
Type 100	347.235	347.230	347.187	347.069

Figure 24 - Relative error percentage for the mm-scaled heat sink mesh refinement. The selected positions converge as the mesh is refined.

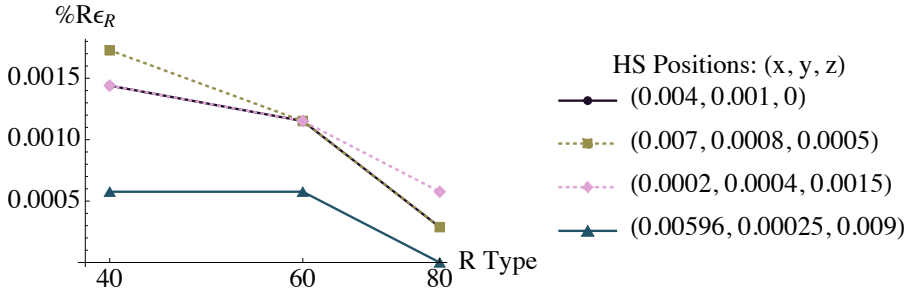

4.2.1.2 mm-scaled heat sink

The mesh convergence was also performed for the mm-scaled heat sink, SSE, case. In this case, Table 13 shows the temperature fields for the different meshes using OpenFOAM. Only four positions were selected for this case because of the less expressive temperature variation among the domain. The temperature for the different positions and different mesh types expresses a very small variation. Figure 24 confirms graphically the relative error percentage reduction as the mesh is refined with very low errors. Equation (139) was used to calculate the relative error percentage.

Figure 25 shows the mm-scaled heat sink (HS) and fins thermal profile for the most refined mesh, type 100. Previously mentioned in section 4.1.3, the HS thermal amplitude does not achieve 0.2K.

Figure 25 - Results for the six-fin for the SSE heat sink case using OpenFOAM type 100.

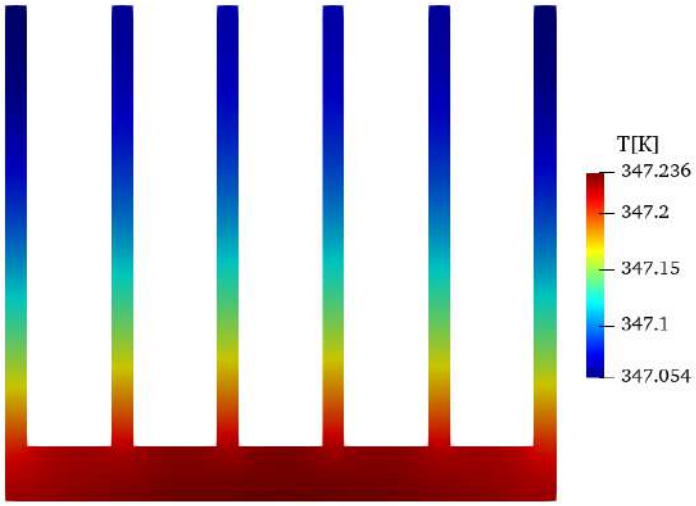

(a) 2D six-fin heat sink thermal profile.

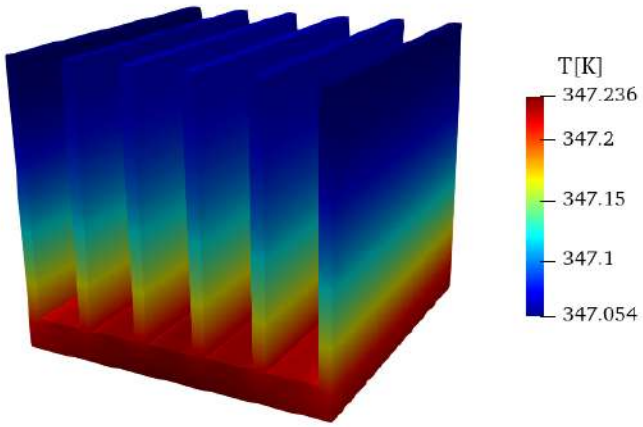

(b) 3D six-fin heat sink thermal profile.

Table 14 - Temperature field T_{OpenFOAM} at different positions (x, y, z) using the OpenFOAM for the small heated chip cm-scaled heat sink case. The first and second positions are located at the HS's base, the third is located at the fin-base contact interface, the fourth e fifth positions are located at the HS's fins. Positions 6 and 7 at the lower table are also located at the HS's base.

Type R	$T(0.1000, 0.10, 0)$	$T(0.004, 0.15, 0.01)$	$T(0.1576, 0.08, 0.02)$	$T(0.196, 0.18, 0.05)$	$T(0.0808, 0.07, 0.16)$	$T(0.1000, 0.10, 0.01)$	$T(0.1000, 0.10, 0.02)$
Type 40	342.428	329.594	330.462	328.019	327.855	337.602	335.748
Type 60	342.958	329.527	330.321	328.049	327.792	337.326	335.672
Type 80	343.272	329.496	330.312	328.029	327.788	337.156	335.616
Type 100	343.495	329.506	330.328	328.036	327.774	337.136	335.612

Figure 26 - Relative error percentage for the small heated chip case mesh refinement. The selected positions converge as the mesh is refined. The first HS position is exactly in the middle of the HS bottom, the region under the heated chip heat flux. This position presented a higher relative error. Positions 6 and 7, at the base, presented lower relative errors as the mesh is refined.

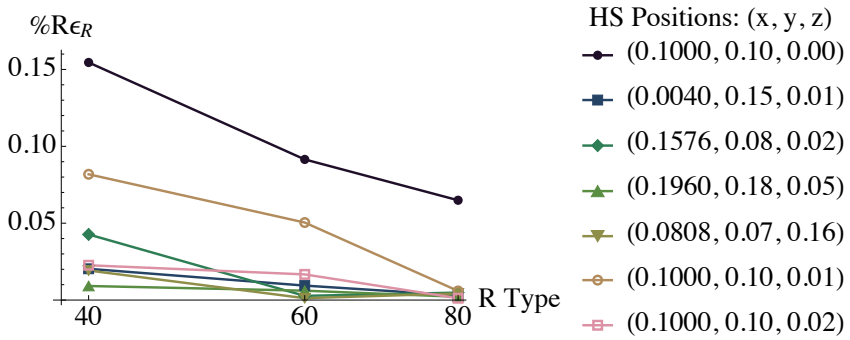

4.2.1.3 Small heated chip heat sink case

The final mesh convergence analysis is performed for the small heated chip heat sink case. In this case, the cm-scaled heat sink receives the source heat from a small heated chip at the base's bottom. The heated chip dissipates the constant intensity of $\dot{q}''_o = 25$ W/cm^2 from the schematic heated chip on Figure 17b, with a surface area of $0.01 \times W^2$, based on the HS width W, and located at the bottom center of the base. Table 14 shows the achieved results, in Kelvin, for seven different positions. Figure 26 presents the relative error percentage between the meshes, calculated using equation (139). The mesh refinement indicates its convergence as the relative error percentage is reduced.

As can be seen in Figure 26, the relative error percentage is reduced as the mesh is refined, hence the mesh convergence is confirmed. The first position is located at the heat chip contact interface $z = 0$ and presented a higher relative error percentage. Other positions were analyzed for the same length and width ($x = 0.1$ and $y = 0.1$) but different heights. Position 6 $(0.1000, 0.10, 0.01)$ and 7 $(0.1000, 0.10, 0.02)$ have the solutions converging as the mesh is refined and present lower relative errors.

Figure 27 - Results for the six-fin for the small heated chip heat sink case using OpenFOAM type 100.

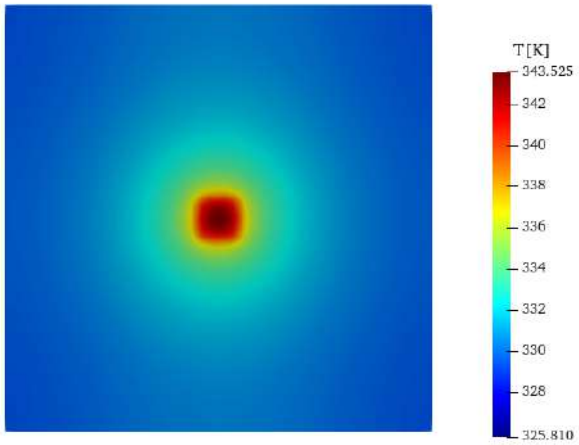

(a) 2D bottom view of the six-fin heat sink thermal profile.

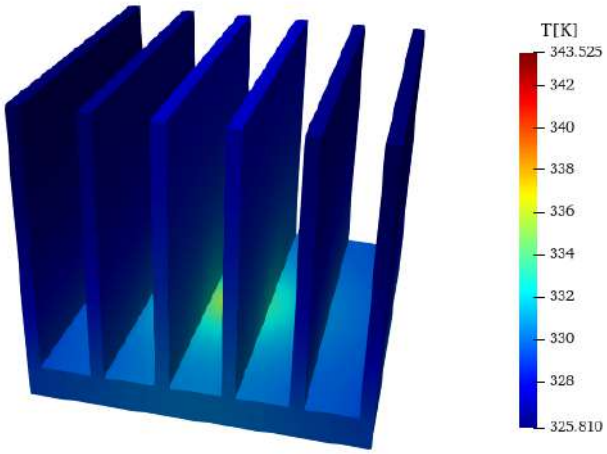

(b) 3D six-fin heat sink thermal profile.

Figure 27 shows the heat sink and fins thermal profile for the most refined mesh, type 100, in the cm-scaled heat sink case with the small heated chip. Analyzing Figure 27, it can be noticed the notorious temperature variation along y-direction. The thermal amplitude between the base's bottom and fin's top is 17.715K.

4.2.2 Verification of the analytical methodology using OpenFOAM

After the mesh convergence verification, the results between the analytical and numerical methodologies are compared. The objective is to verify the analytical approach, which is based on the CITT solutions coupling using the 3Dbase-2Dfin formulations. The cm-scaled heat sink case and the small heated chip heat sink case are verified.

The temperature field T, in Kelvin, is obtained from OpenFOAM. To compare with CITT results, the dimensionless variable Θ is calculated using equation (140) for the CFD simulation:

$$\Theta_{\text{OpenFOAM}} = \frac{T_{\text{OpenFOAM}} - T_f}{\Delta T} \tag{140}$$

where $T_f = 298\text{K}$ and $\Delta T = 100\text{K}$.

4.2.2.1 cm-scaled heat sink case

Figure 28 shows the six fins thermal profiles for the cm-scaled heat sink case using both methodologies. The CITT coupling solution for the 3Dbase-2Dfin and solved on section 4.1.1, present their fins' thermal profile in the continuum grayscale lines. The type 100 OpenFOAM simulation, solved in section 4.2.1.1 present their fins' thermal profile by the colored nodes. ζ_a indicates the fins' dimensionless $z-$direction and Θ the dimensionless temperature.

In this case, the η-variation is not expressive because of the uniform heat flux source at the HS's bottom. For this reason, Figure 28 shows one thermal profile for each fin solved by OpenFOAM and, because the problem is symmetric, the CITT solutions are plotted in similar fins pairs: Fin 1 = 6; Fin 2 = 5; and Fin 3 = 4.

Both solutions present a similar behavior and thermal amplitudes, with small deviations, hence, the analytical methodology accuracy is confirmed.

Figure 28 - Comparison between fins solutions OpenFOAM and CITT in the cm-scaled heat sink case. The CITT solutions are indicated by the gray scaled lines. The fins thermal profiles from the OpenFOAM type 100 simulation are indicated by the colored nodes.

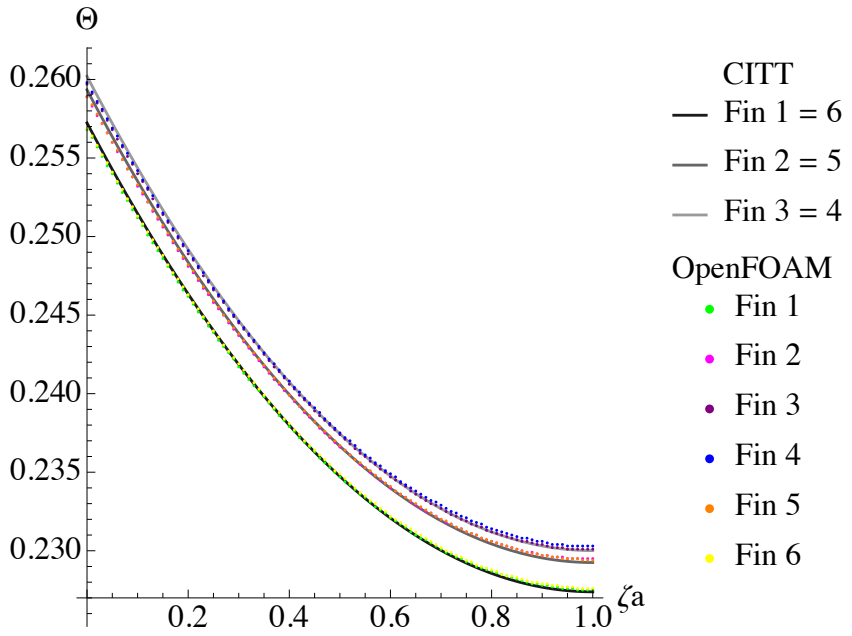

4.2.2.2 Small heated chip heat sink case

Figure 29 shows the fins' profiles for the six-fin small heated chip case using the cm-scaled heat sink. This case verifies the analytical methodology accuracy in different η-positions. This problem is symmetric. The CITT coupling fins solutions for the 3Dbase-2Dfin and solved in section 4.1.4 are indicated by the red-scaled lines. The fins thermal profiles from the OpenFOAM type 100 simulation solved in section 4.2.1.3 are indicated by the blue-scaled nodes.

The thermal behavior observed in Figure 19 is confirmed with the OpenFOAM verification. For sources where the heat flux is not uniform in the η-direction, the temperature profile varies in distinct width positions, as can be seen in Figure 19. As previously observed, fins located far from the heat source, 29b, indicate a similar behavior for different η-positions during the fin's length ζ_a. The thermal variation in the fins' width is, then, more expressive in fins near non-uniforms heat sources.

A small variation in the fins' thermal profile is observed on Figures 29b and 29d. Once again, analytical and numerical solutions present a similar behavior and thermal amplitudes, with small deviations, hence, the analytical methodology accuracy is confirmed.

Figure 29 - Comparison between CITT and OpenFOAM for different η-positions in the small heated chip HS case. The CITT coupling fins solutions for the 3Dbase-2Dfin are indicated by the red-scaled lines. The fins thermal profiles from the OpenFOAM type 100 simulation are indicated by the blue-scaled nodes.

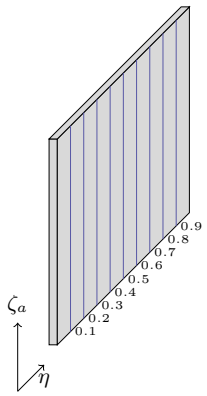

(a) 2D-fin scheme.

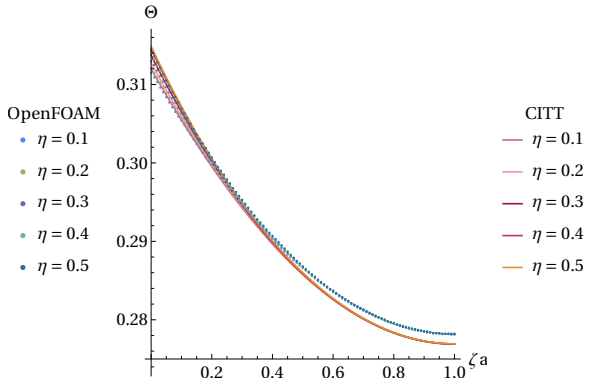

(b) Fin 1=6

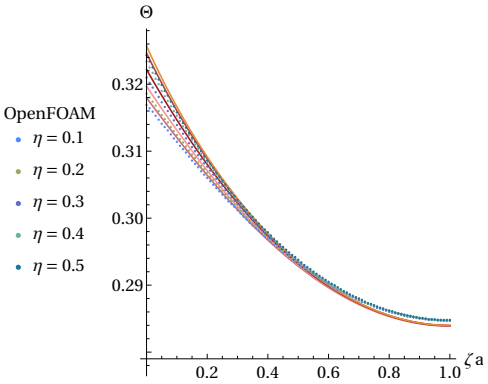

(c) Fin 2=5

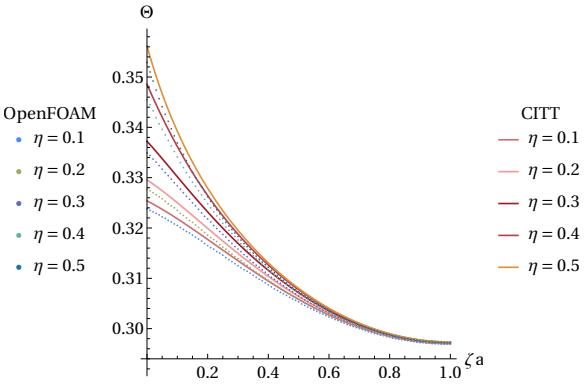

(d) Fin 3=4

4.2.3 Formulation limitation

The purpose of this current section is to show the analytical approach limitations. The CITT and OpenFOAM solutions are compared during this evaluation.

4.2.3.1 One fin: cm-scaled heat sink case

One-fin heat sinks are considered with different thicknesses to evaluate if the analytical formulation is also valid. This case considers an uniform heat flux as the problem's heat source at the base's bottom. $\delta = 0.04 \times W$, $\delta = 0.1 \times W$, $\delta = 0.15 \times W$, and $\delta = 0.2 \times W$ fin thicknesses are tested. Figure 30 presents these results. The left column images 30a,30d, 30g, and 30j show the temperature Θ for the 3D base solved using CITT and its heatlines for $\eta = 0.5$. It must be noticed the existence of ratio aspect in the Figures 30a,30d, 30g, and 30j, for a better examination of the achieved results. The heat sink composed by the $\delta = 0.1 \times W$ fin presented the lowest maximum and minimum temperatures for the HS base.

The center column images 30c,30f, 30i, and 30l indicate the thermal profiles of the overall heat sink using OpenFOAM. The lowest maximum temperature for the heat sink is shown for $\delta = 0.1 \times W$ (30f). The lowest temperature for the fin's top is, conversely, achieved on the case with the thinnest fin with $\delta = 0.04 \times W$, indicated in Figures 30b and 30c.

The right column images 30b,30e, 30h, and 30k show the CITT and OpenFOAM solutions comparison. Figures 30b and 30e indicate a well-suited approximation between both methodologies. Figure 30h demonstrates a fin-thickness limit where the analytical methodology is valid. Figure 30k, however, indicates the mismatch between the numerical and analytical methodologies.

In summary, Figure 30 shows that the limit thickness used in one-fin cm-scaled heat sink cases solved using CITT is $\delta = 0.15 \times W$. The analytical methodology, hence, is not valid for greater thicknesses. The use of α_{avg}, an average value for α when solving the base's top boundary condition, and the partial lumping in x-direction caused the miscalculation of the heat sink temperature field, in these particular cases. The use of larger thickness in fins, however, is less advantageous for heat dissipation and, consequently, do not have industrial applications. This case considers an uniform heat flux as the problem's heat source at the base's bottom.

Figure 30 - Comparison between CITT and OpenFOAM (OF) solutions for one fin with different fin's thicknesses δ. At left, the CITT solution is shown for $\eta = 0.5$, the OF solution is at center and the figure at right presents the fin's thermal profile for both methodologies for $\xi = 0.5$ and $\eta = 0.5$.

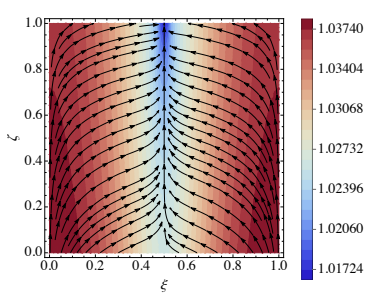

(a) HS base for $\delta = 0.04 \times W$ using CITT.

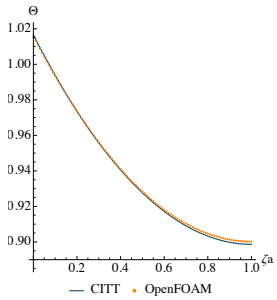

(b) CITT and OF fins comparison.

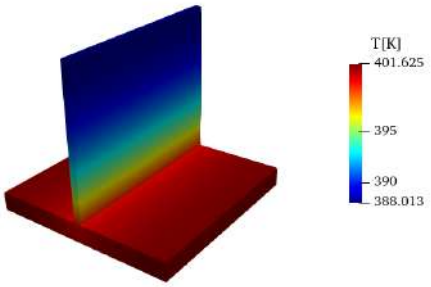

(c) OF for $\delta = 0.04 \times W$.

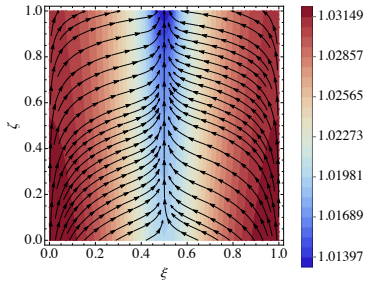

(d) HS base for $\delta = 0.1 \times W$ using CITT.

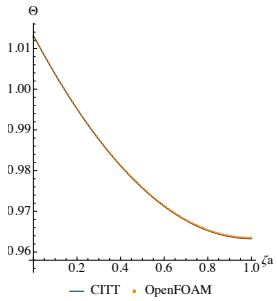

(e) CITT and OF fins comparison.

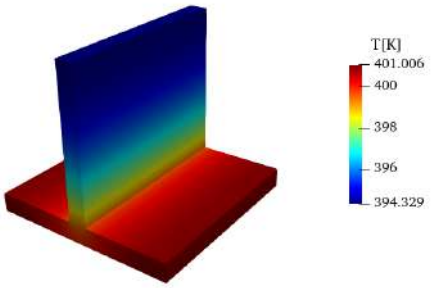

(f) OF for $\delta = 0.1 \times W$.

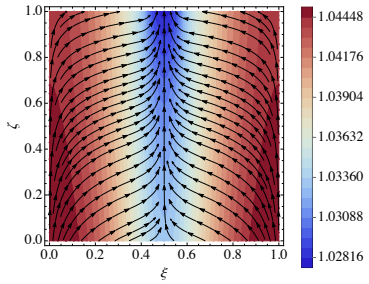

(g) HS base for $\delta = 0.15 \times W$ using CITT.

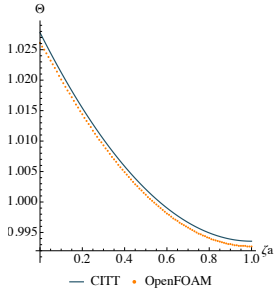

(h) CITT and OF fins comparison.

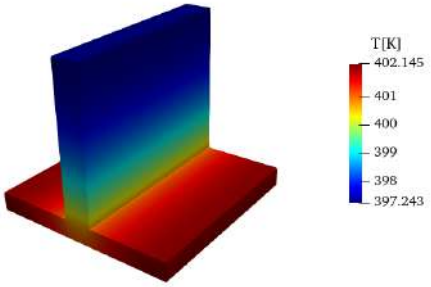

(i) OF for $\delta = 0.15 \times W$.

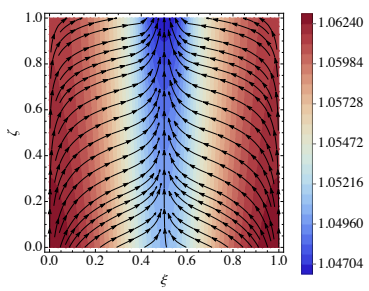

(j) HS base for $\delta = 0.2 \times W$ using CITT.

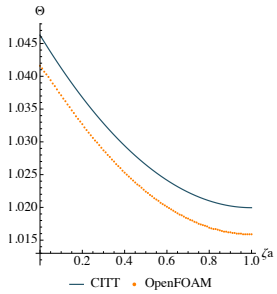

(k) CITT and OF fins comparison.

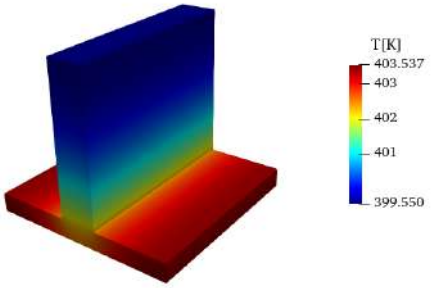

(l) OF for $\delta = 0.2 \times W$.

4.2.3.2 One fin: small heated chip heat sink case

One-fin heat sinks are also considered for the small heated chip heat sink case. In this case, the cm-scaled heat sink receives the source heat from a small heated chip at the base's bottom. The heated chip dissipates the constant intensity of $\dot{q}''_o = 25$ W/cm^2 from the schematic heated chip on Figure 17b, with a surface area of $0.01 \times W^2$, based on the HS width W, and located at the bottom center of the base.

Once again, $\delta = 0.04 \times W$, $\delta = 0.1 \times W$, $\delta = 0.15 \times W$, and $\delta = 0.2 \times W$ fin thicknesses are tested in the cm-scaled heat sink to evaluate if the analytical formulation is also valid. Figures 31 presents the thermal profile using OpenFOAM simulations, and Figure 32 present the fins results for both CITT and OpenFOAM.

The comparison between OpenFOAM and CITT fins' solutions on Figures 32a, 32b, 32c, and 32d indicate the analytical solution to be consistent with the numerical solution.

Figure 31 - OpenFOAM one-fin heat sinks with small heated chip.

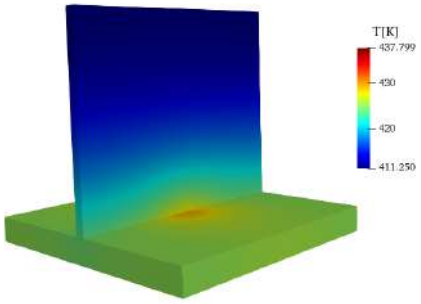

(a) One-fin heat sink with $\delta = 0.04 \times W$.

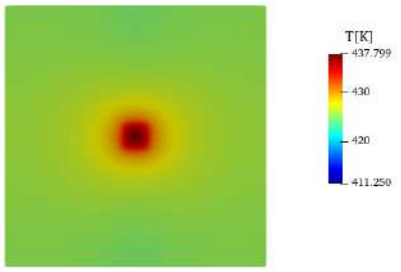

(b) 2D bottom of one-fin with $\delta = 0.04 \times W$.

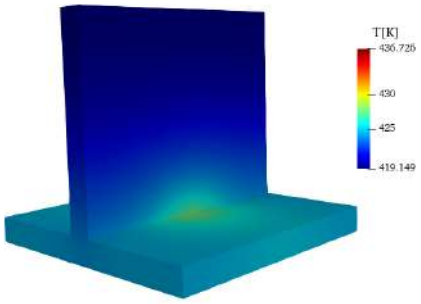

(c) One-fin heat sink with $\delta = 0.1 \times W$.

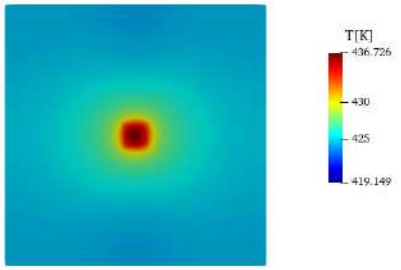

(d) 2D bottom of one-fin with $\delta = 0.1 \times W$.

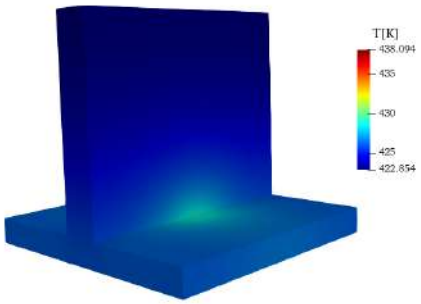

(e) One-fin heat sink with $\delta = 0.15 \times W$.

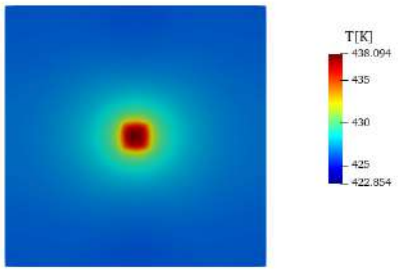

(f) 2D bottom of one-fin with $\delta = 0.15 \times W$.

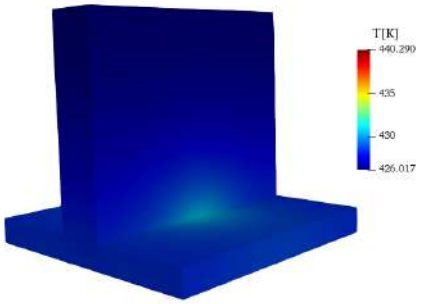

(g) One-fin heat sink with $\delta = 0.2 \times W$.

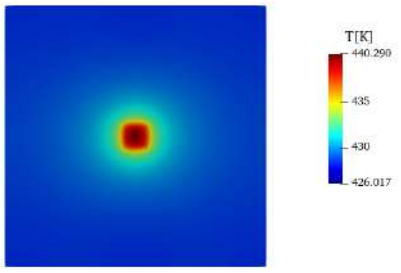

(h) 2D bottom of one-fin with $\delta = 0.2 \times W$.

Figure 32 - Fins' thermal profile comparison between CITT and OpenFOAM solutions for different fin's thicknesses δ for the small heated chip case.

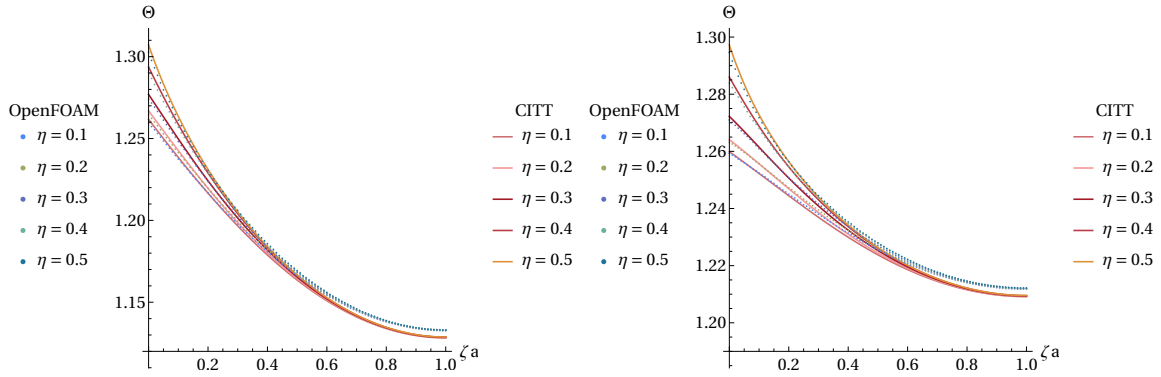

(a) $\delta = 0.04 \times W$.

(b) $\delta = 0.1 \times W$.

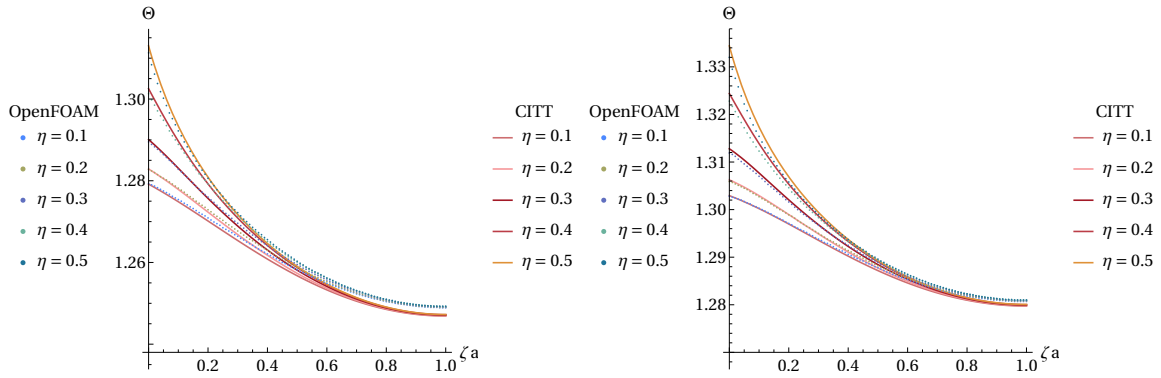

(c) $\delta = 0.15 \times W$.

(d) $\delta = 0.2 \times W$.

Figure 33 - Comparison between CITT and OpenFOAM (OF) solutions non-symmetrical fins array. Both fins have the same thickness $\delta = 0.1 \times W$. At left, the CITT solution is shown for $\eta = 0.5$, the OF solution is at center and the figure at right presents the fin's thermal profile for both methodologies.

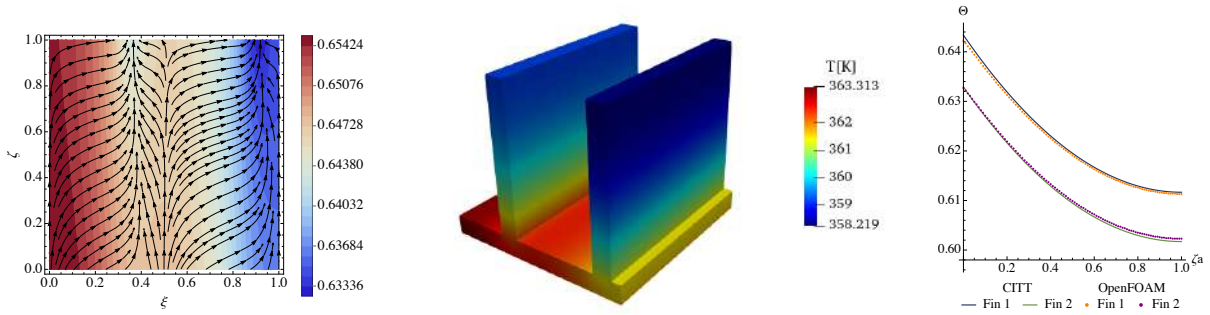

(a) CITT base solution.

(b) OF solution.

(c) CITT and OF fins comparison.

4.2.3.3 Non-simmetric fins array: cm-scaled heat sink case

A non-symmetric heat sink design 33b was tested to evaluate the accuracy of the analytical methodology with a non-symmetric fins array. Two fins with $\delta = 0.1 \times W$ were considered for the cm-scaled heat sink, presenting different thermal profiles as can be seen in Figure 33. A constant heat flux source $\dot{q}''_o = 2000$ W/m^2 is considered at all the base's bottom domain.

Figure 33a presents the temperature field Θ and the heatlines for the HS's base, Figure 33b shows the heat sink thermal profile using OpenFOAM, and the right 33c image presents the comparison between the fins' temperatures using both methodologies. It must be noticed the existence of the aspect ratio in Figure 33a for a better examination of the achieved results, where the results are shown in a square plot.

The CITT solution, in this case, is shown to be consistent with the numerical solution. The same $\alpha_{\text{avg}} = 0.8$ was considered for the fin with $\delta = 0.2 \times W$ thickness, indicated in Figure 30k, and in this present case.

Figure 34 - Non-symmetric contact-interface heat fluxes $\dot{q}''_{ic}$ for the cm-scaled heat sink with the small chip attached at the center of the base's bottom.

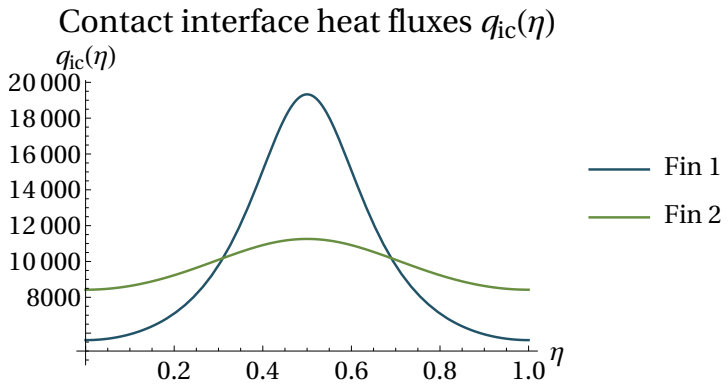

4.2.3.4 Non-simmetric fins array: small heated chip heat sink case

The non-symmetric fins array is now evaluated for the small heated chip heat sink. Once again, two fins with $\delta = 0.1 \times W$ were considered for the cm-scaled heat sink, presenting different thermal profiles as can be seen in Figures 35c and 35d. The fin-base contact interface heat fluxes is shown in Figure 34. Even though different curves modeled the fin-base heat fluxes, the η-direction is symmetric for each fin.

Figures 35c and 35d show that CITT and OpenFOAM solutions are match mostly in all the fins' domain. Also, the base thermal profile for both methodologies are similar. The CITT solution, in this case, is shown to be consistent with the numerical solution.

In summary, the analytical solution solved using CITT is consistent in most of the studied cases. The CITT may present solution unconsistency in one-fin cases with large fin thickness, $\delta_a > 0.15$.

Figure 35 - Comparison between CITT and OpenFOAM (OF) solutions for the non-symmetrical fins array HS.

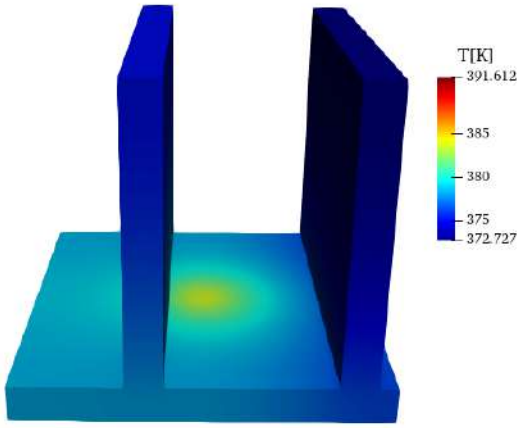

(a) OF heat sink thermal profile.

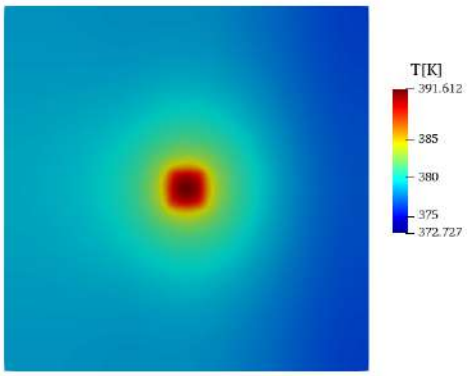

(b) OF heat sink base for $z = 0$.

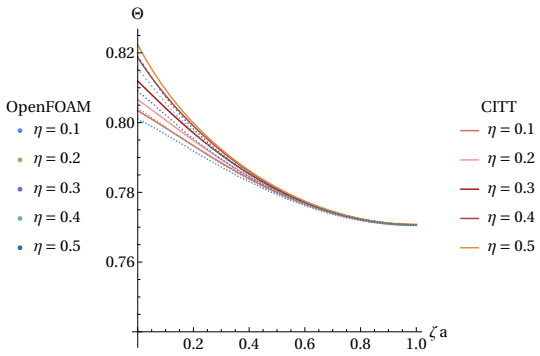

(c) Comparison between CITT and OF for fin 1.

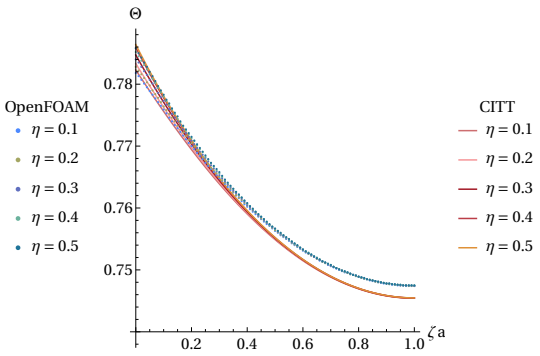

(d) Comparison between CITT and OF for fin 2.

4.2.4 Verification of the 2D fin formulation

Two-dimensional heat conduction is considered on the fins formulation after lumping the x-direction. Since the thickness of the fin is much smaller when compared to its height and width, this assumption is considered for the analytical solution.

The following Figure 36 aims to verify the lumping assumption. The temperature variation in the six-fins thicknesses from the cm-scaled heat sink case is evaluated using the OpenFOAM type 100 simulation in different heights ζ_a.The vertical axis indicates the Θ dimensionless temperature for the six fins at three different positions, ζ_a =0.25, 0.5, and 0.75. The horizontal axis shows the thickness length of δ for the fins. The x-direction may be considered lumped when the temperature at the thickness keeps a constant value during its length of δ. Higher temperatures are noticed for the fins at the lower height, as well as the fins located in the heat sink domain's middle, fins 3, and 4. Fins located at the HS's edge fins 1 and 6, and higher positions leads to a lower temperature field. The temperature maintains as constant on the thickness for all fins. Then, the x-direction lumping is valid.

As can be seen, the temperature is maintained mostly constant during the fins thickness for the different fins and at different positions. Hence, the two-dimensional heat conduction assumption on fins is valid.

Figure 36 - Temperature field Θ in different positions at the fins' thickness using the OpenFOAM type 100 simulation. The horizontal axis shows the thickness length δ for the fins. The vertical axis indicates the dimensionless temperature for the six fins at three different positions ζ_a. The temperature mantains constant on the thickness for all fins.

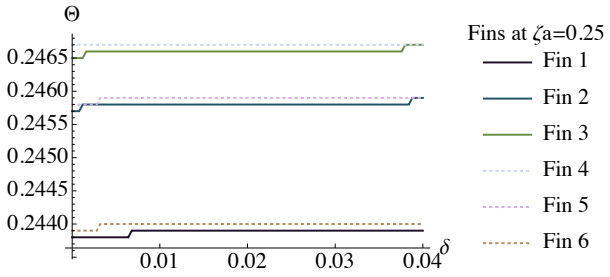

(a) Fins at $\zeta_a = 0.25$

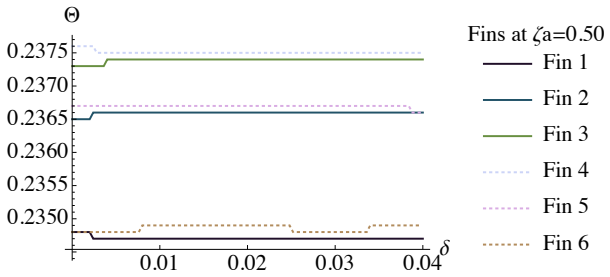

(b) Fins at $\zeta_a = 0.5$

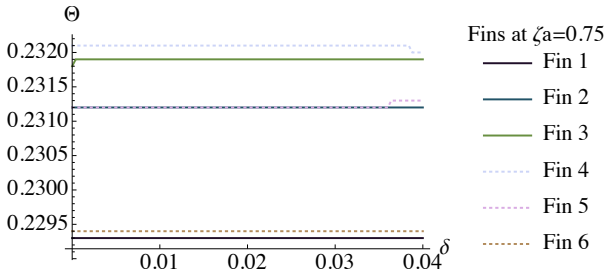

(c) Fins at $\zeta_a = 0.75$

4.2.5 Base height evaluation

The heat transfer is now evaluated for different heat sink's base heights. The purpose is to analyze if the base should have a higher dimension to enhance heat transfer. Two cases are once again considered:

cm-scaled heat sink case: An constant heat flux source $\dot{q}''_o = 2000$ W/m^2 is considered at all the base's bottom domain. Figure 37 shows two heat sinks with different design configurations. Both HS cases present six-fins with $\delta = 0.02 \times W$ and the same total height, however, one case presents a higher base (H) with smaller fins' height (H_a). The left images 37a, 37c, and 37e refer to the heat sink with $H = 0.1 \times W$ and $H_a = 0.8 \times W$. The right images 37b, 37d, and 37f refer to the heat sink with $H = 0.2 \times W$ and $H_a = 0.7 \times W$.

Small heated chip heat sink case: In this case, the cm-scaled heat sink receives the source heat from a small heated chip at the base's bottom. The heated chip dissipates the constant intensity of $\dot{q}''_o = 25$ W/cm^2 from the schematic heated chip on Figure 17b, with a surface area of $0.01 \times W^2$, based on the HS width W, and located at the bottom center of the base.

For both cases, the lowest temperatures are noticed in the higher fins and smaller base height heat sinks, Figures 37a; 37c; 37e for the cm-scaled HS, and 38a; 38c; 39a; 39c; 39e for the small heat chip HS.

From this observation, the heat dissipation enhancement is promoted by larger fins' transversal surfaces, with higher heights for the fins rather than a taller base's height.

Figure 37 - Heat transfer evaluation when the base height is changed. An constant heat flux source in the base's bottom is considered. CITT and OF solutions are shown with the same total HS height but different heights for base and fins. As can be seen on the left figures, the higher fins' surface areas enhance thermal dissipation and, consequently, reduce the HS temperatures.

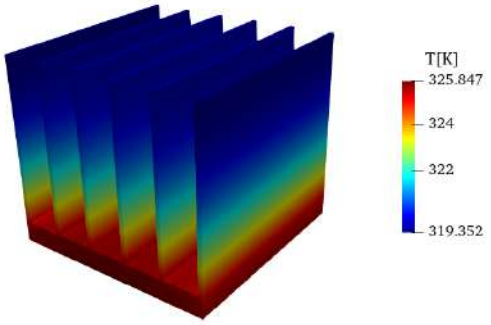

(a) OF for $H = 0.1 \times W$.

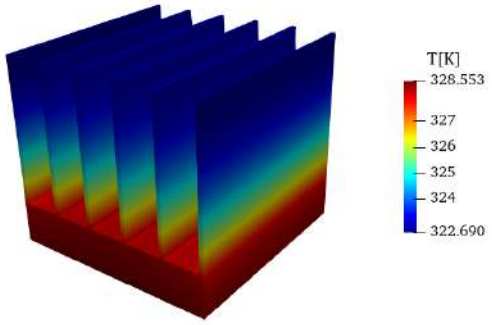

(b) OF for $H = 0.2 \times W$.

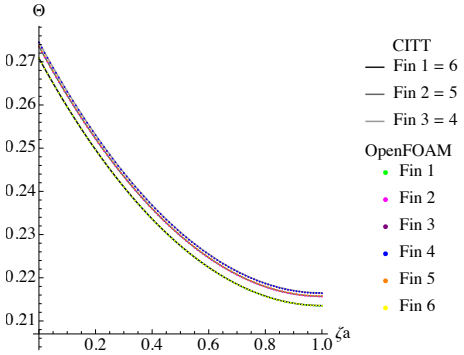

(c) CITT and OF fins comparison $H = 0.1 \times W$.

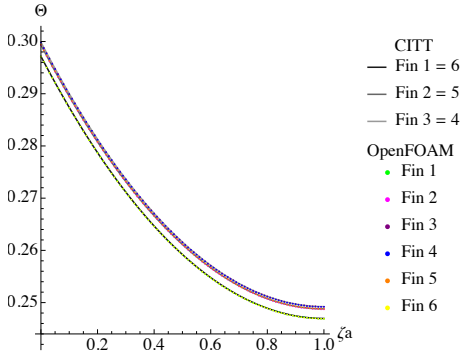

(d) CITT and OF fins comparison $H = 0.2 \times W$.

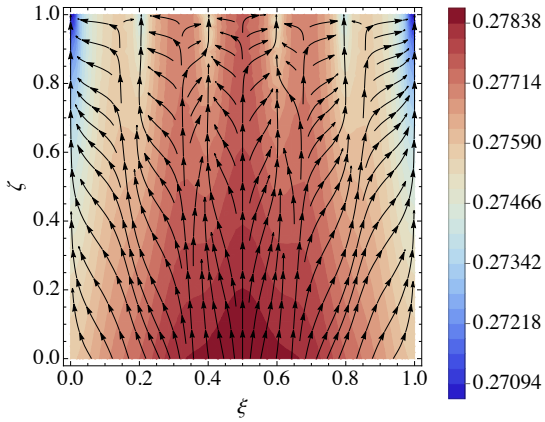

(e) CITT base solution for $H = 0.1 \times W$.

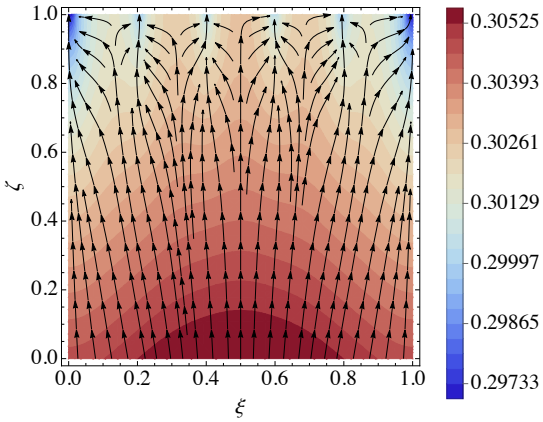

(f) CITT base solution for $H = 0.2 \times W$.

Figure 38 - Heat transfer evaluation when the base height is changed for small heated chip case. CITT and OF solutions are shown with the same total HS height but different heights for base and fins. As can be seen on the left figures, the higher fins' surface areas enhance thermal dissipation and, consequently, reduce the HS temperatures.

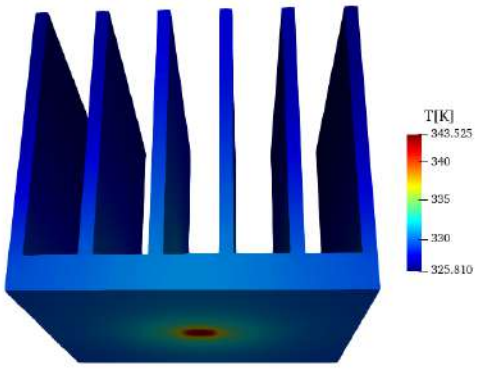

(a) OF for $H = 0.1 \times W$.

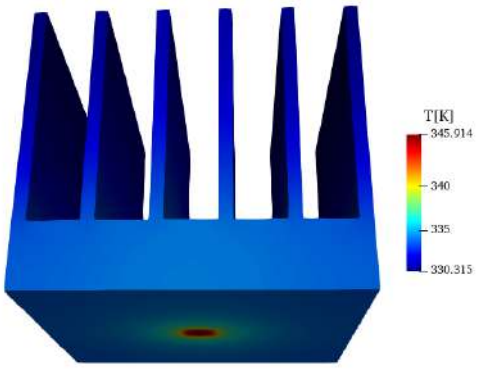

(b) OF for $H = 0.2 \times W$.

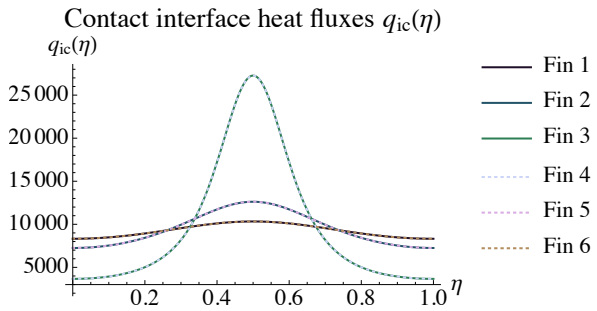

(c) Contact-interface heat fluxes for $H = 0.1 \times W$.

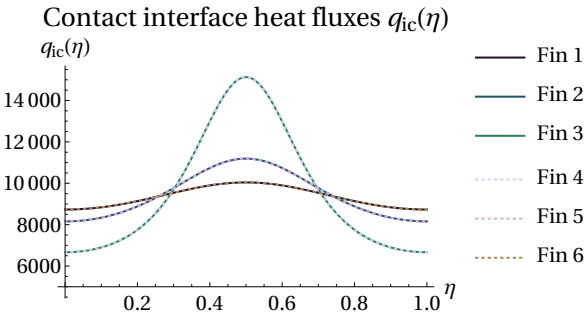

(d) Contact-interface heat fluxes for $H = 0.2 \times W$.

Figure 39 - OpenFOAM one-fin heat sinks with small heated chip.

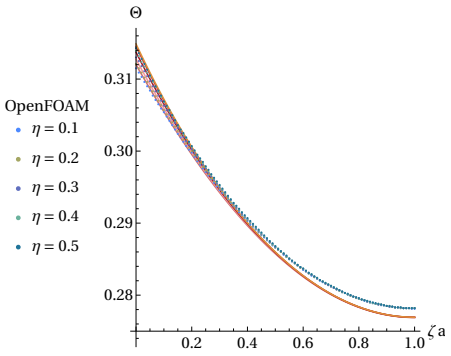

(a) Fin 1=6 comparison for $H = 0.1 \times W$.

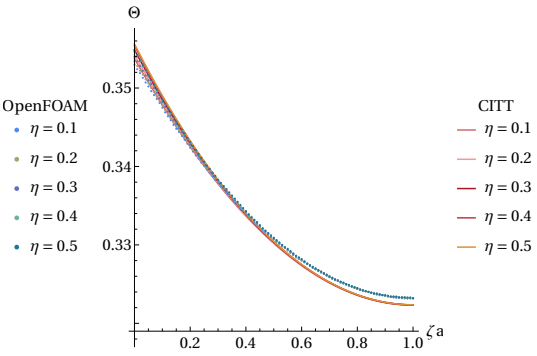

(b) Fin 1=6 comparison for $H = 0.2 \times W$.

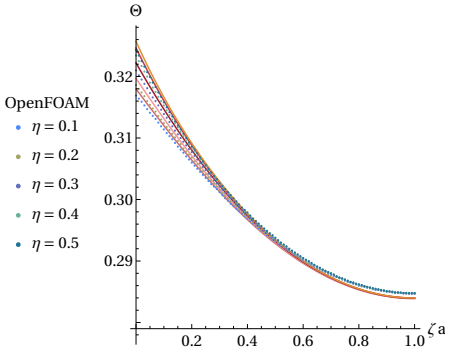

(c) Fin 2=5 comparison for $H = 0.1 \times W$.

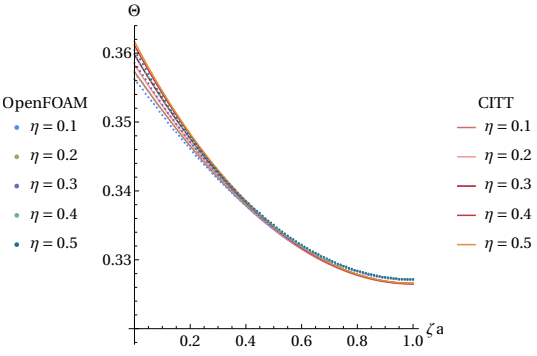

(d) Fin 2=5 comparison for $H = 0.2 \times W$.

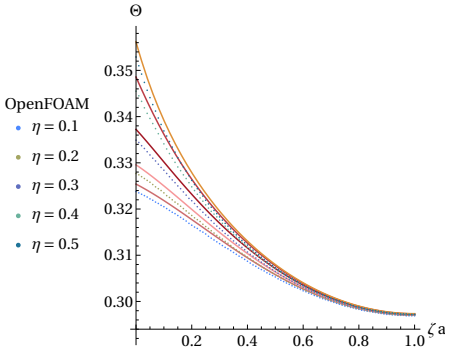

(e) Fin 3=4 comparison for $H = 0.1 \times W$.

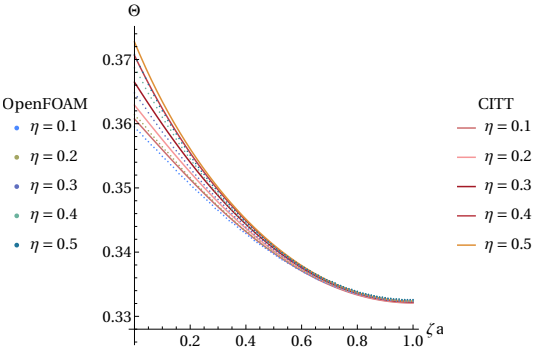

(f) Fin 3=4 comparison for $H = 0.2 \times W$.

4.3 **Longitudinal fin profiles**

The objective of this section is to present different longitudinal fin profiles with their performance characteristics and evaluate the thermal enhancement promoted by the distinct fin geometries. Rectangular, triangular, and convex parabolic fins are evaluated. The cm-scaled heat sink and the same heat transfer coefficient were considered in the different heat sinks tested. An constant heat flux source $\dot{q}''_o = 2000$ W/m^2 is considered for the bases' bottom domain.

The performance characteristics are based on Bejan and Kraus (2003) and Çengel and Ghajar (2011) for one-dimensional longitudinal fins.

Efficiency η_{fin}: Ratio of the heat transferred from the fin to the ideal heat transfer.

$$\eta_{\text{rectangular}} = \frac{\tanh(mH_a)}{mH_a} \tag{141}$$

$$\eta_{\text{triangular}} = \frac{I_1(2mH_a)}{mH_a I_0(2mH_a)} \tag{142}$$

$$\eta_{\text{parabolic}} = \frac{1}{mH_a}\frac{I_{2/3}\left(\frac{4}{3}mH_a\right)}{I_{-1/3}\left(\frac{4}{3}mH_a\right)} \tag{143}$$

where $m = \sqrt{2h/(k\delta_a)}$, h is the heat transfer coefficient, k is the thermal conductivity, δ_a is the fin thickness, and H_a is the fin's height. I is a modified Bessel function. The efficiency of these fin profiles are plotted as a function of mH_a in Figure 40.

Fin effectiveness ϵ_{fin}: Ratio of the heat transfer from the fin to the heat that would be dissipated from the same surface area without fin.

$$\epsilon_{\text{fin}} = \frac{A_{\text{fin}}}{A_{\text{base}}} \times \eta_{\text{fin}}, \quad A_{\text{fin}} = 2 \times H_a \times W, \quad A_{\text{base}} = \delta_a \times W \tag{144}$$

where A_{fin} is the fin's wet area, A_{base} is the fin cross-sectional area and η_{fin} is the fin's efficiency. δ_a is the fin thickness, W is the HS base width and H_a is the fin's height.

Heat sink effectiveness ϵ_{HS}: Ratio of the heat transfer from the heat sink to the heat that would be dissipated from the HS without fins.

$$\epsilon_{\text{HS}} = \frac{(A_{\text{fin}} \times \eta_{\text{fin}} \times \text{n}_{\text{fin}}) + (1 - \delta_a \times \text{n}_{\text{fin}})W \times L}{W \times L} \tag{145}$$

where n_{fin} is the number of fins, δ_a is the fin thickness, W is the HS base width, and L is the HS base length.

Table 15 evaluates the efficiency and effectiveness for the cm-scaled heat sink with $H_a = 0.16$, 6 fins and $mH_a = 0.506912$. The type 100 heat sink was simulated on OpenFOAM

Figure 40 - Fin profiles as function of mH_a. The rectangular fin presents the highest fin efficiency.

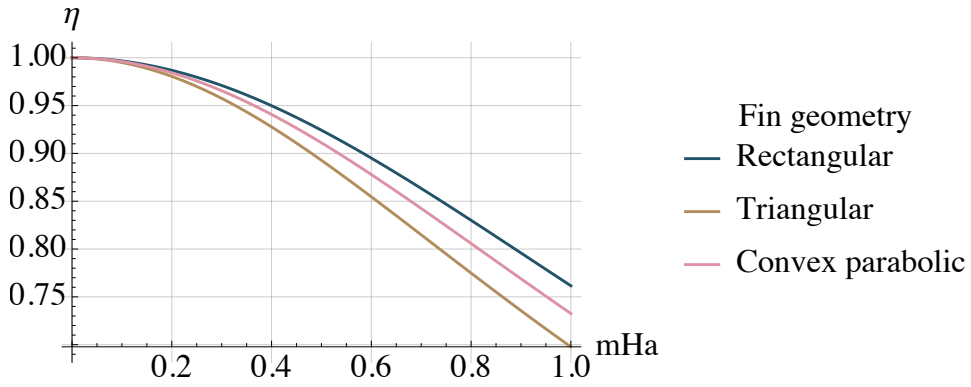

Table 15 - Performance characteristics for different fin profiles. The cm-scaled heat sink was considered with $H_a = 0.16$, 6 fins, and $mH_a = 0.506912$.

Fin profile	η_{fin}	ϵ_{fin}	ϵ_{HS}
Rectangular	0.922321	36.8928	9.80628
Triangular	0.890227	35.6202	9.50085
Parabolic	0.908894	36.3709	9.68102

with different fin profiles. The different geometries are compared in Figure 41 to show the maximum and minimum temperatures achieved by the heat sinks.

As can be seen, the rectangular fin profile presents the highest parameters of fin efficiency and effectiveness for the fin and the heat sink. This conclusion is confirmed by analyzing Figure 41. The most efficient fin profile must present the HS lowest temperature range, which is 3.546K, 5.98K, and 4.927K for the rectangular, triangular, and parabolic heat sinks, respectively. The rectangular profile 41a achieved the lowest range and temperature at the bottom of the heat sink. The heat transfer enhancement promoted by the triangular shape 41b, which presented the lowest fin efficiency, achieved the highest temperature range. From the results, the rectangular profile is the most efficient and effective fin shape, hence, the most appropriate shape to obtain the lowest temperature at the neighborhood of the heated chip.

Figure 41 - Results for different shaped six-fin heat sinks using OpenFOAM type 100. The rectangular profile presented the lowest temperature at the HS base's bottom and the highest temperature at the fins' top. Conversely, the triangular fin shape presented the highest temperature at the bottom of the base and the lowest temperature at the fins' top.

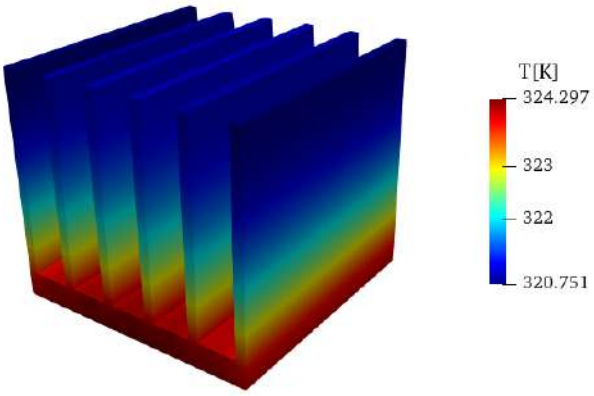

(a) Rectangular fin geometry.

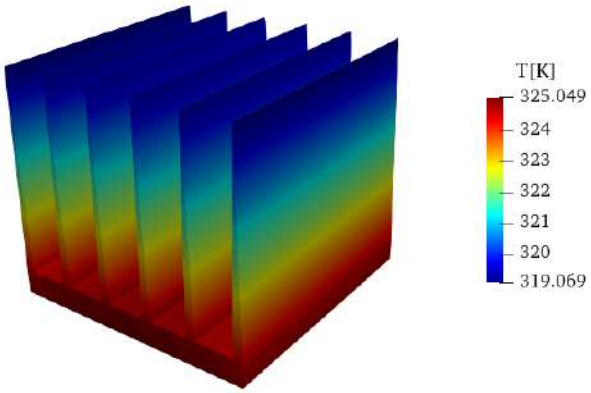

(b) Triangular fin geometry.

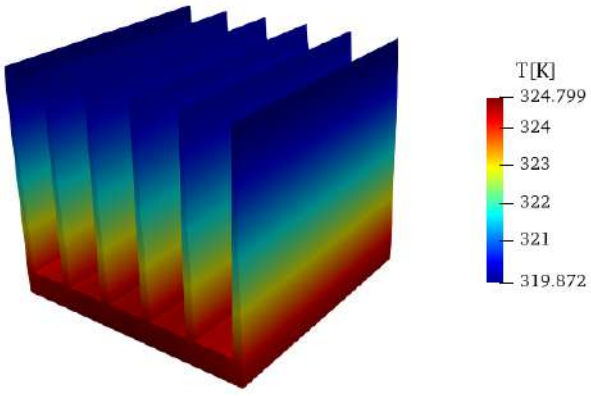

(c) Parabolic fin geometry.

Figure 42 - Seven-fins contact-interface heat fluxes $\dot{q}''_{ic}$ on the cm-scaled heat sink with the non-symmetric chip attached at the center of the base's bottom. A significant increase of the heat flux magnitude can be noticed in the fins near the chip location, especially on the fin 4.

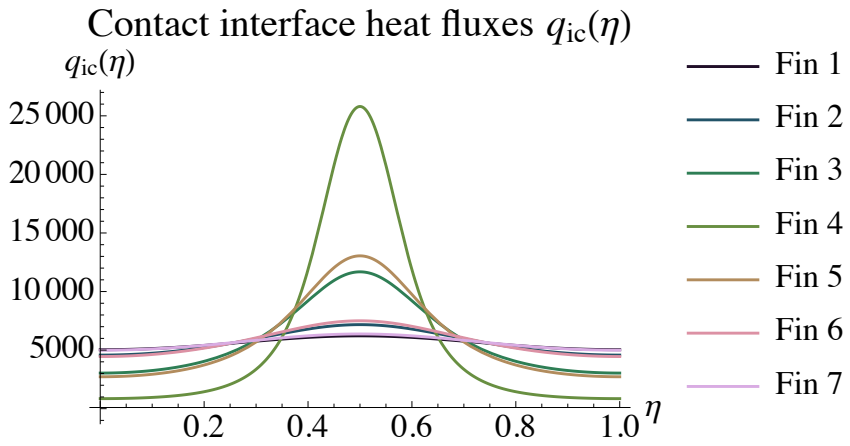

4.4 **Non-symmetric cases.**

4.4.1 Small heated chip with two different intensities

In this case, a non-symmetric heated chip is considered on the seven-fins cm-scaled heat sink to evaluate the thermal behavior of heat sinks for non-symmetric cases. The same heated chip from section 4.1.4 is considered dissipating a constant intensity of $\dot{q}''_o = 25\,\mathrm{W/cm^2}$ in the right-half and $\dot{q}''_o = 15\,\mathrm{W/cm^2}$ in the left-half, as shown in Figure 43b. The contact-interface heat fluxes $\dot{q}''_{ic}$, in this case, are non-symmetric, as can be seen in Figure 42. The thermal profiles for the base are presented in Figures 43c, 43d, 43e and 43f. The fins temperature fields are presented in Figure 44. The thermal profiles for both base and fins are, consequently, also non-symmetrical.

Figure 43 - Results for the 3D base of the non-symmetric cm-scaled case. ξ, η, and ζ are the dimensionless length, width, and height, respectively. The non-symmetric heated chip caused non-symmetric thermal profiles for the HS's base.

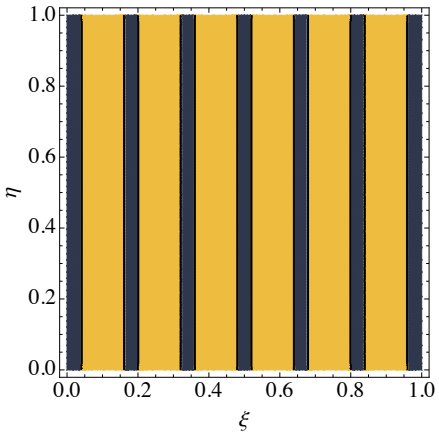

(a) Symmetric seven-fin heat sink layout.

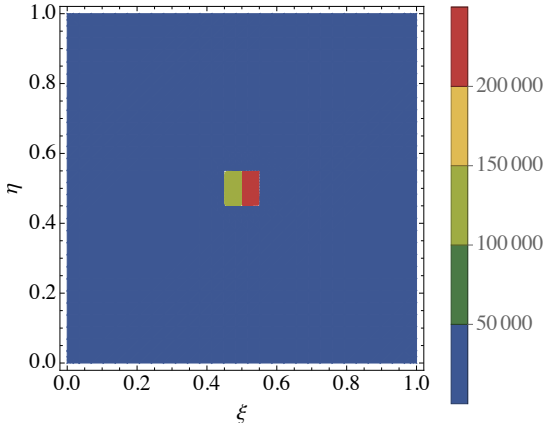

(b) Non-symmetric chip intensity at the bottom of the 3D base.

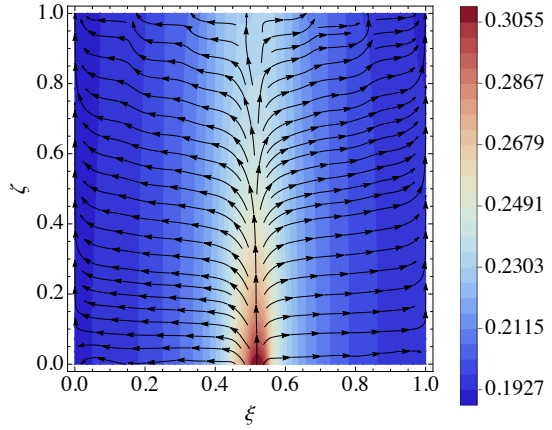

(c) Base's isotherms and heatlines at $\eta = 0.5$.

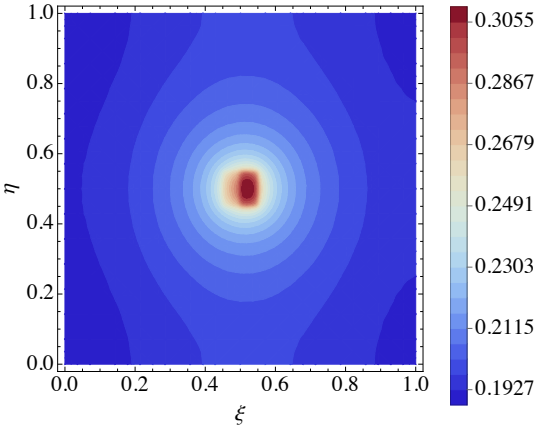

(d) Thermal profile of the base at $\zeta = 0$.

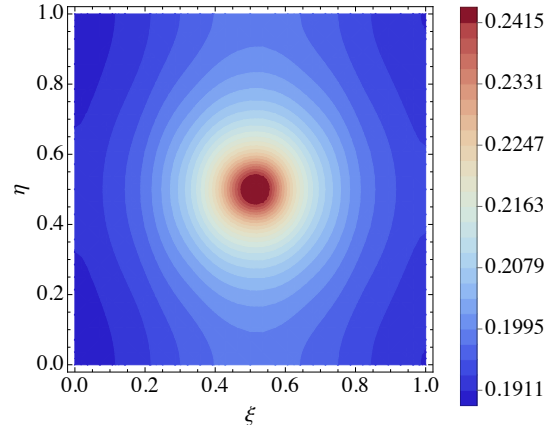

(e) Thermal profile of the base at $\zeta = 0.5$.

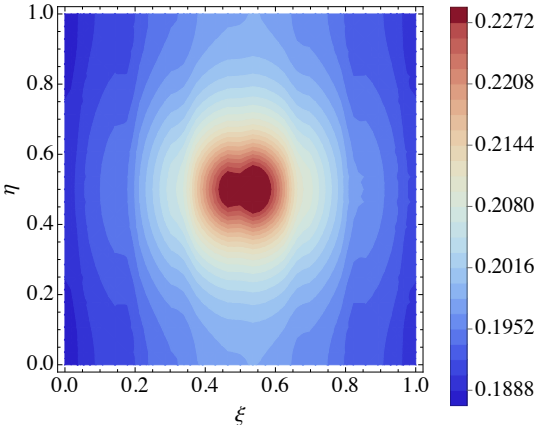

(f) Thermal profile of the base at $\zeta = 1$.

Figure 44 - Results for the 2D fins of the non-symmetric cm-scaled case. The non-symmetric heated chip caused non-symmetric thermal profiles for all the HS's fins, especially for the fins located closer to the heated chip (fins 3,4 and 5).

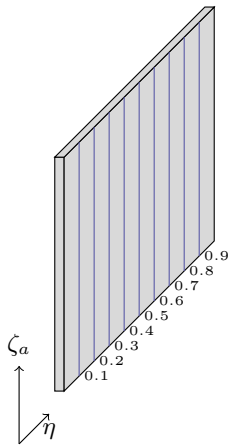

(a) 2D-fin scheme.

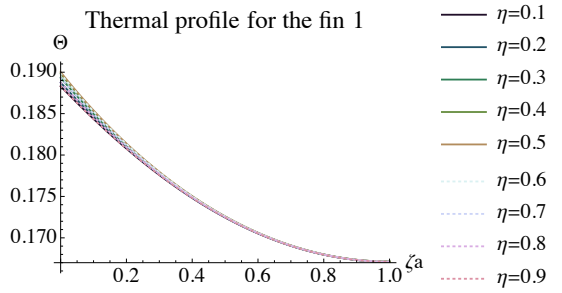

(b) Thermal profile for fin 1.

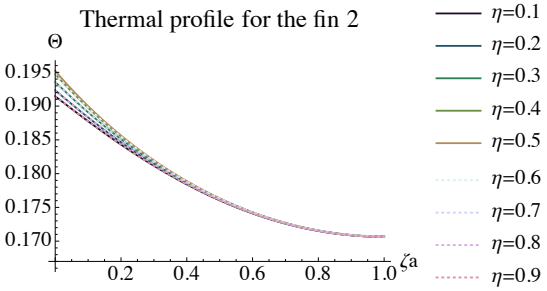

(c) Thermal profile for fin 2.

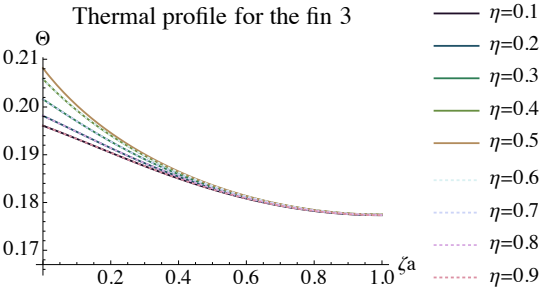

(d) Thermal profile for fin 3.

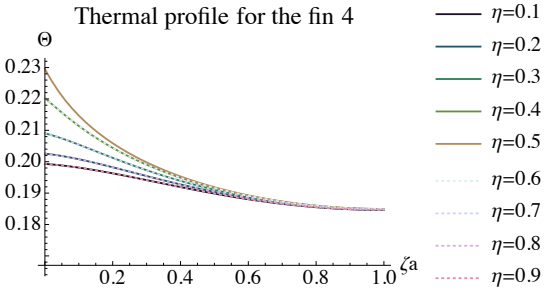

(e) Thermal profile for fin 4.

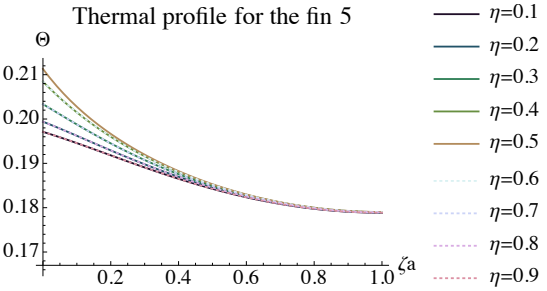

(f) Thermal profile for fin 5.

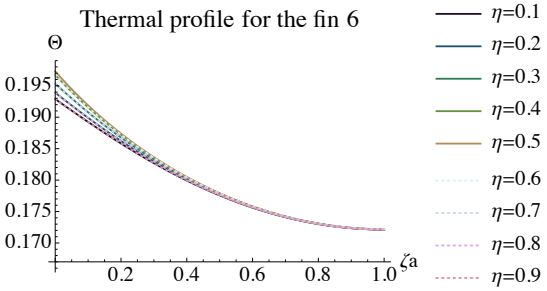

(g) Thermal profile for fin 6.

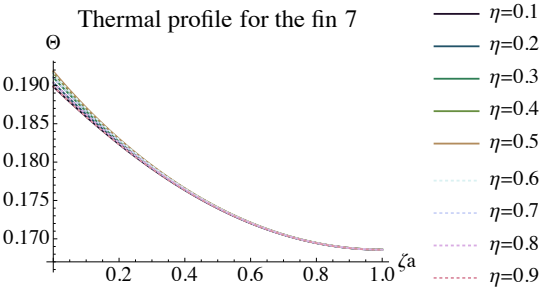

(h) Thermal profile for fin 7.

Table 16 - Temperature field Θ for the mm-scaled case with several non-symmetric hot spots on the heated chip heat sink with $k_{max} = 5000$. ξ_i and ξ_f are indicated on Table 2, and $\xi_{avg} = (\xi_i + \xi_f) \div 2$.

Position	Fin 1	Fin 2	Fin 3	Fin 4	Fin 5	Fin 6	Description
$\Theta_{fin}(0.5, 1)$	0.412752	0.412883	0.412956	0.412986	0.412991	0.412896	Top of fins
$\Theta_{fin}(0.5, 0)$	0.414066	0.41421	0.414282	0.414326	0.414307	0.414182	Bottom of fins
$\Theta_{base}(\xi_{avg}, 0.5, 1)$	0.414066	0.41421	0.414282	0.414326	0.414307	0.414182	Top of Base
$\Theta_{base}(\xi_{avg}, 0.5, 0)$	0.414214	0.414434	0.414432	0.414482	0.414479	0.414323	Bottom of Base

4.4.2 Heat sinks in solid-state electronics (SSE) with hot spots

A simulation for the electronics heat sink case in subsection 4.1.3 is now performed considering also several hot spots in the heated chip. The hot spot effect, in electronics, is caused during the electrical energy conversion and this problem was widely discussed and several solid-state electronics (SSE) cases with hot spots were solved on (CORRÊA; CHALHUB, 2017) and (CORRÊA, 2018).

The mm-scaled heat sink is considered in this case, and the heated chip dissipates uniformly $\dot{q}''_o = 1000$ W/m^2 in all the bottom base surface, as presented in blue on Figure 45a. Several hot spots are observed with different intensities.

The thermal profiles in Figures 45b, 45c and 45d indicate the several heated regions and the thermal profile of the heat sink's base. Hence, Figure 45e shows the non-symmetric contact-interface heat fluxes for the six fins and Figure 46 shows the fins thermal profile. The thermal profiles and Table 16 show a less expressive temperature reduction on the heat sink's thermal profile.

Figure 45 - Results for the 3D base of the mm-scaled case with several non-symmetric hot spots on the heated chip. ξ, η, and ζ are the dimensionless length, width, and height, respectively. The non-symmetric hot spot intensities (W/m^2) of a heated chip caused non-symmetric thermal profiles for the HS's base. A less expressive temperature reduction on the base's thermal profile in the subsection 4.1.3 is also noticed in this case.

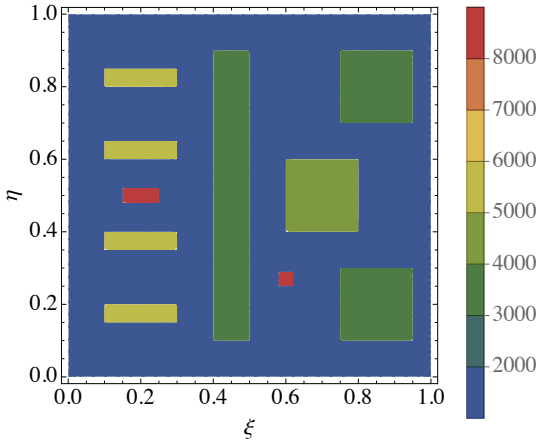

(a) Non-symmetric hot spot intensities at the bottom of the 3D base.

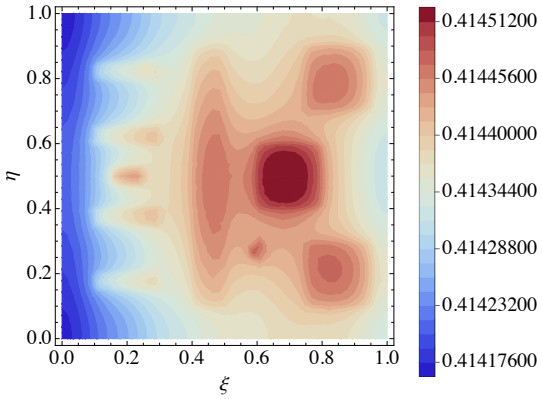

(b) Thermal profile of the base at $\zeta = 0$.

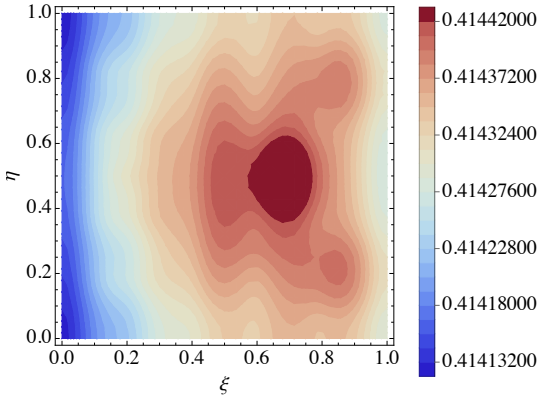

(c) Thermal profile of the base at $\zeta = 0.5$.

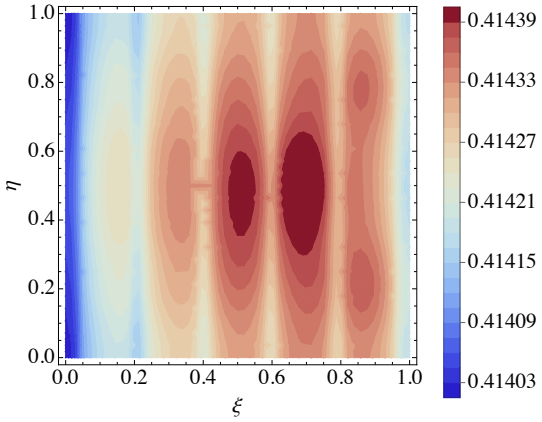

(d) Thermal profile of the base at $\zeta = 1$.

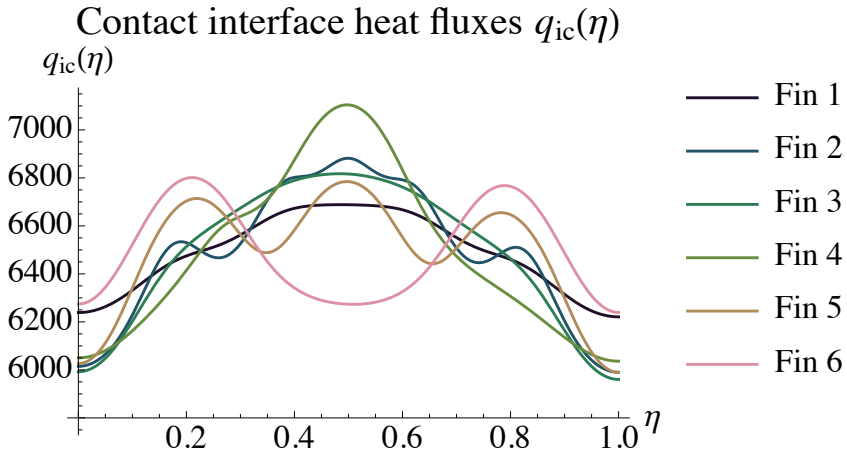

(e) Non-symmetric mm-scaled case contact-interface heat fluxes.

Figure 46 - Results for the 2D fins of the non-symmetric mm-scaled case. A similar thermal behavior between the 2D fins in different η-positions and a less expressive temperature reduction on the fins thermal profile in the subsection 4.1.3 is also noticed in this case.

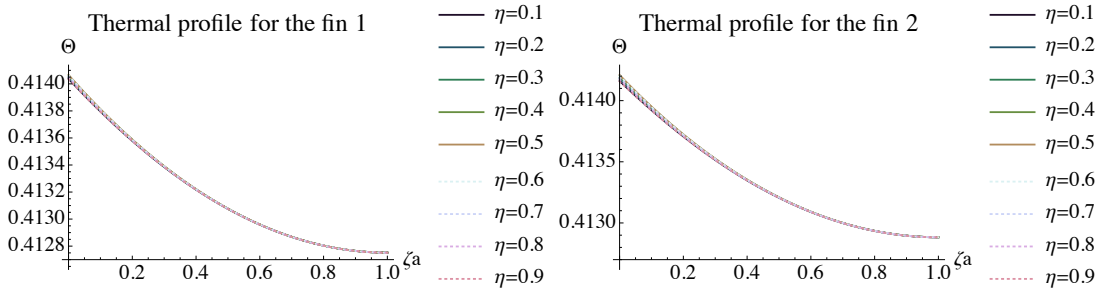

(a) Thermal profile for fin 1.

(b) Thermal profile for fin 2.

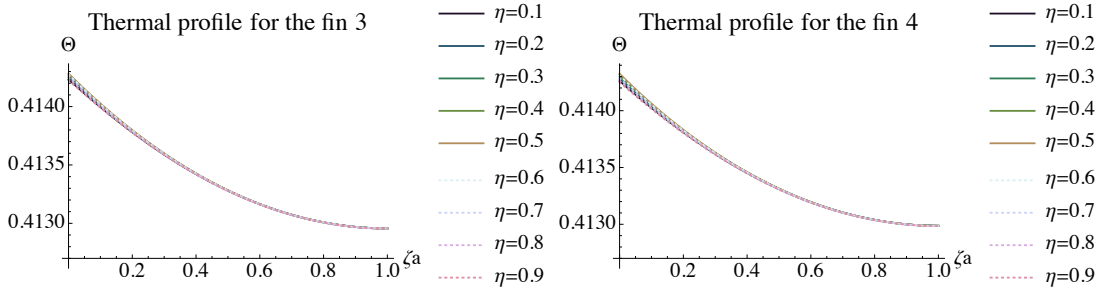

(c) Thermal profile for fin 3.

(d) Thermal profile for fin 4.

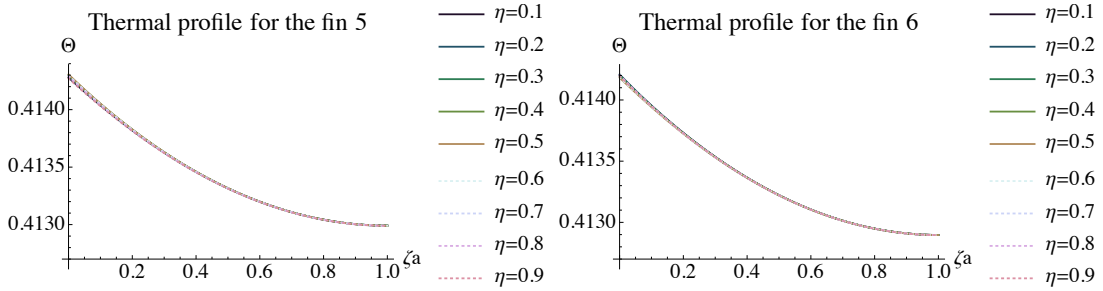

(e) Thermal profile for fin 5.

(f) Thermal profile for fin 6.

4.5 **Heat transfer enhacement promoted by heat sinks**

Finally, the objective of this section is to present different possibilities of heat transfer enhancement promoted by heat sinks and temperature reduction.

The equally spaced cm-scale heat sink dissipates the constant intensity of $\dot{q}''_o = 25$ W/cm^2 from the schematic heated chip on Figure 17b, with a surface area of $0.01 \times W^2$, based on the HS width W, and located at the bottom center of the base. This problem is symmetric and the 2Dbase-1Dfin formulation cannot be used in this problem because the source term varies in the η-direction.

The heat dissipation may be increased using a more conductive material, larger surface area, or more fins. Table 17 indicates the parameters used for each case, which are:

1. Seven-fin cm-scale heat sink with the small heated chip, on Figures 47a, 48a, 49a, 50a, 51a, and 52.

   The same parameters on Table 3 for the cm-scaled heat sink case were used and the same heat transfer coefficient is considered. A significant increase of the heat flux magnitude is noticed between $\eta = 0.4$ and $\eta = 0.6$, at the small chip location neighbor, when Figure 47a is analyzed. The temperatures in heated chip neighborhoods are, consequently, higher than in other parts of the HS, as can be seen in Figures 48a, 49a, 50a and 51a. Figure 51a also indicates the position of the fins by examining the temperature reduction strips in the contour plot, especially at the fourth fin, whose $\dot{q}''_{ic}$ is indicated in green on Figure 47a. The fins located at the HS's center, have a higher variation in their thermal profiles for different η-width positions, especially in centered fins 52d, 52e, and 52f.

2. Change the material thermal properties, on Figures 47b, 48b, 49b, 50b, 51b, and 53.

   The more conductive material reduced the Bi_H, $\mathrm{Bi}_{H_a}\beta_a$, A_1 and A_2 parameters justified by the implementation of higher thermal conductivity. The expected effect analyzing these new parameters is an efficient heat removal for the heated chip source and a less efficient convective heat dissipation by the top of the base and fins.

3. Increase the fin's height, on Figures 47c, 48c, 49c, 50c, 51c, and 54.

   The longer extension of the fins increased all H_a-dependent parameters, which are $\mathrm{Bi}_{H_a}\beta_a$, A_1 and γ_a. The enhancement consequence is a more efficient convective heat dissipation promoted by the base's top and fins.

4. Increase the number of fins, on Figures 47d, 48d, 49d, 50d, 51d, and 55.

   The fins' number increase reduced the channel's spacing, consequently, reducing the Biot parameters Bi_H and $\mathrm{Bi}_{H_a}\beta_a$ for each fin. It must be noticed the use of more fins, in this case, still increased the convective heat dissipation in the overall heat sink.

Table 17 - Dimensionless parameters for the seven-fin cm-scaled heat sink with the small heated chip and the three different heat transfer improving mechanisms heat sinks.

Seven-fins heat sink		Material's change		Fin's height change		Fin's number change	
$\mathrm{Bi}_H =$	8.03×10^{-4}	$\mathrm{Bi}_H =$	4.015×10^{-4}	$\mathrm{Bi}_H =$	8.03×10^{-4}	$\mathrm{Bi}_H =$	7.97×10^{-4}
$\beta = \gamma =$	0.1	$\beta = \gamma =$	0.1	$\beta = \gamma =$	0.1	$\beta = \gamma =$	0.1
$A_1 =$	8.0×10^{-6}	$A_1 =$	4.0×10^{-6}	$A_1 =$	1.0×10^{-5}	$A_1 =$	8.0×10^{-6}
$A_2 =$	1.0×10^{-6}	$A_2 =$	5.0×10^{-7}	$A_2 =$	1.0×10^{-6}	$A_2 =$	1.0×10^{-6}
$\mathrm{Bi}_{H_a}\beta_a =$	0.12848	$\mathrm{Bi}_{H_a}\beta_a =$	0.06424	$\mathrm{Bi}_{H_a}\beta_a =$	0.20075	$\mathrm{Bi}_{H_a}\beta_a =$	0.12752
$\gamma_a =$	0.8	$\gamma_a =$	0.8	$\gamma_a =$	1.0	$\gamma_a =$	0.8
$\alpha_{\mathrm{avg}} =$	0.72	$\alpha_{\mathrm{avg}} =$	0.72	$\alpha_{\mathrm{avg}} =$	0.72	$\alpha_{\mathrm{avg}} =$	0.60

Figure 47 - Contact-interface heat fluxes for the seven-fin cm-scaled heat sink, and using different heat transfer improving mechanisms. A significant increase in the heat flux magnitude can be noticed near the chip location. No expressive modification on $\dot{q}''_{ic}$ is noticed by material modification on 47b, and neither using a larger surface contact on 47c. The more fins, the more heat is distributed by the fins and the lower are the $\dot{q}''_{ic}$ intensities, as seen on 47d.

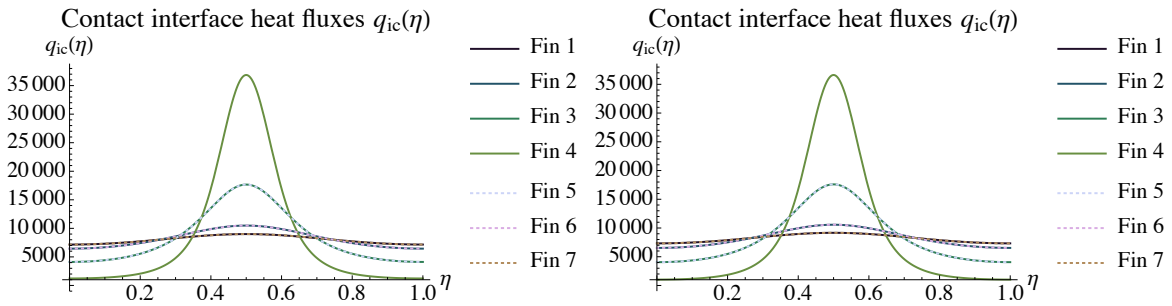

(a) Seven-fins cm-scaled heat sink.

(b) Thermal properties similar to Copper.

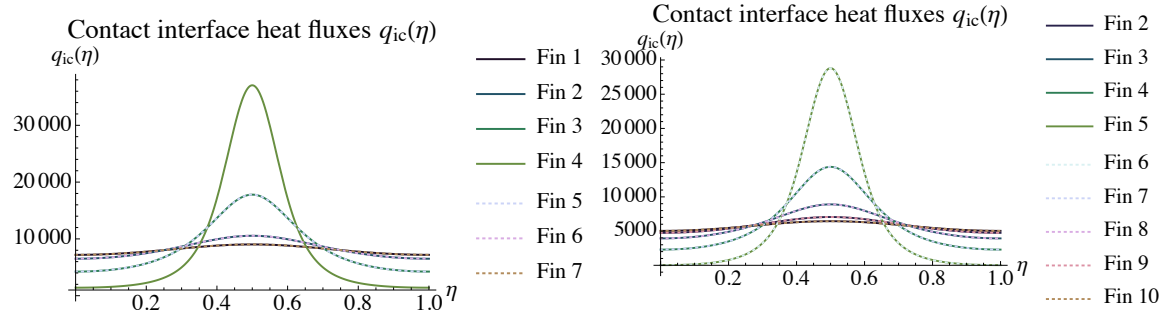

(c) HS with the fin's height $H_a = 1 \times W$.

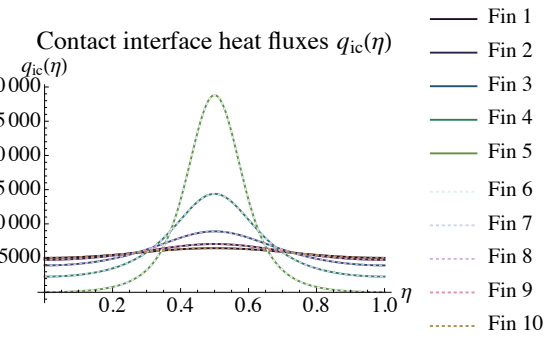

(d) HS with 10 fins.

Figure 48 - Base's isotherms and heatlines at $\eta = 0.5$. ξ, η, and ζ are the dimensionless length, width, and height. The three mechanisms succeeded in reducing the base's temperature. The 10-fin mechanism achieved the lowest temperatures in the overall base, in 48d. Hence, this higher quantity of fins promoted a more disperse flow on the system. Although the more conductive material did not perform that temperature reduction at the overall HS, this mechanism was very efficient in the heat removal from the heated chip, indicated by the lower temperature at the chip-base contact region, in 48b. It must be noticed also the existence of aspect ratio on the for a better examination, the achieved results are shown in a square plot.

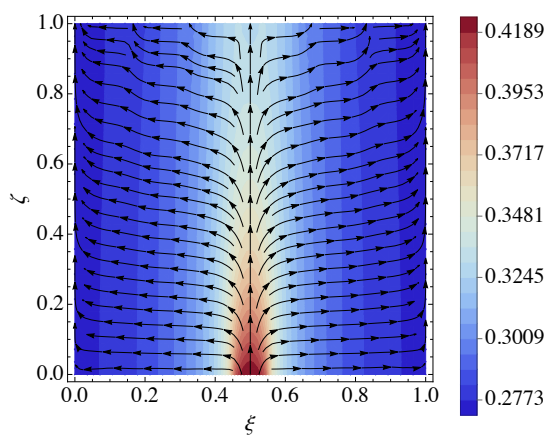

(a) Seven-fins cm-scaled heat sink.

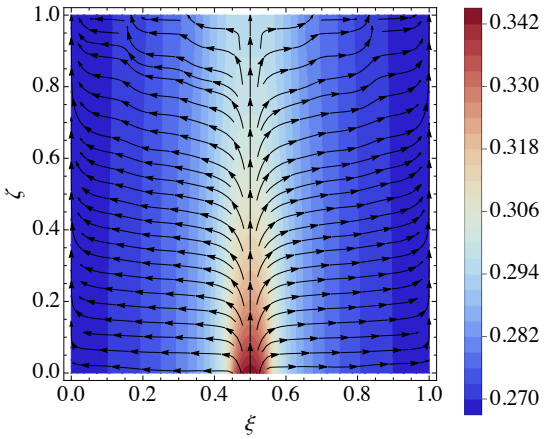

(b) Thermal properties similar to Copper.

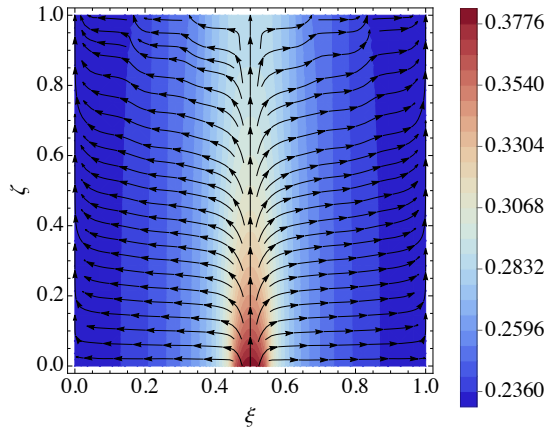

(c) HS with the fin's height $H_a = 1 \times W$.

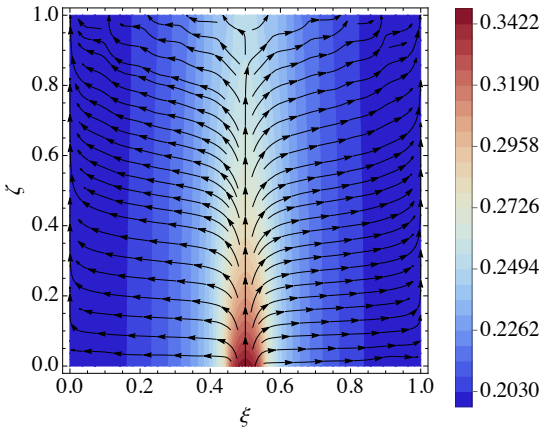

(d) HS with 10 fins.

Figure 49 - Results for the bottom of the 3D base. ξ and η are the dimensionless length and width, respectively, and $\zeta = 0$. The three mechanisms succeeded in reducing the bottom base's temperature. The 10-fin mechanism achieved the lowest thermal amplitude. Although the more conductive material did not perform that temperature reduction at the overall HS, this mechanism was very efficient in heat removal from the heated chip region.

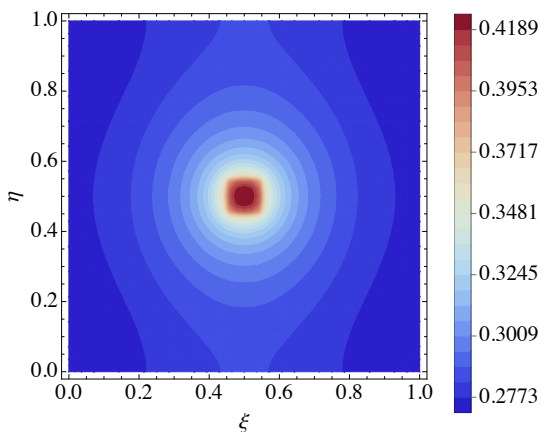

(a) Seven-fins cm-scaled heat sink.

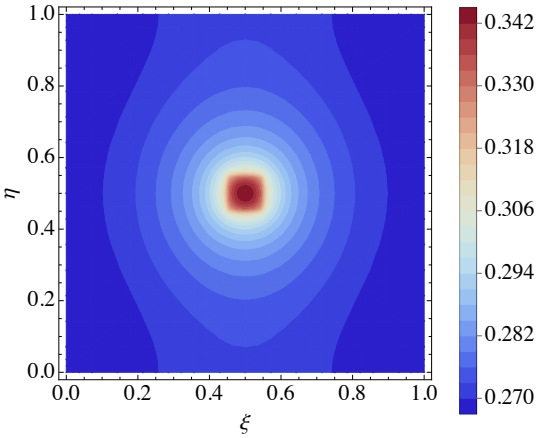

(b) Thermal properties similar to Copper.

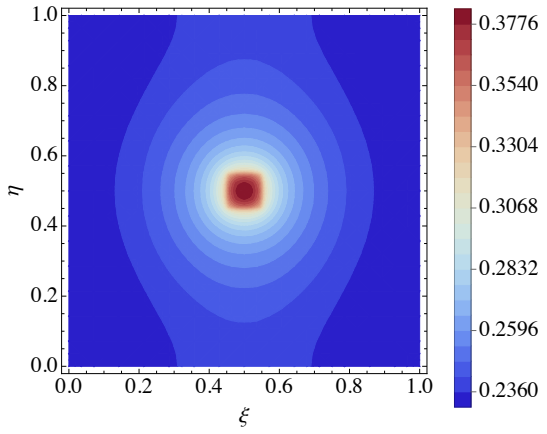

(c) HS with the fin's height $H_a = 1 \times W$.

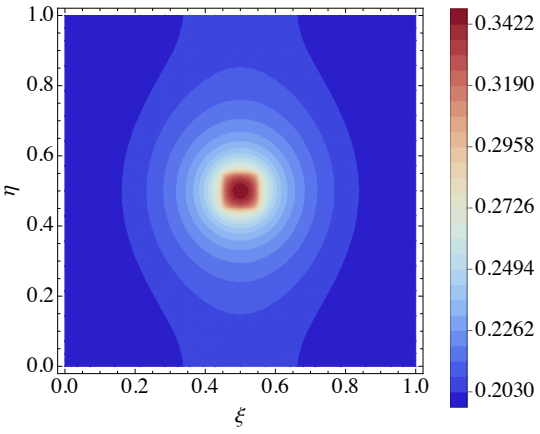

(d) HS with 10 fins.

Figure 50 - Results for the bottom of the 3D base. ξ and η are the dimensionless length and width, respectively, and $\zeta = 0.5$. The three mechanisms succeeded in reducing the bottom base's temperature. The 10-fin mechanism achieved the lowest thermal amplitude values.

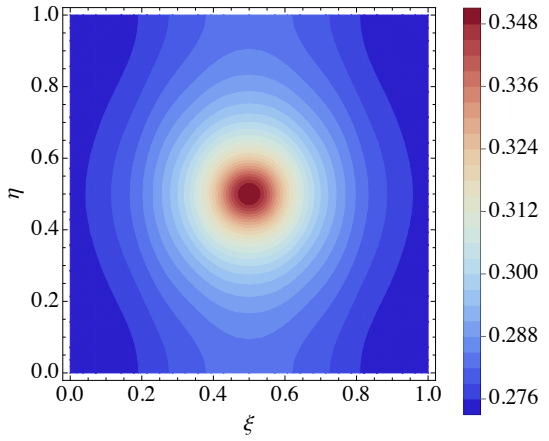

(a) Seven-fins cm-scaled heat sink.

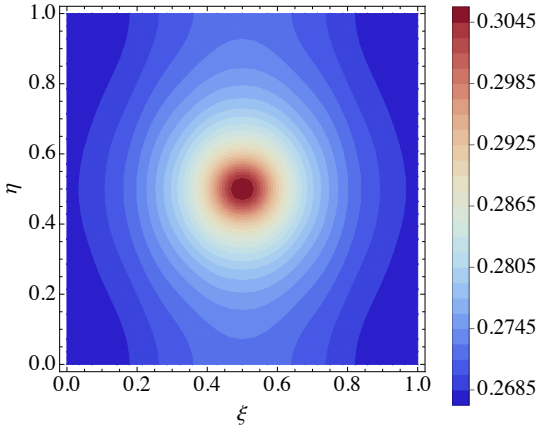

(b) Thermal properties similar to Copper.

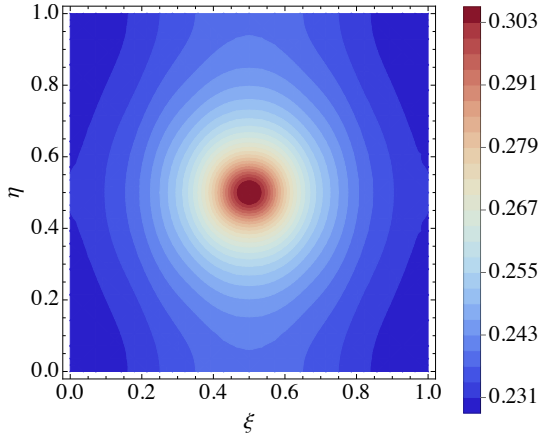

(c) HS with the fin's height $H_a = 1 \times W$.

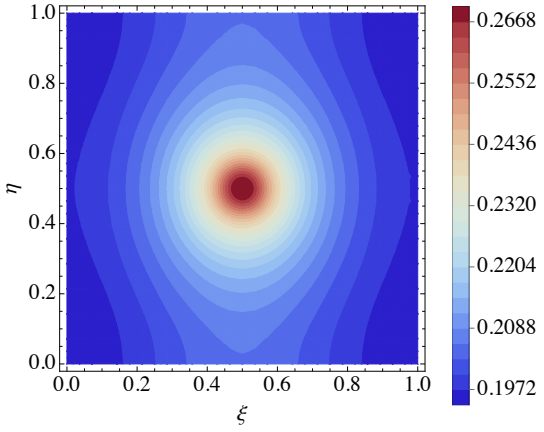

(d) HS with 10 fins.

Figure 51 - Results for the bottom of the 3D base. ξ and η are the dimensionless length and width, respectively, and $\zeta = 1$. The three mechanisms succeeded in reducing the bottom base's temperature. The 10-fin mechanism achieved the lowest thermal amplitude values. Also, the higher quantity of fins for the 10-fins HS caused a different isotherm profile.

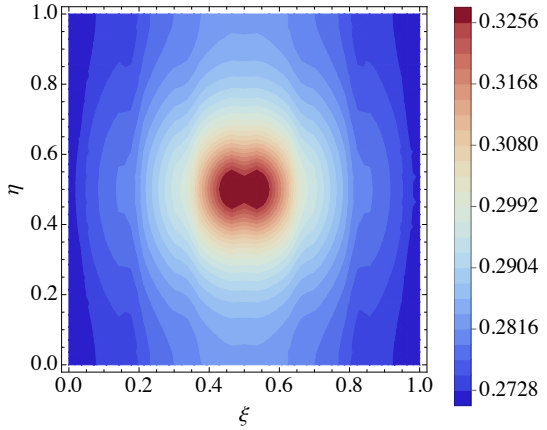

(a) Seven-fins cm-scaled heat sink.

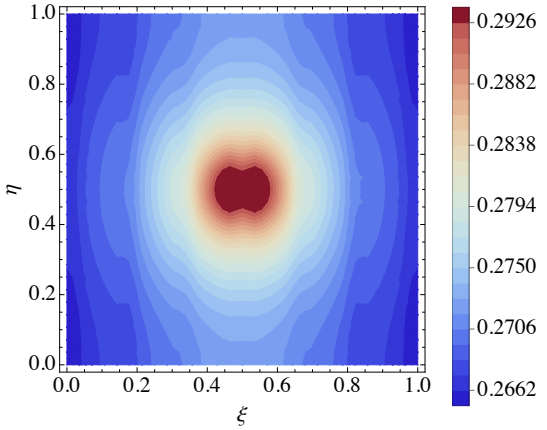

(b) Thermal properties similar to Copper.

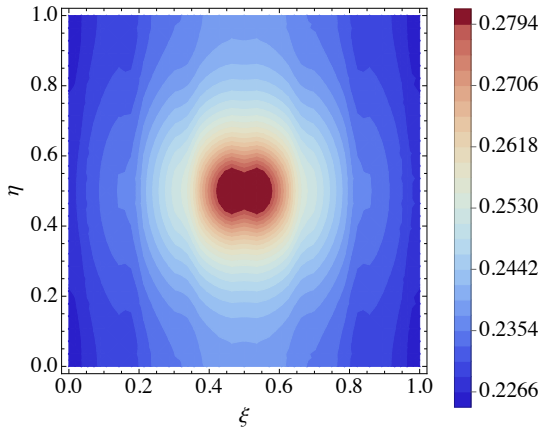

(c) HS with the fin's height $H_a = 1 \times W$.

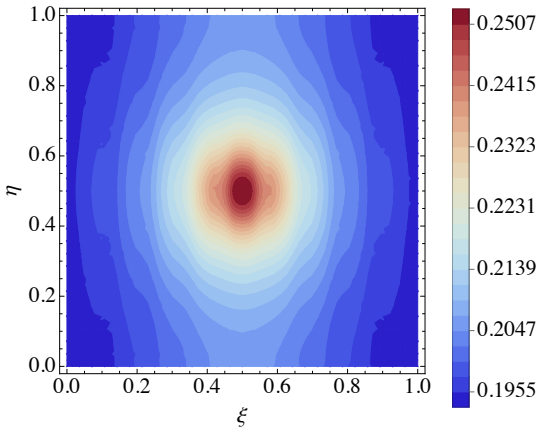

(d) HS with 10 fins.

Figure 52 - 2D fins thermal profile of the seven-fin cm-scaled heat sink with the small heated chip. The selected η-positions are indicated by the blue vertical lines in 52a. The fins temperature varies for different η positions, especially for fins located closer to the heated chip (fins 3,4 and 5) near the fin-base contact interface.

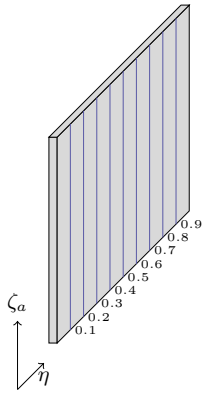

(a) 2D-fin scheme.

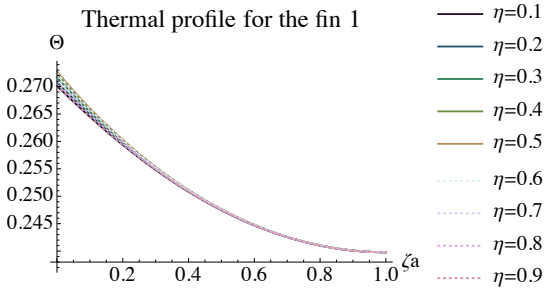

(b) Thermal profile for fin 1.

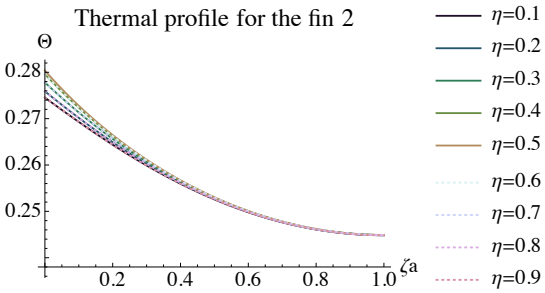

(c) Thermal profile for fin 2.

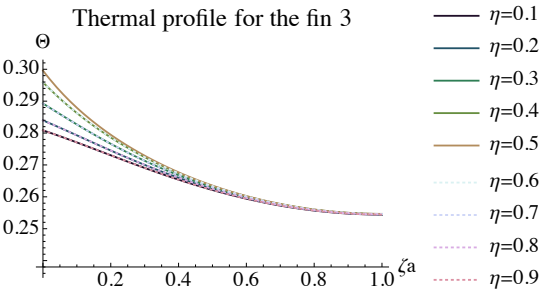

(d) Thermal profile for fin 3.

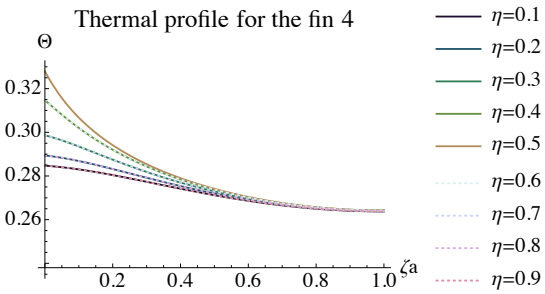

(e) Thermal profile for fin 4.

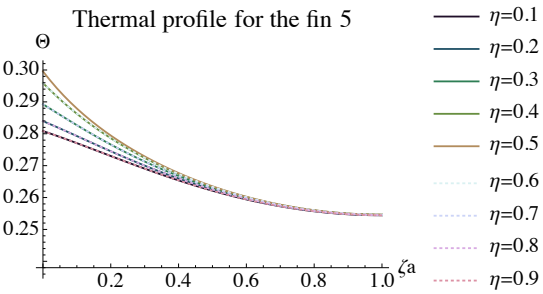

(f) Thermal profile for fin 5.

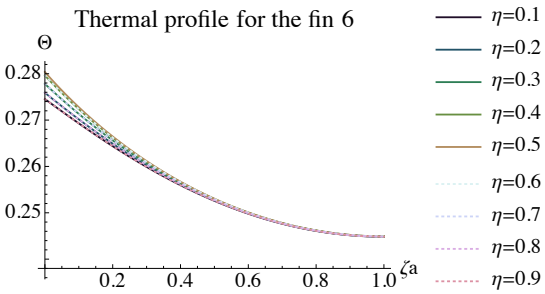

(g) Thermal profile for fin 6.

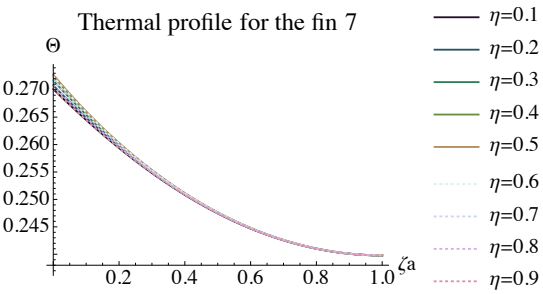

(h) Thermal profile for fin 7.

Figure 53 - 2D fins thermal profile of the seven-fin case with the material's change.

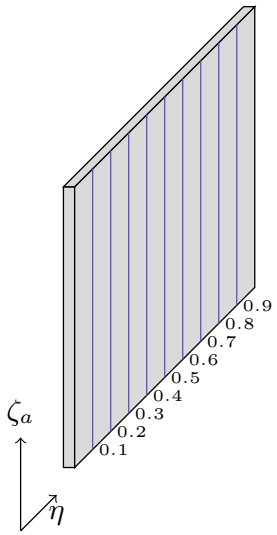

(a) 2D-fin scheme.

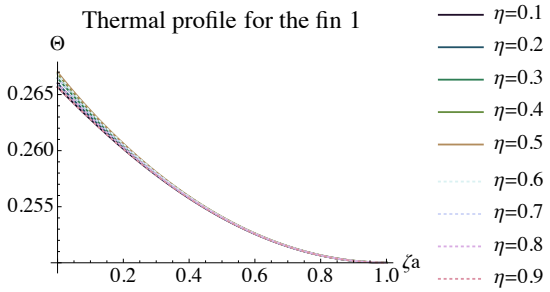

(b) Thermal profile for fin 1.

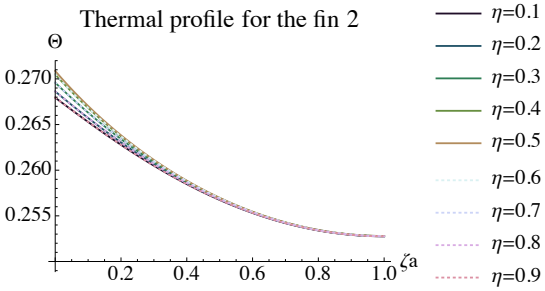

(c) Thermal profile for fin 2.

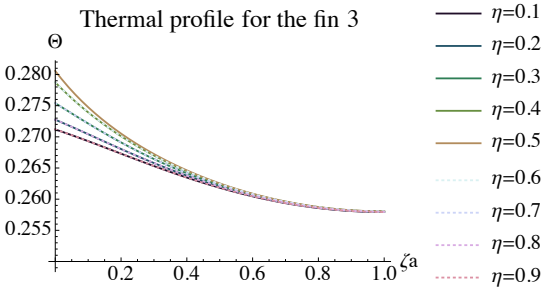

(d) Thermal profile for fin 3.

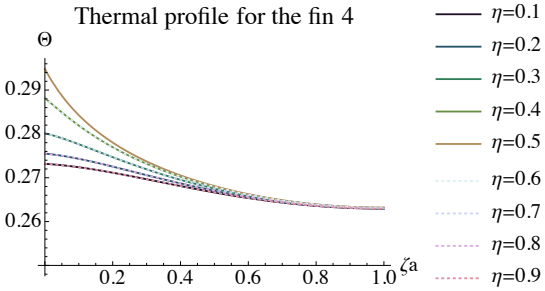

(e) Thermal profile for fin 4.

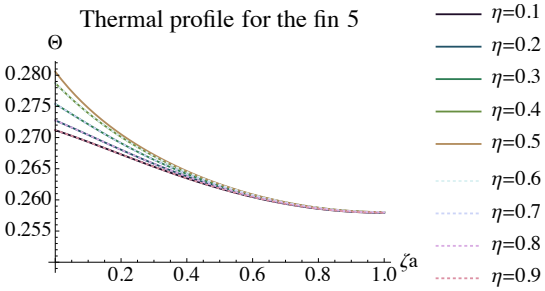

(f) Thermal profile for fin 5.

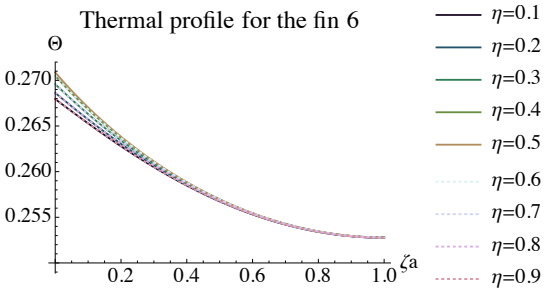

(g) Thermal profile for fin 6.

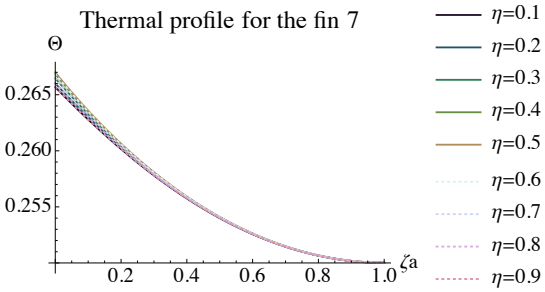

(h) Thermal profile for fin 7.

Figure 54 - 2D fins thermal profile of the seven-fin case with the fin's height change.

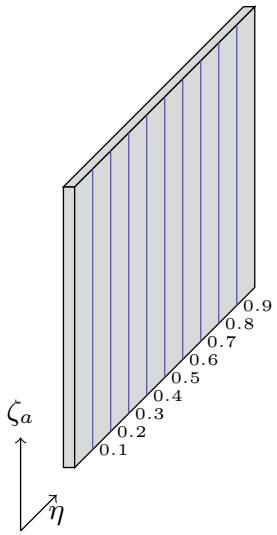

(a) 2D-fin scheme.

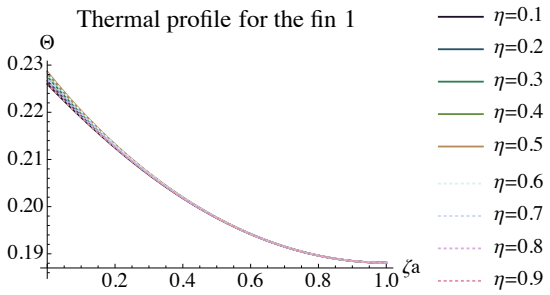

(b) Thermal profile for fin 1.

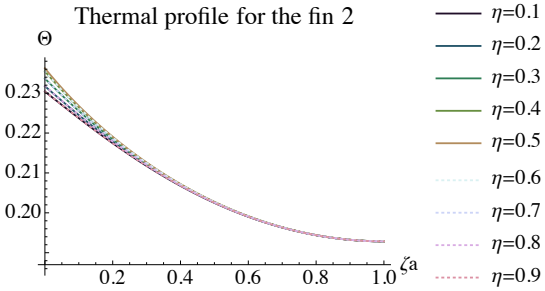

(c) Thermal profile for fin 2.

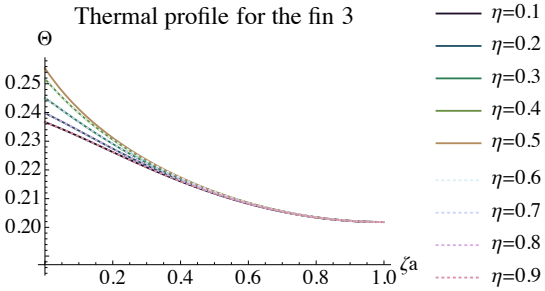

(d) Thermal profile for fin 3.

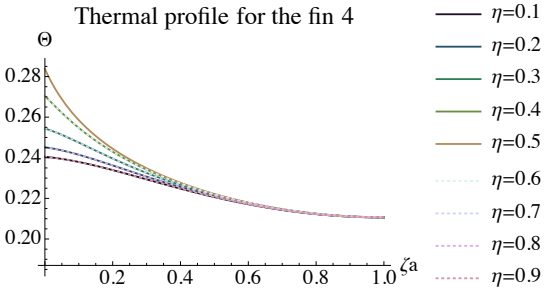

(e) Thermal profile for fin 4.

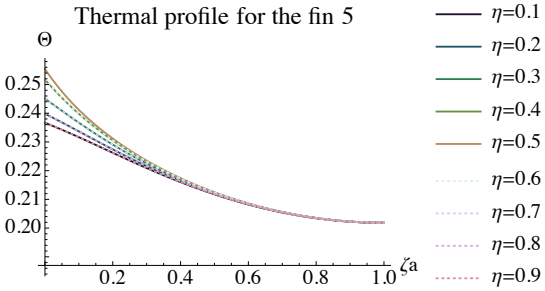

(f) Thermal profile for fin 5.

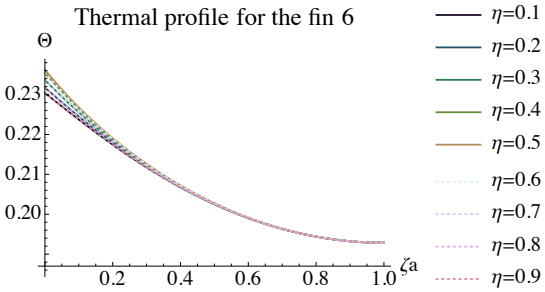

(g) Thermal profile for fin 6.

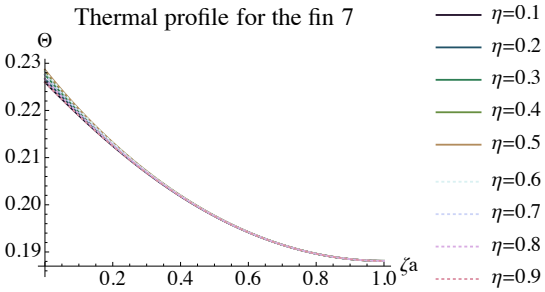

(h) Thermal profile for fin 7.

Figure 55 - 2D fins thermal profile of the seven-fin for the fins' number change case. This problem is symmetric.

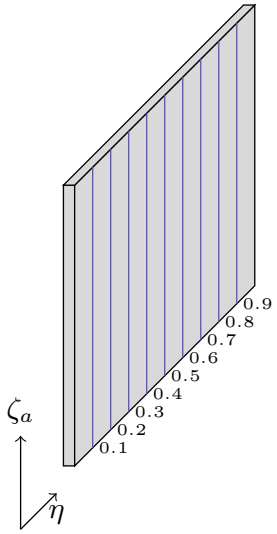

(a) 2D-fin scheme.

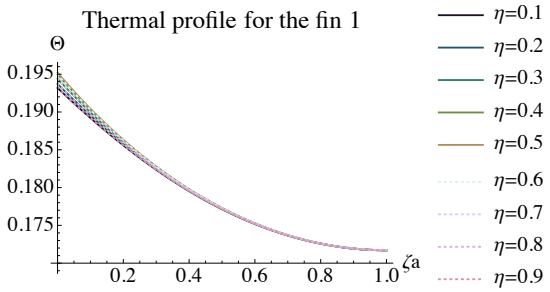

(b) Thermal profile for fin 1=10.

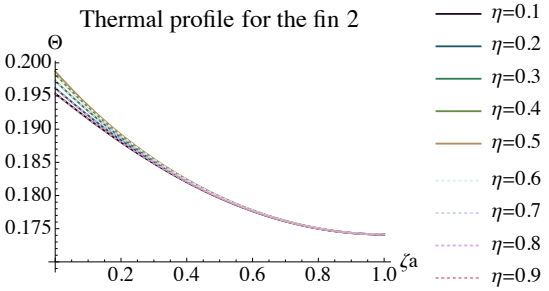

(c) Thermal profile for fin 2=9.

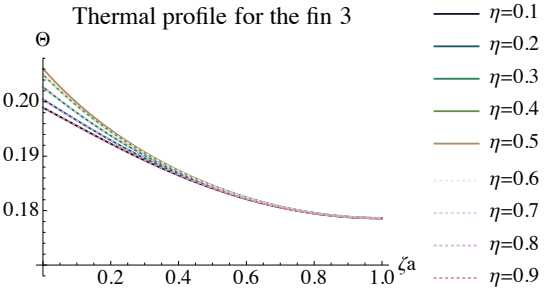

(d) Thermal profile for fin 3=8.

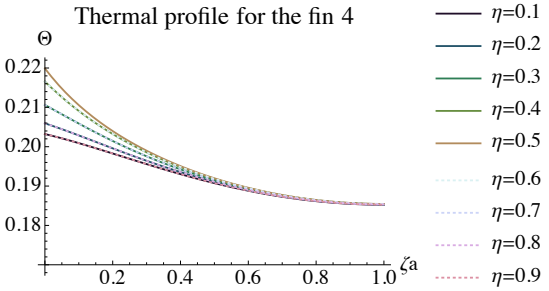

(e) Thermal profile for fin 4=7.

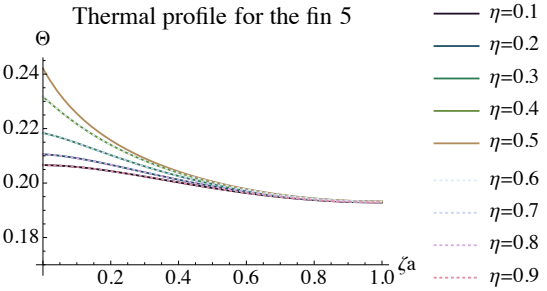

(f) Thermal profile for fin 5=6.

Table 18 - Θ temperature field Table for the seven-fin cm-scaled heat sink with the small heated chip and using three different heat transfer improving mechanisms.

Position	Fin 1	Fin 2	Fin 3	Fin 4	Fin 5	Fin 6	Fin 7	Description
Seven-fins cm-scaled heat sink with small heated chip								
$\Theta_{fin}(0.5,1)$	0.239813	0.244914	0.254654	0.264224	0.254654	0.244914	0.239813	Top of fins
$\Theta_{fin}(0.5,0)$	0.272751	0.28038	0.299604	0.327962	0.299604	0.28038	0.272751	Bottom of fins
$\Theta_{base}(\xi_{avg},0.5,1)$	0.272751	0.28038	0.299604	0.327962	0.299604	0.28038	0.272751	Top of Base
$\Theta_{base}(\xi_{avg},0.5,0)$	0.276042	0.283365	0.305237	0.428365	0.305237	0.283365	0.276042	Bottom of Base
Change of material								
$\Theta_{fin}(0.5,1)$	0.250027	0.252795	0.258048	0.263179	0.258048	0.252795	0.250027	Top of fins
$\Theta_{fin}(0.5,0)$	0.266995	0.270873	0.280576	0.294816	0.280576	0.270873	0.266995	Bottom of fins
$\Theta_{base}(\xi_{avg},0.5,1)$	0.266995	0.270873	0.280576	0.294816	0.280576	0.270873	0.266995	Top of Base
$\Theta_{base}(\xi_{avg},0.5,0)$	0.268671	0.272396	0.283380	0.344943	0.283380	0.272396	0.268671	Bottom of Base
Change in the fin's height								
$\Theta_{fin}(0.5,1)$	0.188118	0.192862	0.201887	0.210734	0.201887	0.192862	0.188118	Top of fins
$\Theta_{fin}(0.5,0)$	0.228639	0.236243	0.255411	0.283731	0.255411	0.236243	0.228639	Bottom of fins
$\Theta_{base}(\xi_{avg},0.5,1)$	0.228639	0.236243	0.255411	0.283731	0.255411	0.236243	0.228639	Top of Base
$\Theta_{base}(\xi_{avg},0.5,0)$	0.231930	0.239218	0.261087	0.384154	0.261087	0.239218	0.231930	Bottom of Base

	Change in the number of fins					
Position	Fin 1=10	Fin 2=9	Fin 3=8	Fin 4=7	Fin 5=6	Description
$\Theta_{fin}(0.5,1)$	0.171723	0.17416	0.178664	0.18546	0.193254	Top of fins
$\Theta_{fin}(0.5,0)$	0.195215	0.198724	0.206093	0.219915	0.242125	Bottom of fins
$\Theta_{base}(\xi_{avg},0.5,1)$	0.195229	0.198718	0.206076	0.219910	0.242139	Top of Base
$\Theta_{base}(\xi_{avg},0.5,0)$	0.197646	0.200898	0.208758	0.224878	0.292212	Bottom of Base

It can be noticed that the fins' number increase has consequently increased the heat dissipation on the overall heat sink. In summary, the more fins, the lower the temperature of the HS, and broader is heat dissipation by the dispersed fins contribution. Even though the chip's flux maintained the same value for both tested cases, the increase in heat dissipation reduced the temperature even at the bottom of the base, where the flux is located.

The enhancement mechanisms are also clear in Table 18, the fourth fin's maximum temperature was initially calculated 0.428365, it was then reduced to much lower values such as 0.344943 and 0.384154, changing the material and the fin's height, respectively. The fins number increase reduced the maximum temperature to 0.292212, on fins 5 and 6.

In summary, the three mechanisms of heat transfer enhancement are efficient. The application of a more conductive material, higher thermal conductivity, promotes a more efficient removal of the heat at its source, but the convective heat transfer is compromised. Increasing the fin's height, the wet area is increased and, consequently, the heat exchange area is larger, increasing the convective heat transfer. The heat removal at the heated chip is not as efficient as expected. Finally, more fins not only increased the total exchange area but also dissipated the heat more homogeneously at the base's top, with lower contact-interface heat fluxes to each fin, removing efficient heat from its source and increasing the convective heat transfer.

CONCLUSIONS

This work presented an analytical approach to obtain the temperature fields of open-sandwich heat sinks using the Classical Integral Transform Technique (CITT). A three-dimension formulation for the base and two-dimension formulation for fins were solved analytically using the CITT and coupled to obtain the interface contact heat fluxes ($\dot{q}''_{ic}$) on each fin. The obtained $\dot{q}''_{ic}$ is applied on the base and fins solutions, and the dimensionless temperature field Θ is calculated for the base and fins.

The eigenfunction expansion heat flux was used to find the interface contact heat fluxes. With this approach, the heat flux is defined as an inversion term and its transformation is used to perform the fin-base coupling. The great advantage of the eigenfunction expansion heat flux approach is the coupling in n_{max} different positions, a much more accurate approach than using polynomial functions.

The achieved results were compared with a simplified version of the methodology to demonstrate the CITT convergence and the relative deviation percentage between the different formulations. Simulations using the open-source CFD software OpenFOAM were also used to compare the achieved results and confirm the analytical methodology accuracy. The computational cost of CITT is much lower when compared with OF simulations. Different geometries were tested and the rectangular fin profile is shown to be the most effective shape.

The developed methodology innovates the study of heat transfer in heat sinks presenting the importance of 2D fin modeling for symmetrical and non-symmetrical cases. Increasing the number of fins, the convective heat transfer is enhanced in the overall heat sink and dissipates the heat in a more homogeneous manner, consequently, it ensures a safe and efficient performance of the heated chip.

Some future works can be performed from the developed methodology presented:

1. Optimization studies.

2. Develop a new formulation for fins and base considering the radiative heat transfer and mutual irradiation between fins.

3. Solve the problem considering the closed sandwich heat sink configuration and for other cooling fluids.

REFERENCES

ADHAM, A. M.; MOHD-GHAZALI, N.; AHMAD, R. Thermal and hydrodynamic analysis of microchannel heat sinks: a review. *Renewable anf Sustainable Energies Reviews*, v. 21, p. 614–622, 2013.

AHMED, H. E.; SALMAN, B.; KHERBEET, A. S.; AHMED, M. Optimization of thermal design of heat sinks: A review. *International Journal of Heat and Mass Transfer*, Elsevier, v. 118, p. 129–153, 2018.

AL-ATHEL, K. S.; ALY, S. P.; ARIF, A. F. M.; MOSTAGHIMI, J. 3d modeling and analysis of the thermo-mechanical behavior of metal foam heat sinks. *International Journal of Thermal Sciences*, Elsevier, v. 116, p. 199–213, 2017.

ALFIERI, F. et al. 3d integrated water cooling of a composite multilayer stack of chips. *Journal of Heat Transfer*, American Society of Mechanical Engineers Digital Collection, v. 132, n. 12, 2010.

ANAND, N.; KIM, S.; FLETCHER, L. The effect of plate spacing on free convection between heated parallel plates. *Journal of Heat Transfer (Transactions of the ASME (American Society of Mechanical Engineers), Series C);(United States)*, v. 114, n. 2, 1992. Disponível em: <https://www.osti.gov/biblio/7265173>.

ARULARASAN, R.; VELRAJ, R. Modeling and simulation of a parallel plate heat sink using computational fluid dynamics. *The International Journal of Advanced Manufacturing Technology*, Springer, v. 51, n. 1-4, p. 415–419, 2010.

AZARKISH, H.; FARAHAT, S.; SARVARI, S. M. H. Comparing the performances of the particle swarm optimization and the genetic algorithm on the geometry design of longitudinal fins. *International Journal of Sciences and Engineering Investigations*, v. 1, p. 70–74, 2012.

AZARKISH, H.; SARVARI, S. M. H.; BEHZADMEHR, A. Optimum design of a longitudinal fin array with convection and radiation heat transfer using genetic algorithm. *International Journal of Thermal Sciences*, v. 49, p. 2222–2229, 2010.

AZIZ, A.; MAKINDE, O. Heat transfer and entropy generation in a two-dimensional orthotropic convection pin fin. *International Journal of Exergy*, Inderscience Publishers, v. 7, n. 5, p. 579–592, 2010.

BABAELAHI, M.; ESHRAGHI, H. Optimum analytical design of medical heat sink with convex parabolic fin including variable thermal conductivity and mass transfer. *Extreme Mechanics Letters*, Elsevier, v. 15, p. 83–90, 2017.

BAR-COHEN, A.; IYENGAR, M.; KRAUS, A. D. Design of optimum plate-fin natural convective heat sinks. *J. Electron. Packag.*, v. 125, n. 2, p. 208–216, 2003.

BEJAN, A.; KRAUS, A. D. *Heat transfer handbook*. [S.l.]: John Wiley & Sons, 2003. v. 1.

BOUAZIZ, N. Fin efficiency in 2d with convection at the tip and dissymmetry of exchange. *Energy Conversion and Management*, Elsevier, v. 50, n. 6, p. 1618–1624, 2009.

BUSHEHRI, M. R. S.; RAMIN, H.; SALIMPOUR, M. R. A new coupling method for slip-flow and conjugate heat transfer in a parallel plate micro heat sink. *International Journal of Thermal Sciences*, Elsevier, v. 89, p. 174–184, 2015.

CHALHUB, D. J. N. M. *Desenvolvimento de soluções para problemas de advecção-difusão combinando transformação integral e métodos discretos*. Dissertação (Mestrado) — Universidade Federal Fluminense- UFF, 2011.

CHALHUB, D. J. N. M. *Solution of the Incompressible Navier-Stokes Equations by projection methods using the Integral Transform Technique*. Tese (Doutorado) — Universidade Federal Fluminense, 2015.

COPELAND, D. Optimization of parallel plate heatsinks for forced convection. In: IEEE. *Sixteenth Annual IEEE Semiconductor Thermal Measurement and Management Symposium (Cat. No. 00CH37068)*. [S.l.], 2000. p. 266–272.

COROMINAS, J. *Heat Sink Analytical Modelling*. Dissertação (Mestrado) — Universitat Politècnica de Catalunya, Escola Tècnica Superior d'Enginyeria Industrial de Barcelona, (Enginyeria Industrial), 2010. Disponível em: <https://books.google.com.br/books?id=LR8ZywEACAAJ>.

CORRÊA, L. M. *Solution of Heat Conduction in Solid-State Electronics utilizing Integral Transforms*. [S.l.], 2018. Bachelor's Thesis.

CORRÊA, L. M.; CHALHUB, D. J. N. M. Solution of the heat conduction in solid-state electronics by integral transforms. In: *24th ABCM International Congress of Mechanical Engineering - COBEM 2017*. Curitiba, Brazil: [s.n.], 2017.

CORRÊA, L. M.; CHALHUB, D. J. N. M. Thermal analysis of heat sinks on solar panels. In: *17th Brazilian Congress of Thermal Sciences and Engineering - ENCIT 2018*. Águas de Lindóia, Brazil: [s.n.], 2018.

CORRÊA, L. M.; CHALHUB, D. J. N. M. Thermal analysis of heat sinks: an analytical approach. In: *25th ABCM International Congress of Mechanical Engineering - COBEM 2019*. Uberlândia, Brazil: [s.n.], 2019.

COSTA, V. Unification of the streamline, heatline and massline methods for the visualization of two-dimensional transport phenomena. *International Journal of Heat and Mass Transfer*, Elsevier, v. 42, n. 1, p. 27–33, 1999.

COTTA, R. M. *Integral Transforms in Computational Heat and Fluid Flow*. [S.l.]: CRC Press, 1993.

COTTA, R. M. et al. Integral transform benchmarks of diffusion, convection–diffusion, and conjugated problems in complex domains. In: *50 Years of CFD in Engineering Sciences*. [S.l.]: Springer, 2020. p. 719–750.

COTTA, R. M.; MIKHAILOV, M. D. *Heat conduction: lumped analysis, integral transforms, symbolic computation*. [S.l.]: Wiley-Blackwell, 1997.

CUCE, P. M.; CUCE, E. Optimization of configurations to enhance heat transfer from a longitudinal fin exposed to natural convection and radiation. *International Journal of Low-Carbon Technologies*, v. 9, p. 305–310, 2014.

DANTAS, L. B. *Heat Transfer Study of Plastic Encapsulated Chips using the Generalized Integral Transform Technique*. Dissertação (Mestrado) — Universidade Federal do Rio de Janeiro, 1996.

DANTAS, L. B.; ORLANDE, H. R. B. A function estimation approach for determining temperature dependent thermophysical properties. *Inverse Problems in Engineering*, v. 3, p. 261–279, 1996.

DENG, Q.-H.; TANG, G.-F. Numerical visualization of mass and heat transport for conjugate natural convection/heat conduction by streamline and heatline. *International Journal of Heat and Mass Transfer*, Elsevier, v. 45, n. 11, p. 2373–2385, 2002.

FERZIGER, J. H.; PERIĆ, M. *Computational methods for fluid dynamics*. [S.l.]: Springer, 2002. v. 3.

FOKAIDES, P. A.; KALOGIROU, S. A. Application of infrared thermography for the determination of the overall heat transfer coefficient (u-value) in building envelopes. *Applied energy*, Elsevier, v. 88, n. 12, p. 4358–4365, 2011.

FURUKAWA, T.; YANG, W.-J.; TORII, S. Stacked packaging laminar-convection-cooled printed circuit using the entropy generation minimization method. *Journal of thermophysics and heat transfer*, v. 22, n. 2, p. 315–318, 2008. Disponível em: <https://deepblue.lib.umich.edu/bitstream/handle/2027.42/76567/AIAA-30451-562.pdf?sequence=1>.

HAHN, D. W.; OZISIK, M. N. *Heat Conduction*. 3. ed. [S.l.]: John Willy & Sons, 2012.

INCROPERA, F. P. Convection heat transfer in electronic equipment cooling. *Journal of Heat Transfer, ASME*, v. 110, p. 1097–1111, 1988.

KALOGIROU, S. A. *Solar energy engineering: processes and systems*. [S.l.]: Academic Press, 2013. 199-200 p.

KHAN, W. A.; YOVANOVICH, M.; CULHAM, J. Optimization of microchannel heat sinks using entropy generation minimization method. In: IEEE. *Twenty-Second Annual IEEE Semiconductor Thermal Measurement And Management Symposium*. [S.l.], 2006. p. 78–86.

KIM, S. J. Methods for thermal optimization of microchannel heat sinks. *Heat transfer engineering*, Taylor & Francis, v. 25, n. 1, p. 37–49, 2004.

KIMURA, S.; BEJAN, A. The “heatline” visualization of convective heat transfer. *Journal of heat transfer*, American Society of Mechanical Engineers, v. 105, n. 4, p. 916–919, 1983.

KNUPP, D. C. *Análise Teórico-Experimental de Transferência de Calor em Nanocompósitos via Transformação Integral e Termografia por Infravermelho*. Dissertação (Mestrado) — Universidade Federal do Rio de Janeiro, 2010.

KREITH, F.; MANGLIK, R. M.; BOHN, M. S. *Principles of heat transfer*. [S.l.]: Cengage learning, 2012.

KRISHNAN, S.; GARIMELLA, S. V.; KANG, S. S. A novel hybrid heat sink using phase change materials for transient thermal management of electronics. *IEEE Transactions on Components and Packaging Technologies*, IEEE, v. 28, n. 2, p. 281–289, 2005.

KUMAR, S.; KUMAR, A.; KOTHIYAL, A. D.; BISHT, M. S. A review of flow and heat transfer behaviour of nanofluids in micro channel heat sinks. *Thermal Science and Engineering Progress*, Elsevier, v. 8, p. 477–493, 2018.

LAMPIO, K.; KARVINEN, R. A new method to optimize natural convection heat sinks. *Heat and Mass Transfer*, Springer, v. 54, n. 8, p. 2571–2580, 2018.

LAUNDER, B. E.; SPALDING, D. B. The numerical computation of turbulent flows. In: *Numerical prediction of flow, heat transfer, turbulence and combustion*. [S.l.]: Elsevier, 1983. p. 96–116.

LEE, S.; EARLY, M.; PELLILO, M. Thermal interface material performance in microelectronic packaging applications. *Microelectronics Journal*, v. 28, p. xiii–xx, 1997.

LEHTINEN, A. *Analytical Treatment of Heat Sinks Cooled by Forced Convection*. Tese (Doutorado) — Tampere University of Technology, 2005.

LIMBASIYA, N.; ROY, A.; HARICHANDAN, A. B. Numerical simulation of heat transfer for microelectronic heat sinks with different fin geometries in tandem and staggered arrangements. *Thermal Science and Engineering Progress*, Elsevier, v. 4, p. 11–17, 2017.

LU, X.; SHI, T.; XIA, Q.; LIAO, G. Thermal conduction analysis and characterization of solder bumps in flip chip package. *Applied Thermal Engineering*, Elsevier, v. 36, p. 181–187, 2012.

MA, S.; BEHBAHANI, A.; TSUEI, Y. Two-dimensional rectangular fin with variable heat transfer coefficient. *International Journal of Heat and Mass Transfer*, Elsevier, v. 34, n. 1, p. 79–85, 1991.

MAHAPATRA, P. S.; MUKHOPADHYAY, A.; MANNA, N. K.; GHOSH, K. Heatlines and other visualization techniques for confined heat transfer systems. *International Journal of Heat and Mass Transfer*, Elsevier, v. 118, p. 1069–1079, 2018.

MALEK, A.; SHABANI, S. M. A. Solving macroscopic and microscopic pin-fin heat sink problems by adapted spectral method. *Computational and Applied Mathematics*, Springer, v. 37, n. 2, p. 1112–1129, 2018.

MALEKZADEH, P.; RAHIDEH, H. Two-dimensional nonlinear transient heat transfer analysis of variable section pin fins. *Energy Conversion and Management*, Elsevier, v. 50, n. 4, p. 916–922, 2009.

MARIN, E. Linear relationships in heat transfer. *Latin American Journal of Physics Education*, v. 3, n. 2, p. 243–245, 2009.

MIKHAILOV, M. D.; OZISIK, M. N. *Unified Analysis and Solutions of Heat and Mass Diffusion*. New York: Wiley, 1984.

MOITSHEKI, R. J.; ROWJEE, A. Steady heat transfer through a two-dimensional rectangular straight fin. *Mathematical problems in engineering*, Hindawi, v. 2011, 2011.

MOORE, G. Moore's law. *Electronics Magazine*, 1965.

MOSAYEBIDORCHEH, S.; HATAMI, M.; MOSAYEBIDORCHEH, T.; GANJI, D. Optimization analysis of convective–radiative longitudinal fins with temperature-dependent properties and different section shapes and materials. *Energy Conversion and Management*, Elsevier, v. 106, p. 1286–1294, 2015.

MOUKALLED, F.; MANGANI, L.; DARWISH, M. et al. *The finite volume method in computational fluid dynamics*. [S.l.]: Springer, 2016.

Naveira-Cotta, C. P.; COTTA, R. M.; ORLANDE, H. R. B. Inverse analysis with integral transformed temperature fields: Identification of thermophysical properties in heterogeneous media. *International Journal of Heat and Mass Transfer*, v. 54, p. 1506–1519, 2011.

ONG, K. E. et al. Optimization of fins used in electronic packaging. *Microelectronics International*, v. 22, p. 10–15, 2005.

PATANKAR, S. Recent developments in computational heat transfer. 1988.

PATANKAR, S. V. *Numerical Heat Transfer and Fluid Flow*. [S.l.]: Hemisphere, 1980.

PATANKAR, S. V.; SPALDING, D. A computer model for three-dimensional flow in furnaces. In: ELSEVIER. *Symposium (International) on Combustion*. [S.l.], 1973. v. 14, n. 1, p. 605–614.

PATANKAR, S. V.; SPALDING, D. B. A calculation procedure for heat, mass and momentum transfer in three-dimensional parabolic flows. In: *Numerical prediction of flow, heat transfer, turbulence and combustion*. [S.l.]: Elsevier, 1971. p. 54–73.

PETERSON, G. P.; ORTEGA, A. Thermal control of electronic equipment and devices. *Advances in Heat Transfer*, v. 20, p. 181–314, 1994.

PINHEIRO, I.; SPHAIER, L.; ALVES, L. de B. Integral transform solution of integro-differential equations in conduction-radiation problems. *Numerical Heat Transfer, Part A: Applications*, v. 73, n. Issue 2, p. 94–114, 2018.

PONTES, J.; MANGIAVACCHI, N. *Fenômenos de Transferência com Aplicações Ciências Físicas e a Engenharia – Volume 1: Fundamentos*. [S.l.]: SBM – Sociedade Brasileira de Matemática, 2016. ISBN 978-85-8337-107-6.

POPOVICI, C. G.; HUDIŞTEANU, S. V.; MATEESCU, T. D.; CHERECHEŞ, N.-C. Efficiency improvement of photovoltaic panels by using air cooled heat sinks. *Energy Procedia*, Elsevier, v. 85, n. 2016, p. 425–432, 2016.

QU, W.; MUDAWAR, I. Analysis of three-dimensional heat transfer in micro-channel heat sinks. *International Journal of heat and mass transfer*, Elsevier, v. 45, n. 19, p. 3973–3985, 2002.

REMSBURG, R. *Advanced thermal design of electronic equipment*. [S.l.]: Springer Science & Business Media, 2011.

RENFER, A. et al. Microvortex-enhanced heat transfer in 3d-integrated liquid cooling of electronic chip stacks. *International Journal of Heat and Mass Transfer*, Elsevier, v. 65, p. 33–43, 2013.

RUNCHAL, A. *50 Years of CFD in Engineering Sciences: A Commemorative Volume in Memory of D. Brian Spalding*. [S.l.]: Springer Nature, 2020.

SHABANY, Y. Radiation heat transfer from plate-fin heat sinks. In: IEEE. *2008 Twenty-fourth Annual IEEE Semiconductor Thermal Measurement and Management Symposium*. [S.l.], 2008. p. 132–136.

SHAERI, M. R.; Bonner III, R. W. Analytical heat transfer model for laterally perforated-finned heat sinks. *International Journal of Heat and Mass Transfer*, Elsevier, v. 131, p. 1164–1173, 2019.

SIMONS, R. Estimating parallel plate-fin heat sink thermal resistance. *Electronics cooling*, v. 9, n. 1, p. 8–9, 2015. Disponível em: <http://s3.electronics-cooling.com/wp-content/uploads/2016/10/Electronics-Cooling-December-2015.pdf#page=10>.

SINGH, S.; KUMAR, D.; RAI, K. Analytical solution of fourier and non-fourier heat transfer in longitudinal fin with internal heat generation and periodic boundary condition. *International Journal of Thermal Sciences*, Elsevier, v. 125, p. 166–175, 2018.

SOBRAL, R. L. *Simulação numérica de aletas num contexto de altas temperaturas*. Tese (Doutorado) — Universidade do Estado do Rio de Janeiro, 2017.

SPALDING, B. Trends, tricks, and try-ons in cfd/cht. In: *Advances in heat transfer*. [S.l.]: Elsevier, 2013. v. 45, p. 1–78.

SPARROW, E.; ECKERT, E. Radiant interaction between fin and base surfaces. 1962.

STREETMAN, B. G.; BANERJEE, S. et al. *Solid state electronic devices*. [S.l.]: Prentice Hall Englewood Cliffs, NJ, 1995. v. 4.

TU, J.; YEOH, G. H.; LIU, C. *Computational fluid dynamics: a practical approach*. [S.l.]: Butterworth-Heinemann, 2018.

TÜRKAKAR, G.; OKUTUCU-ÖZYURT, T. Dimensional optimization of microchannel heat sinks with multiple heat sources. *International Journal of Thermal Sciences*, Elsevier, v. 62, p. 85–92, 2012.

WEI, X.; JOSHI, Y. Optimization study of stacked micro-channel heat sinks for micro-electronic cooling. *IEEE transactions on components and packaging technologies*, IEEE, v. 26, n. 1, p. 55–61, 2003.

XIA, Y.; JACOBI, A. An exact solution to steady heat conduction in a two-dimensional slab on a one-dimensional fin: application to frosted heat exchangers. *International Journal of Heat and Mass Transfer*, Elsevier, v. 47, n. 14-16, p. 3317–3326, 2004.

ZARETABAR, M.; ASADIAN, H.; GANJI, D. Numerical simulation of heat sink cooling in the mainboard chip of a computer with temperature dependent thermal conductivity. *Applied Thermal Engineering*, Elsevier, v. 130, p. 1450–1459, 2018.

ZUBAIR, S. M.; ARIF, A.; SHARQAWY, M. H. Thermal analysis and optimization of orthotropic pin fins: a closed-form analytical solution. *Journal of Heat Transfer*, American Society of Mechanical Engineers, v. 132, n. 3, p. 031301, 2010.

ÇENGEL, Y. A. *Transferência de Calor e Massa: Uma abordagem prática.* [S.l.]: McGraw Hill Education, 2012.

ÇENGEL, Y. A.; GHAJAR, A. J. *Heat and Mass Transfer:Fundamentals and Applications, 4th Edition.* [S.l.]: The McGraw-Hill Companies, Inc, 2011.

APPENDIX A – FiBaCITS algorithm comments

The FiBaCITS algorithm was developed to analyze the heat transfer in heat sinks with multiple rectangular equally-spaced fins. Non-symmetrical fins and one fin cases may be added manually. The α_{avg} for every fin array is calculated in the code as well as the channel spacing. The default fin thickness is $\delta_a = 0.04$, other fin thicknesses may be added.

Two possible dimensions for the problem are described. The "large" type simulates cm-scaled heat sinks, and the "small" type simulates mm-scaled heat sinks. The fins' height H_a and the base's height H are width W-dependents. The default fins' height is $H_a = 0.8 \times W$ and the base's height is $H = 0.1 \times W$, other values may be added.

The heat transfer coefficient is calculated considering $T_f = 298K$, $\epsilon = 0.5$, $\sigma = 5.67 \times 10^{-8}\text{W/m}^2\text{.K}^4$, thermal conductivity of air $k_f = 0.02551$ W/(m× K), the volumetric expansion coefficient $\varrho = 0.0034$, the Prandtl number Pr= 0.73, the kinematic viscosity $\nu = 1.562 * 10^{-5}$ m^2/s, the gravity $g = 9.81$ m/s^2, and the average temperature difference between the heat sink and the environment air $\Delta T_b = 25$ K. These values were considered after studing the works (BAR-COHEN; IYENGAR; KRAUS, 2003) and (FURUKAWA; YANG; TORII, 2008).

The formulation parameters $\beta_a, \text{Bi}_{H_a}, \gamma_a, m_a, A_1, A_2, \beta, \gamma, \text{Bi}_H$ were calculated in the code considering different material properties and heat sinks dimensions for H, H_a, δ_a and W.

Both 2Dbase-1Dfin and 3Dbase-2Dfin formulations are included in the code, however, the 2Dbase-1Dfin is only used for problems where the y-direction variation vanishes.

The comparison between the 2Dbase-1Dfin, 3Dbase-2Dfin, and the OpenFOAM solutions is provided in the code.

APPENDIX B – 3D base benchmark: 1D problem

During the 3D base solution development, a benchmark test was performed. The base is simplified to a 1D problem, where the analytical solution is known and can be easily demonstrated to verify the obtained solution. The scheme of this 1D problem is illustrated in figure 56.

$$\frac{\mathrm{d}^2 T}{\mathrm{d}z^2} = 0 \tag{146a}$$

$$T'(0) = -A_2 \dot{q}''_{\text{gen}} \qquad T'(H) = -\frac{1}{k}\dot{q}''_{\text{conv}}(T) = -\frac{h}{k}\left(T(H) - T_f\right) \tag{146b}$$

where $\dot{q}''_{\text{gen}}$ is the heat flux entering at the bottom of the base. This test doesn't consider fins, only convection, $\dot{q}''_{\text{conv}}(T) = h(T - T_f)$, on the overall top surface of the base.

The base formulation (20) is simplified to the following ODE:

$$\frac{\mathrm{d}^2 \Theta}{\mathrm{d}\zeta^2} = 0 \tag{147a}$$

$$\Theta'(0) = -A_2 \dot{q}''_{\text{gen}} \qquad \Theta'(1) = -\text{Bi}\Theta(1) \tag{147b}$$

The analytical solution, applying the boundary conditions, is:

$$\Theta(\zeta) = -A_2 \dot{q}''_{gen}\zeta + \frac{A_2 \dot{q}''_{gen}}{\text{Bi}} + A_2 \dot{q}''_{gen} \tag{148}$$

This solution (148) is the same obtained solving the transformed equation for the base, considering no fins and $\dot{q}_o$ as $\dot{q}''_{gen}$. Because 1D problems don't present transformed direction, the solution for the inverse term is the same of the transformed equation when $n = 0$ and $m = 0$.

Figure 56 - Simplified 1D base scheme where the system considers the heat moving from the bottom of the base of the heat sink to be cooled by the convection heat transfer mechanism.

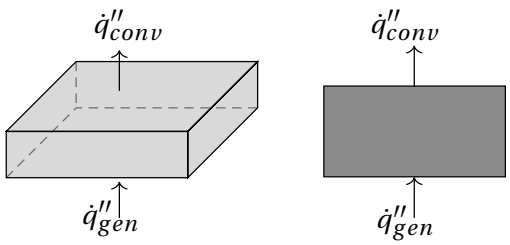

APPENDIX C – Polynomial function heat flux approach

For a first attempt to identify the fin-base interface heat flux, $\dot{q}''_{\text{base}}(\eta)$ and $\dot{q}''_{\text{fin}}(\eta)$ are modeled as a third-degree polynomial function, described on equation (149). Having the heat flux as a polynomial function, the objective of the fin-base coupling is to obtain the coefficients. It was chosen to use a third-degree function because higher-order polynomials can manifest large oscillations and, consequently, numerical errors.

$$\dot{q}''_{\text{base}}(\eta) = \dot{q}''_{\text{fin}}(\eta) = a_j\eta^3 + b_j\eta^2 + c_j\eta + d_j \tag{149}$$

where a, b, c, and d are coefficients of the heat flux function which must be determined and j is the index for the fin. Each fin has a different heat flux value and, for each j-fin, the four coefficients must be obtained. To obtain the a, b, c and d coefficients, two random positions η_x must be used. In summary, two η_x values are used to solve the coupling equations (112 and 113) twice for one fin, four values of η_x are used for 2 fins, six values of η_x are used for 3 fins and so on. After the coefficients are found, $\dot{q}''_{ic}$ is rewritten substituting the unknowns for the obtained coefficients.

The attempt of considering the fin-base interface heat flux as polynomial functions, however, is not a precise approach. The coupling using polynomials needs a few points to be matched, only the required to find the polynomial coefficients. The selected points determine that equality occurs only at those positions and not at the entire domain, hence, it provides different functions depending on the selections. Appendix D shows some results using this approach (CORRÊA; CHALHUB, 2019).

APPENDIX D – Research Publications

This appendix mentions the published and presented works during the studies at the Mechanical Engineering Graduate Program of the Universidade do Estado do Rio de Janeiro.

The article "COMPARISON BETWEEN SINGLE AND DOUBLE INTEGRAL TRANSFORMATION SOLUTIONS OF HEAT CONDUCTION IN SOLID-STATE ELECTRONICS" was published on RETERM - Revista da Engenharia Térmica, volume 18, number 2. Two different integral transform approaches are implemented in this work for modeling the temperature field in Solid State Electronics (SSE) with several heat generations in the domain of the microchip and external convection.

The article "THERMAL ANALYSIS OF HEAT SINKS FOR ELECTRONIC COMPONENTS COOLING USING INTEGRAL TRANSFORMS" was published on "Revista de Engenharia da Universidade Católica de Petrópolis" - REUCP, volume 14, number 1.

The proceeding article "THERMAL ANALYSIS OF HEAT SINKS IN SOLAR PANELS" was presented at the 17th Brazilian Congress of Thermal Sciences and Engineering in 2018. This work presents an initial approach of heat sinks using integral transforms, and the transformed equation is solved numerically.

The proceeding article "THERMAL ANALYSIS OF HEAT SINKS: AN ANALYTICAL APPROACH" was presented at the 25th International Congress of Mechanical Engineering in 2019. This work presents a similar analytical approach of heat sinks using integral transforms. For the interface contact heat flux, the third-degree polynomial function was used.

ENCIT 2018

ABCM Associação Brasileira de Engenharia e Ciências Mecânicas

17th Brazilian Congress of Thermal Sciences and Engineering
November 25th-28th, 2018, Águas de Lindóia, SP, Brazil

ENCIT-2018-0084
THERMAL ANALYSIS OF HEAT SINKS IN SOLAR PANELS

Lívia M. Corrêa
Daniel J. N. M. Chalhub
[1]Dept. of Mechanical Engineering, Group for Studies and Environmental Simulations in Reservoirs (GESAR), Rio de Janeiro State University (UERJ), Rua Fonseca Teles, 121, 20940-903, Rio de Janeiro, RJ, Brazil
livcorrea@yahoo.com.br, daniel.chalhub@uerj.br

Abstract. *This work proposes an analytical approach of the heat transfer analysis in heat sinks applied on cooling electronic components of solar panels. On the bottom of the base of the heat sink, the presence of the oncoming heat flux from a heaten solid-state electronic needs to have its heat dissipated, in order to ensure a profitable performance of the solar panel. Since the thickness of the base is small compared to other dimensions of the heat sink, a partial lumping approach in z-direction is performed and the final mathematical formulation is two dimensional, considering also the heat flux source term. In order to obtain the final solution, the Classical Integral Transform Technique is applied and four diferent cases are presented: the heat sink without any fin, with one, two fins and with four fins. The achieved results are compared by the increase of the heat dissipation affecting the final temperature of the heat sink.*

Keywords: *Thermal Analysis, Heat Sink, Classical Integral Transform Technique*

1. INTRODUCTION

The solar energy has been used since ancient civilizations for heating and light purposes. Archeological evidence has shown that many ancient cultures built their houses according the principles of passive solar design, Chen (2011). In the last centuries, however, the sun energy has been applied directly to make electricity. In 1839, Alexandre Becquerel discovered that certain materials produced small amounts of electric current when exposed to light, Shah *et al.* (1999). In 1954, D.M. Chapin, C.S. Fuller and G.L. Pearson, of Bell Laboratory, patented a way of making electricity directly from sunlight using silicon-based solar cells, Gotzberger *et al.* (2002). The solar energy and specially photovoltaics (PV) is a promising alternative source due to its advantages: abundance, pollution free and renewability and has been more and more implemented all over the world, Singh (2013).

Several researches have been studying how to enhance photovoltaic systems. It is known that high temperatures decrease the efficiency of PV systems, (Cuce and Cuce, 2012). The electronic components of solar panels system present high temperatures when in operation and this heat may affect the system's performance. Cooling them with cost-effetive modifications such as heat sinks may be a considered key point to minimize the electronic components temperature.

The thermal dissipation promoted by heat sinks has motivated several works about analysis and optimization of fins in heat sinks. The work of Teertstra *et al.* (2000) presented an analytical model to approach the average heat transfer rate for forced convection, air cooled, plate fin heat sinks. The work of Lehtinen (2005) analyzed both heat conduction and convection in fins applying well-known analytical and experimental results for convective heat transfer. The geometry of the fin was also studied for maximizing the heat transfer. The work of Ong *et al.* (2005), for instance, analysed different geometries of rectangular and cylindrical fins optimizations for maximum heat dissipation on electronic components. The behavior of different geometric parameter heat sinks with rectangular fins was also analyzed by Anselmo (2016). The work of Azarkish *et al.* (2010) investigated the geometry of the longitudinal fins with variable cross sectional area achieving its optimum fin profile using genetic algorithm. On the other hand, Cuce and Cuce (2014) tested different rectangular fins configurations to produce the maximum heat loss in a specific volume and length of fin numerically exposed to convection and radiation heat transfer.

The Integral Transform Technique is a powerful method to solve differential equations based on separation of variables method and is classified as Classical (CITT) or Generalized (GITT). The CITT is an all analytical method and is most applied in linear problems, Chalhub *et al.* (2014). The GITT is a hybrid analytical-numerical technique and transforms nonlinear partial differential equation models to a coupled nonlinear system of ordinary differential equations (ODEs) to be solved numerically. Sphaier and Cotta (2000) applied the Integral Transform Technique on the solution of a multidimensional partial differential models within irregularly shaped domains. Braga Junior (2015) also applied the GITT in order to obtain the heat transfer solution in heterogeneous mediums such as Functionally Graded Materials with variable properties. The Integral Transform Technique has been previouly applied on electronic problems. Dantas (1996) have applied the GITT for the solution of heat transfer in microchips. She considered an encapsulated microchip and also

different thermal conductivity layers over the chip thickness. Recently, Corrêa and Chalhub (2017) presented the solution of Solid State Electronics with one heat generation on its domain and solved by Classical Integral Transform Technique.

This work proposes an analytical approach to analyze the heat transfer occurence in heat sinks applied on electronic components of solar panels. On the bottom of the base of the heat sink, there is the presence of the oncoming heat flux from the heaten solid-state electronic, which needs its heat to be dissipated. The top of the base of the heat sink presents fins to increase the heat dissipation to the environment and, consequently, cool the chip. The mathematical formulation for the fins is developed and the heat transfer coefficient for convection depends on the position of the fins. The final formulation for the problem is applied on the base of the heat sink. Since the thickness of the base is small compared to other dimensions of the heat sink, a partial lumping approach in z-direction is performed and the final mathematical formulation is two dimensional, considering also the heat flux source term. In order to obtain the final solution, the Classical Integral Transform Technique is applied. In this case, however, the transformed equation cannot be solved analitically and requires a numerical discretization. A truncation error is involved since the infinite summation must be truncated. This error decreases as the number of summation terms (truncation order) is increased, and the solution converges to a final value. The results show an analysis of the proposed approach for comparison purposes of the final temperature of the heat sink without any fin, with one, with two fins and with four fins.

2. MATHEMATICAL FORMULATION OF PARALLEL PLATE FINS

For this approach, rectangular fins were modelled on the heat sink working on steady state. The boundary conditions applied on the fin are fixed temperature at the base of the heat sink (isothermal base) and convection at the fin longitudinal end.

$$\frac{\mathrm{d}}{\mathrm{d}x_a}\left(k_a A_a \frac{\mathrm{d}T}{\mathrm{d}x_a}\right) - P_a h(T - T_f) = 0 \quad \text{for} \quad 0 \le x_a \le L_a \tag{1a}$$

$$T|_{x_a=0} = T_b; \qquad -k_a \left.\frac{\mathrm{d}T}{\mathrm{d}x_a}\right|_{x=L_a} = h(T(L_a) - T_f) \tag{1b}$$

where k_a is the thermal conductivity of the fin, A_a is the transversal area of the fin, P_a is the perimeter of the fin, h is the heat transfer coefficient by convection and L_a is the length of the fin.

The nondimensionalization leads to the following mathematical formulation for the fin:

$$\frac{\mathrm{d}^2\Theta}{\mathrm{d}\xi_a^2} - m^2\Theta = 0 \quad \text{for} \quad 0 \le \xi_a \le 1 \tag{2a}$$

$$\Theta(0) = 1 \qquad \left.\frac{\mathrm{d}\Theta}{\mathrm{d}\xi_a}\right|_{x=1} = -\mathrm{Bi}_a\Theta(1) \tag{2b}$$

The non-dimensional groups are defined as:

$$\xi_a = \frac{x_a}{L_a}; \quad \Theta = \frac{T - T_f}{T_b - T_f}; \quad \mathrm{Bi}_a = \frac{hL_a}{k_a}; \quad m^2 = \frac{Bi_a P_a L_a}{A_a}; \tag{3}$$

The solution for (2a) is:

$$\Theta(\xi_a) = \frac{m\cosh(m(1-\xi_a)) + Bi_a \sinh(m(1-\xi_a))}{m\cosh(m) + Bi_a \sinh(m)} \tag{4}$$

The heat flux in each fin of the heat sink is:

$$\dot{q_a}'' = -k_a(T - T_f)\left.\frac{\mathrm{d}\Theta}{\mathrm{d}\xi_a}\right|_{\xi_a=0} \rightarrow \dot{q_a}'' = k_a(T - T_f)\frac{m\,(\mathrm{Bi}_a\cosh(m) + m\sinh(m))}{m\cosh(m) + \mathrm{Bi}_a\sinh(m)} = h_{fin}(T - T_f) \tag{5}$$

where:

$$h_{fin} = k_a \frac{m\,(\mathrm{Bi}_a\cosh(m) + m\sinh(m))}{m\cosh(m) + \mathrm{Bi}_a\sinh(m)} \tag{6}$$

3. PROBLEM FORMULATION

The mathematical formulation of the heat conduction at the base of the heat sink is given by the energy equation in steady-state after applying a partial lumping approach in z-direction.

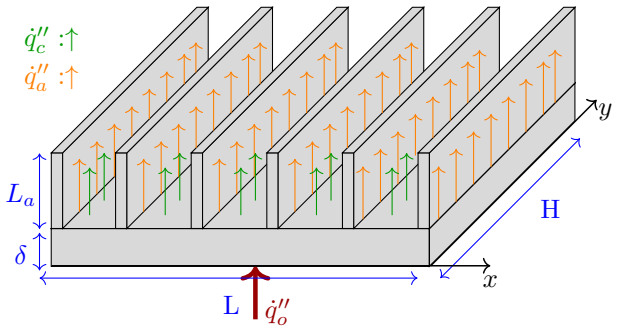

Figure 1: Schematical view of heat sink

For this work, it is considered a heat flux from the chip ($\dot{q_o}''$) acting over the heat sink. The convection flux ($\dot{q}_c''$) happens in the top surface of the heat sink, however, where the fin is located, the heat flux is the heat flux from the fin ($\dot{q_a}''$) of the heat sink:

$$\dot{q}_h''(x) = \begin{cases} \dot{q_a}'' = h_{fin}(T - T_f) & \text{if } x_{ai_K} \leq x \leq x_{af_K} \\ \dot{q_c}'' = h_{conv}(T - T_f) & \text{if } x < x_{ai_K} \text{ or } x > x_{af_K} \end{cases}$$

For this reason, is possible define the heat transfer coefficient for convection (h) dependent of its location on the base of the heat sink. On the region where the fins are located, h assume h_{fin} value and where there isn't fin h assume h_{conv} value:

$$h(x) = \begin{cases} h_{fin} & \text{if } x_{ai_K} \leq x \leq x_{af_K} \\ h_{conv} & \text{if } x < x_{ai_K} \text{ or } x > x_{af_K} \end{cases}$$

where x_{ai_K} and x_{af_K} indicates the boundaries of the K fins.

The formulation is showed bellow with its respective boundary conditions.

$$k\left(\frac{\partial^2 T(x,y)}{\partial x^2} + \frac{\partial^2 T(x,y)}{\partial y^2}\right) = \frac{\dot{q}_h''(x)}{\delta} - \frac{\dot{q}_o''(x,y)}{\delta} \quad \text{for} \quad 0 \leq x \leq L \quad \text{and} \quad 0 \leq y \leq H \tag{7}$$

$$\left.\frac{\partial T}{\partial x}\right|_{x=0} = 0; \quad \left.\frac{\partial T}{\partial x}\right|_{x=L} = 0; \quad \left.\frac{\partial T}{\partial y}\right|_{y=0} = 0; \quad \left.\frac{\partial T}{\partial y}\right|_{y=H} = 0; \tag{8}$$

where T is the temperature, k is the thermal conductivity of the plate, $\dot{q}_o''$ is the heat flux from the chip to the heat sink, T_f is the environment air temperature, h is the convection heat transfer coefficient and L, H and δ are the dimensions of the chip in x, y and z directions respectively.

The nondimensionalization of the problem leads to the following mathematical formulation:

$$\frac{\partial^2 \Theta}{\partial \xi^2} + \frac{\beta^2 \partial^2 \Theta}{\partial \eta^2} - \text{Bi}(\xi)\gamma\Theta = -Q(\xi,\eta) \quad \text{for} \quad 0 \leq \xi \leq 1 \quad \text{and} \quad 0 \leq \eta \leq 1 \tag{9}$$

$$\left.\frac{\partial \Theta}{\partial \xi}\right|_{\xi=0} = 0; \quad \left.\frac{\partial \Theta}{\partial \eta}\right|_{\eta=0} = 0; \quad \left.\frac{\partial \Theta}{\partial \xi}\right|_{\xi=1} = 0; \quad \left.\frac{\partial \Theta}{\partial \eta}\right|_{\eta=1} = 0; \tag{10}$$

The non-dimensional groups are defined as:

$$\xi = \frac{x}{L}; \quad \eta = \frac{y}{H}; \quad \Theta = \frac{T - T_f}{T_b - T_f}; \quad \beta = \frac{L}{H}; \quad \gamma = \frac{L}{\delta}; \quad \text{Bi}(\xi) = \frac{h(\xi)L}{k}; \quad Q(\xi,\eta) = \frac{\dot{q}_o'' L^2}{k\delta\Delta T}. \tag{11}$$

where β and γ are aspect ratios, $\text{Bi}(\xi)$ is the Biot number and depends of ξ, Θ is the dimensionless temperature, ξ and η are the dimensionless versions of x and y; and Q is the heat flux acting over the domain from the chip to the base of the heat sink. The chip is located at the center of the base.

4. SOLUTION BY CLASSICAL INTEGRAL TRANSFORM TECHNIQUE

In order to solve the proposed problem, the Classical Integral Transform Technique (CITT) is applied. This is an analytical technique that uses expansions of the sought solution in terms of an infinite orthogonal basis of eigenfunctions, keeping the solution process always within a continuous domain. In order to establish the transformation pair, the

temperature field is written as function of an orthogonal eigenfunctions obtained from the following auxiliary eigenvalue problem known as the Helmholtz classic problem in cartesian coordinates, where $\Psi(\eta)$ are the eigenfunctions and λ_n are the eigenvalues. For this particular problem, the case where λ= 0 also exists.

The solution of the equation (9) is defined as:

$$\Theta = \sum_{n=0}^{\infty} \frac{\bar{\Theta}(\xi)\Psi_n(\eta)}{N_n} \tag{12}$$

where $\bar{\Theta}_n(\xi)$ and $\Psi_n(\eta)$ are the functions to be solved separally in order to find the temperature field and are eigenfunctions. $\bar{\Theta}_n(\xi)$ is also the transformed version of Θ. N_n is the norm and is defined as:

$$N_n = \int_0^1 \Psi_n^2 \mathrm{d}\eta \tag{13}$$

In order to establish the transformation pair, the temperature field is written as functions of an orthogonal eigenfunctions obtained from the following auxiliary eigenvalue problem known as the Helmholtz classic problem in cartesian coordinates, where $\Psi(\eta)$ are the eigenfunctions and λ_n are the eigenvalues. For this particular problem, the case where $\lambda = 0$ also exists.

This step is solved just as separation of variables and the objective is to find the values of the eigenfunction $\Psi_n(\eta)$.

$$\Psi_n''(\eta) + \lambda_n^2 \Psi_n(\eta) = 0 \tag{14a}$$

$$\Psi_n'(0) = 0; \quad \Psi_n'(1) = 0. \tag{14b}$$

Solving the differential equation, the solution shows that the eigenfunction is formed by sines and cosines. Applying the boundary conditions, the term formed by sines is eliminated from the solution and the values of the eigenvalues λ_n are found.

For $\lambda = 0$, the solution of the eigenvalue problem is given by:

$$\Psi_0(\eta) = 1; \qquad \lambda_0 = 0; \tag{15}$$

and for $\lambda > 0$:

$$\Psi_n(\eta) = \cos(\lambda_n \eta); \qquad \lambda_n = n\pi, \quad \text{for} \quad n = 1, 2, 3, \ldots \tag{16}$$

To apply the CITT, the transformation pair is defined.

$$\text{Transformation} \quad \Rightarrow \quad \bar{\Theta}_n(\xi) = \int_0^1 \Theta \Psi_n(\eta) \mathrm{d}\eta \tag{17}$$

$$\text{Inversion} \quad \Rightarrow \quad \Theta = \sum_{n=0}^{\infty} \frac{\bar{\Theta}_n(\xi)\Psi_n(\eta)}{N_n} \tag{18}$$

The equation (9) is written again, multiplied by Ψ_n and integrated in the domain for η. The objective in this step is obtain the transformed equation by the replacement of the terms with the transformation input for the transformation term.

$$\int_0^1 \frac{\partial^2 \Theta}{\partial \xi^2} \Psi_n d\eta + \beta^2 \int_0^1 \frac{\partial^2 \Theta}{\partial \eta^2} \Psi_n d\eta - \mathrm{Bi}(\xi)\gamma \int_0^1 \Theta \Psi_n d\eta = -\int_0^1 Q \Psi_n d\eta \tag{19a}$$

Finally, the transformed equation is obtained:

- For $\lambda > 0$:

$$\bar{\Theta}_n'' - (\beta^2 \lambda_n^2 + \mathrm{Bi}(\xi)\gamma)\bar{\Theta}_n = -\bar{Q}_n(\xi) \tag{20}$$

where $\bar{Q}_n$ is given by:

$$\bar{Q}_n(\xi) = \int_0^1 Q(\xi, \eta)\Psi_n(\eta)\mathrm{d}\eta \tag{21}$$

The transformed boundary conditions are:

$$\bar{\Theta}_n'(0) = 0; \quad \bar{\Theta}_n'(1) = 0 \tag{22}$$

This equation cannot be solved analytically because of the dependence of ξ on Biot number. For this reason, the equation (20) is solved numerically using partial differential equation discretization with Finite Element Method.

- For $\lambda = 0$:

$$\bar{\Theta}_0'' - (\mathrm{Bi}(\xi)\gamma)\bar{\Theta}_0 = -\bar{Q}_0(\xi) \tag{23}$$

where $\bar{Q}_0$ is given by:

$$\bar{Q}_0(\xi) = \int_0^1 Q(\xi,\eta)\Psi_0(\eta)\mathrm{d}\eta = \int_0^1 Q(\xi,\eta)\mathrm{d}\eta \tag{24}$$

The transformed boundary conditions are:

$$\bar{\Theta}_0'(0) = 0; \quad \bar{\Theta}_0'(1) = 0 \tag{25}$$

Again, the equation cannot be solved analytically for the same previous reason and the equation (23) is solved numerically using Finite Element Method.

Finally, in order to obtain the final temperature field, the inversion formula (18) must be utilized and the summation must be truncated to a finite value ($n_{\max}$).

5. RESULTS AND DISCUSSION

After describing the problem, the parallel plate fins formulation and the solution methodology, in this section the results are shown. The heat sink (HS) presents an square dimension and, consequently, β values 1. The value of $\mathrm{Bi}\gamma$ for convection is 0.1 and on the regions where the fins are located $\mathrm{Bi}\gamma$ is 3. The heat flux from the chip is shown is figure 2a.

In the current work, four different cases were tested. The first one was the heat sink without fins, under the effects of heat flux from the chip and convection. The second case has its heat dissipation increased by one fin with width of 0.1 of the length of the heat sink. The 2D view of the heat sink is shown on figure 2b. Third case introduces two fins on the heat sink. It must be noticed that the width of each sink must be same as the previous case for heat dissipation comparison. The width of the fin affects the value of Biot and, for this reason, the same width is applied in all the fins of this work. Figure 2c shows the two-fin heat sink. Finally, a four-fin layout heat sink was tested, which is a more common heat-sink layout and is shown on figure 2d. The edges of the chip and the fins are indicated on table 1.

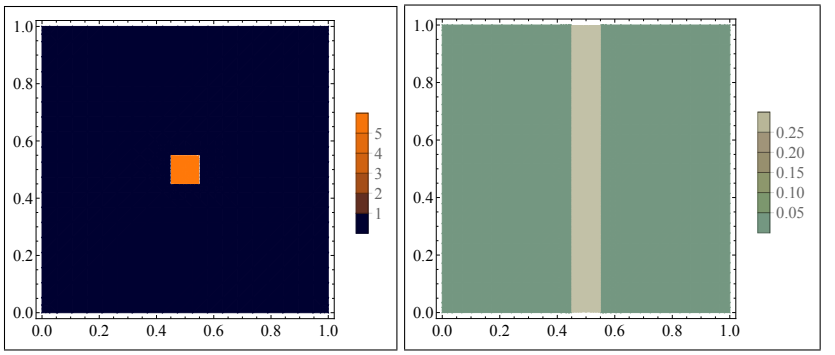

(a) Heat flux of the chip (b) One fin

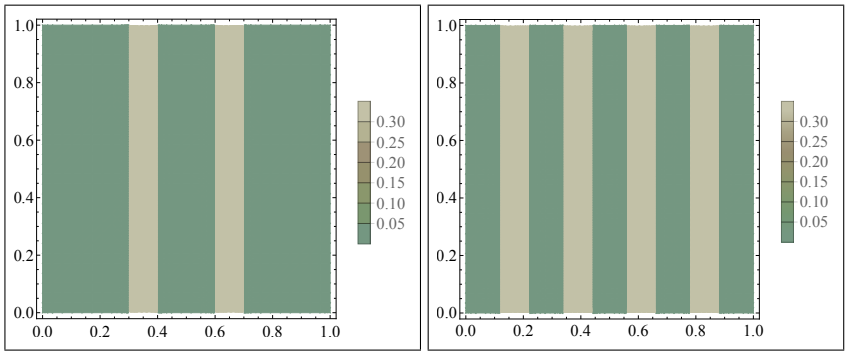

(c) Two fins (d) Four fins

Figure 2: Contour plot of the heat flux and the fin layout for the considered cases.

Table 1: Edges of chip and fins

Components of HS	ξ_i	ξ_f	η_i	η_f	Components of HS	ξ_i	ξ_f	η_i	η_f
heat flux	0.45	0.55	0.45	0.55	4-fin case	0.12	0.22	0	1
1-fin case	0.45	0.55	0	1	4-fin case	0.34	0.44	0	1
2-fin case	0.3	0.4	0	1	4-fin case	0.56	0.66	0	1
2-fin case	0.6	0.7	0	1	4-fin case	0.78	0.88	0	1

The results of convergence for the four different cases solved by CITT are presented on table 2. For analyzing the convergence of the solution six different positions of the heat sink were selected. One position is at the center of the heat sink and at the region were the chip is located, (0.5,0.5). This position (0.5,0.5) is also where is found the maximum temperature of the heat sink. Also, two positions which are not at the chip location very close, though, were selected to be analyzed, which are positions (0.42,0.58) and (0.56,0.44). The position (0.6,0.7) is next to the chip, not as close as the previous positions. And, finally, two positions far from the chip, which were (0.2,0.7) and (0.8,0.3). $n_{\max}$ refers to the number of terms which are summed before truncated.

The first part of table 2 shows the convergence obtained for no-fins case. It can be noticed that the solution converged very fast on the far-from-chip locations, in contrast, the center of the heat sink location, which is where the chip is located, the temperature is higher. At the locations near the chip, the temperature was also higher and took more terms to converge. While 10 terms were sufficient for fully convergence at (0.2,0.7), 200 terms were necessary for the convergence at (0.56,0.44).

The convergence results for one-fin case is shown on the second part of the table 2. First, it can be noticed a decreased on the temperature at all the selected positions of the heat sink, justifying the application of fins in order to increase the heat dissipation. As can be seen, a truncation order of $n_{\max} = 150$ was necessary for the convergence of position (0.5,0.5) while only 10 terms were necessary for the convergence for position (0.8,0.3). At (0.6,0.7), 20 terms were required for its fully convergence.

The convergence results for the two-fin heat sink layout are presented on the third part of table 2. The addiction of the second fin increased the heat dissipation and, consequently, the temperature of the heat sink was lower in this case. In this case, also, at the center of the heat sink, the fully convergence required 250 terms instead of 150 of the previous cases. The complexity of this case may be a reason which justify more terms to be summed. This increase of terms to be summed also happens at positions (0.42,0.58) and (0.56,0.44), which required also 250 terms for these positions solution convergence.

Finally, the last part of table 2 shows the results for the four-fin layout heat sink. Similarly from the two-fin layout, more terms were necessary for the fully convergence at (0.5,0.5), 350 terms in this position. In contrast, in this case, the position (0.42,0.58) had converged requiring less terms, 150, and (0.6,0.7) converged summing 100 terms, the same as the previous case. The temperature along the heat sink had reduced about half from the two-fin layout, which states that the efficiency of increasing fins to heat sinks in order to increase the heat dissipation and reduce the temperature.

After analyzing the CITT convergence table 2, now it is shown the thermal profile of the solution by CITT in all the four different layouts of heat sink. The figure 3a shows the solution for the heat sink without fins, the one-fin heat sink solution is shown on figure 3b and the two-fin and four-fin layout solution are figures 3c and 3d, respectively.

Analyzing figure 3a, it can be noticed at first the isotherms curves that bounds the region where the chip is located. One important detail to be noticed is also the size of the inner dark red isotherm, which presents similar dimensions as the chip. The temperature in the no-fin heat sink varies between a little more than 0.6175 and a little less than 0.5975. Figure 3b presents one fin at the center of the heat sink and the increase of the heat dissipation on the region of the fin is noticed by the darker blue stains exactly where the fin is found. The size of the inner dark red isotherm is smaller in this case, indicating again a more intense heat dissipation. Also, all the heat sink presents lower temperatures in comparison with the previous case without fins.

Figure 3c shows the CITT solution for the two-fin case, which has a visual expressive reduction of temperature where the fins are located, at $0.3 \leq \xi \leq 0.4$ and $0.6 \leq \xi \leq 0.7$. Also, the inner dark red isotherm is smaller from the one-fin case and all the heat sink presents lower temperatures from the previous cases, the maximum temperature on this heat sink does not achieve 0.1. Finally, the four-fin layout heat sink is shown in figure 3d. Because, this layout present equally spaced fins in all the extension of the heat sink, the thermal profile of this case resemble with the no-fin case. However, the inner dark red isotherm is reduced to a small point on the profile and maximum temperature at the heat sink is reduced from 0.619608, of the no-fin case, to 0.0576527 with this current layout. This four-fin case is, then, the most efficient heat sink layout shown in this work, dissipating more heat and reducing the temperature for the lower values.

Table 2: Temperature $\Theta(\xi, \eta)$ convergence for different layouts of heat sink solved by CITT

No fin						
$n_{\max}$	Θ(0.2, 0.7)	Θ (0.42, 0.58)	Θ(0.5, 0.5)	Θ(0.56, 0.44)	Θ(0.6, 0.7)	Θ(0.8, 0.3)
10	0.599113	0.608526	0.619605	0.611228	0.602554	0.599113
20	0.599113	0.608530	0.619775	0.611252	0.602550	0.599113
50	0.599113	0.608526	0.619605	0.611228	0.602551	0.599113
100	0.599113	0.608526	0.619610	0.611224	0.602551	0.599113
150	0.599113	0.608526	0.619608	0.611224	0.602551	0.599113
200	0.599113	0.608526	0.619608	0.611225	0.602551	0.599113
250	0.599113	0.608526	0.619608	0.611225	0.602551	0.599113
300	0.599113	0.608526	0.619608	0.611225	0.602551	0.599113
350	0.599113	0.608526	0.619608	0.611225	0.602551	0.599113
One fin						
$n_{\max}$	Θ(0.2, 0.7)	Θ(0.42, 0.58)	Θ(0.5, 0.5)	Θ(0.56, 0.44)	Θ(0.6, 0.7)	Θ(0.8, 0.3)
10	0.153132	0.159512	0.168785	0.161935	0.153887	0.153132
20	0.153132	0.159414	0.169485	0.161726	0.153883	0.153132
50	0.153132	0.159411	0.169315	0.161702	0.153883	0.153132
100	0.153132	0.159411	0.169320	0.161698	0.153883	0.153132
150	0.153132	0.159411	0.169318	0.161698	0.153883	0.153132
200	0.153132	0.159411	0.169318	0.161699	0.153883	0.153132
250	0.153132	0.159411	0.169318	0.161699	0.153883	0.153132
300	0.153132	0.159411	0.169318	0.161699	0.153883	0.153132
Two fins						
$n_{\max}$	Θ(0.2, 0.7)	Θ(0.42, 0.58)	Θ(0.5, 0.5)	Θ(0.56, 0.44)	Θ(0.6, 0.7)	Θ(0.8, 0.3)
10	0.0763385	0.0842956	0.0948784	0.0871884	0.0782018	0.0763385
20	0.0763385	0.0841974	0.0955795	0.0869797	0.0781976	0.0763385
50	0.0763385	0.0841937	0.0954094	0.0869557	0.0781982	0.0763385
100	0.0763385	0.0841937	0.0954142	0.0869515	0.0781981	0.0763385
150	0.0763385	0.0841936	0.0954121	0.0869519	0.0781981	0.0763385
200	0.0763385	0.0841935	0.0954119	0.0869521	0.0781981	0.0763385
250	0.0763385	0.0841936	0.0954122	0.0869520	0.0781981	0.0763385
300	0.0763385	0.0841936	0.0954122	0.0869520	0.0781981	0.0763385
350	0.0763385	0.0841936	0.0954122	0.0869520	0.0781981	0.0763385
Four fins						
$n_{\max}$	Θ(0.2, 0.7)	Θ(0.42, 0.58)	Θ(0.5, 0.5)	Θ(0.56, 0.44)	Θ(0.6, 0.7)	Θ(0.8, 0.3)
10	0.0374997	0.0465666	0.057119	0.0494305	0.0405881	0.0374997
20	0.0374997	0.0464686	0.0578201	0.0492219	0.0405839	0.0374997
50	0.0374997	0.0464649	0.0576499	0.0491979	0.0405845	0.0374997
100	0.0374997	0.0464648	0.0576547	0.0491937	0.0405844	0.0374997
150	0.0374997	0.0464647	0.0576527	0.0491941	0.0405844	0.0374997
200	0.0374997	0.0464647	0.0576525	0.0491943	0.0405844	0.0374997
250	0.0374997	0.0464647	0.0576527	0.0491943	0.0405844	0.0374997
300	0.0374997	0.0464647	0.0576528	0.0491942	0.0405844	0.0374997
350	0.0374997	0.0464647	0.0576527	0.0491942	0.0405844	0.0374997
400	0.0374997	0.0464647	0.0576527	0.0491942	0.0405844	0.0374997
450	0.0374997	0.0464647	0.0576527	0.0491942	0.0405844	0.0374997

6. CONCLUSION

This paper presented the thermal analysis of a heat sink dissipating heat from a solid-state electronic utilized on a solar panel solved by Classical Integral Transform Technique. The mathematical formulation of parallel plate fins was described and applied on the problem formulation. The ξ dependence on the Biot number made unworkable the achievement of an analytical solution for the problem. However, the numerical discretization by Finite Element Method made possible to solve the differential equations (20) and (23). To obtain the final value of θ, the $n_{\max}$ terms needed to be summed until its fully convergence.

The convergence analysis showed that CITT has a great performance having no difficulties to obtain high accuracy with very few terms in the solution summation far from the heat flux, and required more terms near the chip. The Classical Integral Transform Technique has shown to be a good alternative method for this kind of problem. Finally, the inclusion of fins performed the expected solution, which was the progressive reduction of the temperature as the number of fins with

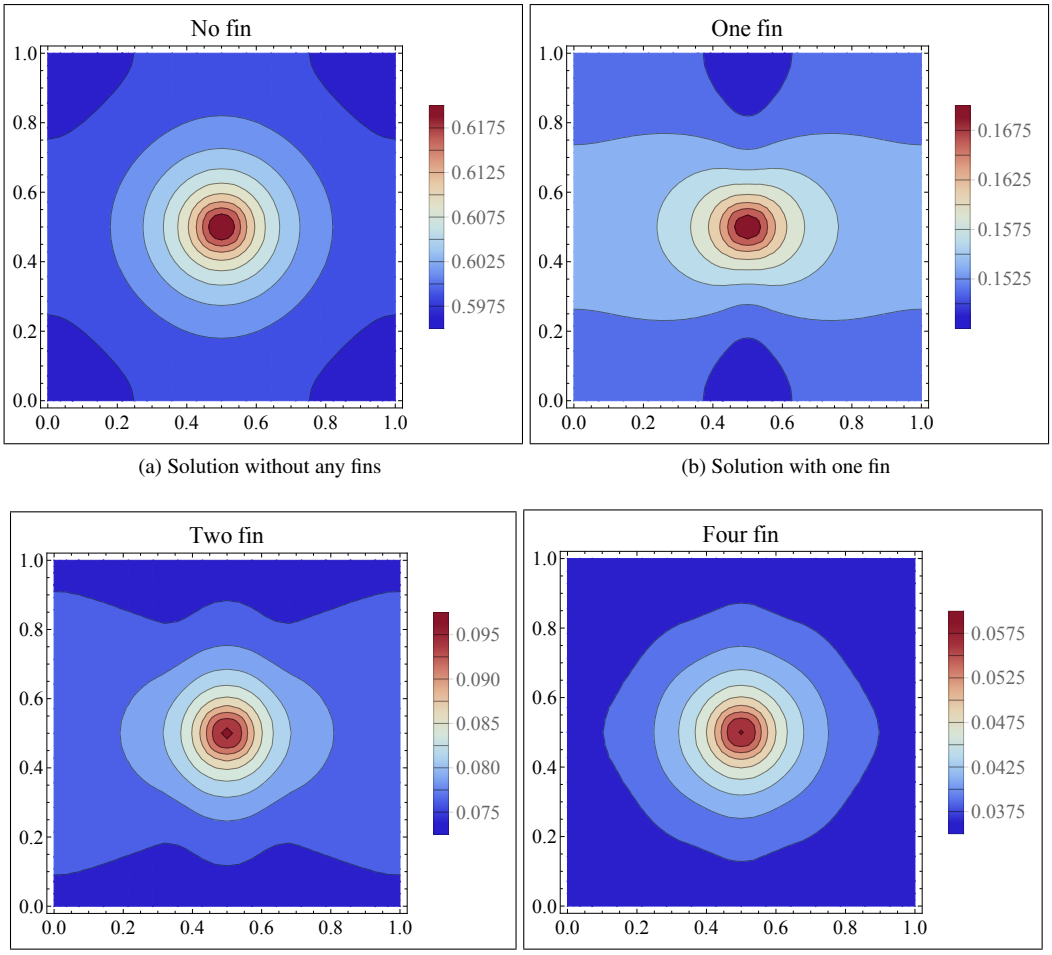

(a) Solution without any fins

(b) Solution with one fin

(c) Solution with two fins

(d) Solution with four fins

Figure 3: Contour plot of the CITT solutions for the considered cases.

same width was increased. The four-fin layout was the most efficient for dissipating the oncoming heat flux and reducing the temperature.

7. REFERENCES

Anselmo, B.C.S., 2016. *Análise dos Parâmetros Geométricos e Estatística Usando Minitab no Estudo da Convecção Natural em Dissipadores*. Master's thesis, Universidade Federal de Itajubá.

Azarkish, H., Sarvari, S.M.H. and Behzadmehr, A., 2010. "Optimum design of a longitudinal fin array with convection and radiation heat transfer using genetic algorithm". *International Journal of Thermal Sciences, Vol. 49, pg 2222-2229*.

Braga Junior, N.R., 2015. *Solução de Problemas de Autovalor em Meios Heterogêneos via Transformada Integral Generalizada*. Master's thesis, UFF.

Chalhub, D.J.N.M., Sphaier, L.A. and de B Alves, L.S., 2014. "Semi-analytical method for the solution of the poisson equation derived from the navier-stokes using integral transform". In *ASME 2014 12th International Conference on Nanochannels, Microchannels and Minichannels collocated with the ASME 2014 4th Joint US-European Fluids Engineering Division Summer Meeting*.

Chen, C.J., 2011. *Physics of Solar Energy*. John Wiley & Sons.

Corrêa, L.M. and Chalhub, D.J.N.M., 2017. "Solution of the heat conduction in solid-state electronics by integral transforms". In *24th ABCM International Congress of Mechanical Engineering*.

Cuce, P.M. and Cuce, E., 2012. "A novel model of photovoltaic modules for parameter estimation and thermodynamic assessment". *International Journal of Low-Carbon Technologies 7, 159-165*.

Cuce, P.M. and Cuce, E., 2014. "Optimization of configurations to enhance heat transfer from a longitudinal fin exposed to natural convection and radiation". *International Journal of Low-Carbon Technologies 9, pg 305-310*.

Dantas, L.B., 1996. *Estudo da Transferência de Calor por Encapsulamento Plástico Usando a Técnica da Transformada Integral Generalizada*. Master's thesis, Universidade Federal do Rio de Janeiro.

Gotzberger, A., Luther, J. and Willeke, G., 2002. "Solar cells: Past, present, future". *Solar Energy Materials and Solar Cells, vol 74, pgs 1-11*.

Lehtinen, A., 2005. *Analytical Treatment of Heat Sinks Cooled by Forced Convection*. Ph.D. thesis, Tampere University of Technology.

Ong, K.E., Lee, K.O., Seetharamu, K.N., Azid, I.A., Quadir, G.A., Zainal, Z.A. and Goh, T.J., 2005. "Optimization of fins used in electronic packing". *Microelectronics International*.

Shah, A., Torres, P., Tscharner, R., Wyrsch, N. and Keppner, H., 1999. "Photovoltaic technology: The case for thin-film solar cells". *Science VOL 285, pg 692-698*.

Singh, G.K., 2013. "Solar power generation by pv (photovoltaic) technology: A review". *Energy Volume 53, Pages 1-13*.

Sphaier, L. and Cotta, R., 2000. "Integral transform analysis of multidimensional eigenvalue problems within irregular domains". *Numerical Heat Transfer Part B*.

Teertstra, P., Yovanovich, M.M. and Culham, J.R., 2000. "Analytical forced convection modeling of plate fin heat sinks". *Journal of Electronics Manufacturing, Vol. 10, No. 4, pg 253-261*.

8. RESPONSIBILITY NOTICE

The authors are the only responsible for the printed material included in this paper.

25th ABCM International Congress of Mechanical Engineering
October 20-25, 2019, Uberlândia, MG, Brazil

COBEM-2019-0300
THERMAL ANALYSIS OF HEAT SINKS: AN ANALYTICAL APPROACH

Lívia M. Corrêa
Daniel J. N. M. Chalhub
Graduate Program of Mechanical Engineering (PPG-EM), Group for Studies and Environmental Simulations in Reservoirs (GESAR), Rio de Janeiro State University (UERJ), Rua Fonseca Teles, 121, 20940-903, Rio de Janeiro, RJ, Brazil
livcorrea@yahoo.com.br, daniel.chalhub@eng.uerj.br

Abstract. *In this work, the thermal analysis of heat sinks is proposed using an analytical approach. The mathematical modeling is composed of a three-dimensional base and two-dimensional fins. The oncoming heat flux from a heated chip attached at the bottom of the base needs to be cooled to ensure its good performance and long service life. For this reason, fins coupled at the top of the base of the heat sink are responsible for increasing the heat transfer and cool the system. Also at the top of the base, the air is flowing between fins contributing to the temperature's reduction of the system. The Classical Integral Transform Technique is applied for solving the formulation of fins and the base. The results show the more fins attached to the base, the lower is the temperature of the base in the heat sink.*

Keywords: *Thermal Analysis, Heat Sink, Classical Integral Transform Technique*

1. INTRODUCTION

The thermal management in Solid-State Electronics (SSE) has been one critical issue in the design of modern electronic devices. The size reduction and the need for a better and more efficient power dissipation have motivated several studies about the cooling of electronic components. Cost-effective modifications such as heat sinks are considered a key point to minimize SSE's temperature.

Heat sinks and, more specifically, their heat dissipation instigated several works about analysis and optimization of their fins and how to enhance it for minimum temperature, consequently avoiding over-heated SSE. The work of Teertstra *et al.* (2000) presented an analytical model to approach the average heat transfer rate for forced convection, air-cooled, plate-fin heat sinks. The work of Lehtinen (2005) analyzed both heat conduction and convection in fins applying well-known analytical and experimental results for convective heat transfer. The geometry of the fin was also studied for maximizing the heat transfer. The work of Azarkish *et al.* (2010) investigated the geometry of the longitudinal fins with variable cross-sectional area achieving its optimum fin profile using a genetic algorithm. On the other hand, Cuce and Cuce (2014) tested different rectangular fins configurations to produce the maximum heat loss in a specific volume and length of fin numerically exposed to convection and radiation heat transfer.

Some recent heat sink problems were analyzed using analytical and numerical methodologies. One can mention the research developed by Türkakar and Okutucu-Özyurt (2012) regarding a dimensional optimization of silicon heat sinks for located multiple heat sources by minimizing the thermal resistance at constant pumping power. Furthermore, the work from Singh *et al.* (2018) used the LaPlace transform technique to solve the temperature distribution of 1D fin with internal heat generation and periodic boundary condition. The work (Zaretabar *et al.*, 2018) presents a heat transfer numerical simulation of a heat sink installed on a square chip of a computer using the fourth-order Runge-Kutta method to solve the non-linear heat transfer equation. Another numerical research which was developed by Malek and Shabani (2018) simulates macro and microscope heat transfer utilizing different formulations for different scales. The used methodology is based on spectral methods, solving it numerically by spectral discretization and finite differences method. The microscope analysis uses the dual-phase lag formulation and for the macroscope problems, commercial software was used for the simulations.

The Classical Integral Transform Technique is a powerful analytical method based on the separation of variables method and is mainly applied in linear problems, (Chalhub *et al.*, 2014). Integral transforms have been previously applied to electronic problems. Dantas (1996), for example, applied the integral transform technique on an encapsulated microchip problem and obtained the solution considering different thermal conductivity layers over the chip thickness. More recently, Corrêa and Chalhub (2017) presented the solution of Solid-state Electronics with one heat generation on its domain and solved by Classical Integral Transform Technique. For dealing with heat sinks, previously, Corrêa and Chalhub (2018b) presented a heat sink analysis considering different values for the heat transfer coefficient depending on the position of the fins. Also, Pinheiro *et al.* (2018) proposed the application of the Integral Transforms for solving the conjugated

radiation-conduction in a finned-tube configuration problem.

In this work, a thermal analysis of heat sinks (HS), which dissipate the oncoming heat from a Solid State Electronic, is proposed using an analytical approach. The mathematical modeling is composed of a three-dimensional base and bi-dimensional fins. First, the Classical Integral Transform Technique is used for solving the fins formulation, in the function of the heat flux which arrives from the base, which is an unknown value. To obtain the final solution for the 3D base, the Classical Integral Transform Technique is also applied. For the base, however, two directions instead of one, as happened on the fins, need to be transformed. For this reason, it is necessary to have a double summation for the inversion term and, as a consequence, more terms were required for its full convergence. The achieved solution depends on the heat flux which leaves the base to the fin, which is an unknown value. After achieving the solutions for fins and base, they are coupled to find the value of the heat flux in the fin-base contact interface. Finally, fins and base solutions are calculated again applying the heat flux value. The results show an analysis of the proposed approach of the heat sink base's temperature with one, two and six equally spaced fins. This developed routine also includes the possibility of having non-equally spaced fins.

2. TWO-DIMENSIONAL PARALLEL PLATE FINS FORMULATION

The mathematical formulation for the heat transfer on the rectangular fins is given by the energy equation in steady state. The material is considered isotropic. Since the thickness of the fin is much smaller when compared to its height and width, a partial lumping approach is performed in the x-direction and the final formulation is two-dimensional. The convection heat flux is also considered both sides of the fin. The fin is connected to the base on its bottom surface, as indicated in Figure 2. For this reason, the lower boundary is the contact interface flux between fin-base, $\dot{q}''_{base}$, which varies on y-direction. Hence, insulation is considered on the upper end of the fin.

$$k\left(\frac{\partial^2 T(y,z)}{\partial z^2}+\frac{\partial^2 T(y,z)}{\partial y^2}\right)=\frac{2h(T-T_f)}{\Delta x} \quad \text{for} \quad 0\le y\le W \quad \text{and} \quad 0\le z\le H_a \tag{1a}$$

$$-k\left.\frac{\partial T}{\partial z}\right|_{z=0}=\dot{q}''_{base}(y); \quad \left.\frac{\partial T}{\partial z}\right|_{z=H_a}=0; \quad \left.\frac{\partial T}{\partial y}\right|_{y=0}=0; \quad \left.\frac{\partial T}{\partial y}\right|_{y=W}=0 \tag{1b}$$

where T is the temperature in ^{o}C, k is the thermal conductivity of the fin in W/(m.K), h is the convection heat transfer coefficient in W/(m^2.K), T_f is the temperature of the surrounding air in ^{o}C, $\dot{q}''_{base}$ is the contact interface flux between fin-base in W/m^2. Δx, W and H_a are the dimensions of the fin in x, y and z directions, respectively, in m.

The non-dimensionalization of the problem leads to the following mathematical formulation:

$$\frac{\partial^2\Theta}{\partial\zeta_a^2}+\gamma_a^2\frac{\partial^2\Theta}{\partial\eta^2}-(2\mathrm{Bi}_{H_a}\beta_a)\Theta=0 \quad \text{for} \quad 0\le\eta\le 1 \quad \text{and} \quad 0\le\zeta_a\le 1 \tag{2a}$$

$$\left.\frac{\partial\Theta}{\partial\zeta_a}\right|_{\zeta_a=0}=-A_1\dot{q}''_{base}(\eta); \quad \left.\frac{\partial\Theta}{\partial\zeta_a}\right|_{\zeta_a=1}=0; \quad \left.\frac{\partial\Theta}{\partial\eta}\right|_{\eta=0}=0; \quad \left.\frac{\partial\Theta}{\partial\eta}\right|_{\eta=1}=0 \tag{2b}$$

The non-dimensional groups are defined as:

$$\zeta_a=\frac{z}{H_a}; \quad \eta=\frac{y}{W}; \quad \Theta=\frac{T-T_f}{\Delta T}; \quad \beta_a=\frac{H_a}{\Delta x}; \quad \gamma_a=\frac{H_a}{W}; \quad \mathrm{Bi}_{H_a}=\frac{hH_a}{k}; \quad A_1=\frac{H_a}{k\Delta T} \tag{3}$$

where ζ_a and η are the dimensionless versions of z and y, Θ is the dimensionless temperature, β_a and γ_a are aspect ratios, Bi_a is the Biot number and A_1 is a value which combines the height of the fin, its thermal conductivity and the expected temperature range for the problem (ΔT).

3. THREE-DIMENSIONAL HEAT SINK BASE FORMULATION

The base of the heat sink presents the same materials properties of the fin and a total contact between base and fin is considered. The energy equation on the steady-state was also used for the mathematical formulation for the base, dealing now with a three-dimensional heat conduction problem. The contact interface flux between base and fin is combined with the convection flux when there is a vacancy of fins and then applied as a boundary condition on the top of the base. The oncoming heat flux from the chip is described as the boundary condition on the bottom of the base of the HS and insulation is considered for the other boundaries, in this work.

Figure 1 describes the schematic problem, their dimensions, and heat fluxes positions. It can be noticed the presence of one fin that receives the fin-base flux in all the extension of its width and the increase of the surface contact area on the system is responsible for more efficient heat dissipation of the system. The vacancy of fins allows that air cools the remain parts of the top surface of the HS, indicated by the convection flux by light blue arrows. The oncoming heat flux from the heated chip, $\dot{q}''_o$, is indicated by the red square at the bottom surface of the base.

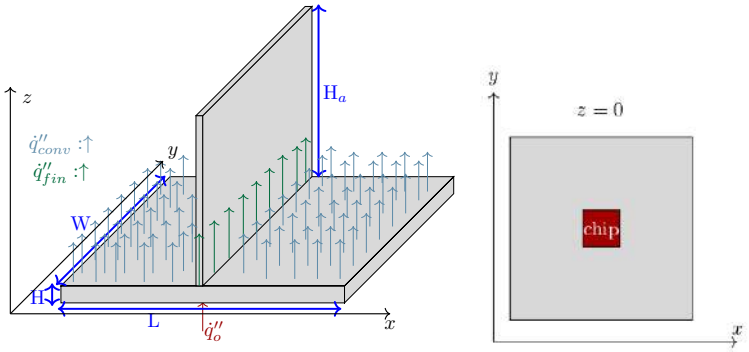

Figure 1: Heat sink front view.

The formulation for the base is shown below:

$$k\left(\frac{\partial^2 T}{\partial x^2}+\frac{\partial^2 T}{\partial y^2}+\frac{\partial^2 T}{\partial z^2}\right)=0 \quad \text{for} \quad 0\le x\le L, \quad 0\le y\le W \quad \text{and} \quad 0\le z\le H \tag{4a}$$

$$\left.\frac{\partial T}{\partial x}\right|_{x=0}=0; \quad \left.\frac{\partial T}{\partial x}\right|_{x=L}=0; \quad \left.\frac{\partial T}{\partial y}\right|_{y=0}=0; \quad \left.\frac{\partial T}{\partial y}\right|_{y=W}=0 \tag{4b}$$

$$-k\left.\frac{\partial T}{\partial z}\right|_{z=0}=\dot{q}''_o(x,y); \quad -k\left.\frac{\partial T}{\partial z}\right|_{z=H}=[\alpha(x)]\dot{q}''_{conv}+[1-\alpha(x)]\dot{q}''_{fin}(y) \tag{4c}$$

where T is the temperature in ^{o}C, k is the thermal conductivity of the base in W/(m.K), $\dot{q}''_o$ is the oncoming flux from the heated chip, $\dot{q}''_{conv}$ is the convection flux at the top of the base and $\dot{q}''_{fin}$ is the contact interface flux between fin-base, all of them in W/m^2. L, W and H are the dimensions of the fin in x, y, and z directions, respectively, in m. The parameter α is an embracing parameter to simplify the integral transform technique solution and defined as 0 or 1, indicates the position of the fins and the output flow present at a given position of x:

$$\alpha=\begin{cases}0 & \text{if the top is in contact with the fin, } (\dot{q}''_{fin}) \text{ is the boundary heat flux}\\ 1 & \text{if there is only convection in this position, } (\dot{q}''_{conv}) \text{ is the boundary heat flux}\end{cases} \tag{5}$$

The convection flux at the top of the base $\dot{q}''_{conv}$ is defined as:

$$\dot{q}''_{conv}=h(T-T_f) \tag{6}$$

where h is the convection heat transfer coefficient in W/(m^2.K) and T_f is the temperature of the surrounding air in ^{o}C.

The non-dimensionalization of the problem leads to the following mathematical formulation:

$$\frac{\partial^2\Theta}{\partial\zeta^2}+\beta^2\frac{\partial^2\Theta}{\partial\eta^2}+\gamma^2\frac{\partial^2\Theta}{\partial\xi^2}=0 \quad \text{for} \quad 0\le\xi\le 1, \quad 0\le\eta\le 1 \quad \text{and} \quad 0\le\zeta\le 1 \tag{7a}$$

$$\left.\frac{\partial\Theta}{\partial\xi}\right|_{\xi=0}=0; \quad \left.\frac{\partial\Theta}{\partial\xi}\right|_{\xi=1}=0; \quad \left.\frac{\partial\Theta}{\partial\eta}\right|_{\eta=0}=0; \quad \left.\frac{\partial\Theta}{\partial\eta}\right|_{\eta=1}=0 \tag{7b}$$

$$\left.\frac{\partial\Theta}{\partial\zeta}\right|_{\zeta=0}=-A_2\dot{q}''_o(\xi,\eta); \quad \left.\frac{\partial\Theta}{\partial\zeta}\right|_{\zeta=1}=[-\alpha(\xi)]\mathrm{Bi}_H\Theta+[\alpha(\xi)-1]\,A_2\dot{q}''_{fin}(\eta) \tag{7c}$$

The non-dimensional groups are defined as:

$$\zeta=\frac{z}{H}; \quad \eta=\frac{y}{W}; \quad \xi=\frac{x}{L}; \quad \Theta=\frac{T-T_f}{\Delta T}; \quad \beta=\frac{H}{L}; \quad \gamma=\frac{H}{W}; \quad \mathrm{Bi}_H=\frac{hH}{k}; \quad A_2=\frac{H}{k\Delta T} \tag{8}$$

where ζ, η and ξ are the dimensionless versions of z, y and x, Θ is the dimensionless temperature, β and γ are aspect ratios, Bi_H is the Biot number and A_2 is a value which combines the height of the fin, its thermal conductivity and the range of temperature expected for the problem (ΔT).

4. FIN-BASE COUPLING

Two assumptions are performed to couple the fin and base equations, which are considered having perfect contact. On the contact interface between fin and base, the temperature of the base at the top boundary and the position of the fin is the

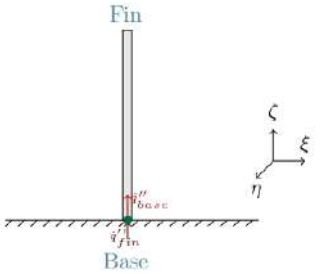

Figure 2: Fin-base coupling.

same temperature of the fin at the bottom boundary. This also happens to the heat fluxes, where the flux leaving the base on the position of the fin has the same intensity of the one which enters on the fin. Figure 2 shows a scheme in fin-base and the required conditions for the perfect interface contact, which are described below:

$$\dot{q}''_{base}(\eta) = \dot{q}''_{fin}(\eta) = \dot{q}''_{ic}(\eta) \tag{9}$$

$$\Theta_{base}(\text{position of the fin, prescripted value of } \eta, \text{ top of base}) = \Theta_{fin}(\text{prescripted value of } \eta, \text{ bottom of fin}) \tag{10}$$

Solving the equations separately so that $\dot{q}''_{base}$ and $\dot{q}''_{fin}$ are unknown values yet then, these mathematical equalities are performed and the value of $\dot{q}''_{base}$ and $\dot{q}''_{fin}$ are obtained. For this work, the heat fluxes may vary on η-direction and, for this reason, the heat fluxes $\dot{q}''_{base}$ and $\dot{q}''_{fin}$ are defined as:

$$\dot{q}''_{ic}(\eta) = \dot{q}''_{base}(\eta) = \dot{q}''_{fin}(\eta) = a_i\eta^3 + b_i\eta^2 + c_i\eta + d_i \tag{11}$$

where a, b, c and d are the coefficients for the heat flux and i defines the fin which the heat flux belongs.

The fin and base equations are solved again replacing the unknown values for the new calculated values and finally, obtaining the temperature field for the coupled fin-base heat sink.

5. SOLUTION BY CLASSICAL INTEGRAL TRANSFORM TECHNIQUE

The analytical approach of this work will be achieved utilizing the Classical Integral Transform Technique. This is an analytical technique that uses expansions of the sought solution in terms of an infinite orthogonal basis of eigenfunctions, keeping the solution process always within a continuous domain. Because we are dealing with a 2D fin and a three-dimensional base, the inversion term would have a single summation for the fin while a double summation would be necessary for the base. The single and double summation had been already discussed and compared in (Chalhub *et al.*, 2014) and (Corrêa and Chalhub, 2018a), and for both previous works, it was concluded that the double requires more terms for the full convergence. The methodology of each part of the heat sink is described below.

5.1 CITT Solution for fin

To obtain the solution for the fin, the Classical Integral Transform Technique (CITT) is applied. As a precondition to establishing the transformation pair, the temperature field is written as a function of orthogonal eigenfunctions obtained from the following auxiliary eigenvalue problem known as the Helmholtz classic problem in cartesian coordinates. The eigenvalue problem proposed to be solved on the fin is in the η direction, where $\Psi(\eta)$ are the eigenfunctions and λ_n are the eigenvalues. For this particular problem, the case where $\lambda = 0$ also exists.

$$\Psi''_n(\eta) + \lambda_n^2\Psi_n(\eta) = 0 \tag{12a}$$

$$\Psi'_n(0) = 0, \quad \Psi'_n(1) = 0 \tag{12b}$$

Solving the differential equation, the solution shows that the eigenfunction is formed by sines and cosines. Applying the boundary conditions, the term formed by sines is eliminated from the solution and the values of the eigenvalues λ_n are found.

For $\lambda = 0$, the solution of the eigenvalue problem is given by:

$$\Psi_0(\eta) = 1; \qquad \lambda_0 = 0 \tag{13}$$

and for $\lambda > 0$:

$$\Psi_n(\eta) = \cos(\lambda_n\eta); \qquad \lambda_n = n\pi, \quad \text{for} \quad n = 1, 2, 3, \ldots \tag{14}$$

The transformation pair for the fin is defined as:

$$\text{Transformation} \quad \Rightarrow \quad \bar{\Theta}_n(\zeta) = \int_0^1 \Theta \Psi_n(\eta) \mathrm{d}\eta \tag{15}$$

$$\text{Inversion} \quad \Rightarrow \quad \Theta = \sum_{n=0}^{\infty} \frac{\bar{\Theta}_n(\zeta)\Psi_n(\eta)}{N_{y_n}} \tag{16}$$

where N_{y_n} is the norm and is described in equation (32).

The equation (2a) is written again, multiplied by Ψ_n and integrated into the domain for η. The objective in this step is to obtain the transformed equation by the replacement of the terms with the transformation input for the transformation term.

$$\int_0^1 \frac{\partial^2 \Theta}{\partial \zeta_a^2} \Psi_n \mathrm{d}\eta + \gamma_a \int_0^1 \frac{\partial^2 \Theta}{\partial \eta^2} \Psi_n \mathrm{d}\eta - 2\mathrm{Bi}_{H_a} \beta_a \int_0^1 \Theta \Psi_n \mathrm{d}\eta = 0 \tag{17}$$

Finally, the transformed equation is obtained:

- For $\lambda > 0$:

$$\bar{\Theta_{a}}_n'' - (\gamma_a^2 \lambda_n^2 + 2\mathrm{Bi}_{H_a}\beta_a)\bar{\Theta}_n = 0 \tag{18}$$

The transformed boundary conditions are:

$$\bar{\Theta}_n'(0) = -A_1 \dot{q}_{base}''(\eta); \qquad \bar{\Theta}_n'(1) = 0 \tag{19}$$

- For $\lambda = 0$:

$$\bar{\Theta_{a}}_0'' - (2\mathrm{Bi}_{H_a}\beta_a)\bar{\Theta}_0 = 0 \tag{20}$$

The transformed boundary conditions are:

$$\bar{\Theta}_0'(0) = -A_1 \dot{q}_{base}''(\eta); \qquad \bar{\Theta}_0'(1) = 0 \tag{21}$$

The transformed equation achieve an analytical solution, shown on equations (22) and (23):

$$\bar{\Theta}_n(\zeta_a) = \frac{A_1 e^{\zeta \mathrm{a}\left(-\sqrt{2\mathrm{Bi}\beta \mathrm{a} + \pi^2 \gamma \mathrm{a}^2 n^2}\right)} \left(e^{2\zeta \mathrm{a}\sqrt{2\mathrm{Bi}\beta \mathrm{a} + \pi^2 \gamma \mathrm{a}^2 n^2}} + e^{2\sqrt{2\mathrm{Bi}\beta \mathrm{a} + \pi^2 \gamma \mathrm{a}^2 n^2}}\right)}{\left(e^{2\sqrt{2\mathrm{Bi}\beta \mathrm{a} + \pi^2 \gamma \mathrm{a}^2 n^2}} - 1\right)\sqrt{2\mathrm{Bi}\beta \mathrm{a} + \pi^2 \gamma \mathrm{a}^2 n^2}} \times \int_0^1 \dot{q}_{base}''(\eta)\cos(n\pi\eta)\mathrm{d}\eta \tag{22}$$

$$\bar{\Theta}_0(\zeta_a) = \frac{A_1 e^{-\sqrt{2\mathrm{Bi}\beta \mathrm{a}}\zeta \mathrm{a}} \left(e^{2\sqrt{2\mathrm{Bi}\beta \mathrm{a}}\zeta \mathrm{a}} + e^{2\sqrt{2\mathrm{Bi}\beta \mathrm{a}}}\right)}{\sqrt{2\mathrm{Bi}\beta \mathrm{a}}\left(e^{2\sqrt{2\mathrm{Bi}\beta \mathrm{a}}} - 1\right)} \int_0^1 \dot{q}_{base}''(\eta)\mathrm{d}\eta \tag{23}$$

5.2 CITT Solution for the base

After solving the transformed equation for the fin depending on $\dot{q}_{base}''$, the solution using the Classical Integral Transform Technique for the base is developed. As it was mentioned before, the three-dimensional base must be transformed in two directions, which are η, presenting a similar eigenvalue problem as the fin, and ξ.

$$\Psi_n''(\eta) + \lambda_n^2 \Psi_n(\eta) = 0 \tag{24a}$$
$$\Psi_n'(0) = 0, \quad \Psi_n'(1) = 0 \tag{24b}$$

$$\Xi_m''(\xi) + \mu_m^2 \Xi_m(\xi) = 0 \tag{25a}$$
$$\Xi_m'(0) = 0, \quad \Xi_m'(1) = 0 \tag{25b}$$

The eigenfunctions $\Psi(\eta)$ and $\Xi(\xi)$ are solved. λ_n are the eigenvalues of $\Psi(\eta)$ and μ_m are the eigenvalues of $\Xi(\xi)$.

For $\lambda > 0$:

$$\Psi_n(\eta) = \cos(\lambda_n \eta); \qquad \lambda_n = n\pi, \quad \text{for} \quad n = 1, 2, 3, \ldots \tag{26}$$

For $\lambda = 0$:

$$\Psi_0(\eta) = 1; \qquad \lambda_0 = 0 \tag{27}$$

For $\mu > 0$:

$$\Xi_m(\xi) = \cos(\mu_m \xi); \qquad \mu_m = m\pi, \quad \text{for} \quad m = 1, 2, 3, \ldots \tag{28}$$

For $\mu = 0$:

$$\Xi_0(\xi) = 1; \qquad \mu_0 = 0 \tag{29}$$

The transformation pair for the base is defined as:

$$\text{Transformation} \quad \Rightarrow \quad \bar{\bar{\Theta}}_{nm}(\zeta) = \int_0^1 \int_0^1 \Theta \Psi_n(\eta) \Xi_m(\xi) \mathrm{d}\eta \mathrm{d}\xi \tag{30}$$

$$\text{Inversion} \quad \Rightarrow \quad \Theta = \sum_{n=0}^{\infty} \sum_{m=0}^{\infty} \frac{\bar{\bar{\Theta}}_{nm}(\zeta) \Psi_n(\eta) \Xi_m(\xi)}{N_{y_n} N_{x_m}} \tag{31}$$

where $\bar{\bar{\Theta}}_{nm}$ is the transformed version of Θ. N_{y_n} and N_{x_m} are the norms and are defined in (32).

$$N_{x_m} = \int_0^1 \Xi_m^2 \mathrm{d}\xi; \quad N_{y_n} = \int_0^1 \Psi_n^2 \mathrm{d}\eta \tag{32}$$

The equation (7a) is written again, multiplied by Ψ_n and Ξ_m and integrated in the domain for η and ξ. The objective in this step is to obtain the transformed equation by the replacement of the terms with the transformation input for the transformation term.

$$\int_0^1 \int_0^1 \frac{\partial^2 \Theta}{\partial \zeta^2} \Psi_n \Xi_m \mathrm{d}\eta \mathrm{d}\xi + \beta^2 \int_0^1 \int_0^1 \frac{\partial^2 \Theta}{\partial \eta^2} \Psi_n \Xi_m \mathrm{d}\eta \mathrm{d}\xi + \gamma^2 \int_0^1 \int_0^1 \frac{\partial^2 \Theta}{\partial \xi^2} \Psi_n \Xi_m \mathrm{d}\eta \mathrm{d}\xi = 0 \tag{33}$$

For dealing with the transformed boundary condition at the top of the base, some simplifications are performed. The parameter α, which was defined previously as an embracing parameter for the integral transform simplification, and the dependence on ξ of α turns impracticable to obtain the transformed term. Consequently, $\alpha(\xi)$ is approximated to an average value α_{avg}, described on Equation (34). This approximation was performed to simplify the obtaining of the analytical solution. The convection term is written considering an average value for α, as shown below, becoming a constant value in all the domain of ξ, which values 1:

$$\alpha_{avg} = \int_0^1 \alpha(\xi) \mathrm{d}\xi \tag{34}$$

The convection term is written again, applying the α_{avg} :

$$-\int_0^1 \int_0^1 \alpha(\xi) \mathrm{Bi}_H \Theta(\xi, \eta, 1) \Xi_m(\xi) \Psi_n(\eta) \mathrm{d}\eta \mathrm{d}\xi = -\alpha_{avg} \mathrm{Bi}_H \int_0^1 \int_0^1 \Theta(\xi, \eta, 1) \Xi_m(\xi) \Psi_n(\eta) \mathrm{d}\eta \mathrm{d}\xi = \\ - \alpha_{avg}(\xi) \mathrm{Bi}_H \bar{\bar{\Theta}}_{nm} \tag{35}$$

The term which connects fin-base is rewritten substituting the $\alpha(\xi)$ for 0 at the regions where the fins are located.

$$A_2 \int_0^1 \int_0^1 (\alpha(\xi) - 1) \dot{q}''_{fin}(\eta) \Xi_m(\xi) \Psi_n(\eta) \mathrm{d}\eta \mathrm{d}\xi = -A_2 \sum_{j=1}^{\mathrm{n_{fin}}} \int_0^1 \int_{\xi_{i_j}}^{\xi_{f_j}} \dot{q}''_{fin}(\eta) \Xi_m(\xi) \Psi_n(\eta) \mathrm{d}\xi \mathrm{d}\eta \tag{36}$$

where $\mathrm{n_{fin}}$ is the number of fins, ξ_i refers to the position where the fin begins and ξ_f where it ends.

Convection and interface contact terms are reunited and the final top boundary condition which is used for solving the transformed equations is:

$$\bar{\bar{\Theta}}'(1) = -\alpha_{avg} \mathrm{Bi}_H \bar{\bar{\Theta}}(1) - A_2 \sum_{j=1}^{\mathrm{n_{fin}}} \int_0^1 \int_{\xi_{i_j}}^{\xi_{f_j}} \dot{q}''_{fin}(\eta) \Psi_n(\eta) \Xi_m(\xi) \mathrm{d}\xi \mathrm{d}\eta \tag{37}$$

Finally, the transformed equation is obtained for different values of the eigenvalues:

- For $\lambda > 0$ and $\mu > 0$:

$$\bar{\bar{\Theta}}''_{nm} - (\beta^2\mu_m^2 + \gamma^2\lambda_n^2)\bar{\bar{\Theta}}_{nm} = 0 \tag{38}$$

The transformed boundary conditions are:

$$\bar{\bar{\Theta}}'_{nm}(0) = -A_2 \int_0^1 \int_0^1 \dot{q}''_o(\xi,\eta)\Xi_m(\xi)\Psi_n(\eta)\mathrm{d}\eta\mathrm{d}\xi; \tag{39}$$

$$\bar{\bar{\Theta}}'_{nm}(1) = -\alpha_{avg}\mathrm{Bi}_H\bar{\bar{\Theta}}_{nm}(1) - A_2\sum_{j=1}^{\mathrm{n_{fin}}}\int_0^1\int_{\xi_{i_j}}^{\xi_{f_j}} \dot{q}''_{fin}(\eta)\Psi_n(\eta)\Xi_m(\xi)\mathrm{d}\xi\mathrm{d}\eta \tag{40}$$

- For $\lambda > 0$ and $\mu = 0$:

$$\bar{\bar{\Theta}}''_{n0} - (\gamma^2\lambda_n^2)\bar{\bar{\Theta}}_{n0} = 0 \tag{41}$$

The transformed boundary conditions are:

$$\bar{\bar{\Theta}}'_{n0}(0) = -A_2 \int_0^1 \int_0^1 \dot{q}''_o(\xi,\eta)\Psi_n(\eta)\mathrm{d}\eta\mathrm{d}\xi; \tag{42}$$

$$\bar{\bar{\Theta}}'_{n0}(1) = -\alpha_{avg}\mathrm{Bi}_H\bar{\bar{\Theta}}_{n0}(1) - A_2\sum_{j=1}^{\mathrm{n_{fin}}}\int_0^1\int_{\xi_{i_j}}^{\xi_{f_j}} \dot{q}''_{fin}(\eta)\Psi_n(\eta)\mathrm{d}\xi\mathrm{d}\eta \tag{43}$$

- For $\lambda = 0$ and $\mu > 0$:

$$\bar{\bar{\Theta}}''_{0m} - (\beta^2\mu_m^2)\bar{\bar{\Theta}}_{0m} = 0 \tag{44}$$

The transformed boundary conditions are:

$$\bar{\bar{\Theta}}'_{0m}(0) = -A_2 \int_0^1 \int_0^1 \dot{q}''_o(\xi,\eta)\Xi_m(\xi)\mathrm{d}\eta\mathrm{d}\xi; \tag{45}$$

$$\bar{\bar{\Theta}}'_{0m}(1) - \alpha_{avg}\mathrm{Bi}_H\bar{\bar{\Theta}}_{0m}(1) - A_2\sum_{j=1}^{\mathrm{n_{fin}}}\int_0^1\int_{\xi_{i_j}}^{\xi_{f_j}} \dot{q}''_{fin}(\eta)\Xi_m(\xi)\mathrm{d}\xi\mathrm{d}\eta \tag{46}$$

- For $\lambda = 0$ and $\mu = 0$:

$$\bar{\bar{\Theta}}''_{00} = 0 \tag{47}$$

The transformed boundary conditions are:

$$\bar{\bar{\Theta}}'_{00}(0) = -A_2 \int_0^1 \int_0^1 \dot{q}''_o(\xi,\eta)\mathrm{d}\eta\mathrm{d}\xi; \tag{48}$$

$$\bar{\bar{\Theta}}'_{00}(1) = -\alpha_{avg}\mathrm{Bi}_H\bar{\bar{\Theta}}_{00}(1) - A_2\sum_{j=1}^{\mathrm{n_{fin}}}\int_0^1\int_{\xi_{i_j}}^{\xi_{f_j}} \dot{q}''_{fin}(\eta)\mathrm{d}\xi\mathrm{d}\eta \tag{49}$$

After performing these modifications, it was achieved an analytical solution for each equation. To obtain the final temperature of the 3D-base, the inversion formula (31) is applied.

6. RESULTS

The problem was described, the parallel plate fins formulation and the solution methodology were explained. After achieving an analytical solution for base and fins formulations, the fin-base coupling was performed and the heat flux $\dot{q}''_{ic}$ was obtained. The heat flux was then applied on the base and fin solutions and now, in this section, the results are shown. For all the tested cases, it was considered a square chip, as shown in Figure 3, with a constant flux of 200000 W/m^2, β and γ value 0.25 each. The values for the fins are $\mathrm{Bi}_{H_a}\beta_a = 3$ and $\gamma_a = 0.5$. A_1 and A_2 value 5×10^{-6} and 2.5×10^{-6}, respectively.

For the first layout, it was tested a heat sink with one fin at the middle of the base with 0.1 of length. It was considered $\mathrm{Bi}_H = 0.01$ and $\alpha_{avg} = 0.9$. The layout for this first case can be observed in Figure 4a, as well as the boundary condition

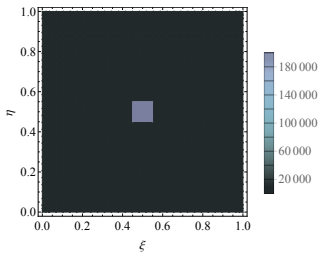

Figure 3: Chip coupled at the bottom of the base of HS and its heat flux.

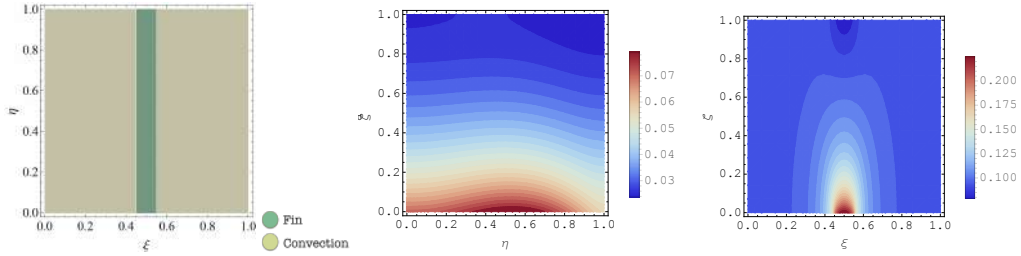

(a) Contour plot of the 1-fin Layout. (b) Solution for the fin. (c) Solution for Bi_H=0.01 with η fixed in 0.5.

Figure 4: Contour plot of the CITT solution for the 3D base(ξ, η, ζ) for the case with one fin and Bi_H=0.01.

at the top of the base of the HS. The heat flux in the fin-base contact interface is indicated on equation (50) and the thermal profile of the fin is shown in Figure 4b.

$$\dot{q}''_{ic} = \dot{q}''_{base} = \dot{q}''_{fin} = 16386.6 - 8460.39\eta + 72522\eta^2 - 74769.4\eta^3 \tag{50}$$

It can be noticed a parabolic thermal profile for the 2D-fin, whose temperature achieve 0.0789451 at the position (0.5,0), the same value at (0.5,0.5,0) on the 3D-base, which proves the assumption of the fin and base having the same temperature at their interface. At the position (0.5,1), the fin achieves $\Theta = 0.0252085$. The solution for the base is shown in Figure 4c, where isotherms curves bound the region where the chip is located in dark red, indicating warmer regions, and the position of the fin in dark blue for the regions with lower temperatures. It must be noticed the existence of ratio aspect in all the base Figures, for a better examination of the achieved results, the results are shown in a square plot. The base's hottest region is next to the chip's heat flux and the coolest region is near to the fin. Hence, it is important to be noticed the temperature field of the heat sink is not symmetric because of the non-symmetrical interface contact heat flux $\dot{q}''_{ic}$.

The second and third cases aim to evaluate how the increase of convection and fins enhance the cooling of the heat sink. The second case keeps α_{avg} and the layout of the first case and increases the value of Bi_H from 0.01 to 0.1 to evaluate how intense is the cooling of the system when the convection is intensified. The heat flux in the fin-base contact interface for this second case is indicated on equation (51) and, again, non-symmetrical interface contact heat fluxes caused not symmetric temperature field on the heat sink.

$$\dot{q}''_{ic} = 7487.2 - 8448.38\eta + 70929\eta^2 - 72980.2\eta^3 \tag{51}$$

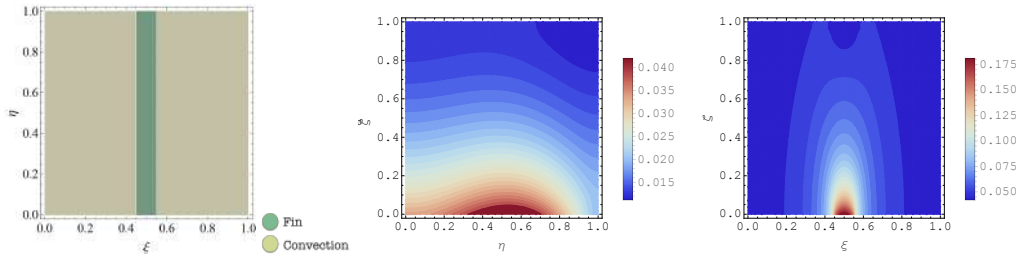

(a) Contour plot of the 1-fin Layout. (b) Solution for the fin. (c) Solution for $\mathrm{Bi}_H = 0.1$ with η fixed in 0.5.

Figure 5: Contour plot of the CITT solution for the 3D base(ξ, η, ζ) for the case with one fin in the middle of the HS and $\mathrm{Bi}_H = 0.1$.

The enhance of convection on the heat sink promoted higher thermal dissipation and reduced the temperature field on the HS, in comparison with the first case. The temperature of the 2D-fin at (0.5,0), which was 0.0789451, was reduced to

0.0419756 on this second case and at the top of the fin (0.5,1) was reduced to 0.0125758 from 0.0252085 of the previous case. However, if it is increased the number of fins in the HS, the thermal dissipation is passive and, consequently, more interesting to the industry.

The third case presents a different layout with 2 fins equally spaced from the middle of the base, shown in Figure 6a. It was considered $\mathrm{Bi}_H = 0.01$ and $\alpha_{avg} = 0.8$. Both fins presented similar non-symmetrical heat flux in the fin-base contact interface, indicated on equation (52):

$$\dot{q}''_{ic_1} = \dot{q}''_{ic_2} = 8585.24 - 743.681\eta + 24017.7\eta^2 - 27076.8\eta^3 \tag{52}$$

Because the fins present the same heat flux $\dot{q}''_{ic}$, the thermal profile is also the same, shown in Figure 6b. It can be noticed a relevant reduction on the fin temperature field in comparison with the first case tested (1 fin). This reduction in the temperature field is also noticed at the base. The temperature at the interface fin-base is 0.0415168 for both fins. The thermal profile for the base is shown in Figure 6c, where the location of the fins is indicated by darker blue color isotherm region at the top of the base.

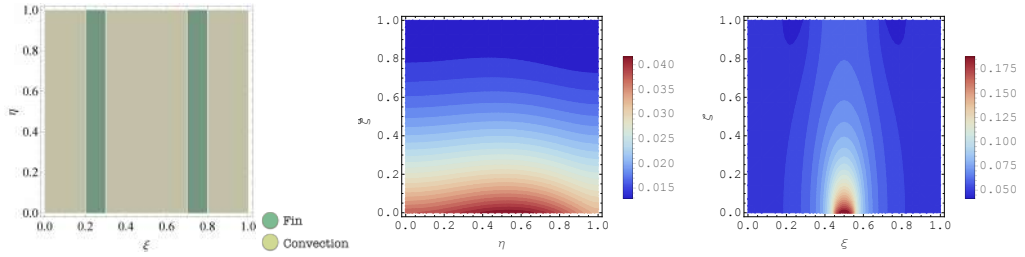

(a) Contour plot of the 2-fin Layout. (b) Solution for the fins. (c) Solution for $\mathrm{Bi}_H = 0.01$ with η fixed in 0.5.

Figure 6: Contour plot of the CITT solution for the 3D base(ξ, η, ζ) for the case with two fins on the HS and $\mathrm{Bi}_H = 0.01$.

Analyzing Figures 5b and 5c for the second case and Figures 6b and 6c for the third case, it can be noticed the temperature ranges of the fin and base bounds the same intensity. In other words, despite different thermal profiles, the increase in Biot number promoted a similar thermal dissipation in comparison with the increase in the number of fins. However, it is more profitable to increase the number of fins, which promotes passive cooling, than enhance the heat transfer coefficient convection, which would require the use of a fan or other forced convection mechanisms. For this reason, the inclusion of fins in heat sinks is a more efficient cooling mechanism.

Finally, the final case proposes a layout with six finner fins, which is a layout more usual in the industry, shown in Figure 7a. It was considered $\mathrm{Bi}_H = 0.01$ and $\alpha_{avg} = 0.7$. The thermal profile for the third fin and base are shown in Figures 7b and 7c, respectively.

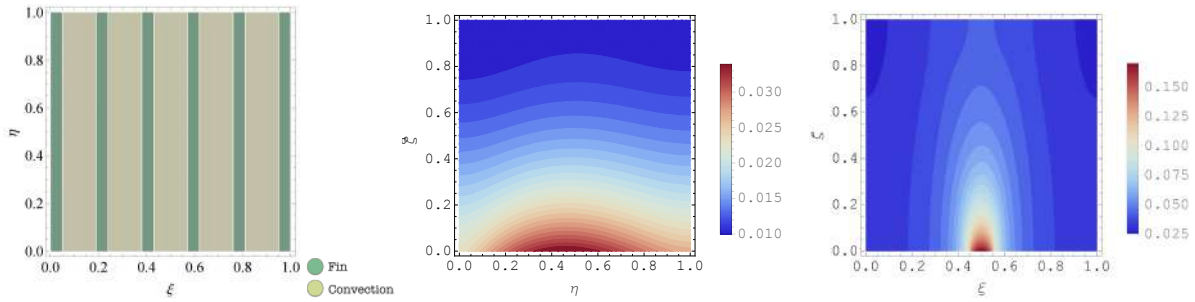

(a) Contour plot of the 6-fin Layout. (b) Solution for the third fin. (c) Solution for $\mathrm{Bi}_H = 0.01$ with η fixed in 0.5.

Figure 7: Contour plot of the CITT solution for the 3D base(ξ, η, ζ) for the case with six fins on the HS and $\mathrm{Bi}_H = 0.01$.

The fact of having more fins distributed on the overall base, in fact, decreased the overall temperature of the base of the HS, contributing for a good performance of the heated chip, which keeps sending a heat flux to the bottom base at steady-state. In other words, the temperature along the heat sink had a sensitive reduce from the one-fin layout, which states that the efficiency of increasing fins to heat sinks to increase the heat dissipation and reduce the temperature.

7. CONCLUSION

This paper presented the thermal analysis of a heat sink dissipating heat from a solid-state electronic, solved utilizing the Classical Integral Transform Technique, which has shown to be a good alternative method for this kind of problem.

The parallel plate fins were described as two-dimensional and the base was formulated as three-dimensional. First, it was solved the formulation for the fin using the CITT single transformation. After obtained the analytical solution for the 2D-fin, the formulation for the 3D-base was solved using double transformations of the CITT and also achieved an analytical approach. Both solutions were coupled considering perfect contact assumptions and the interface contact heat flux between fin and base was found. Finally, this heat flux was applied to the fins and base solutions.

Different layouts of heat sinks, consequently, promote different heat fluxes between fin-base. The temperature field for both base and fins are not symmetric because of the non-symmetrical interface contact heat flux. The increase in the number of fins or convection enhances the heat dissipation on heat sinks. However, it was shown that is more profitable to add fins than enhance the heat transfer convection coefficient. Finally, the addition of fins performed the expected solution, which was the progressive reduction of the temperature as the number of fins increased. The six-fin layout was the most efficient for dissipating the oncoming heat flux and reducing the temperature.

8. ACKNOWLEDGEMENTS

The authors would like to acknowledge the financial support provided by CNPq, CAPES and FAPERJ, Brazilian agencies for the fostering of sciences.

9. REFERENCES

Azarkish, H., Sarvari, S.M.H. and Behzadmehr, A., 2010. "Optimum design of a longitudinal fin array with convection and radiation heat transfer using genetic algorithm". *International Journal of Thermal Sciences*, Vol. 49, pp. 2222–2229.

Chalhub, D.J.N.M., Sphaier, L.A. and de B Alves, L.S., 2014. "Semi-analytical method for the solution of the poisson equation derived from the navier-stokes using integral transform". In *ASME 2014 12th International Conference on Nanochannels, Microchannels and Minichannels collocated with the ASME 2014 4th Joint US-European Fluids Engineering Division Summer Meeting*. Chicago, Illinois, USA.

Corrêa, L.M. and Chalhub, D.J.N.M., 2017. "Solution of the heat conduction in solid-state electronics by integral transforms". In *24th ABCM International Congress of Mechanical Engineering - COBEM 2017*. Curitiba, Brazil.

Corrêa, L.M. and Chalhub, D.J.N.M., 2018a. "Comparison between single and double integral transformation of heat conduction in solid-state electronics". In *X Congresso Nacional de Engenharia Mecânica - CONEM 2018*. Salvador, Brazil.

Corrêa, L.M. and Chalhub, D.J.N.M., 2018b. "Thermal analysis of heat sink on solar panels". In *17th Brazilian Congress of Thermal Sciences and Engineering - ENCIT 2018*. Águas de Lindóia, Brazil.

Cuce, P.M. and Cuce, E., 2014. "Optimization of configurations to enhance heat transfer from a longitudinal fin exposed to natural convection and radiation". *International Journal of Low-Carbon Technologies*, Vol. 9, No. 4, pp. 305–310.

Dantas, L.B., 1996. *Estudo da Transferência de Calor por Encapsulamento Plástico Usando a Técnica da Transformada Integral Generalizada*. Master's thesis, Universidade Federal do Rio de Janeiro.

Lehtinen, A., 2005. *Analytical Treatment of Heat Sinks Cooled by Forced Convection*. Ph.D. thesis, Tampere University of Technology.

Malek, A. and Shabani, S.M.A., 2018. "Solving macroscopic and microscopic pin-fin heat sink problems by adapted spectral method". *Computational and Applied Mathematics*, Vol. 37, No. 2, pp. 1112–1129.

Pinheiro, I., Sphaier, L. and de B. Alves, L., 2018. "Integral transform solution of integro-differential equations in conduction-radiation problems". *Numerical Heat Transfer, Part A: Applications*, Vol. 73, No. Issue 2, pp. 94–114.

Singh, S., Kumar, D. and Rai, K., 2018. "Analytical solution of fourier and non-fourier heat transfer in longitudinal fin with internal heat generation and periodic boundary condition". *International Journal of Thermal Sciences*, Vol. 125, pp. 166–175.

Teertstra, P., Yovanovich, M.M. and Culham, J.R., 2000. "Analytical forced convection modeling of plate fin heat sinks". *Journal of Electronics Manufacturing*, Vol. 10, No. 4, pp. 253–261.

Türkakar, G. and Okutucu-Özyurt, T., 2012. "Dimensional optimization of microchannel heat sinks with multiple heat sources". *International Journal of Thermal Sciences*, Vol. 62, pp. 85–92.

Zaretabar, M., Asadian, H. and Ganji, D., 2018. "Numerical simulation of heat sink cooling in the mainboard chip of a computer with temperature dependent thermal conductivity". *Applied Thermal Engineering*, Vol. 130, pp. 1450–1459.

10. RESPONSIBILITY NOTICE

The authors are the only responsible for the printed material included in this paper.